New electron-deficient pi-conjugated systems for potential application in organic photovoltaics.

Pablo Simon Marques

DOCTORAT MATIERE BRETAGNE MOLECULES LOIRE ET MATERIAUX

université angers

THESE DE DOCTORAT DE

L'UNIVERSITE D'ANGERS
COMUE UNIVERSITE BRETAGNE LOIRE

ECOLE DOCTORALE N° 596
Matière Molécules et Matériaux
Spécialité : Chimie Organique, Science de Matériaux

Par
Pablo SIMÓN MARQUÉS

New electron-deficient pi-conjugated systems for potential application in organic photovoltaics

Thèse présentée et soutenue à Angers, le 16 octobre 2020
Unité de recherche : Laboratoire MOLTECH-Anjou – CNRS UMR 6200
Thèse N° : 190402

Composition du Jury :

Rapporteurs

Gilles Ulrich	Directeur de Recherche CNRS, Université de Strasbourg
Sébastien Clément	Professeur des Universités, Université de Marseille

Examinateurs

Raquel Andreu	Profesor Titular de Universidad, Universidad de Zaragoza
Bruno Shmaltz	Maître de Conférences HDR, Université de Tours

Directeurs de thèse

Clément Cabanetos	Chargé de Recherche HDR, Université d'Angers
Philippe Blanchard	Directeur de Recherche CNRS, Université d'Angers

Invité

David Beljonne	Directeur de Recherche FNRS, Université de Mons

Gusanos de tierra
Comen el cuerpo que este mármol cierra,
Mas los de la conciencia en esta calma,
Hartos del cuerpo ya, comen del alma.

Epitafio a un pecador
Francisco de Quevedo

Je pense, donc je suis.

Discours de la méthode
René Descartes

…
Whoever has been beaten down must rise to his feet!
Whoever is lost must fight back!
Whoever has recognized his condition—how can anyone stop him?
Because the vanquished of today will be tomorrow's victors
And 'never' will become: 'already today'!

In praise of dialectic
Bertolt Brecht

SEPOMO project

This thesis has been carried out within the frame of a Marie Sklodowska-Curie Action (MSCA) entitled SEPOMO for 'Spin for Efficient Photovoltaic Devices based on Organic Molecules'. The mission of this research project was to attract and train promising Early Stage Researchers (ESRs) for a career in science and technology, by engaging them in exciting research and training activities regarding the field of organic solar cells. In this context, it claims to prepare a next generation of highly motivated and scholarly-trained researchers to ensure and promote the world-wide position of Europe in the field of organic electronics. The project involves fifteen ESR enrolled in ten host organizations spread in six different countries, as shown in the figure below.

RUG, The Netherlands

UOXF, United Kingdom

TUC, Germany

UW, Germany

UM, Belgium

TUD, Germany

Heliatek, Germany

EURECAT, Spain

ICMAB, Spain

UA, France

The overall scientific objectives of the project are (i) to understand and tune the spin dependent mechanisms involved in light harvesting within OSCs, as a pathway to improve the efficiency of charge generation and reduce the recombination; and (ii) to enhance the performance and lifetime of the devices.

As the ESR number 14 and within the work package related to materials and samples, some of my goals were mainly devoted to the synthesis of conjugated molecular architectures for OPV applications, including donors and non fullerene acceptors. Besides organic synthesis, I have also been trained in analytical methods including NMR, thermal characterization, optical spectroscopy, electrochemistry, the preparation and characterization of thin films and

the fabrication of photovoltaic devices. As an organic chemist, many collaborative efforts have been carried out to supply materials for our project partners, allowing them to study new materials. For instance, several donor materials were shipped to Barcelona (ICMAB and EURECAT), Dresden (TUD and Heliatek) and Groningen (RUG). On the other hand, different home-made NFAs were studied in Chemnitz (TUC) and Heliatek GmbH. Due to the ample and diverse scope of compounds prepared during the thesis, only representative examples were selected in this manuscript.

Moreover, it is important to note that I had the opportunity to spend two months in the University of Mons under the supervision of Dr David Beljonne and Giacomo Londi (ESR 7), where I was trained in theoretical calculation/computational chemistry. Performed during this Belgian secondment, the possible doping mechanisms of conjugated polymers by borane Lewis acids were thus investigated in collaboration with the Center for Polymers and Organic Solids at the University of Santa Barbara. As a result, I could now accomplish simulation of materials complementarily to my experimental research for a better structure-property relationship understanding.

Table of contents

List of abbreviations and symbols

A	Electron-accepting block/material
AM	Air mass
AIL	Anode interface layer
BDD	Benzo[1,2-*c*:4,5-*c*']dithiophene-4,8-dione
BDT	Benzo[1,2-*b*:4,5-*b*']dithiophene
BHJ	Bulk heterojunction
BODIPY	Boron-dipyrromethenes
BTXA	1*H*,3*H*-Thioxantheno[2,1,9-*def*]isochromene-1,3-dione
BTXI	2-(Alkyl)-1*H*-thioxantheno[2,1,9-*def*]isoquinoline-1,3(2*H*)-dione
BT	Benzo[*c*][1,2,5]thiadiazole
BTz	Benzo[*d*][1,2,3]triazole
CIGS	Copper indium gallium selenide
CIL	Cathode interface layer
CV	Cyclic voltammetry
CT	Charge-transfer
D	Electron-donating block/material
DCI	Dicyanovinylindanone
DCM	Dichloromethane
DCV	Dicyanovinyl
DFT	Density functional theory
DMAC	*N*,*N*-dimethylacetamide
DMF	*N*,*N*-dimethylformamide
DPP	Diketopyrrolopyrrole
dppf	Bis(diphenylphosphino)ferrocene
DSSC	Dye-sensitized solar cells
EI	Electron Impact
E_{gap}	Energy gap
E_{pa}	Oxidation peak potential (V)
E_{pc}	Reduction peak potential (V)
EQE	External quantum efficiency
ETL	Electron transporting layer
FAB	Fast atomic bombardment
Fc/Fc^{+}	Ferrocene /ferrocenium redox couple
FF	Fill factor
ffBT	Difluorobenzothiadiazole
FTO	Fluorine doped tin oxide
GmbH	*Gesellschaft mit beschränkter Haftung* (Company with limited liability)

HOMO	Highest occupied molecular orbital
HRMS	High-resolution mass spectrometry
HTL	Hole-transporting layer
HTM	Hole-transporting material
ICL	Interconnecting layer
IDT	Indacenodithiophene
IDTT	Indacenodithieno[3,2-*b*]thiophene
ITO	Indium tin oxide
FT-IR	Fourier-transform infrared
J	Current density (mA cm^{-2})
J_{max}	Maximum current density (mA cm^{-2})
J_{sc}	Short circuit current density (mA cm^{-2})
LDA	Lithium diisopropylamide
LUMO	Lowest unoccupied molecular orbital
MALDI	Matrix-assisted laser desorption/ionization
MO	Molecular orbital
MS	Mass spectrometry
Mw	Molecular weight
NBS	*N*-bromosuccinimide
NDI	Naphthalenediimide
NFA	Non-fullerene acceptor
NIR	Near infrared
NMR	Nuclear magnetic resonance
NOESY	Nuclear Overhauser effect spectroscopy
OFET	Organic field-effect transistor
OLED	Organic light-emitting diode
OPV	Organic photovoltaics
OSC	Organic solar cells
Pc	Phthalocyanine
$PC_{61}BM$	[6,6]-phenyl-C_{61}-butyric acid methyl ester
$PC_{71}BM$	[6,6]-phenyl-C_{71}-butyric acid methyl ester
PCE	Power conversion efficiency (%)
PDI	Perylenediimide
PEDOT	Poly(3,4-ethylenedioxythiophene)
PESA	Photoelectron spectroscopy in air
PHJ	Bilayer/planar heterojunction
PhD	Philosophiæ Doctor
P_i	Irradiating power (mW cm^{-2})
P_{max}	Maximum power (mW cm^{-2})
PPV	Polyparaphenyle vinylene

PSC	Perovskite solar cells
PSS	Polystyrene sulfonate
PT	Polythiophene
PV	Photovoltaics
rpm	Revolutions per minute
SCL	*Systèmes Conjugués Linéaires*
SCLC	Space charge limited current
SubPc	Subphthalocyanine
SPhos	2-Dicyclohexylphosphino-2',6'-dimethoxybiphenyl
TD-DFT	Time-dependent density functional theory
THF	Tetrahydrofuran
TLC	Thin-layer chromatography
TMS	Trimethylsilyl
toe	Tonnes of oil equivalent
TOF	Time-of-flight
TPA	Triphenylamine
T_{sub}	Sublimation temperature
UV	Ultraviolet
V	Voltage (V)
V_{max}	Maximum voltage (V)
V_{oc}	Open circuit voltage (V)
Xantphos	4,5-Bis(diphenylphosphino)-9,9-dimethylxanthene
ε	Molar extinction coefficient (L mol^{-1} cm^{-1})
η	Power conversion efficiency (%)
λ	Wavelength (nm)
μ_e	Electron mobility (cm^2 V^{-1} s^{-1})
Φ_f	Fluorescence quantum yield
Φ_Δ	Singlet-oxygen quantum yield

Chapter 1
Introduction

1 Context

Ra, Inti, Helios, Trundholm, Tonatiuh, Amaterasu… Since the dawn of humanity, the sun has received diverse names and representations among the different ages and cultures, always as a symbol of fertility, justice, and most importantly, power. Centuries later, our ancestors could not be more right.

The continuously growing world population, together with our consumerist way of life, have caused the energy demand to soar in the last decades. The energy consumption is indeed and currently estimated around 13.8 million tonnes of oil equivalent (toe) for the 2019, while "only" 8 millions were used in 2000 and 2, in the fifties.[1]

Nowadays, fossil fuels still represent an important source of energy, though the hydrocarbon supplies diminish and the greenhouse gas produced during their combustion has triggered the global warming, since their detrimental effects are undoubtedly visible. Meanwhile, nuclear energy shows similar problematics with limited uranium stocks and highly polluting waste after their use and above all, a critical risk related to the management of aging power plants.

Therefore, greener and replenishable, renewable energies have been settled as the landmark against these issues. Wind power, hydropower, solar energy, geothermal and bioenergy, are examples of the latter that already exist and are expected to replace fossil and nuclear sources in the forthcoming years to fight the climate change. In this context, this manuscript will focus on the photovoltaic conversion. The sun indeed irradiates in only one day around 6000 times the equivalent of energy that human kind consumes in one years. Albeit it is not possible to exploit all of this energy, the conversion of a simple fraction would strongly contribute in solving many of the abovementioned problems.

2 Photovoltaics

The Photovoltaic effect was discovered in 1839 by Alexandre Becquerel,[2,3] when he observed the photon-absorption phenomenon in a semiconductor material under illumination. The energy brought by the photon allows the promotion of an electron to the excited state of the semiconductor, generating a hole-electron pair named exciton that can further be dissociated in two separated charges leading to an electric current when collected at the electrodes.

Nevertheless, it was not until the mid-fifties (1954) that the first examples of photovoltaic cells were prepared.[4] Theses preliminary devices from the Bell Telephone Laboratories inspired the today well-known first generation of solar cells based on silicon p-n junction. One of the best advantages of this technology is the efficient photoconversion with a record at 26.7% for monocrystalline silicon, 22.3% for polycrystalline and 10.2% for amorphous silicon.[5,6] Together with the huge investment of the Chinese market, this technology represents 93% of the current solar panel production.[7] However, and even if prices are more than ever competitive, silicon-based solar cells suffer from many drawbacks such as the recycling issues, high weight of their modulus (that usually require floor framing modifications), their rigidity and weak efficiencies indoor or under diffused light. Consequently, all these disadvantages have prompted the development of a second generation of solar cells.

The latter is based on crystalline inorganic materials such as the CIGS (copper indium gallium selenide, $CuInGaSe_2$), GaAs (gallium arsenide) and CdTe (cadmium telluride) that show photovoltaic conversion of 23.4%, 30.5% and 25.2% respectively.[5,6] These semiconductors with improved optical absorption properties with respect to the first generation, have led to record of efficiency in single-junction structures. Besides, they can be manufactured as thin-film solar cells (with photoactive layers of few nanometer thickness), improving notably the lightness and flexibility of the devices, opening new doors to their integration into the urban landscape. Nonetheless, the scarcity of some of the constituting elements as well as their toxicity dampen their competition with silicon technology, albeit there are already implemented in several niche markets.[8]

Hence, to solve some of the issues observed with the inorganic technology such as toxicity, rigidity, processing or recycling, the third and last generation of solar cells is based on organic or hybrid (organic-inorganic) semiconductors divided in three different subfamilies namely the Dye Sensitized Solar Cells (DSSCs), the Perovskite Solar Cells (PSCs) and Organic Solar Cells (OSCs).

The concept of highly efficient DSSCs,[9,10] improved in 1991 by M. Grätzel, consists in a wide band gap inorganic semiconductor (titanium dioxide, TiO_2) sensitized on the surface by a dye and an electrolyte forming a photoelectrochemical system.[11] With at least one transparent electrode, the photoexcited dyes can transfer of one their electron into the conduction band of the inorganic oxide. The oxidized photosensitizer then accepts an electron from the electrolyte redox mediator that will be, in turn, regenerated at the counter electrode. With a rapid growth of efficiencies, these type of devices have attracted considerable research efforts. However, with a current maximum power conversion efficiency around 14%[12] and stability issues, mainly due to electrolyte leakage, researchers have turned to solution/liquid-free devices.[13]

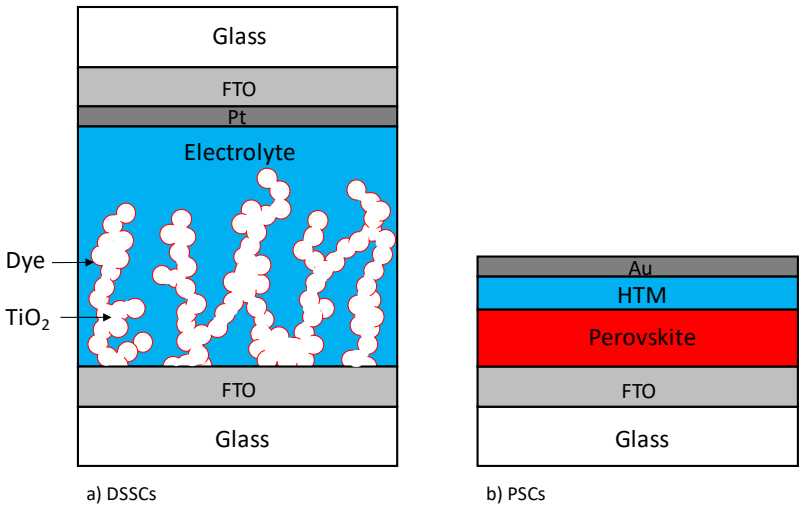

Figure 1. Architecture representation of n-type DSSCs(a) and PSCs (b).

One of the recent breakthrough was operated by Misayaka and co-workers who published in 2009 the first incorporation of a perovskite material in DSSC type solar cell as the light absorber.[14] While modest efficiencies of *ca* 3.8% were achieved, the latter were multiplied by a factor 3 in only three years by the Snaith group's (University of Oxford), by reporting a new metal halide perovskite structure ($CH_3NH_3PbX_3$ with X an halogen) and cell

design, since the electrolyte solution was simply replaced by a hole transporting material (HTM) spun-cast on top of the perovskite.[15]

From this, PSCs have created a craze within the community with more than 2000 publications per year in the last lustrum resulting in an impressive photovoltaic conversion record of 25.2%.[16,17] Even so, perovskite cells have many detractors arguing about the toxicity of the lead. Though research community is finding some solution to the important stability issues mainly related to the high moisture sensitivity of the perovskite itself, the latter drawbacks are currently hampering the large-scale implementation of this technology.[18]

Eventually, the last subcategory of the third generation, deals with OSCs consisting in organic thin films as active layers, encapsulated between two electrodes. Considering that my PhD work has been performed in this context, the structures, working principle and characteristics will be deeply developed in the following paragraph.

3 Organic Photovoltaics (OPVs)

3.1 History of OPVs

To find the first examples of solar cells employing organic materials as the main active layer, we have to move back to 1958,[19] when magnesium phthalocyanine (**MgPh**) and tetramethyl *p*-phenylenediamine (**TMPD**) were subsequently coated between two electrodes. This devices architecture, that introduced the phthalocyanine as electron-donating material and the oxidized amine film as a conductive layer, led to a very limited power output.

In the following years, attention was focused on the use of a single organic semiconductor sandwiched between two metal electrodes of different work functions. These so-called Schottky cells largely developed in the seventies, embedded heterocyclic macrocycles stemming from/or involved in the photosynthesis process such as porphyrins as well as phthalocyanines[19–21] and other dyes like merocyanines[22] and squaraines.[23]

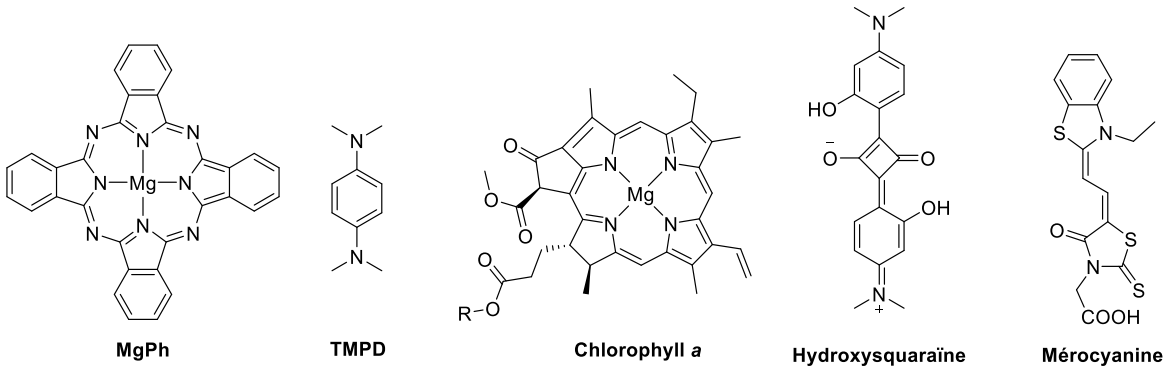

Figure 2. Chemical structure of the first organic semiconductors introduced in OSCs.

The photovoltaic conversions obtained with these single-material devices were notably inefficient (< 1%). In these devices, the strongly bounded hole-electron pair, namely the exciton, created after absorption of the light by the organic layer, could not easily dissociate in free charges due to the poor driving forces of the electrodes and thereby, most of the power was dissipated from recombination losses.

It was not until 1986 that the donor-acceptor concept was once reconsidered and renewed.[24] Tang indeed prepared and reported a bilayer structure with two organic materials with different electron-affinity and ionization potentials. By combining copper phthalocyanine (**CuPc**) as the electron-donating compound and a perylenebisbenzimidazole (**PCTBI**) as the electron-accepting material, resulting in a better exciton dissociation, a promising power conversion efficiency of *ca* 1% was reached.

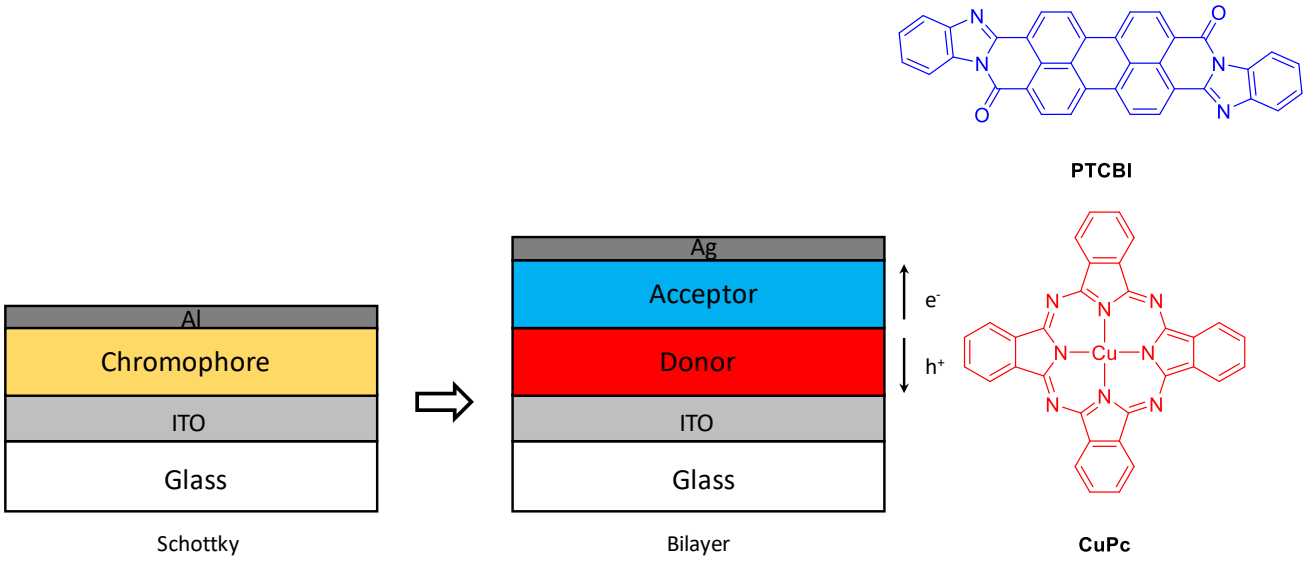

*Figure 3. Architecture of Schottky and Tang's devices and chemical structure of **CuPc** and **PTCBI**.*

This achievement, thus introducing the concept of donor-acceptor heterojunction by combining a semiconductor with good hole transport properties (donor) with another one presenting antagonist properties, *i.e.*, good electron transport features (acceptor), has been taken up over decades and is still considered for the evaluation of new materials. Consequently, this planar heterojunction architecture is ideal to explain the working principle of an organic solar cell.

3.2 Working Principle

Usually, the generation of a photocurrent in a heterojunction type OSCs results from, the absorption of photons by both the donor or the acceptor material in the active layer.[25]

Hence, the absorption of an incident photon promotes an electron from one semiconducting-material highest-occupied molecular orbital (HOMO) into its lowest unoccupied molecular orbital (LUMO), creating an electron-hole pair, so-called an exciton. The latter migrates to the donor-acceptor heterojunction, where the Coulomb attractions should be overcome to generate free charges carriers. Consequently, with optimized energy levels, the exciton can dissociate into an electron and a hole, leading to the electron-transfer from the donor to the acceptor material (Channel 1, Figure 4. left) or a hole-transfer from the acceptor to the donor (Channel 2, Figure 4. right).

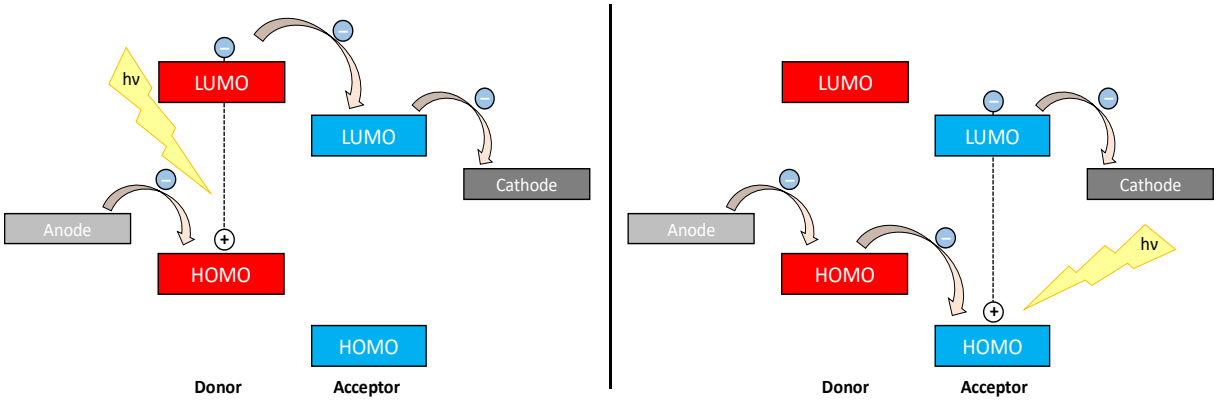

Figure 4. Energetic diagram of photocurrent generation process. Donor as light absorber (left) and acceptor as light absorber (right).

Thereafter, the applied electric field drives the separated charges carriers to their respective electrodes. In an ideal photovoltaic system, this process is envisaged with high quantum yield producing a large photocurrent generation. Nevertheless, other complex phenomena during the progression hamper its completion through charge recombination,

exciton non-radiative decay leading to low exciton lifetime, or other factors such as improper morphology and modest charge mobility.[26,27] These topics trigger the attention of experimental and theoretical physicists/physicochemists that help to shed light on the mechanisms of generation and extraction of charges, though it will not be further explain herein.

3.3 Device Characterization

The performances of solar cell devices are assessed by measuring the current, voltage, maximum power and efficiency generated after irradiation by light, which is partially converted into electric power. Depicted in Figure 5, the *J-V* graph is the most common plot used for characterization. Representing the current density *J vs* the bias *V* applied to the electrodes, keys parameters can be extracted for better understanding of the working features of OSCs.

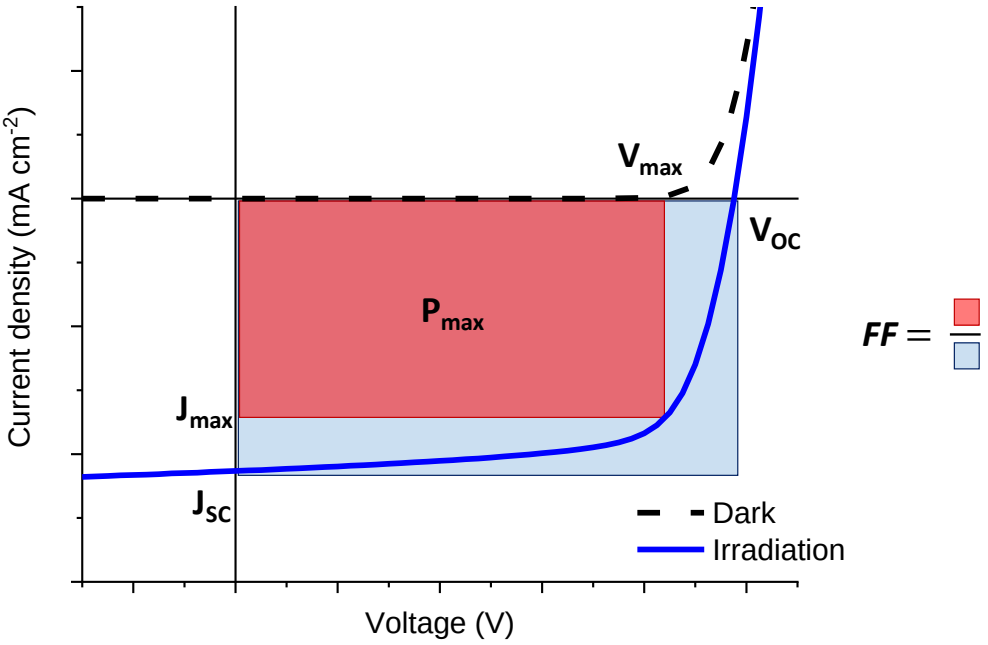

Figure 5. J-V curves of an OSC in the dark and under illumination and extracted parameters.

- **Open circuit voltage** (V_{OC}, units in V) matches with the bias obtained once the current is equal to zero. This value is directly proportional to the energy differences between

the HOMO of the donor and the LUMO of the acceptor.[27] However, it has been demonstrated that this parameter is also affected by several factors including the morphology (crystallinity) or thermodynamic and non-radiative recombination (V_{OC} losses).

- **Short circuit current density** (J_{SC}, units in mA.cm^{-2}), conversely is the current measured when the applied voltage is null. Linked to the active layer absorption and thereby, to its thickness, other factors such as the exciton non-geminated recombination and charge mobilities are known to affect this value.
- The **fill factor** (*FF*, %) is defined as the quotient of the maximum power (P_{max}) by the product of J_{SC} and V_{OC} (eq. 1). The *FF* gives an estimation of the *J-V* curve ideality. Many factors like geminated recombination, charge transport or the interlayer contacts have repercussions on this term.

$$FF = \frac{P_{max}}{V_{OC} \times Jsc} = \frac{V_{max} \times J_{max}}{V_{OC} \times Jsc} = \frac{\square}{\square} \quad (1)$$

- **Power conversion efficiency** (PCE or η) of a solar cell device, is the electric power measured with respect to the irradiated one. Hence, it is usually calculated by dividing the P_{max} by the incident light power (P_i) (eq. 2), normally an Air Mass 1.5 Global (AM 1.5 G) of 100 mW.cm^{-2}.

$$PCE = \frac{P_{max}}{P_i} = \frac{V_{OC} \times J_{SC} \times FF}{P_i} \quad (2)$$

Besides the *J-V* curves the External Quantum Efficiency (EQE), also known as Incident-photon-to-electron Conversion Efficiency (IPCE), is another of the fundamental parameters to evaluate the performances of a solar cell. It affords the estimated number of collected electrons in the circuit per incident photons at each wavelength (Figure 6).

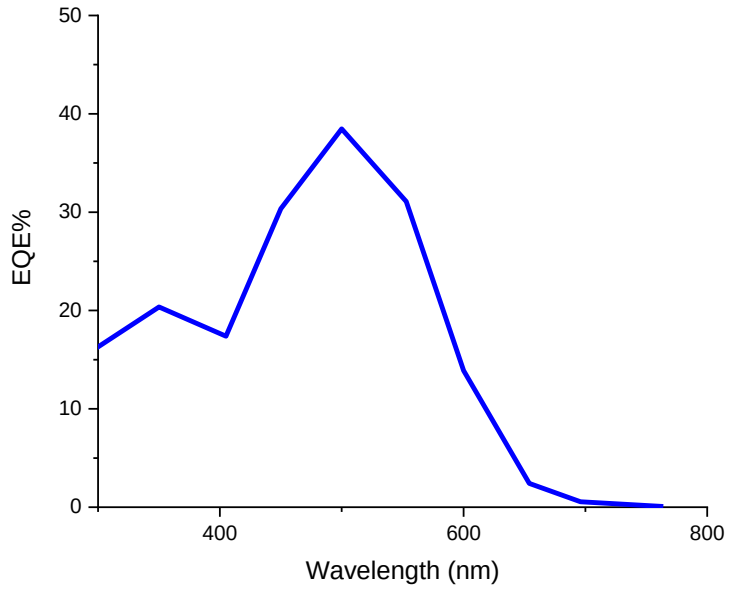

Figure 6. EQE spectrum of an OSC.

This experiment is generally correlated to the absorption patterns of the active layer constituting materials and used to evaluate their respective contributions.

3.4 Organic Solar Cells Architecture

The abovementioned bilayer or planar heterojunction (PHJ) architecture, developed by Tang (*vide infra*), was rapidly adopted by the OSC community and even today is still widely used to evaluate the potential of new organic materials.[28] Although really accessible and highly reproducible, the short exciton life-time in organic semiconductors limits their diffusion to *ca* 20 nm.[29,30] Consequently, the thickness of the constituting layers is tied to this magnitude, thus limiting the light absorption and subsequently the J_{SC} of the device. To tackle this issue, a new OSC architecture, called bulk heterojunction (BHJ), was investigated by different groups in the first half of the nineties.[31,32] In this architecture, the donor and acceptor materials are blended together and deposited as a single film, creating interpenetrated networks (Figure 7).

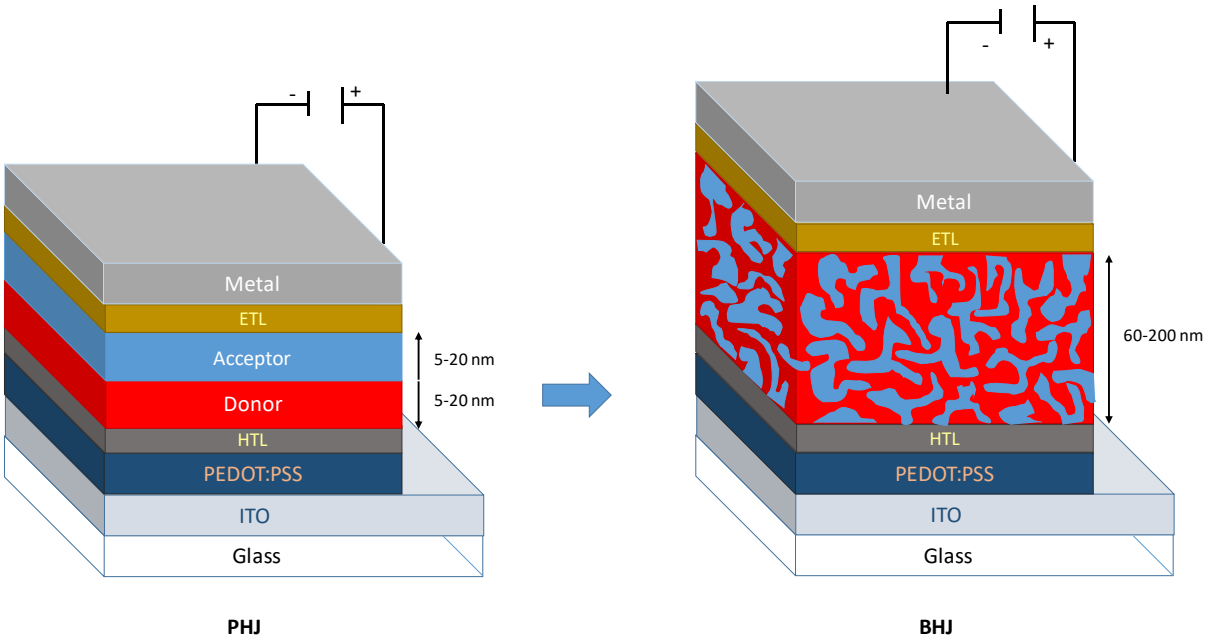

Figure 7. Architecture representation of PHJ (left) and BHJ (right) devices.

The domain distribution usually allows thicker active layers and increases the surfaces contact, thus improving the absorption and exciton dissociation. Nevertheless, controlling the formation of these nanodomains (*ca* 20 nm), able to transport the charge to the electrodes, appeared challenging and required many empirical optimizations.

Regarding the structure of the solar cells, the "standard" or "conventional" configuration uses a transparent anode (mainly indium tin oxide, ITO) on top of a transparent substrate (glass or plastic). Before depositing the donor and the acceptor material, it is common to find different interlayers. Conductive materials (*e.g.* PEDOT:PSS, MoO_x)[33,34] and hole-transporting layers (HTL, *e.g.* **α-NPB**, **BPAPF**) are introduced to flatten and smoothen the surface and to improve the hole extraction at the anode.[35,36] Eventually, an electron-transporting layer (ETL, *e.g.* **BCP**, LiF)[37,38] precedes the metal cathode, typically Al or Ca. These devices usually suffer from stability issues, mainly due to the hygroscopic nature of the ETL and cathodes, and require drastic encapsulation processes to reach decent lifetimes.

To tackle this problem, the concept of "inverted" solar cells has been introduced and follows similar layer assemble, albeit with an upside down charge movements. Indeed, by applying an interlayer over the ITO such as ZnO or TiO_x,[39,40] a transparent cathode can be obtained. In contrast, the anode becomes the top-layer, being a non-moisture sensitive metal (*e.g.* Au, Ag) with higher work function than the cathode.

Beyond improving the stability, such architecture is compatible with the fabrication of multi-junction solar cells that have recently reached record efficiencies of *ca* 18%. For instance, tandem devices correspond to the superimposition of two (or more) sub-cells connected in series with complementary absorption. As a result the V_{oc} obtained is the sum of each sub-cell and the absorption is extended to a wider energy range of photons, improving noteworthy the OSCs parameters.[41] Nonetheless, the architecture of tandem configurations are complex and the control of the morphology, contact interfaces and interlayers is not straightforward and require specific facilities and practical skills.

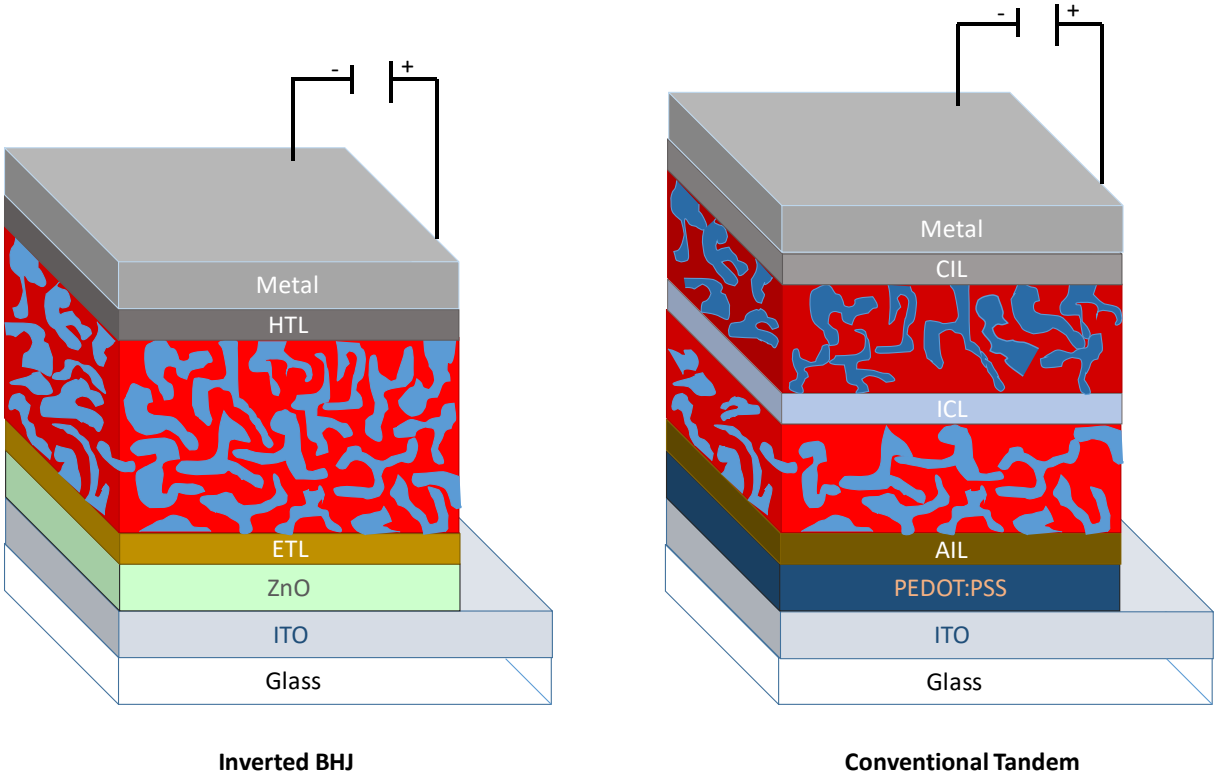

Figure 8. Architecture representation of inverted BHJ (left) and conventional tandem (right) devices. AIL stands for anode interface layer; ICL for interconnecting layer and CIL for cathode interface layer.

3.5 Donor Materials

3.5.1 Conjugated Polymers

Due to their exceptional electronic and morphological properties,[42–44] conjugated polymers were set as promising organic materials for OPVs. Macromolecular conjugated structures, prepared by connecting different aromatic or heteroaromatic cycles,[45,46] represent the most studied family within the donor organic semiconductors applied to organic solar cells.

The first promising results were generated in BHJ configuration with poly(*p*-phenylene vinylene) (PPV) derivatives that afforded efficiencies of *ca* 3% when combined with a fullerene derivative as acceptor.[47,48] Thereafter, efforts to enhance the absorption in the visible range drove the research to use less aromatic cycles than benzene to favor the π-electronic delocalization. In this context, polythiophene (PT) derivatives have been largely investigated. Besides, the limited solubility of polythiophene itself, encouraged the introduction of solubilizing alkyl chains at the β-position of thiophene affording poly(3-alkylthiophenes), P3ATs, *e.g.* poly(3-methylthiophene) **P3MT** and poly(3-octylthiophene) **P3OT**, which show better processability.[49] Among all, the regioregular poly(3-hexylthiophene) (**P3HT**) played a crucial role in the BHJ OSC progress and appears to be one of the most studied polymer. When **P3HT** is blended with the [6,6]-phenyl-C_{61}-butyric acid methyl ester (**$PC_{61}BM$**) in OSCs, PCEs starting from scratches and going up to 5% have been reported,[50] while even *ca* 7% efficiency has been reached by using a non-fullerene acceptor (NFA).[51] However, the potential of **P3HT**-based solar cells is limited by its high HOMO level (*ca* - 5.1 eV) and large optical band gap (1.9 eV). To tackle this issue, electron-withdrawing esters were introduced in the **PDCBT** backbone, reaching impressive conversions of 7.2% with [6,6]-phenyl-C_{71}-butyric acid methyl ester (**$PC_{71}BM$**)[52] and more than 10% with a NFA (**ITIC**).[53]

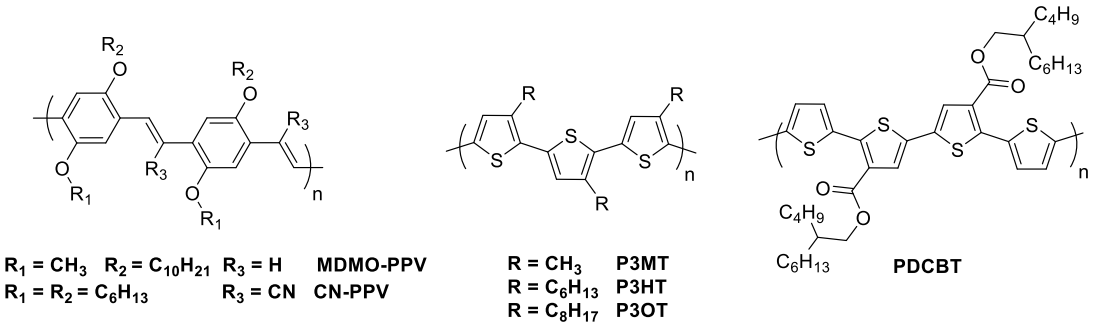

*Figure 9. Chemical structure of **PPV** and **PT** polymers.*

Consequenlty, copolymers $(D\text{-}A)_n$ built by alternating an electron-rich and an electron-deficient units have been recognized as the predominating configuration to achieve low-band gap materials and successful photovoltaic performances. By modifying the electron density of the monomers and the internal push-pull effect, the optical and electronic properties can be easily tuned to harvest more solar energy. To that end, the copolymerization of the electron-rich benzo-[1,2-*b*:4,5-*b'*]dithiophene (BDT) and the ester-substituted thieno[3,4-*b*]thiophene (TT) as the electron-deficient unit, resulted in a new family entitled the PTB (Figure 10). For

instance, subsequent modification of the functional groups and side-chain substitution afforded high-performance polymer donors, such as **PTB7**, **PTB7-Th** or **PBDT-TS1**.[54] After optimization of these polymer:**$PC_{71}BM$** based devices, milestone PCEs exceeding the 10% have been shown.[55] Indeed, the excellence of these materials has prompted the commercial availability of this family, especially **PTB7-Th**, which has been screened with numerous NFAs, yielding impressive achievements.[56,57]

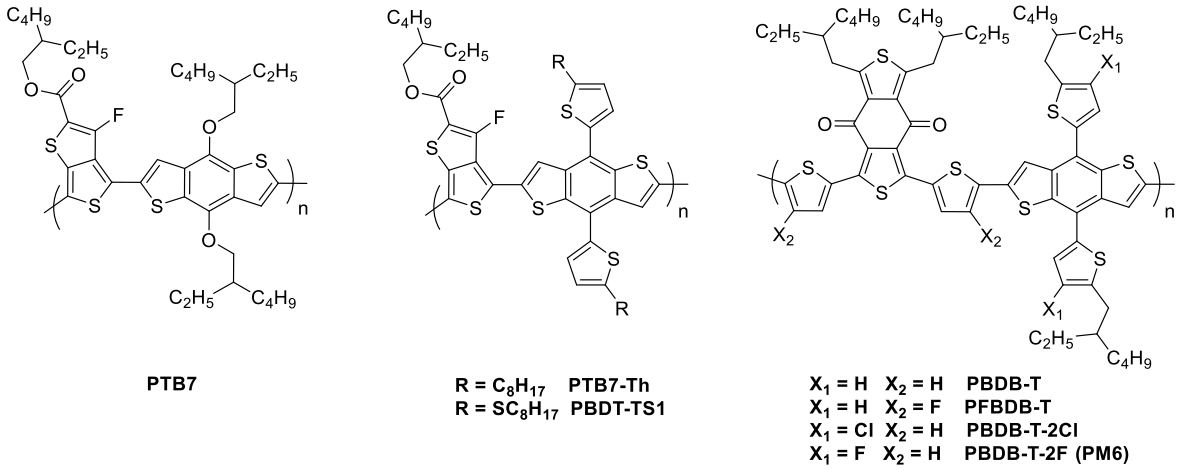

*Figure 10. Chemical structure of **PTB** and **BDD** polymers.*

Following this trend, by coupling the donor BDT block with the accepting benzo-[1,2-*c*:4,5-*c'*]dithiophene-4,8-dione (BDD) unit, Hou *et al.* synthesized the **PBDB-T** *(vide supra)*.[58] It turned out that the introduction of the BDD building block favors the intramolecular π-π interactions thanks to the large planar framework. This wide-band gap polymer has played an important role for the NFA-based organic solar cells, since some of the breakthroughs obtained in the last decade were performed using this material or derivatives. Several publications were directly focused on functionalizing the **PBDB-T** with electron-withdrawing halogen atoms such as fluorine or chlorine. These slight modifications induce a red-shifted absorption, a stabilization of the HOMO level and strengthened the intermolecular interactions, leading to excellent PCEs when blended with suitable indacenodithieno[3,2-*b*]-thiophene NFAs (*e.g.* **PFBDBT-T**, 13.2%; **PBDB-T-2Cl**, 14.4%).[59,60] Notably, the **PBDB-T-2F** analogue, also called **PM6**, has become more recently the polymer *"à la mode"*, owing to current records achieved with the thienothienoindole-based NFAs reaching PCEs of *ca* 15% (see paragraph below on NFAs).

On the other hand, benzothiadiazole (BT) is also a well-known electron-withdrawing scaffold that has been widely used in organic electronics and therefore organic photovoltaics. Though plenty of conjugated D-A polymers have been synthesized, results obtain with difluorobenzothiadiazole (ffBT) and oligothiophene based copolymers should be highlighted (Figure 11).[61–63]

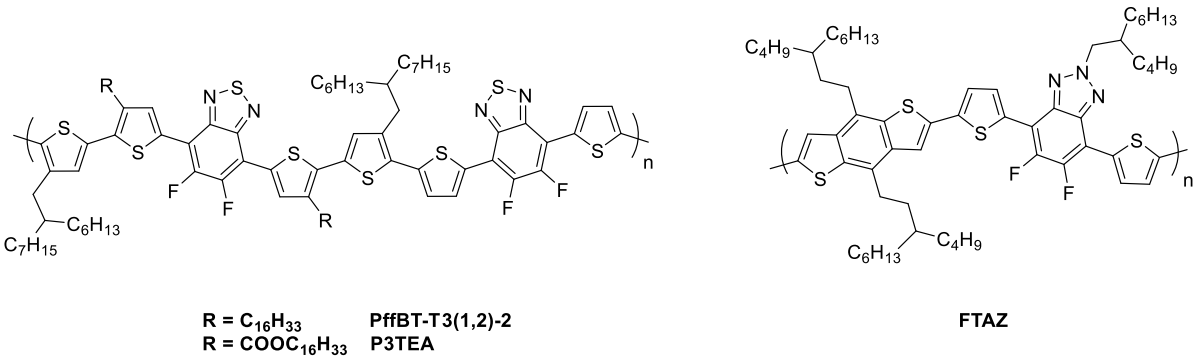

*Figure 11. Chemical structure of **BT** and **BTz** polymers*

These materials indeed showed an interesting temperature-dependent aggregation, providing a subtle tool to affect the morphology of the blend and thereby, optimizing the active layer. Yan *et al.* prepared in 2016 the **PffBT-T3(1,2)-2** polymer that performed well with a reported PCE of 10.7% when blended with **$PC_{71}BM$**.[64] Interestingly, no more than 7% PCE were achieved when the fullerene was replaced by a NFA.[65] Hence, the same group later reported some side chains substitution (*vide supra*) resulting in a stabilization of the HOMO level and a decrease of the crystallinity. The perfect match of the energy levels of this new polymer, namely **P3TEA**, combined with a PDI-based NFAs (**SF-PDI_2**) improved the conversion up to 9.5%.[66,67] Eventually, substituting the top sulfur atom of the BT group by a nitrogen, thus affording the benzo[*d*][1,2,3]triazole accepting group (BTz), brings an additional and valuable position to graft additional side chains. Energetically speaking, the LUMO level rises compared to the BT block, leading to larger optical band gaps and making their absorption appropriate complementary with narrow-band gap NFAs. For instance, copolymerizing the abovementioned BDT donating unit with a difluorinated BTz, afforded the **FTAZ** polymer that reached 7.1% efficiency in fullerene-based OSCs, with a moderate J_{SC} of *ca* 11.8 $mA.cm^{-2}$.[68] Interestingly, the use of NFA can once again pull up these values, since Zhan *et al.* reported a J_{SC} of 20.7 $mA.cm^{-2}$ resulting in a PCE of 12.5%.[69]

Though highly efficient, the conjugated donor-polymers present, nonetheless, some drawbacks arising from their molecular weight variations. The batch-to-batch deviations can indeed affect the energetics, molecular packing and charge charrier transport.[70] Moreover, the presence of metal traces (and/or heavy atoms such as tin) and the long and expensive synthetic routes, have incentivized the development of well-defined molecular donors.

3.5.2 Molecular Donors

These discrete materials are characterized by a high reproducibility in synthesis and purification in comparison with their polymer counterparts. Other advantage is their potential compatibility with both solution- and *vacuum*-processes.

While the first examples of OPVs were based on the use of small molecules, these materials gained great interest in the first decade of 2000 with the exploration and functionalization of simple structures such as the acene family or oligothiophenes. By combining $\mathbf{C_{60}}$ as acceptor with donors like α-sexithiophene (**6T**), pentacene or rubrene, the PCE reaches values of 1.5%, 2.7% and 2.9% respectively that were, at that time, promising and competitive with macromolecular materials.[71–73]

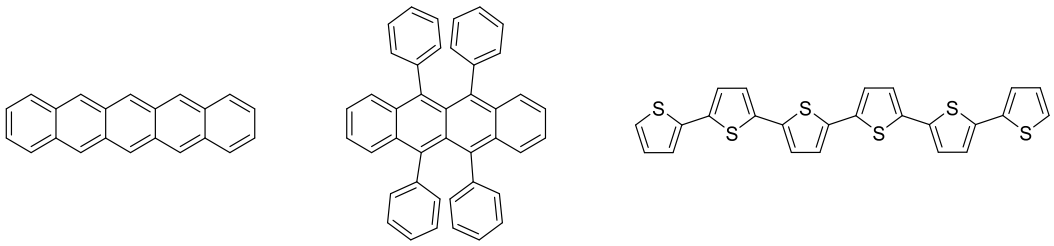

Figure 12. Chemical structure of acenes and oligothiophene donor materials.

Among all synthesized structures, the push-pull molecules (D-π-A) have attracted considerable research attention. Due to their accessible synthesis and wide possibility of structural modifications, these compounds have triggered the attention of the SCL (*"Systèmes Conjugués Linéaires"*) group for the last 15 years. After the pioneer work of J. Roncali *et al*. in 2006 on a star-shaped triphenylamine (TPA) push-pull molecule as donor material for OPV,[74] our group has indeed developed numerous active and simple materials taking advantage of the strong electron-donating properties and high hole-mobility of the triarylamines (TAAs) (Figure 13).

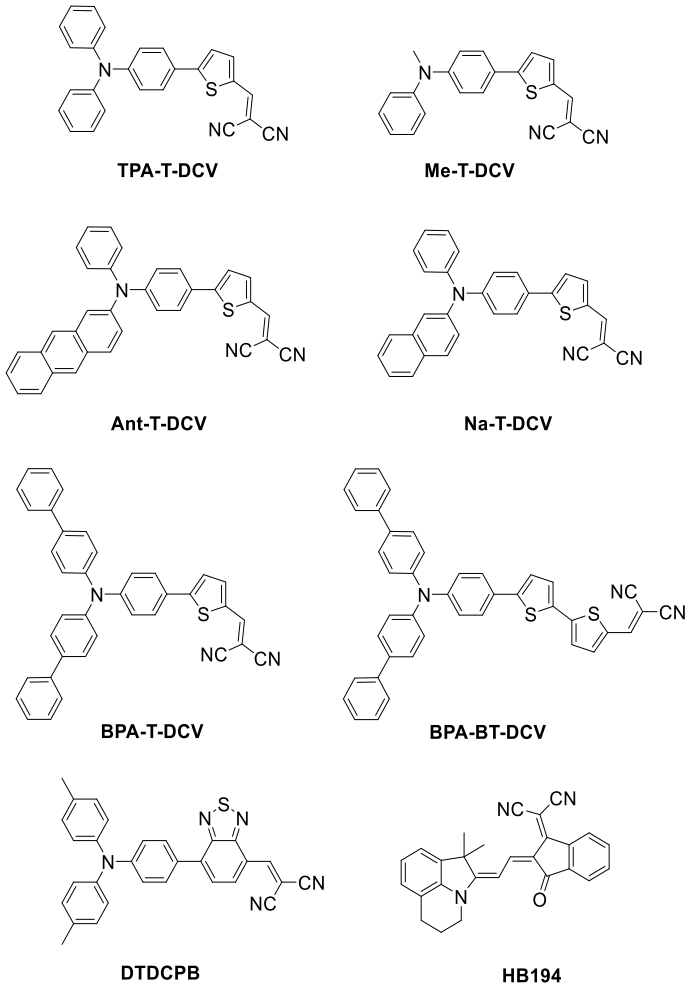

Figure 13. Chemical structures of push-pull small-molecule donors.

Starting from a TPA donor block, connected to a dicyanovinyl (DCV) acceptor unit through a thiophene spacer, **TPA-T-DCV** was set as a reference compound.[75] Photovoltaic conversions exceeding 2.5% in PHJ devices with $\mathbf{C_{60}}$ were firstly achieved revealing the potential of a simple molecular architecture that can be prepared in only two steps.[76,77] Thereafter, device engineering and optimization improved the PCE to 3.7% with $\mathbf{C_{70}}$ and 4.0% in co-evaporated BHJ-based solar cells.[36,78] In addition to devices engineering, structural modification of the TPA block resulted in considerable impact over the energetics, charge transport properties and therefore the photovoltaic performances. For instance, replacing one of the outer phenyl constituting the TPA unit by an anthryl (**Ant-T-DCV**) or a naphthyl (**Na-T-DCV**) resulted in an improvement of the hole-mobilities, *i.e.* a three- and five-fold increase respectively (*ca* 3.6×10^{-6} $cm^2V^{-1}s^{-}1$ and 5.0×10^{-5} $cm^2V^{-1}s^{-1}$).[79,80] On the other hand, when a simple methyl group is used (**Me-T-DCV**), unexpected reduction of the gap was monitored in thin film combined with a drastic improvement of the hole-transport properties (*ca* 5.0×10^{-4}

$cm^2V^{-1}s^{-1}$ *vs* 1×10^{-5} $cm^2V^{-1}s^{-1}$ for **TPA-T-DCV**), resulting in an higher power conversion efficiency (3.3% vs 2.5% for **TPA-T-DCV**).[81] Within the frame of this thesis, it is noteworthy that biphenylamine-based push-pull derivatives (**BPA-T-DCV** and **BPA-BT-DCV**) were prepared leading to outstanding hole-mobilities of *ca* 1.0×10^{-3} $cm^2V^{-1}s^{-1}$ associated to FFs among the highest achieved so far with small molecular donors (> 73%).[82] Beyond the chemistry "Made in Angers",[83] D-π-A small molecules have demonstrated excellent PCE since merocyanine dye **HB194** has achieved 6.1% PCE[84] and Forrest *et al.* reported efficiencies of 9.8% and 15% in tandem devices with the TAA-based donor **DTDCPB**.[85–87]

From an efficiency perspective, symmetrical A-D-A molecules led to the highest PCEs reported so far. Usually stemming from oligothiophene chemistry, the introduction of electron-withdrawing units on each terminal side of the molecular backbones broadens the absorption region while reducing the band gap and thus improving the limited absorbance of linear oligothiophenes (Figure 14).

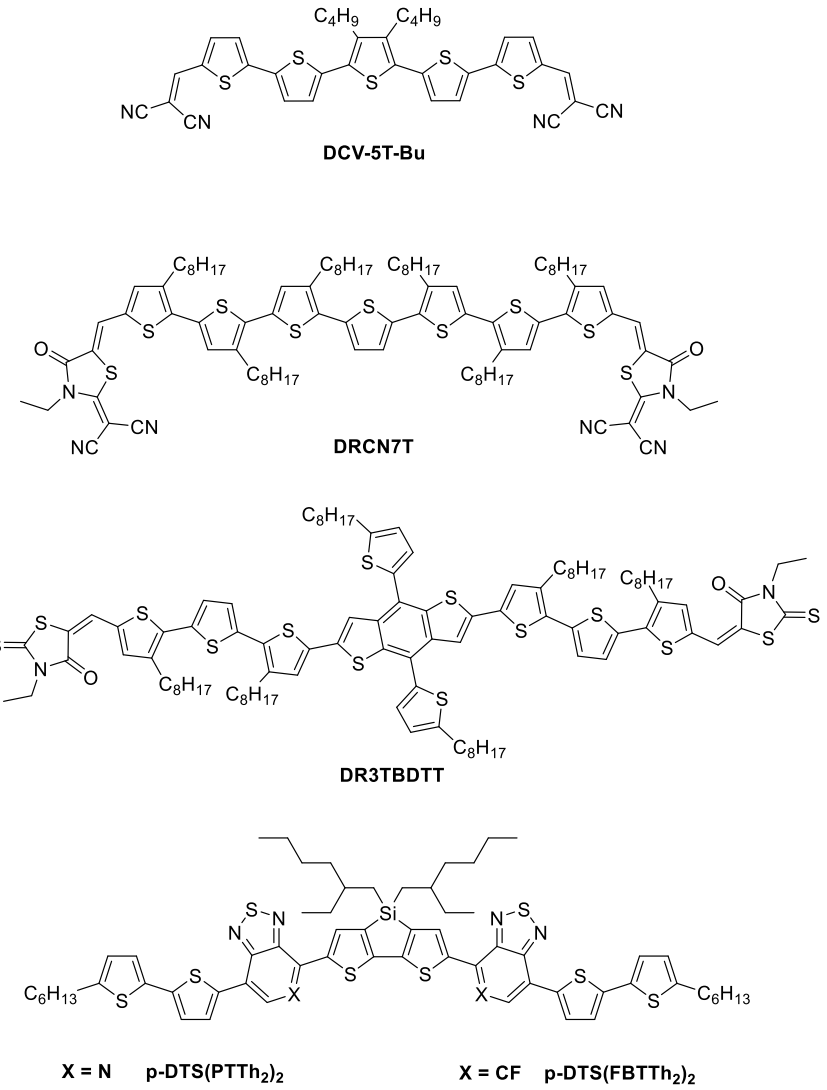

Figure 14. Chemical structures of A-D-A small-molecule donors.

Pioneered by P. Bäuerle and coworkers, a series of oligothiophenes of different lengths and side chain substitutions, end-capped with DCV groups was described.[88,89] With excellent results in terms of efficiency obtained in *vacuum*-processed BHJ devices and the simplicity of the synthesis, P. Bäuerle founded with K. Leo a start-up that later would become one of the leading company in the field, namely Heliatek.[90] They patented in 2013 a record of 13% PCE in multiple-junction solar cells with a quinquethiophene compound (**DCV-T5-Bu**) used as the donor material,[91] which can be presumably found nowadays in the commercial products of this company.

Soluble analogues, namely **DRCN7T** and **DR3TBDTT** (*vide supra*), showed high conversion efficiencies of 9.3% and 8.1%, when blended with **$PC_{71}BM$**[92,93] in single-junction OSCs and similar values (*ca* 7.0%) were afforded by the D'-A-D-A-D' donor compounds

prepared by the group of G. Bazan , *i.e.* the **p-DTS(PTTh$_2$)$_2$** and **p-DTS(FBTTh$_2$)$_2$**.[94,95] However, the synthesis and cost of these materials are notably incremented due to the high number of alkyl chains and complexity of the building blocks.

Finally, considering that one key parameter of the active layer is the light absorption, dyes have naturally been functionalized and evaluated as donor materials (Figure 15). Among numerous examples, including the phthalocyanine used by Tang in 1986, the development and application of porphyrin derivatives[96,97] led to promising PCE of *ca* 9.0% (*e.g.* **DPPEZnP-BzTBO**:**PC$_{61}$BM** blend).[98] Their smaller relatives, namely the BODIPYs, have also been successfully used as donor materials with performances of *ca* 7.0% and 9.9% reached in single-junction and tandem solar cells, respectively.[99,100] Eventually, diketopyrrolopyrrole (DPP)-based molecules have been designed[101] achieving conversions above 7% when associated to fullerene derivatives.[102]

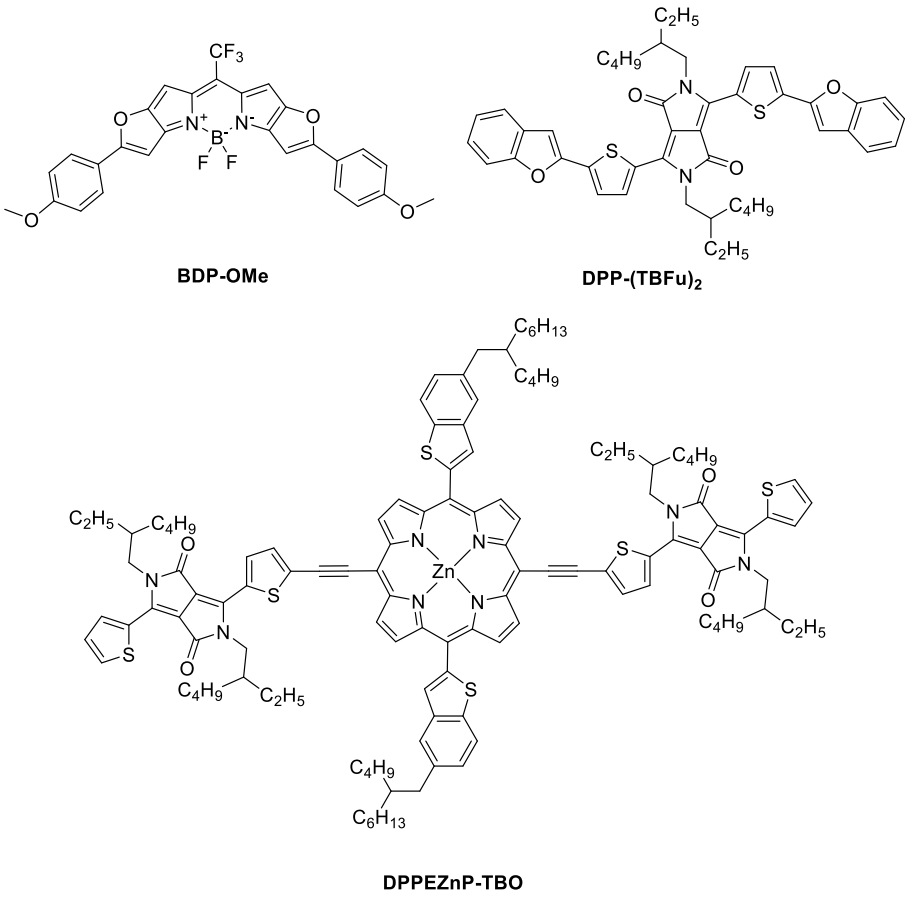

Figure 15. Chemical structures of dye-based small-molecule donors.

3.6 Acceptor Materials

3.6.1 Fullerene Derivatives

Discovered by serendipity, the carbon-allotrope "buckyballs", or fullerene derivatives, were isolated from graphite vaporization experiments that aimed at understanding the mechanisms by which long-chain carbon molecules are formed in interstellar space.[103] The more favored cluster, namely the **C_{60}**, also labeled as buckminsterfullerene as an homage to the American architect Buckminster Fuller, was clearly established as one of the most studied acceptor semiconductors. The actual production process is based on the electric arc vaporization of graphite under inert atmosphere. Optimization led to the commercialization and therefore implementation of fullerene derivatives in the early commercially considered organic electronic devices. Scoping the fullerene properties highlights the unique capacity to reversibly accept up to six electrons.[104] Besides, the homogeneous delocalization of their frontier molecular orbitals (MOs) along with the tridimensional structure induces outstanding isotropic charge-transport mobilities.[105] This delocalization of bonding/valence electrons promotes also strong intermolecular interactions (π-π stacking) leading to the formation of nanodomains, essential for efficient organic solar cells.

In comparison to **C_{60}**, the more expensive **C_{70}** in which the high degree of symmetry is broken, shows additional electronic transitions and improved absorbance with a weak contribution between 400-600 nm. All together, this derivative was able to reach higher PCEs that the ones obtained with **C_{60}**. Highly insoluble, these two reference acceptors have been always deposited by *vacuum*-process and were functionalized *via* cycloaddition and subsequent photoisomerization to achieve solution-processable analogues, namely the **$PC_{61}BM$** and **$PC_{71}BM$** (Figure 16).[106]

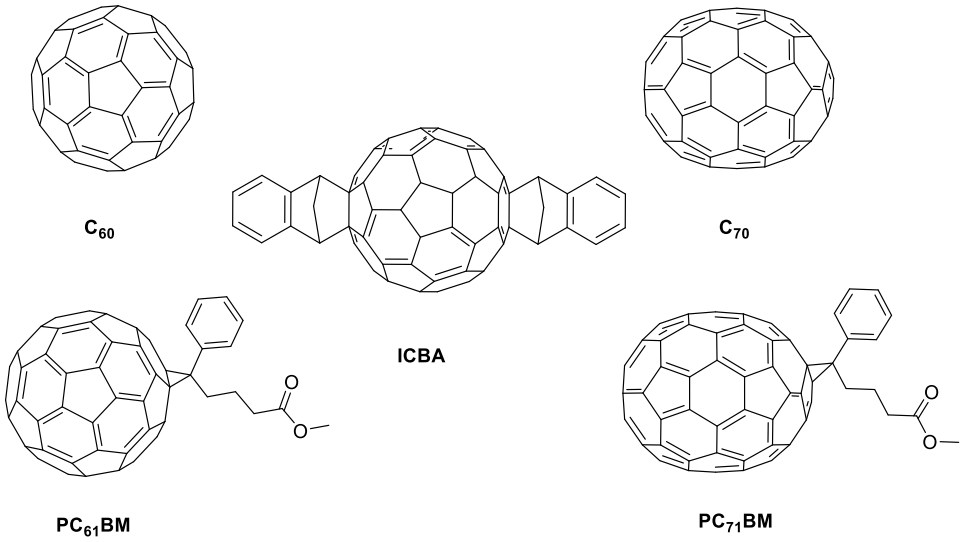

Figure 16. Chemical structure of fullerene derivatives for OPV.

ICBA, another soluble analogue, was obtained by double reaction with indene motifs raising the LUMO level hence enabling, in principle, higher V_{oc} and making it more suitable for wide-band gap polymers. Once blended with the **P3HT**, PCEs up to 6.5% were achieved mainly due to higher V_{OC} (0.84 V *vs* 0.58 V with **$PC_{61}BM$**).[107]

However, the small malleability to tune the energy levels, the limited absorption in the visible, the low yields obtained during the different explored synthetic routes, have prompted the research for other alternatives, mainly towards the Non-Fullerene Acceptors.

3.6.2 Non-Fullerene Acceptors

Fullerene derivatives dominated the acceptor role during almost the past two decades setting up the PCE records between 12-13%. With the explosion of publications on perovskites solar cells, interest to the field faded until the first promising results on NFAs. Once demonstrated, the latter have taken much attention owing to their higher versatility, in terms of chemical modification and adaptation of the absorption and energy levels and were responsible of the renewal of the OPV. The goal has been accomplished and efficiencies > 13% have been reported in a short period of time and now flirting with the 18%, making them once again competitive with respect to the other emerging solar technologies.

The rylene family has been historically investigated due to their availability, high molar extinction coefficient, good electron-affinity and mobility, as well as their excellent thermal

and (photo)chemical stability. Depending on the nature of the linkage between the sub naphthalene units, it is possible to synthesize different derivatives from a naphthalene, to a perylene, terrylene or even quaterrylene (Figure 17).[108]

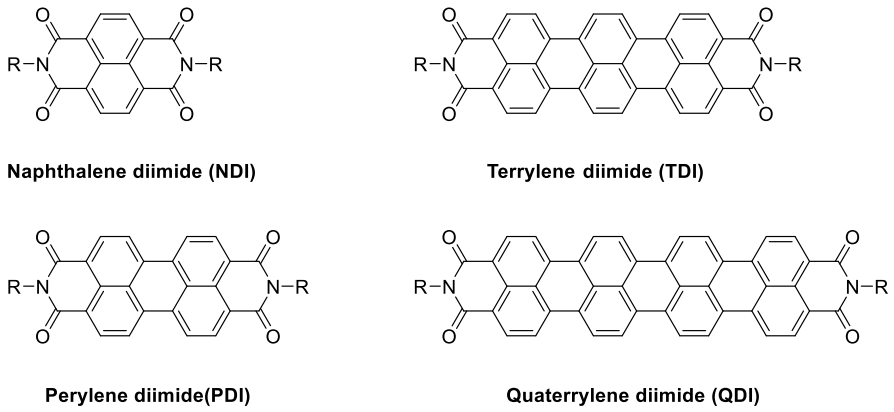

Figure 17. Chemical structure of rylene diimide materials.

Apart from major contributions of the perylene diimide derivatives, which will be discussed in detail in the Chapter 2, the naphthalene diimide bloc (NDI) has attracted considerable research interest, particularly for the preparation of NFA-based solar cells (Figure 18).

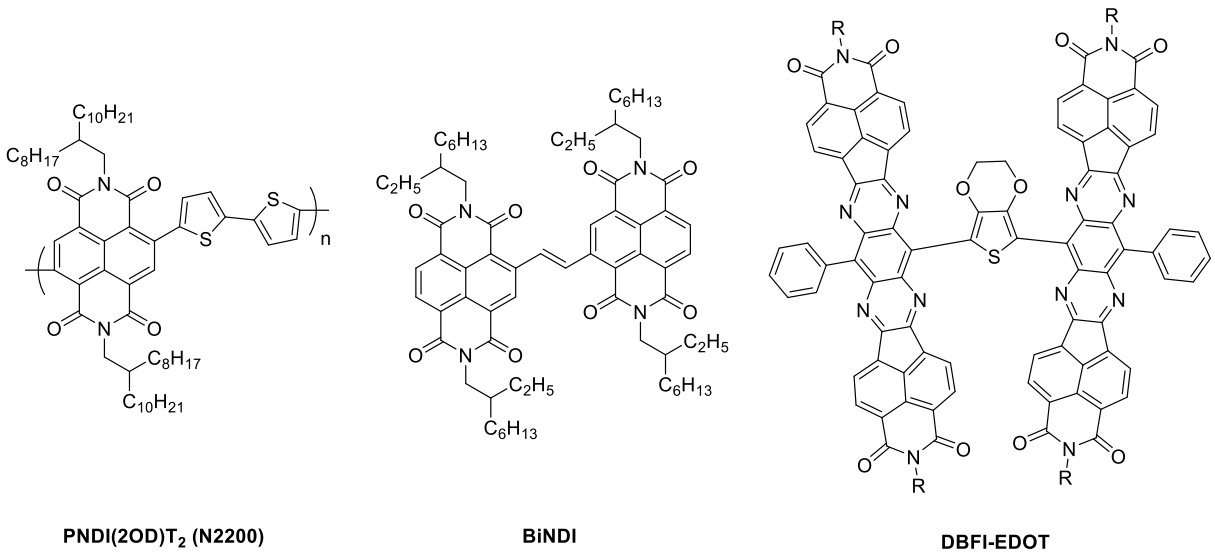

Figure 18. Chemical structure of naphthalene mono- and diimide derivatives for NFA-based OSCs.

Implemented as electron-withdrawing block in *n*-type polymers,[109] impressive results have been obtained in all-polymer devices with PCE higher than 10% (**N2200:PTzBI-Si** blend).[110,111] However, it is noteworthy that only few number of approaches using NDI or naphthalene monoimide for the preparation of small-molecular NFAs (*e.g.* **BiNDI**, **DBFI-EDOT**)

with good or modest photovoltaic performances are reported in the literature.[112,113] Regarding the terrylene and quaterrylene derivatives, their solubility issues turned out to be a major challenge resulting in scarce contributions and modest PCEs.[114,115]

Already mentioned as building block for small-molecule donor materials, the ambipolar character of DPP made it straightforwardly a potential candidate for NFAs (Figure 19).[116]

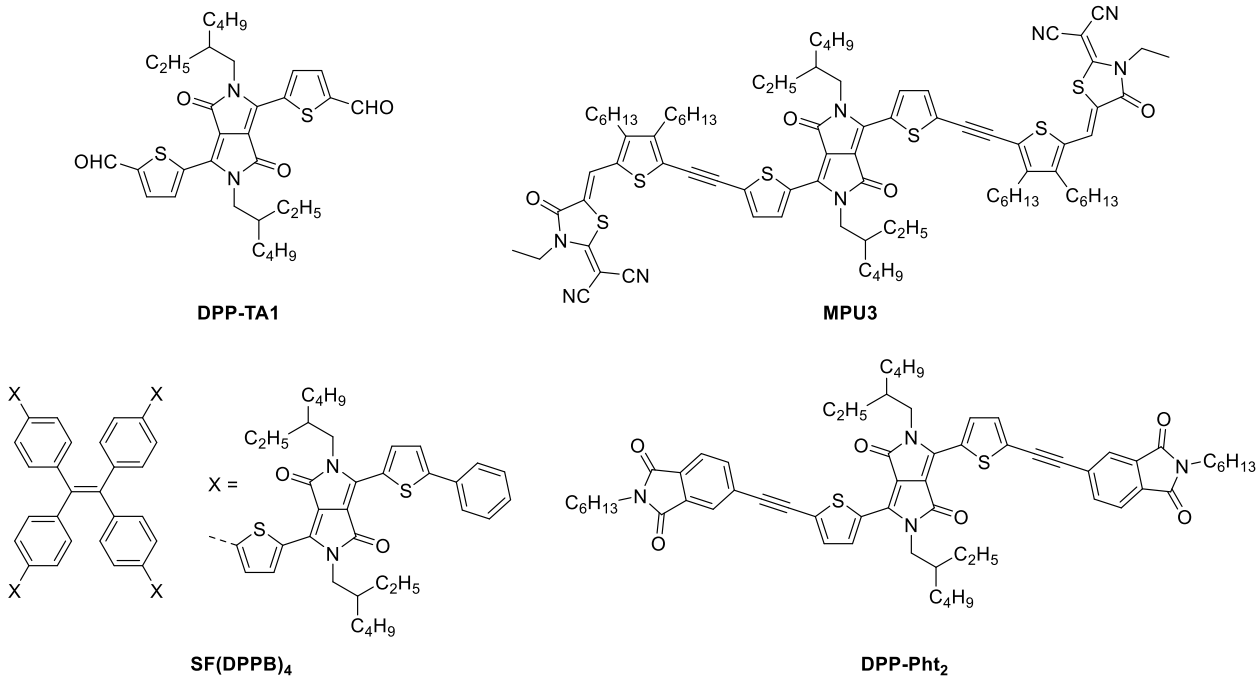

Figure 19. Chemical structure of PDD-based NFAs.

Though the first examples of devices prepared by mixing simple acceptors such as the **DPP-TA1** with **P3HT** led to low performances (*e.g.* 0.3%,),[117] the ease of synthesis and functionalization allowed the preparation of more complexes molecules such as the **DPP-Pht$_2$** or the **SF(DPPB)$_4$** that reached a PCE of 3.0 and 5.1% respectively when blended with the **P3HT**.[118–120] The actual PCE record of 9.2% within this type of molecules has been reported in the case of **MPU3** that was combined with a small-molecular donor leading to an all-small molecule and fullerene-free organic solar cell.[121]

Symmetrical ladder-type blocks have attracted considerable attention for the design of efficient NFAs. Starting in the early 2010, Sellinger *et al.* synthesized a vinazene end-capped derivative with a BT central core (*e.g.* **V-BT**, **ET-BT**) performing at 1.4% with P3HT and 1.1% with a DPP derivative used as donor material.[122,123] The use of electron-donating centers, such

as a fluorene connected to indane-1,3-diones accepting blocks, thus affording the A-D-A **FEHIDT**,[124] paved the way to the current trend of molecular design to compete in the race of efficiency. The indacenothiophene and indacenodithieno[3,2-*b*]thiophene embedded as central core rapidly appeared essential for the development of high performance OSCs. These derivatives have contributed to a second upturn of the organic photovoltaic technology by almost doubling, in a short period of time, the records achieved with fullerene derivatives. Taking **ITIC**[125] (Figure 20) as the reference material, several modifications in the chemical edifice broke the establish records consecutively and more importantly incentivized the research in new A-D-A based NFAs. Note that a deepest presentation of this family will be described in the next chapter.

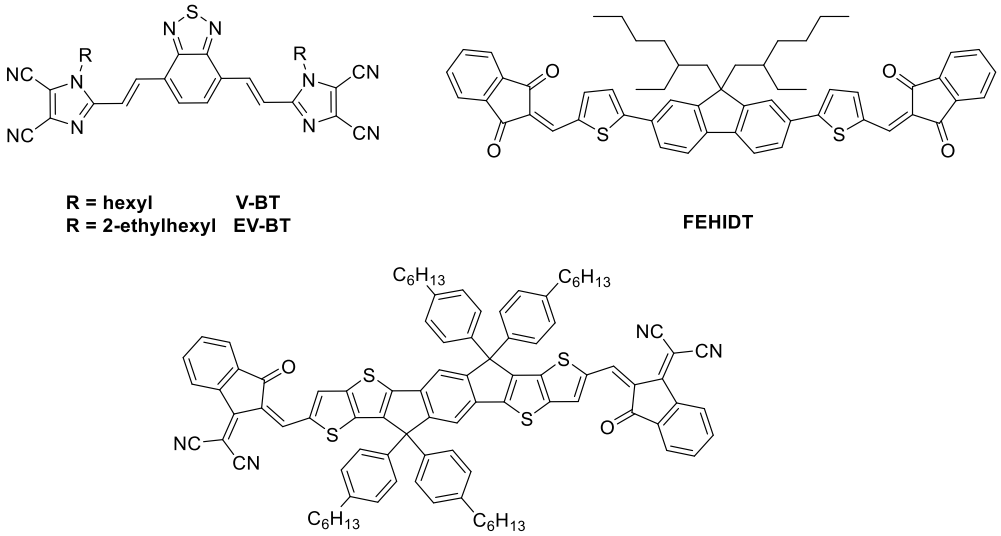

*Figure 20. Chemical structure of vinazene derivatives, **FHIDT**, and **ITIC**.*

A new class of NFA, **Y6**, by employing a ladder-type electron-deficient dithienothiophen[3.2-*b*]-pyrrolobenzothiadiazole core was reported in 2019 by Zou and coworkers.[126] OSCs made from **Y6**, with the polymer **PM6**, in standard and inverted architectures exhibited high efficiency of 15.7% and a certified value of 14.9%. Subsequently Ge *et al*. prepared a ternary blend introducing **$PC_{71}BM$** and performing 16.6% PCE.[127] The key-structure suffers from a smooth distortion induced by the pyrrole alkyl chains, this conformation prevents the over-aggregation keeping an intramolecular charge-transport channel. The exceptional performance shown by **Y6** have prompted dozens of publications in

less than one year, either modifying the chemical structure of the acceptor or adjusting the donor polymer (Figure 21 and Table 1).[128,129]

The low-band gap acceptor, to which belongs the **Y6**, has demonstrated their high potential with certain wide-band gap copolymers (Figure 21), by harvesting most of the visible NIR light. For instance, PCEs above 15% were reached when combined with the BDT-based **PM6** polymer. Then, the Ding group has reported a series of BDT-copolymers including the 5*H*-dithieno[3,2-*b*:2',3'-*d*]thienoaryl units (*e.g.* **L1**, **L2**, **D16**, **D18**).[130–132] It turned out that PCEs obtained with **D16** and **D18** were the highest photoconversion achieved in the time these words were written, PCEs of 16.2% and 18.2% respectively. The same group prepared an ultra-wide-band gap donor, namely **W1** that reached an efficiency higher than 16% once again with **Y6** thus confirming the key role of a complementary absorption.[133] In this context, it is mandatory to mention that the low-cost and accessible polymer synthesized by Li *et al*., labeled **PTQ10**,[134] was also able to rank among the most performing materials, with a PCE of 16.5%, when blended with a purchased **Y6**.

Regarding the chemical engineering over the abovementioned NFAs, the aliphatic substitution and the acceptor blocks have been widely modified. Adapting the center alkyl chains, Yan group changed and studied the impact of the branching position by synthesizing the **N3** and resulting in a slight improvement of the efficiency (15.8% and 16.5% in binary and ternary blends respectively).[135] In line with this, Hou *et al.* showed that replacing the 2-ethylhexyl unit by 2-butyloctyl and subsequently the fluorine atoms by chlorine afforded a better performing acceptor that allowed the PCE to jump to 17.0% (**PM6**:**BTP-4Cl-12** blend)[136] and eventually 17.5% with a *n*-nonyl edge chains (**PM6**:**BTP-eC9** blend).[137]

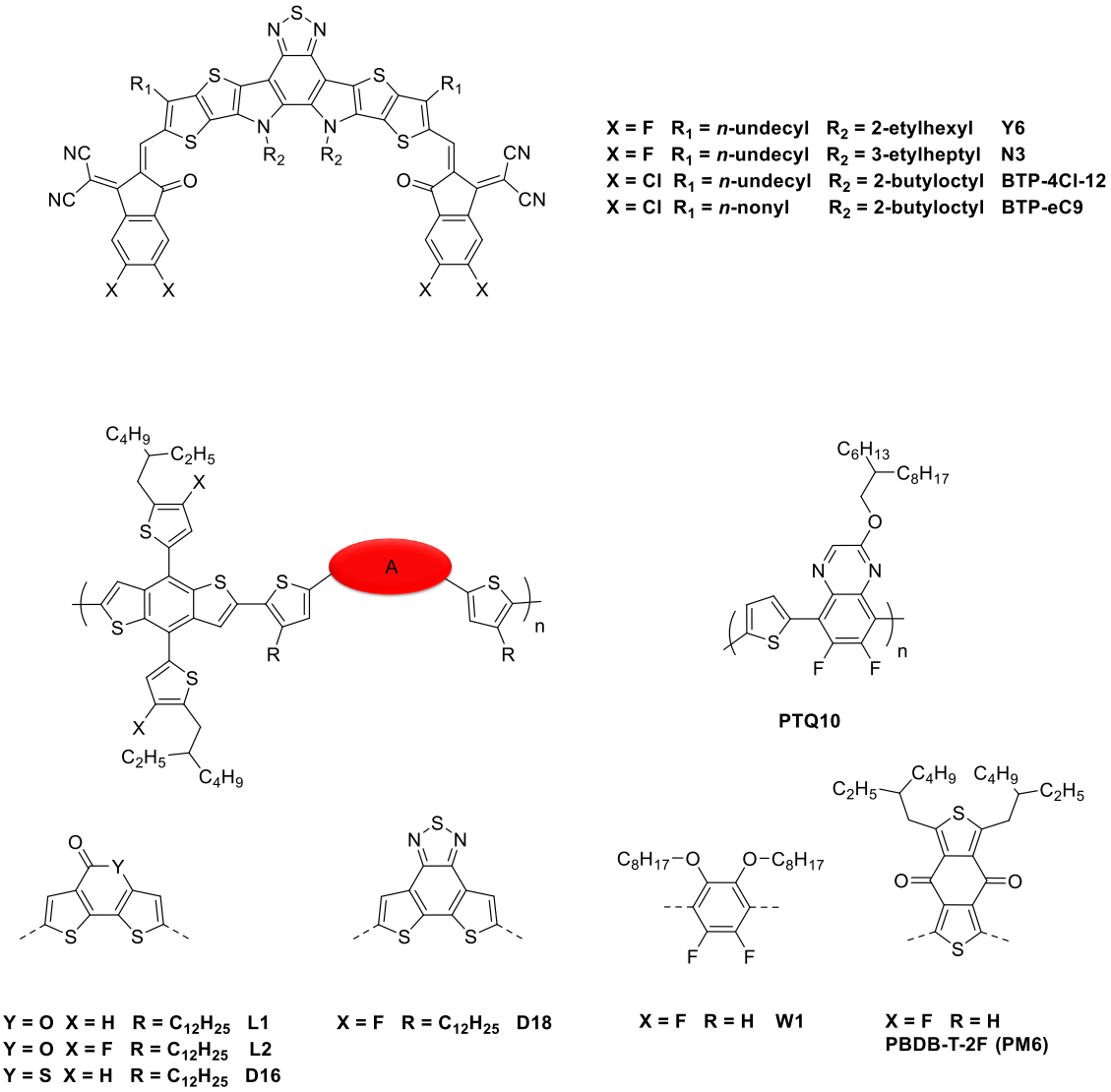

*Figure 21. Chemical structure of **Y6** derivatives and counterpart donor polymers.*

*Table 1. Photovoltaic parameters of single-junction BHJ OSCs based on **Y6**.*

Active Layer	V_{oc} (V)	J_{sc} (mA/cm^2)	*FF* %	PCE %$_{(ave)}$	Ref.
PM6:Y6	0.83	25.3	74.8	15.7	126
PM6:Y6:PC$_{71}$BM	0.85	25.7	76.4	16.6	127
L1:Y6	0.80	23.9	74.7	14.4	130
L2:Y6	0.87	20.5	70.2	12.6	130
P2F-EHp:Y6	0.81	26.7	74.1	15.7	129
W1:Y6	0.88	25.9	70.7	16.2	133
Pt10:Y6	0.81	26.5	76.3	16.4	128
PTQ10:Y6	0.83	26.7	75.1	16.5	134
D16:Y6	0.85	25.6	74.9	16.2	131
D18:Y6	0.86	27.7	76.6	18.2	132
PM6:N3	0.84	25.8	73.9	15.8	135
PM6:N3:PC$_{71}$BM	0.85	25.7	76.6	16.5	135
PM6:BTP-4Cl-12	0.86	25.6	77.6	17.0	136
PM6:BTP-eC9	0.84	26.2	81.1	17.4	137

Despite the zenith of polymer-based solar cells in the last years (in the academic area), nowadays *vacuum*-process still has many advantages in large-manufacture solar cells, since maintaining high-efficiency photoconversions appears difficult for other techniques, *e.g.* spin-coating, doctor-blade, screen- or inkjet-printing; especially when talking about scaling the surfaces to cm^2 or even m^2. Moreover, compared to the synthetically challenging high performing solution-processable materials, *vacuum* compatible molecules have to be, by their nature, simple and of low molecular weight. However, small-molecule NFAs have been somewhat precluded from the evaporation-process, due to the noteworthy success of **C_{60}** and **C_{70}** in the *vacuum*-deposited devices.

Although it is true that first bilayer OSCs used PDI derivatives as sublimated acceptors, the strong π-π solid-state interactions hamper their evaporability and only PCEs < 2% were afforded.[138–140] In 2007, Bäuerle *et al.* found that DCV end-capped terthiophenes (**DCV3T**, Figure 22), performed well as acceptor, showing V_{OCs} of *ca* 1.0 V, in stark contrast with values obtained with fullerene and PDI derivatives.[141] Though low PCEs were measured, Meredith and coworkers synthesized two BT-based push-pull molecules used as NFA, namely **K12** and **YF25**,[142,143] that were demonstrated to be processable either by *vacuum*- or solution-deposition. A similar example has been reported by Bernède in collaboration with our group, where the aforementioned push-pull **TPA-T-DCV** (Figure 13) was successfully used as acceptor when combined with an aluminum phthalocyanine donor (**AlPcCl**).[144] A PCE of 1% was obtained with PHJ devices and 4% when a supplementary layer of **C_{60}** was added.

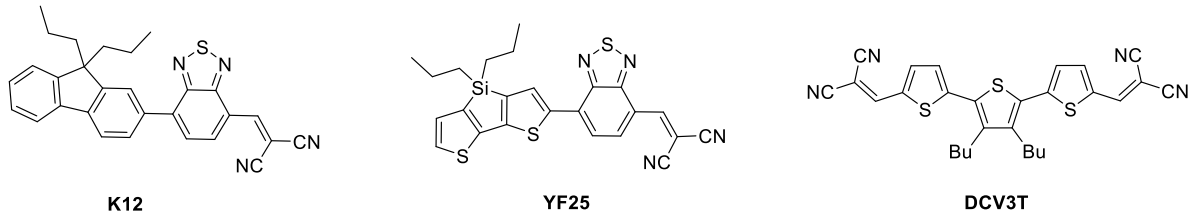

Figure 22. Chemical structure of evaporable small NFA molecules.

In this sense, Jones *et al.* demonstrated the use of boron subphthalocyanine chloride (**SubPc**), a typical donor material, as electron-accepting layer in single-junction evaporated-OSCs with tetracene as donor yielding a conversion of 2.9%.[145] Likewise, Torres' group tuned the electronic properties of the diimino-isoindole-based macrocycle (Figure 23) to improve

the electron-withdrawing character and therefore the photovoltaic performances of the devices. Hence, PCEs higher than 3% were achieved with perfluorinated phthalocyanines (**F_{12}SubPc** and **F_{13}SubPc**)[146] and up to 4% with the **FSubPcDimer** mixture of topoisomers (Figure 23).[147]

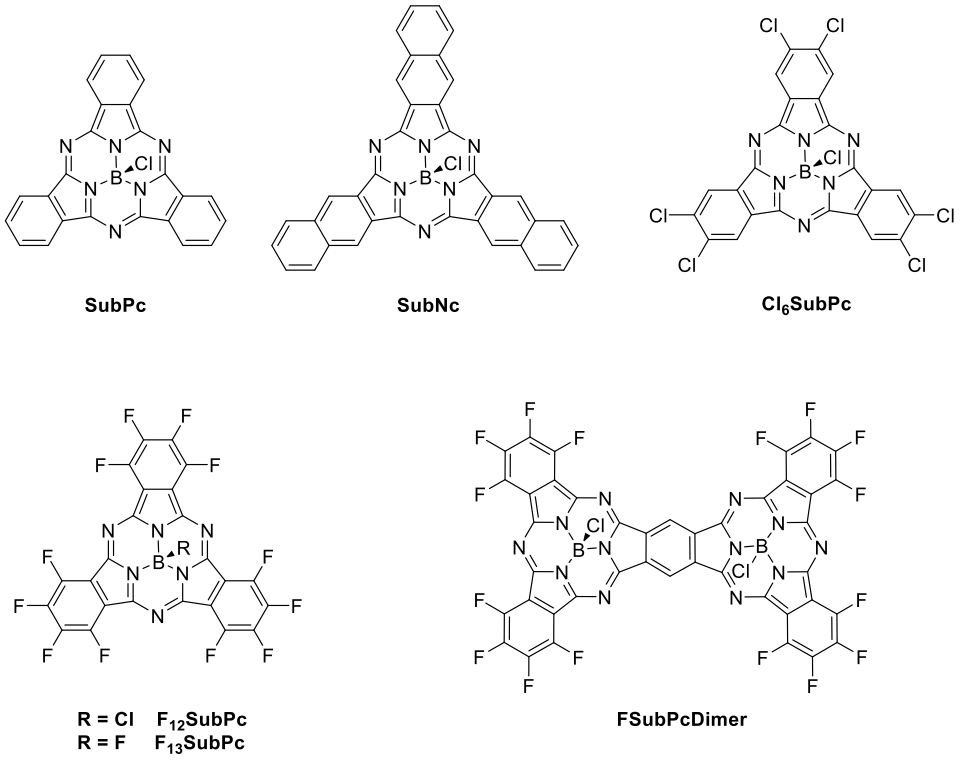

Figure 23. Chemical structure of SubPc-based NFAs.

Interestingly, the chlorinated **Cl_6SubPc** was able to improve the photoconversion to 6.9% when paired with a **SubNc** donor in an all-subphthalocyanine-based solar cells.[148,149] Eventually, an impressive PCE of 8.4% was obtained with a three-layer PHJ device corresponding to the subsequent evaporation of **α-6T**, **SubNc** and **SubPc**. It turned out that the intermediate (**SubNc**) and acceptor (**SubPc**) layer complementarily favored a two-step exciton dissociation that ends in the extraordinary performances of this cascade structure.[150]

4 Thesis objectives

The main objective of this thesis work has been devoted to the design, synthesis and characterization of new NFAs to rationalize fine structure-properties relationships. Moreover, it is noteworthy that special emphasis was placed on the organic synthesis to try to keep and

develop simple and accessible routes through the evaluation of different pathways to, therefore, find the best alternative.

NFAs have overwhelmingly taken the attention of the OSCs community in the last years, nevertheless, the outstanding high-efficient devices have been prepared with complex structures and processed by spin-coating, thus making the up-scaling a true challenge for large surface areas. Consequently, simple molecular NFA structures with accessible synthetic route have been considered during this thesis.

In the first part of Chapter 2, the straightforward synthesis of solution-processable NFA derivatives based on a central perylene diimide core difunctionalized with sterically hindered thiophene-based π-systems, will be described while the impact of the regioisomerism in these materials on their photovoltaic performance will be discussed.

Moreover, considering the lack of evaporable NFA materials, we have identified a need and tried to address the preparation and use of different low-molecular weight organic semiconductors as acceptors for OPV. In this context, the second part of Chapter 2 deals with i) the size reduction of efficient and well-known ladder-type NFAs and ii) the synthesis and photovoltaic evaluation of a new family of small IDT derivatives.

The last chapter will be more exploratory focusing on the synthesis of new electron-deficient benzothioxanthene derivatives, a family of rylene-type compounds that has been scarcely developed compared to their NDI and PDI counterparts and which could be of interest for organic electronics.

References

(1) www.iea.org.
(2) Becquerel, A. E. *Comptes Rendus Acad. Sci.* **1839**, *9*, 145–149.
(3) Becquerel, A. E. *Comptes Rendus Acad. Sci.* **1839**, *9*, 561–567.
(4) Chapin, D. M.; Fuller, C. S.; Pearson, G. L. A New Silicon P-n Junction Photocell for Converting Solar Radiation into Electrical Power. *J. Appl. Phys.* **1954**, *25* (5), 676–677.
(5) www.nrel.gov https://www.nrel.gov/pv/cell-efficiency.html.
(6) Green, M. A.; Dunlop, E. D.; Hohl-Ebinger, J.; Yoshita, M.; Kopidakis, N.; Ho-Baillie, A. W. Y. Solar Cell Efficiency Tables (Version 55). *Prog. Photovoltaics Res. Appl.* **2020**, *28* (1), 3–15.
(7) ISE Fraunhofer. *Photovoltaics Report*; 2020.
(8) www.ctf-solar.de.
(9) Gerischer, H.; Michel-Beyerle, M. E.; Rebentrost, F.; Tributsch, H. Sensitization of Charge Injection into Semiconductors with Large Band Gap. *Electrochim. Acta* **1968**, *13* (6), 1509–1515.
(10) Tributsch, H.; Calvin, M. Electrochemistry of Excited Molecules: Photo-Electrochemical Reactions of Chlorophylls. *Photochem. Photobiol.* **1971**, *14* (2), 95–112.
(11) O'Regan, B.; Grätzel, M. A Low-Cost, High-Efficiency Solar Cell Based on Dye-Sensitized Colloidal TiO2 Films. *Nature* **1991**, *353* (6346), 737–740.
(12) Kakiage, K.; Aoyama, Y.; Yano, T.; Oya, K.; Fujisawa, J. I.; Hanaya, M. Highly-Efficient Dye-Sensitized Solar Cells with Collaborative Sensitization by Silyl-Anchor and Carboxy-Anchor Dyes. *Chem. Commun.* **2015**, *51* (88), 15894–15897.
(13) Wu, J.; Lan, Z.; Hao, S.; Li, P.; Lin, J.; Huang, M.; Fang, L.; Huang, Y. Progress on the Electrolytes for Dye-Sensitized Solar Cells. *Pure Appl. Chem.* **2008**, *80* (11), 2241–2258.
(14) Kojima, A.; Teshima, K.; Shirai, Y.; Miyasaka, T. Organometal Halide Perovskites as Visible-Light Sensitizers for Photovoltaic Cells. *J. Am. Chem. Soc.* **2009**, *131* (17), 6050–6051.
(15) Lee, M. M.; Teuscher, J.; Miyasaka, T.; Murakami, T. N.; Snaith, H. J. Efficient Hybrid Solar Cells Based on Meso-Superstructured Organometal Halide Perovskites. *Science* **2012**, *338* (6107), 643–647.
(16) Cherney, E. C.; Lopchuk, J. M.; Green, J. C.; Baran, P. S. A Unified Approach to Ent-Atisane Diterpenes and Related Alkaloids: Synthesis of (-)-Methyl Atisenoate, (-)-Isoatisine, and the Hetidine Skeleton. *J. Am. Chem. Soc.* **2014**, *136* (36), 12592–12595.
(17) Ouedraogo, N. A. N.; Chen, Y.; Xiao, Y. Y.; Meng, Q.; Han, C. B.; Yan, H.; Zhang, Y. Stability of All-Inorganic Perovskite Solar Cells. *Nano Energy* **2020**, *67* (November 2019), 104249.
(18) Babayigit, A.; Ethirajan, A.; Muller, M.; Conings, B. Toxicity of Organometal Halide Perovskite Solar Cells. *Nat. Mater.* **2016**, *15* (3), 247–251.
(19) Kearns, D.; Calvin, M. Photovoltaic Effect and Photoconductivity in Laminated Organic Systems. *J. Chem. Phys.* **1958**, *29* (4), 950–951.
(20) Flohn, B.; Fletcher, M. Chlorophyll-a Photovoltaic Cells. *Nature* **1975**, *254* (1972), 507–509.
(21) Tang, C. W.; Albrecht, A. C. Photovoltaic Effects of Metal-Chlorophyll-a-Metal Sandwich Cells. *J. Chem. Phys.* **1975**, *2139* (1975), 2139–2149.
(22) Ghosh, A. K.; Feng, T. Merocyanine Organic Solar Cells Merocyanine Organic Solar Cells. *Appl. Phys. Lett.* **2011**, *49* (August), 5982.
(23) Merritt, V. Y.; Hovel, H. J. Organic Solar Cells of Hydroxy Squarylium. *Appl. Phys. Lett.* **1976**, *29* (7), 414–415.
(24) Tang, C. W. Two-Layer Organic Photovoltaic Cell. *Appl. Phys. Lett.* **1986**, *48* (2), 183–185.
(25) Zhang, G.; Zhao, J.; Chow, P. C. Y.; Jiang, K.; Zhang, J.; Zhu, Z.; Zhang, J.; Huang, F.; Yan, H. Nonfullerene Acceptor Molecules for Bulk Heterojunction Organic Solar Cells. *Chem. Rev.* **2018**, *118* (7), 3447–3507.
(26) Proctor, C. M.; Love, J. A.; Nguyen, T. Q. Mobility Guidelines for High Fill Factor Solution-Processed Small Molecule Solar Cells. *Adv. Mater.* **2014**, *26* (34), 5957–5961.
(27) Ramirez, I.; Causa', M.; Zhong, Y.; Banerji, N.; Riede, M. Key Tradeoffs Limiting the Performance of Organic Photovoltaics. *Adv. Energy Mater.* **2018**, *8* (28), 1703551.
(28) Baert, F.; Cabanetos, C.; Allain, M.; Silvestre, V.; Leriche, P.; Blanchard, P. Thieno[2,3-b]Indole-Based Small Push-Pull Chromophores: Synthesis, Structure, and Electronic Properties. *Org. Lett.* **2016**, *18* (7), 1582–1585.
(29) Paul, H.; David, C.; Rand, B. P. Strategies for Increasing the Efficiency of Heterojunction Organic Solar Cells: Material Selection and Device Architecture. *Acc. Chem. Res.* **2009**, *42* (11), 1740–1747.
(30) Peumans, P.; Yakimov, A.; Forrest, S. R. Small Molecular Weight Organic Thin-Film Photodetectors and

Solar Cells. *J. Appl. Phys.* **2003**, *93* (7), 3693–3723.
(31) Hiramoto, M.; Fujiwara, H.; Yokoyama, M. P-i-n like Behavior in Three-layered Organic Solar Cells Having a Co-deposited Interlayer of Pigments. *J. Appl. Phys.* **1992**, *72* (8), 3781–3787.
(32) Yu, G.; Gao, J.; Hummelen, J. C.; Wudl, F.; Heeger, A. J. Polymer Photovoltaic Cells: Enhanced Efficiencies via a Network of Internal Donor-Acceptor Heterojunctions. *Science (80-.).* **1995**, *270* (5243), 1789–1791.
(33) Kirchmeyer, S.; Reuter, K. Scientific Importance, Properties and Growing Applications of Poly(3,4-Ethylenedioxythiophene). *J. Mater. Chem.* **2005**, *15* (21), 2077–2088.
(34) Kim, D. Y.; Subbiah, J.; Sarasqueta, G.; So, F.; Ding, H.; Irfan; Gao, Y. The Effect of Molybdenum Oxide Interlayer on Organic Photovoltaic Cells. *Appl. Phys. Lett.* **2009**, *95* (9), 3–6.
(35) Hirade, M.; Adachi, C. Small Molecular Organic Photovoltaic Cells with Exciton Blocking Layer at Anode Interface for Improved Device Performance. *Appl. Phys. Lett.* **2011**, *99* (15), 11–14.
(36) Choi, J. W.; Kim, C. H.; Pison, J.; Oyedele, A.; Tondelier, D.; Leliège, A.; Kirchner, E.; Blanchard, P.; Roncali, J.; Geffroy, B. Exploiting the Potential of 2-((5-(4-(Diphenylamino)Phenyl)Thiophen-2-Yl) Methylene)Malononitrile as an Efficient Donor Molecule in Vacuum-Processed Bulk-Heterojunction Organic Solar Cells. *RSC Adv.* **2014**, *4* (10), 5236–5242.
(37) Peumans, P.; Bulović, V.; Forrest, S. R. Efficient Photon Harvesting at High Optical Intensities in Ultrathin Organic Double-Heterostructure Photovoltaic Diodes. *Appl. Phys. Lett.* **2000**, *76* (19), 2650–2652.
(38) Brabec, C. J.; Shaheen, S. E.; Winder, C.; Sariciftci, N. S.; Denk, P. Effect of LiF/Metal Electrodes on the Performance of Plastic Solar Cells. *Appl. Phys. Lett.* **2002**, *80* (7), 1288–1290.
(39) Kuwabara, T.; Sugiyama, H.; Yamaguchi, T.; Takahashi, K. Inverted Type Bulk-Heterojunction Organic Solar Cell Using Electrodeposited Titanium Oxide Thin Films as Electron Collector Electrode. *Thin Solid Films* **2009**, *517* (13), 3766–3769.
(40) Sun, Y.; Seo, J. H.; Takacs, C. J.; Seifter, J.; Heeger, A. J. Inverted Polymer Solar Cells Integrated with a Low-Temperature-Annealed Sol-Gel-Derived ZnO Film as an Electron Transport Layer. *Adv. Mater.* **2011**, *23* (14), 1679–1683.
(41) Li, G.; Chang, W. H.; Yang, Y. Low-Bandgap Conjugated Polymers Enabling Solution-Processable Tandem Solar Cells. *Nat. Rev. Mater.* **2017**, *2* (8), 1–13.
(42) Chiang, C. K.; Fincher, C. R.; Park, Y. W.; Heeger, A. J.; Shirakawa, H.; Louis, E. J.; Gau, S. C.; MacDiarmid, A. G. Electrical Conductivity in Doped Polyacetylene. *Phys. Rev. Lett.* **1977**, *39* (17), 1098–1101.
(43) Shirakawa, H.; Louis, E. J.; MacDiarmid, A. G.; Chiang, C. K.; Heeger, A. J. Synthesis of Electrically Conducting Organic Polymers: Halogen Derivatives of Polyacetylene, (CH)X. *J. Chem. Soc. Chem. Commun.* **1977**, No. 16, 578–580.
(44) Günes, S.; Neugebauer, H.; Sariciftci, N. S. Conjugated Polymer-Based Organic Solar Cells. *Chem. Rev.* **2007**, *107* (4), 1324–1338.
(45) Argun, A. A.; Aubert, P. H.; Thompson, B. C.; Schwendeman, I.; Gaupp, C. L.; Hwang, J.; Pinto, N. J.; Tanner, D. B.; MacDiarmid, A. G.; Reynolds, J. R. Multicolored Electrochromisin in Polymers: Structures and Devices. *Chem. Mater.* **2004**, *16* (23), 4401–4412.
(46) Beaujuge, P. M.; Reynolds, J. R. Color Control in π-Conjugated Organic Polymers for Use in Electrochromic Devices. *Chem. Rev.* **2010**, *110* (1), 268–320.
(47) Shaheen, S. E.; Brabec, C. J.; Sariciftci, N. S.; Padinger, F.; Fromherz, T.; Hummelen, J. C. 2.5% Efficient Organic Plastic Solar Cells. *Appl. Phys. Lett.* **2001**, *78* (6), 841–843.
(48) Wienk, M. M.; Kroon, J. M.; Verhees, W. J. H.; Knol, J.; Hummelen, J. C.; Van Hal, P. A.; Janssen, R. A. J. Efficient Methano[70]Fullerene/MDMO-PPV Bulk Heterojunction Photovoltaic Cells. *Angew. Chemie - Int. Ed.* **2003**, *42* (29), 3371–3375.
(49) Al-Ibrahim, M.; Roth, H. K.; Schrödner, M.; Konkin, A.; Zhokhavets, U.; Gobsch, G.; Scharff, P.; Sensfuss, S. The Influence of the Optoelectronic Properties of Poly(3-Alkylthiophenes) on the Device Parameters in Flexible Polymer Solar Cells. *Org. Electron.* **2005**, *6* (2), 65–77.
(50) Dang, M. T.; Hirsch, L.; Wantz, G. P3HT:PCBM, Best Seller in Polymer Photovoltaic Research. *Adv. Mater.* **2011**, *23* (31), 3597–3602.
(51) Holliday, S.; Ashraf, R. S.; Wadsworth, A.; Baran, D.; Yousaf, S. A.; Nielsen, C. B.; Tan, C. H.; Dimitrov, S. D.; Shang, Z.; Gasparini, N.; et al. High-Efficiency and Air-Stable P3HT-Based Polymer Solar Cells with a New Non-Fullerene Acceptor. *Nat. Commun.* **2016**, *7*, 1–12.
(52) Zhang, M.; Guo, X.; Ma, W.; Ade, H.; Hou, J. A Polythiophene Derivative with Superior Properties for Practical Application in Polymer Solar Cells. *Adv. Mater.* **2014**, *26* (33), 5880–5885.
(53) Qin, Y.; Uddin, M. A.; Chen, Y.; Jang, B.; Zhao, K.; Zheng, Z.; Yu, R.; Shin, T. J.; Woo, H. Y.; Hou, J. Highly Efficient Fullerene-Free Polymer Solar Cells Fabricated with Polythiophene Derivative. *Adv. Mater.* **2016**, *28* (42), 9416–9422.

(54) Dou, L.; Liu, Y.; Hong, Z.; Li, G.; Yang, Y. Low-Bandgap Near-IR Conjugated Polymers/Molecules for Organic Electronics. *Chem. Rev.* **2015**, *115* (23), 12633–12665.
(55) Zhang, S.; Ye, L.; Hou, J. Breaking the 10% Efficiency Barrier in Organic Photovoltaics: Morphology and Device Optimization of Well-Known PBDTTT Polymers. *Adv. Energy Mater.* **2016**, *6* (11), 1–20.
(56) Hwang, Y. J.; Courtright, B. A. E.; Ferreira, A. S.; Tolbert, S. H.; Jenekhe, S. A. 7.7% Efficient All-Polymer Solar Cells. *Adv. Mater.* **2015**, *27* (31), 4578–4584.
(57) Liu, F.; Zhou, Z.; Zhang, C.; Vergote, T.; Fan, H.; Liu, F.; Zhu, X. A Thieno[3,4-b]Thiophene-Based Non-Fullerene Electron Acceptor for High-Performance Bulk-Heterojunction Organic Solar Cells. *J. Am. Chem. Soc.* **2016**, *138* (48), 15523–15526.
(58) Qian, D.; Ye, L.; Zhang, M.; Liang, Y.; Li, L.; Huang, Y.; Guo, X.; Zhang, S.; Tan, Z.; Hou, J. Design, Application, and Morphology Study of a New Photovoltaic Polymer with Strong Aggregation in Solution State. *Macromolecules* **2012**, *45* (24), 9611–9617.
(59) Fei, Z.; Eisner, F. D.; Jiao, X.; Azzouzi, M.; Röhr, J. A.; Han, Y.; Shahid, M.; Chesman, A. S. R.; Easton, C. D.; McNeill, C. R.; et al. An Alkylated Indacenodithieno[3,2-b]Thiophene-Based Nonfullerene Acceptor with High Crystallinity Exhibiting Single Junction Solar Cell Efficiencies Greater than 13% with Low Voltage Losses. *Adv. Mater.* **2018**, *30* (13), 1800728.
(60) Zhang, S.; Qin, Y.; Zhu, J.; Hou, J. Over 14% Efficiency in Polymer Solar Cells Enabled by a Chlorinated Polymer Donor. *Adv. Mater.* **2018**, *30* (20), 1–7.
(61) Ibraikulov, O. A.; Ngov, C.; Chávez, P.; Bulut, I.; Heinrich, B.; Boyron, O.; Gerasimov, K. L.; Ivanov, D. A.; Swaraj, S.; Méry, S.; et al. Face-on Orientation of Fluorinated Polymers Conveyed by Long Alkyl Chains: A Prerequisite for High Photovoltaic Performances. *J. Mater. Chem. A* **2018**, *6* (25), 12038–12045.
(62) Chen, Z.; Cai, P.; Chen, J.; Liu, X.; Zhang, L.; Lan, L.; Peng, J.; Ma, Y.; Cao, Y. Low Band-Gap Conjugated Polymers with Strong Interchain Aggregation and Very High Hole Mobility towards Highly Efficient Thick-Film Polymer Solar Cells. *Adv. Mater.* **2014**, *26* (16), 2586–2591.
(63) Liu, Y.; Lai, J. Y. L.; Chen, S.; Li, Y.; Jiang, K.; Zhao, J.; Li, Z.; Hu, H.; Ma, T.; Lin, H.; et al. Efficient Non-Fullerene Polymer Solar Cells Enabled by Tetrahedron-Shaped Core Based 3D-Structure Small-Molecular Electron Acceptors. *J. Mater. Chem. A* **2015**, *3* (26), 13632–13636.
(64) Hu, H.; Jiang, K.; Yang, G.; Liu, J.; Li, Z.; Lin, H.; Liu, Y.; Zhao, J.; Zhang, J.; Huang, F.; et al. Terthiophene-Based D-A Polymer with an Asymmetric Arrangement of Alkyl Chains That Enables Efficient Polymer Solar Cells. *J. Am. Chem. Soc.* **2015**, *137* (44), 14149–14157.
(65) Lin, H.; Chen, S.; Hu, H.; Zhang, L.; Ma, T.; Lai, J. Y. L.; Li, Z.; Qin, A.; Huang, X.; Tang, B.; et al. Reduced Intramolecular Twisting Improves the Performance of 3D Molecular Acceptors in Non-Fullerene Organic Solar Cells. *Adv. Mater.* **2016**, *28* (38), 8546–8551.
(66) Zhao, J.; Li, Y.; Lin, H.; Liu, Y.; Jiang, K.; Mu, C.; Ma, T.; Lin Lai, J. Y.; Hu, H.; Yu, D.; et al. High-Efficiency Non-Fullerene Organic Solar Cells Enabled by a Difluorobenzothiadiazole-Based Donor Polymer Combined with a Properly Matched Small Molecule Acceptor. *Energy Environ. Sci.* **2015**, *8* (2), 520–525.
(67) Liu, J.; Chen, S.; Qian, D.; Gautam, B.; Yang, G.; Zhao, J.; Bergqvist, J.; Zhang, F.; Ma, W.; Ade, H.; et al. Fast Charge Separation in a Non-Fullerene Organic Solar Cell with a Small Driving Force. *Nat. Energy* **2016**, *1* (7), 1–7.
(68) Price, S. C.; Stuart, A. C.; Yang, L.; Zhou, H.; You, W. Fluorine Substituted Conjugated Polymer of Medium Band Gap Yields 7% Efficiency in Polymer-Fullerene Solar Cells. *J. Am. Chem. Soc.* **2011**, *133* (12), 4625–4631.
(69) Lin, Y.; Zhao, F.; Prasad, S. K. K.; Chen, J.-D.; Cai, W.; Zhang, Q.; Chen, K.; Wu, Y.; Ma, W.; Gao, F.; et al. Balanced Partnership between Donor and Acceptor Components in Nonfullerene Organic Solar Cells with >12% Efficiency. *Adv. Mater.* **2018**, *30* (16), 1706363.
(70) Lee, H. K. H.; Li, Z.; Constantinou, I.; So, F.; Tsang, S. W.; So, S. K. Batch-to-Batch Variation of Polymeric Photovoltaic Materials: Its Origin and Impacts on Charge Carrier Transport and Device Performances. *Adv. Energy Mater.* **2014**, *4* (16), 1–8.
(71) Sakai, J.; Taima, T.; Saito, K. Efficient Oligothiophene:Fullerene Bulk Heterojunction Organic Photovoltaic Cells. *Org. Electron.* **2008**, *9* (5), 582–590.
(72) Yoo, S.; Domercq, B.; Kippelen, B. Efficient Thin-Film Organic Solar Cells Based on Pentacene/C 60 Heterojunctions. *Appl. Phys. Lett.* **2004**, *85* (22), 5427–5429.
(73) Pandey, A. K.; Nunzi, J. M. Rubrene/Fullerene Heterostructures with a Half-Gap Electroluminescence Threshold and Large Photovoltage. *Adv. Mater.* **2007**, *19* (21), 3613–3617.
(74) Roquet, S.; Cravino, A.; Leriche, P.; Alévêque, O.; Frère, P.; Roncali, J. Triphenylamine-Thienylenevinylene Hybrid Systems with Internal Charge Transfer as Donor Materials for Heterojunction Solar Cells. *J. Am. Chem. Soc.* **2006**, *128* (10), 3459–3466.

(75) Blanchard, P.; Malacrida, C.; Cabanetos, C.; Roncali, J.; Ludwigs, S. Triphenylamine and Some of Its Derivatives as Versatile Building Blocks for Organic Electronic Applications. *Polym. Int.* **2019**, *68* (4), 589–606.
(76) Leliège, A.; Régent, C. H. Le; Allain, M.; Blanchard, P.; Roncali, J. Structural Modulation of Internal Charge Transfer in Small Molecular Donors for Organic Solar Cells. *Chem. Commun.* **2012**, *48* (71), 8907–8909.
(77) Grolleau, J.; Gohier, F.; Allain, M.; Legoupy, S.; Cabanetos, C.; Frère, P. Rapid and Green Synthesis of Complementary D-A Small Molecules for Organic Photovoltaics. *Org. Electron. physics, Mater. Appl.* **2017**, *42*, 322–328.
(78) Leliège, A.; Grolleau, J.; Allain, M.; Blanchard, P.; Demeter, D.; Rousseau, T.; Roncali, J. Small D-π-A Systems with o-Phenylene-Bridged Accepting Units as Active Materials for Organic Photovoltaics. *Chem. - A Eur. J.* **2013**, *19* (30), 9948–9960.
(79) Jiang, Y.; Cabanetos, C.; Jungsuttiwong, S.; Alberga, D.; Adamo, C.; Roncali, J. Effects of Anthryl Groups on the Charge Transport and Photovoltaic Properties of Small Triarylamine-Based Donor-Acceptor Molecules: A Joint Experimental and Theoretical Study. *ChemistrySelect* **2017**, *2* (22), 6296–6303.
(80) Mohamed, S.; Demeter, D.; Laffitte, J.-A.; Blanchard, P.; Roncali, J. Structure-Properties Relationships in Triarylamine-Based Donor-Acceptor Molecules Containing Naphtyl Groups as Donor Material for Organic Solar Cells. *Sci. Rep.* **2015**, *5* (1), 9031.
(81) Jiang, Y.; Cabanetos, C.; Allain, M.; Liu, P.; Roncali, J. Manipulation of the Band Gap and Efficiency of a Minimalist Push–Pull Molecular Donor for Organic Solar Cells. *J. Mater. Chem. C* **2015**, *3* (20), 5145–5151.
(82) Marqués, P. S.; Andrés Castán, J. M.; Josse, P.; Blais, M.; Habibi, A. H.; Ramirez, I.; Walzer, K.; Roncali, J.; Blanchard, P.; Cabanetos, C. Effect of 4-Biphenyl Groups on the Charge Transport and Photovoltaic Properties of Arylamine Based Push–Pull Systems. *New J. Chem.* **2020**.
(83) Cabanetos, C.; Blanchard, P.; Roncali, J. Arylamine Based Photoactive Push-Pull Molecular Systems: A Brief Overview of the Chemistry "Made in Angers." *Chem. Rec.* **2019**, *19* (6), 1123–1130.
(84) Steinmann, V.; Kronenberg, N. M.; Lenze, M. R.; Graf, S. M.; Hertel, D.; Meerholz, K.; Bürckstümmer, H.; Tulyakova, E. V.; Würthner, F. Simple, Highly Efficient Vacuum-Processed Bulk Heterojunction Solar Cells Based on Merocyanine Dyes. *Adv. Energy Mater.* **2011**, *1* (5), 888–893.
(85) Burlingame, Q.; Coburn, C.; Che, X.; Panda, A.; Qu, Y.; Forrest, S. R. Centimetre-Scale Electron Diffusion in Photoactive Organic Heterostructures. *Nature* **2018**, *554* (7690), 77–80.
(86) Che, X.; Li, Y.; Qu, Y.; Forrest, S. R. High Fabrication Yield Organic Tandem Photovoltaics Combining Vacuum- and Solution-Processed Subcells with 15% Efficiency. *Nat. Energy* **2018**, *3* (5), 422–427.
(87) Che, X.; Xiao, X.; Zimmerman, J. D.; Fan, D.; Forrest, S. R. High-Efficiency, Vacuum-Deposited, Small-Molecule Organic Tandem and Triple-Junction Photovoltaic Cells. *Adv. Energy Mater.* **2014**, *4* (18), 1400568.
(88) Fitzner, R.; Reinold, E.; Mishra, A.; Mena-Osteritz, E.; Bäuerle, P.; Ziehlke, H.; Körner, C.; Leo, K.; Riede, M.; Weil, M.; et al. Dicyanovinyl-Substituted Oligothiophenes: Structure-Property Relationships and Application in Vacuum-Processed Small Molecule Organic Solar Cells. *Adv. Funct. Mater.* **2011**, *21* (5), 897–910.
(89) Fitzner, R.; Mena-Osteritz, E.; Mishra, A.; Schulz, G.; Reinold, E.; Weil, M.; Körner, C.; Ziehlke, H.; Elschner, C.; Leo, K.; et al. Correlation of π-Conjugated Oligomer Structure with Film Morphology and Organic Solar Cell Performance. *J. Am. Chem. Soc.* **2012**, *134* (27), 11064–11067.
(90) www.heliatek.com.
(91) Andre Weiss, Serge Vetter, Dirk Hildebrandt, Gunter Mattersteig, O. G. New Heterocyclic Compound, Useful in an Optoelectronic Component Such as Solar Cell, Organic LED, Organic FET and a Photodetectoritle. DE102012104247A1, 2012.
(92) Zhang, Q.; Kan, B.; Liu, F.; Long, G.; Wan, X.; Chen, X.; Zuo, Y.; Ni, W.; Zhang, H.; Li, M.; et al. Small-Molecule Solar Cells with Efficiency over 9%. *Nat. Photonics* **2014**, *9* (1), 35–41.
(93) Zhou, J.; Zuo, Y.; Wan, X.; Long, G.; Zhang, Q.; Ni, W.; Liu, Y.; Li, Z.; He, G.; Li, C.; et al. Solution-Processed and High-Performance Organic Solar Cells Using Small Molecules with a Benzodithiophene Unit. *J. Am. Chem. Soc.* **2013**, *135* (23), 8484–8487.
(94) Sun, Y.; Welch, G. C.; Leong, W. L.; Takacs, C. J.; Bazan, G. C.; Heeger, A. J. Solution-Processed Small-Molecule Solar Cells with 6.7% Efficiency. *Nat. Mater.* **2012**, *11* (1), 44–48.
(95) Van Der Poll, T. S.; Love, J. A.; Nguyen, T. Q.; Bazan, G. C. Non-Basic High-Performance Molecules for Solution-Processed Organic Solar Cells. *Adv. Mater.* **2012**, *24* (27), 3646–3649.
(96) Mahmood, A.; Hu, J. Y.; Xiao, B.; Tang, A.; Wang, X.; Zhou, E. Recent Progress in Porphyrin-Based Materials for Organic Solar Cells. *J. Mater. Chem. A* **2018**, *6* (35), 16769–16797.
(97) Gao, K.; Miao, J.; Xiao, L.; Deng, W.; Kan, Y.; Liang, T.; Wang, C.; Huang, F.; Peng, J.; Cao, Y.; et al. Multi-

Length-Scale Morphologies Driven by Mixed Additives in Porphyrin-Based Organic Photovoltaics. *Adv. Mater.* **2016**, *28* (23), 4727–4733.

(98) Liang, T.; Xiao, L.; Gao, K.; Xu, W.; Peng, X.; Cao, Y. Modifying the Chemical Structure of a Porphyrin Small Molecule with Benzothiophene Groups for the Reproducible Fabrication of High Performance Solar Cells. *ACS Appl. Mater. Interfaces* **2017**, *9* (8), 7131–7138.

(99) Srinivasa Rao, R.; Bagui, A.; Hanumantha Rao, G.; Gupta, V.; Singh, S. P. Achieving the Highest Efficiency Using a BODIPY Core Decorated with Dithiafulvalene Wings for Small Molecule Based Solution-Processed Organic Solar Cells. *Chem. Commun.* **2017**, *53* (51), 6953–6956.

(100) Li, T. Y.; Meyer, T.; Ma, Z.; Benduhn, J.; Korner, C.; Zeika, O.; Vandewal, K.; Leo, K. Small Molecule Near-Infrared Boron Dipyrromethene Donors for Organic Tandem Solar Cells. *J. Am. Chem. Soc.* **2017**, *139* (39), 13636–13639.

(101) Walker, B.; Tamayo, A. B.; Dang, X. D.; Zalar, P.; Seo, J. H.; Garcia, A.; Tantiwiwat, M.; Nguyen, T. Q. Nanoscale Phase Separation and High Photovoltaic Efficiency in Solution-Processed, Small-Molecule Bulk Heterojunction Solar Cells. *Adv. Funct. Mater.* **2009**, *19* (19), 3063–3069.

(102) Wang, J. L.; Wu, Z.; Miao, J. S.; Liu, K. K.; Chang, Z. F.; Zhang, R. B.; Wu, H. Bin; Cao, Y. Solution-Processed Diketopyrrolopyrrole-Containing Small-Molecule Organic Solar Cells with 7.0% Efficiency: In-Depth Investigation on the Effects of Structure Modification and Solvent Vapor Annealing. *Chem. Mater.* **2015**, *27* (12), 4338–4348.

(103) Kroto, H. W.; Heath, J. R.; O'Brien, S. C.; Curl, R. F.; Smalley, R. E. C60: Buckminsterfullerene. *Nature* **1985**, *318* (6042), 162–163.

(104) Echegoyen, L.; Echegoyen, L. E. Electrochemistry of Fullerenes and Their Derivatives. *Acc. Chem. Res.* **1998**, *31* (9), 593–601.

(105) He, Y.; Li, Y. Fullerene Derivative Acceptors for High Performance Polymer Solar Cells. *Phys. Chem. Chem. Phys.* **2011**, *13* (6), 1970–1983.

(106) Hummelen, J. C.; Knight, B. W.; Lepeq, F.; Wudl, F.; Yao, J.; Wilkins, C. L. Preparation and Characterization of Fulleroid and Methanofullerene Derivatives. *J. Org. Chem.* **1995**, *60* (3), 532–538.

(107) Zhao, G. J.; He, Y. J.; Li, Y. 6.5% Efficiency of Polymer Solar Cells Based on Poly(3-Hexylthiophene) and Indene-C60 Bisadduct by Device Optimization. *Adv. Mater.* **2010**, *22* (39), 4355–4358.

(108) Chen, L.; Li, C.; Müllen, K. Beyond Perylene Diimides: Synthesis, Assembly and Function of Higher Rylene Chromophores. *J. Mater. Chem. C* **2014**, *2* (11), 1938–1956.

(109) Sommer, M. Conjugated Polymers Based on Naphthalene Diimide for Organic Electronics. *J. Mater. Chem. C* **2014**, *2* (17), 3088–3098.

(110) Fan, B.; Ying, L.; Zhu, P.; Pan, F.; Liu, F.; Chen, J.; Huang, F.; Cao, Y. All-Polymer Solar Cells Based on a Conjugated Polymer Containing Siloxane-Functionalized Side Chains with Efficiency over 10%. *Adv. Mater.* **2017**, *29* (47), 1–7.

(111) Fan, B.; Zhong, W.; Ying, L.; Zhang, D.; Li, M.; Lin, Y.; Xia, R.; Liu, F.; Yip, H.-L.; Li, N.; et al. Surpassing the 10% Efficiency Milestone for 1-Cm2 All-Polymer Solar Cells. *Nat. Commun.* **2019**, *10* (1), 4100.

(112) Hwang, Y. J.; Li, H.; Courtright, B. A. E.; Subramaniyan, S.; Jenekhe, S. A. Nonfullerene Polymer Solar Cells with 8.5% Efficiency Enabled by a New Highly Twisted Electron Acceptor Dimer. *Adv. Mater.* **2016**, *28* (1), 124–131.

(113) Liu, Y.; Zhang, L.; Lee, H.; Wang, H. W.; Santala, A.; Liu, F.; Diao, Y.; Briseno, A. L.; Russell, T. P. NDI-Based Small Molecule as Promising Nonfullerene Acceptor for Solution-Processed Organic Photovoltaics. *Adv. Energy Mater.* **2015**, *5* (12), 2–9.

(114) Tang, F.; Zhu, D.; Liang, N.; Hou, J.; Wang, Z. Terrylene Diimide-Based Middle-Low Bandgap Electron Acceptors for Organic Photovoltaics. *J. Mater. Chem. C* **2020**, *8* (13), 4441–4446.

(115) Feng, J.; Liang, N.; Jiang, W.; Meng, D.; Xin, R.; Xu, B.; Zhang, J.; Wei, Z.; Hou, J.; Wang, Z. Twisted Terrylene Dyes: Synthesis and Application in Organic Solar Cells. *Org. Chem. Front.* **2017**, *4* (5), 811–816.

(116) Zhao, C.; Guo, Y.; Zhang, Y.; Yan, N.; You, S.; Li, W. Diketopyrrolopyrrole-Based Conjugated Materials for Non-Fullerene Organic Solar Cells. *J. Mater. Chem. A* **2019**, *7* (17), 10174–10199.

(117) Karsten, B. P.; Bijleveld, J. C.; Janssen, R. A. J. Diketopyrrolopyrroles as Acceptor Materials in Organic Photovoltaics. *Macromol. Rapid Commun.* **2010**, *31* (17), 1554–1559.

(118) Josse, P.; Dalinot, C.; Jiang, Y.; Dabos-Seignon, S.; Roncali, J.; Blanchard, P.; Cabanetos, C. Phthalimide End-Capped Thienoisoindigo and Diketopyrrolopyrrole as Non-Fullerene Molecular Acceptors for Organic Solar Cells. *J. Mater. Chem. A* **2015**, *4* (1), 250–256.

(119) Josse, P.; Labrunie, A.; Dalinot, C.; McAfee, S. M.; Dabos-Seignon, S.; Roncali, J.; Welch, G. C.; Blanchard, P.; Cabanetos, C. Effect of Side Chains on the Electronic and Photovoltaic Properties of Diketopyrrolopyrrole-Based Molecular Acceptors. *Org. Electron.* **2016**, *37*, 479–484.

(120) Li, S.; Liu, W.; Shi, M.; Mai, J.; Lau, T. K.; Wan, J.; Lu, X.; Li, C. Z.; Chen, H. A Spirobifluorene and Diketopyrrolopyrrole Moieties Based Non-Fullerene Acceptor for Efficient and Thermally Stable Polymer Solar Cells with High Open-Circuit Voltage. *Energy Environ. Sci.* **2016**, *9* (2), 604–610.

(121) Privado, M.; De La Cruz, P.; Biswas, S.; Singhal, R.; Sharma, G. D.; Langa, F. A Non-Fullerene All Small Molecule Solar Cell Constructed with a Diketopyrrolopyrrole-Based Acceptor Having a Power Conversion Efficiency Higher than 9% and an Energy Loss of 0.54 EV. *J. Mater. Chem. A* **2018**, *6* (25), 11714–11724.

(122) Woo, C. H.; Holcombe, T. W.; Unruh, D. A.; Sellinger, A.; Frechet, J. M. J. Phenyl vs Alkyl Polythiophene: A Solar Cell Comparison Using a Vinazene Derivative as Acceptor. *Chem. Mater.* **2010**, *22* (5), 1673–1679.

(123) Walker, B.; Han, X.; Kim, C.; Sellinger, A.; Nguyen, T. Q. Solution-Processed Organic Solar Cells from Dye Molecules: An Investigation of Diketopyrrolopyrrole: Vinazene Heterojunctions. *ACS Appl. Mater. Interfaces* **2012**, *4* (1), 244–250.

(124) Winzenberg, K. N.; Kemppinen, P.; Scholes, F. H.; Collis, G. E.; Shu, Y.; Singh, T. B.; Bilic, A.; Forsyth, C. M.; Watkins, S. E. Indan-1,3-Dione Electron-Acceptor Small Molecules for Solution-Processable Solar Cells: A Structure-Property Correlation. *Chem. Commun.* **2013**, *49* (56), 6307–6309.

(125) Lin, Y.; Wang, J.; Zhang, Z. G.; Bai, H.; Li, Y.; Zhu, D.; Zhan, X. An Electron Acceptor Challenging Fullerenes for Efficient Polymer Solar Cells. *Adv. Mater.* **2015**, *27* (7), 1170–1174.

(126) Yuan, J.; Zhang, Y.; Zhou, L.; Zhang, G.; Yip, H. L.; Lau, T. K.; Lu, X.; Zhu, C.; Peng, H.; Johnson, P. A.; et al. Single-Junction Organic Solar Cell with over 15% Efficiency Using Fused-Ring Acceptor with Electron-Deficient Core. *Joule* **2019**, *3* (4), 1140–1151.

(127) Yan, T.; Song, W.; Huang, J.; Peng, R.; Huang, L.; Ge, Z. 16.67% Rigid and 14.06% Flexible Organic Solar Cells Enabled by Ternary Heterojunction Strategy. *Adv. Mater.* **2019**, *31* (39), 1–8.

(128) Xu, X.; Feng, K.; Bi, Z.; Ma, W.; Zhang, G.; Peng, Q. Single-Junction Polymer Solar Cells with 16.35% Efficiency Enabled by a Platinum(II) Complexation Strategy. *Adv. Mater.* **2019**, *31* (29), 1–7.

(129) Fan, B.; Zeng, Z.; Zhong, W.; Ying, L.; Zhang, D.; Li, M.; Peng, F.; Li, N.; Huang, F.; Cao, Y. Optimizing Microstructure Morphology and Reducing Electronic Losses in 1 Cm2 Polymer Solar Cells to Achieve Efficiency over 15%. *ACS Energy Lett.* **2019**, *4* (10), 2466–2472.

(130) Liu, J.; Liu, L.; Zuo, C.; Xiao, Z.; Zou, Y.; Jin, Z.; Ding, L. 5H-Dithieno[3,2-b:2′,3′-d]Pyran-5-One Unit Yields Efficient Wide-Bandgap Polymer Donors. *Sci. Bull.* **2019**, *64* (22), 1655–1657.

(131) Xiong, J.; Jin, K.; Jiang, Y.; Qin, J.; Wang, T.; Liu, J.; Liu, Q.; Peng, H.; Li, X.; Sun, A.; et al. Thiolactone Copolymer Donor Gifts Organic Solar Cells a 16.72% Efficiency. *Sci. Bull.* **2019**, *64* (21), 1573–1576.

(132) Liu, Q.; Jiang, Y.; Jin, K.; Qin, J.; Xu, J.; Li, W.; Xiong, J.; Liu, J.; Xiao, Z.; Sun, K.; et al. 18% Efficiency Organic Solar Cells. *Sci. Bull.* **2020**, *65* (4), 272–275.

(133) Wang, T.; Qin, J.; Xiao, Z.; Meng, X.; Zuo, C.; Yang, B.; Tan, H.; Yang, J.; Yang, S.; Sun, K.; et al. A 2.16 EV Bandgap Polymer Donor Gives 16% Power Conversion Efficiency. *Sci. Bull.* **2020**, *65* (3), 179–181.

(134) Wu, Y.; Zheng, Y.; Yang, H.; Sun, C.; Dong, Y.; Cui, C.; Yan, H.; Li, Y. Rationally Pairing Photoactive Materials for High-Performance Polymer Solar Cells with Efficiency of 16.53%. *Sci. China Chem.* **2020**, *63* (2), 265–271.

(135) Jiang, K.; Wei, Q.; Lai, J. Y. L.; Peng, Z.; Kim, H. K.; Yuan, J.; Ye, L.; Ade, H.; Zou, Y.; Yan, H. Alkyl Chain Tuning of Small Molecule Acceptors for Efficient Organic Solar Cells. *Joule* **2019**, *3* (12), 3020–3033.

(136) Cui, Y.; Yao, H.; Hong, L.; Zhang, T.; Tang, Y.; Lin, B.; Xian, K.; Gao, B.; An, C.; Bi, P.; et al. Organic Photovoltaic Cell with 17% Efficiency and Superior Processability. *Natl. Sci. Rev.* **2019**, 1–8.

(137) Cui, Y.; Yao, H.; Zhang, J.; Xian, K.; Zhang, T.; Hong, L.; Wang, Y.; Xu, Y.; Ma, K.; An, C.; et al. Single-Junction Organic Photovoltaic Cells with Approaching 18% Efficiency. *Adv. Mater.* **2020**, *32* (19), 1–7.

(138) Forrest, S. R.; Leu, L. Y.; So, F. F.; Yoon, W. Y. Optical and Electrical Properties of Isotype Crystalline Molecular Organic Heterojunctions. *J. Appl. Phys.* **1989**, *66* (12), 5908–5914.

(139) De Bettignies, R.; Nicolas, Y.; Blanchard, P.; Levillain, E.; Nunzi, J. M.; Roncali, J. Planarized Star-Shaped Oligothiophenes as a New Class of Organic Semiconductors for Heterojunction Solar Cells. *Adv. Mater.* **2003**, *15* (22), 1939–1943.

(140) Rostalski, J.; Meissner, D. Photocurrent Spectroscopy for the Investigation of Charge Carrier Generation and Transport Mechanisms in Organic p/n-Junction Solar Cells. *Sol. Energy Mater. Sol. Cells* **2000**, *63* (1), 37–47.

(141) Uhrich, C.; Schueppel, R.; Petrich, A.; Pfeiffer, M.; Leo, K.; Brier, E.; Kilickiran, P.; Baeuerle, P. Organic Thin-Film Photovoltaic Cells Based on Oligothiophenes with Reduced Bandgap. *Adv. Funct. Mater.* **2007**, *17* (15), 2991–2999.

(142) Schwenn, P. E.; Gui, K.; Nardes, A. M.; Krueger, K. B.; Lee, K. H.; Mutkins, K.; Rubinstein-Dunlop, H.; Shaw, P. E.; Kopidakis, N.; Burn, P. L.; et al. A Small Molecule Non-Fullerene Electron Acceptor for Organic Solar Cells. *Adv. Energy Mater.* **2011**, *1* (1), 73–81.

(143) Fang, Y.; Pandey, A. K.; Nardes, A. M.; Kopidakis, N.; Burn, P. L.; Meredith, P. A Narrow Optical Gap Small Molecule Acceptor for Organic Solar Cells. *Adv. Energy Mater.* **2013**, *3* (1), 54–59.

(144) Cattin, L.; Cabanetos, C.; El Mahlali, A.; Arzel, L.; Morsli, M.; Blanchard, P.; Bernède, J. C. Smart Geometrical Approach to Intercalate a Highly Absorbing and Quite Resistive Electron Donor Layer in Ternary Organic Photovoltaic Cells. *Org. Electron.* **2020**, *76* (2019), 105463.

(145) Beaumont, N.; Cho, S. W.; Sullivan, P.; Newby, D.; Smith, K. E.; Jones, T. S. Boron Subphthalocyanine Chloride as an Electron Acceptor for High-Voltage Fullerene-Free Organic Photovoltaics. *Adv. Funct. Mater.* **2012**, *22* (3), 561–566.

(146) Gommons, H.; Aernouts, T.; Verreet, B.; Heremans, P.; Medina, A.; Claessens, C. C.; Torres, T. Perfluorinated Subphthalocyanine as a New Acceptor Material in a Small-Molecule Bilayer Organic Solar Cell. *Adv. Funct. Mater.* **2009**, *19* (21), 3435–3439.

(147) Verreet, B.; Rand, B. P.; Cheyns, D.; Hadipour, A.; Aernouts, T.; Heremans, P.; Medina, A.; Claessens, C. G.; Torres, T. A 4% Efficient Organic Solar Cell Using a Fluorinated Fused Subphthalocyanine Dimer as an Electron Acceptor. *Adv. Energy Mater.* **2011**, *1* (4), 565–568.

(148) Verreet, B.; Cnops, K.; Cheyns, D.; Heremans, P.; Stesmans, A.; Zango, G.; Claessens, C. G.; Torres, T.; Rand, B. P. Decreased Recombination through the Use of a Non-Fullerene Acceptor in a 6.4% Efficient Organic Planar Heterojunction Solar Cell. *Adv. Energy Mater.* **2014**, *4* (8), 1–8.

(149) Cnops, K.; Zango, G.; Genoe, J.; Heremans, P.; Martinez-Diaz, M. V.; Torres, T.; Cheyns, D. Energy Level Tuning of Non-Fullerene Acceptors in Organic Solar Cells. *J. Am. Chem. Soc.* **2015**, *137* (28), 8991–8997.

(150) Cnops, K.; Rand, B. P.; Cheyns, D.; Verreet, B.; Empl, M. A.; Heremans, P. 8.4% Efficient Fullerene-Free Organic Solar Cells Exploiting Long-Range Exciton Energy Transfer. *Nat. Commun.* **2014**, *5* (1), 3406.

Chapter 2
Non-Fullerene Acceptor Materials

1 Perylene Diimide based Non-Fullerene acceptors

1.1 Introduction

Discovered in the early 1910s,[151,152] the perylene-3,4,9,10-tetracarboxylic acid diimide derivatives (PDIs) were originally used as industrial pigments. They result from the research developed by Harmon Colors (USA) and Farbwerke Hoechst AG (Germany) in the middle of the twentieth century,[153] aiming at preparing a large variety of colours from the red to black range (e.g. Pigment Violet 29, Pigment Red 179, etc.).

PDI derivatives are industrially afforded through a 5-step synthesis (Scheme 1) starting from the oxidation of acenaphthene thus generating the corresponding dicarboxylic acid anhydride, which is subsequently treated with ammonia to provide naphthalene-1,8-dicarboxylic acid imide. The oxidative homocoupling of the latter, yields the perylene-3,4,9,10-tetracarboxylic diimide (**PTCDI**), that is further hydrolysed with concentrated H_2SO_4 to afford the dianhydride precursor (**PTCDA**). Eventually, the reaction of aliphatic amines or anilines with **PTCDA** furnished, in high yields, several (more or less) soluble PDIs for direct application in the dyes and pigments industry.[154]

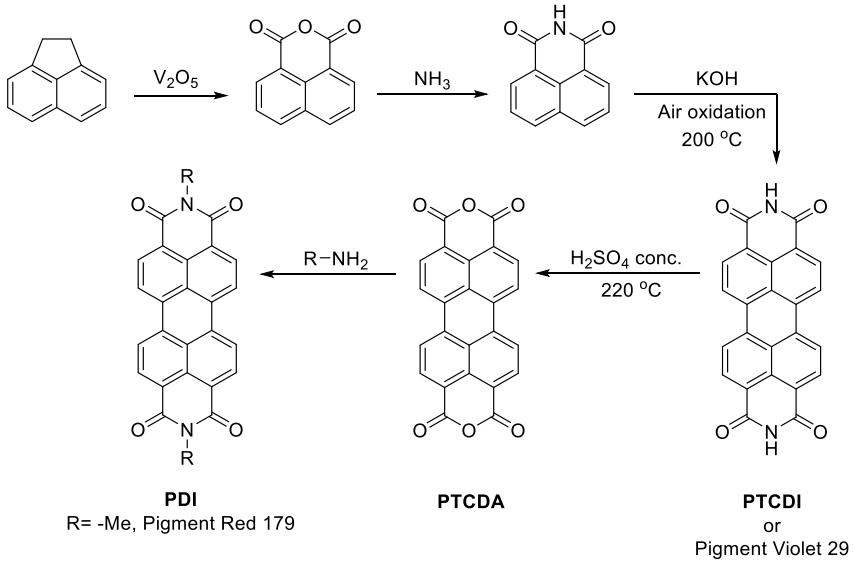

Scheme 1. Preparation of N,N'-disubsituted PDIs.

Besides the chemical, photo and thermal stability that make these materials suitable for textile and industrial paint applications, perylene dyes present singular optical, redox and charge transport properties, combining a near-unity fluorescence quantum yields and strong electron-accepting character. The merge of these properties has prompted the use of PDIs as

organic semiconductor materials in organic electronics and more precisely in organic field-effect transistors (OFETs),[155,156] organic dye lasers,[157,158] fluorescent solar concentrator[159] and OPVs,[160] *inter alia*.

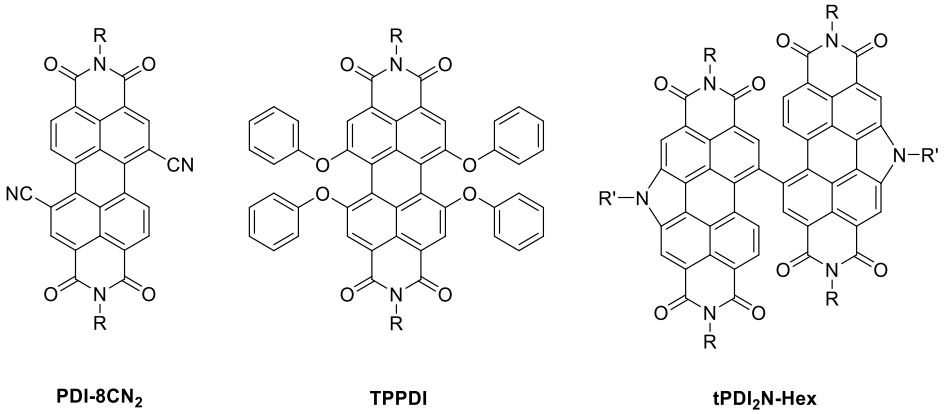

Figure 24. Structures of PDI derivatives implemented in OFETs, dye lasers and OPV respectively.

Regarding the latter application, which is the main topic of this thesis work, the PDI was already introduced as an electron-accepting material in the first example of PHJ solar cell reported by Tang in 1986, as discussed in Chapter 1. Since then, huge progress has been achieved, attracting considerable research attention for the preparation of NFAs used in efficient BHJs solar cells. They have been great competitors to fullerene derivatives, due to their easier chemical functionalization and their stronger and tunable absorption. Nevertheless, their extended π-conjugated structure typically suffers from an excessive π–π stacking tendency, resulting in the formation of micrometer-sized crystallites that are detrimental for the creation of phase segregation of donor and acceptor in nanodomains and thereby, an efficient charge separation once embedded in BHJ solar cells. To tackle this issue, twisted structures have been introduced disrupting the aggregation tendency and reducing the crystallinity. On the other hand, this design also results in decreasing the electron mobility and hampering the J_{SC}, *FF* and therefore PCE improvements.[161] Hence, to reduce the PDI domain size, the OPV community has developed various strategies, establishing a balance between the crystallinity and the electron transport ability. Reported by Wang and coworkers, a family of PDI dimers (single-bond linked) exhibited a promising PCE of 4.5% for the simple dimer **SdiPDI** when blended with the donor polymer **PTB7-Th**.[162] The introduction of S and Se bridges in the bay position was found to induce intermolecular interactions between the new heteroatoms and modifies the energy levels showing a higher PCE of *ca* 7.2% and 8.4% for

SdiPDI-S and **SdiPDI-Se**, respectively.[163,164] In parallel, Nuckolls *et al.* developed a helical PDI family consisting in fused PDI units with a two-carbon bridge.[165,166] Keeping the good absorption performance and slightly reducing aggregation, **hPDI1**, **hPDI3**, **hPDI4** are still characterized by relatively high electron mobilities resulting in PCEs of 5.9% (**PTB7-Th:hPDI1**), 7.9% (**PTB7:hPDI3**) and 8.3% **(PTB7-Th:hPDI4**). Among other design principle, the development of PDI-tetramer structures can be cited.[65] For instance Yan's group reported two tetramers based on tetrathienylbenzene (TTB)[167] demonstrating that fused PDI derivative (**FTTB-PDI4**), with less twisted geometry, are characterized by descent charge transport ability and electron mobilities in the blend. Ring-fusion was then applied, improving the efficiency from 7.1% for the non-fused compound (**P3TA:TTB-PDI4**) to 10.6% for **P3TA:FTTB-PDI4**, which is the highest PCE value for PDI-based acceptors to date (Figure 25).

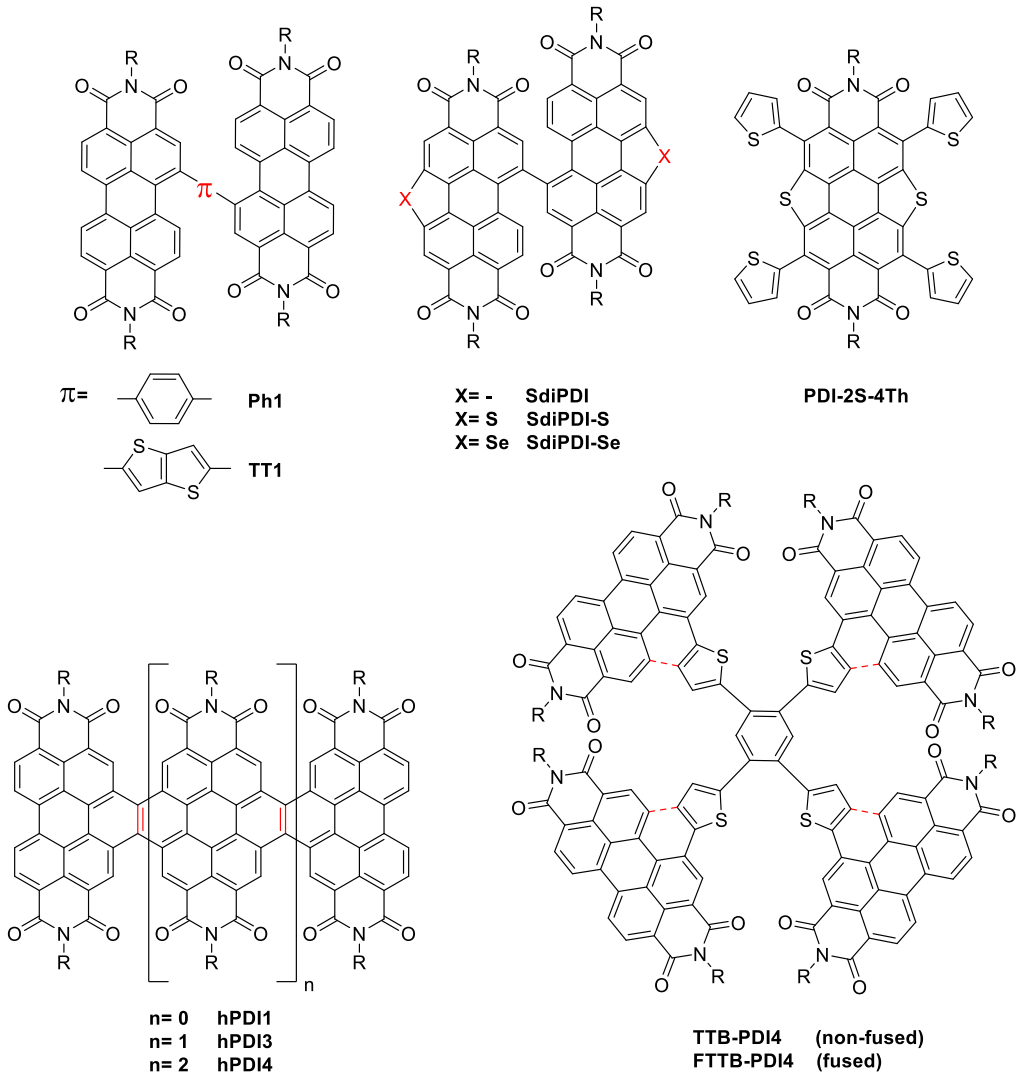

Figure 25. Example of PDI based NFAs.

To reach these large variety of structures, molecular engineering has played an important role paving the way for the functionalization of the peripheral positions, namely the *ortho* (2,5,8,11) and, predominantly, the bay (1,6,7,12) positions (Scheme 2).

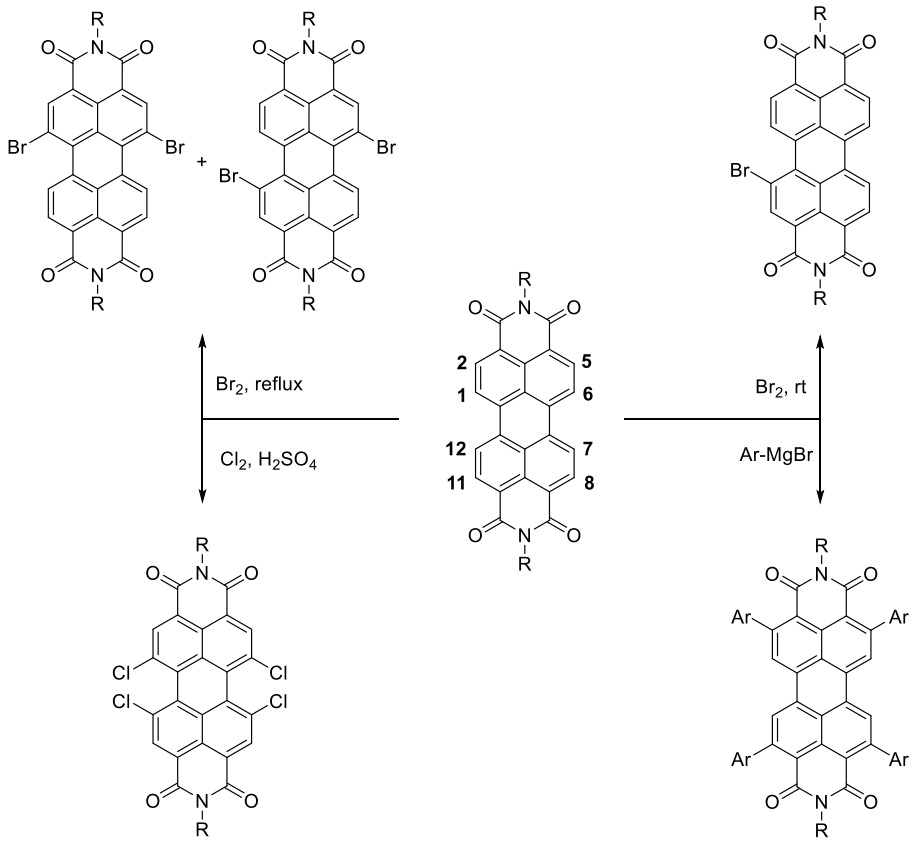

Scheme 2. Preparation of PDI derivatives through different methodologies.

The headland or *ortho* substitution was achieved in the past years by ruthenium and iridium catalyzed reactions, where regioselective borylation was completed, paving the way to palladium coupling.[168–170] More recently, Li *et al.* published a synthetic method affording 2,5,8,11-tetraryl PDIs in only one step, through the capture of aromatic Grignard reagents (*e.g.* **PDI-2S-4Th**, Figure 25).[171] On the other hand, hundreds of NFAs have been synthesized *via* bay functionalization, through a selective and easy halogenation. The reaction of PDI with chlorine in presence of sulfuric acid, leads to the tetrachlorinated compound in high yields.[172] Besides, while the mono-brominated core could be straightforward obtained after reaction with bromine in mild conditions,[173] higher temperatures promote the dibromination of the bay positions, providing the *1,7*-dibrominated precursor which has led to many published molecular and macromolecular π-functional PDI based materials.[174,175] Also generated during the reaction, but in smaller ratio, the *1,6*-isomer has not triggered such interest. Conversely,

the presence of the latter, considered as an impurity, has even motivated the development of purification procedures and methods.[176]

Most of the studies to date regarding the *1,7*- and *1,6*- PDI isomers, have focused on the comparison of their properties, whereas their impact on the material application has been scarcely discussed in peer publications. In fact, and to the best of our knowledge, there is only one article describing the synthesis of the two *1,6* and *1,7*-dibromo PDI isomers, their purification and their functionalization either by triphenylamine (TPA) or benzodithiophene (BDT) moieties leading to NFAs.[177] In all cases, the *1,7*-isomers led to the best PCEs (*ca* 0.67%) attributed to a better morphology of the photoactive layer. To gain further insight into the properties of *1,6* or *1,7* PDI isomers, particularly from a charge transport point of view, and bring more examples to confirm or not a trend for their use as NFAs, the synthesis and direct comparison of two new indeno[1,2-b]thiophene (IDT) end-capped PDI regioisomers (*1,6* and *1,7*) were considered.

1.2 Synthesis and Characterization

Chosen herein to restrain aggregation, two bulky IDT-derived blocks **3** were introduced in bay position of a PDI platform. The synthesis of **3** was adapted from a reported procedure.[178] First, a pallado-catalysed Stille reaction between the methyl 2-bromobenzoate **1** and the 2-tributylstannylthiophene afforded compound **2** in quantitative yield (Scheme 3).

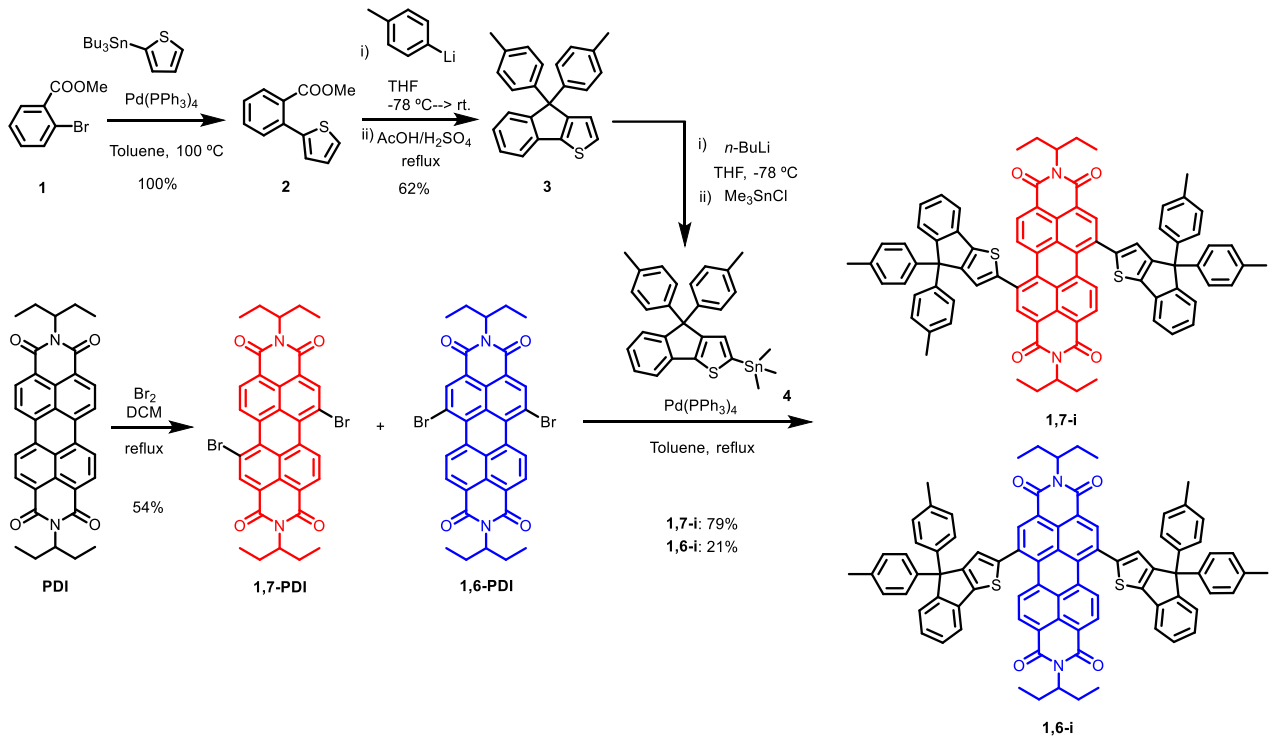

*Scheme 3. Synthetic route to **1,6-i** and **1,7-i**.*

The latter was then treated with *p*-tolyllithium to generate a benzyl alcohol intermediate that was subsequently cyclized under acidic conditions. The resulting indeno[1,2-*b*]thiophene **3** was finally stannylated in presence of *n*-BuLi and trimethyltin chloride. In parallel, a 3:1 ratio mixture of *1,7* and *1,6* dibrominated PDIs was efficiently prepared following a method reported by Rybtchinski *et al.*[179] This mixture was directly engaged in a final Stille cross-coupling reaction with the stannyl derivative **4** affording target isomers (**1,6-i** and **1,7-i**) that were easily separated by column chromatography.

Analyzed by ^{1}H NMR spectroscopy, the two isomers exhibit similar sets of signals with only subtle changes, as depicted in Figure 26. In fact, only the singlet signal associated to the proton born by the thiophene ring showed a significantly different chemical shift at 6.96 ppm and 7.17 pm for **1,6-i** and **1,7-i** respectively (pink circle, Figure 26, ^{1}H-NMR).

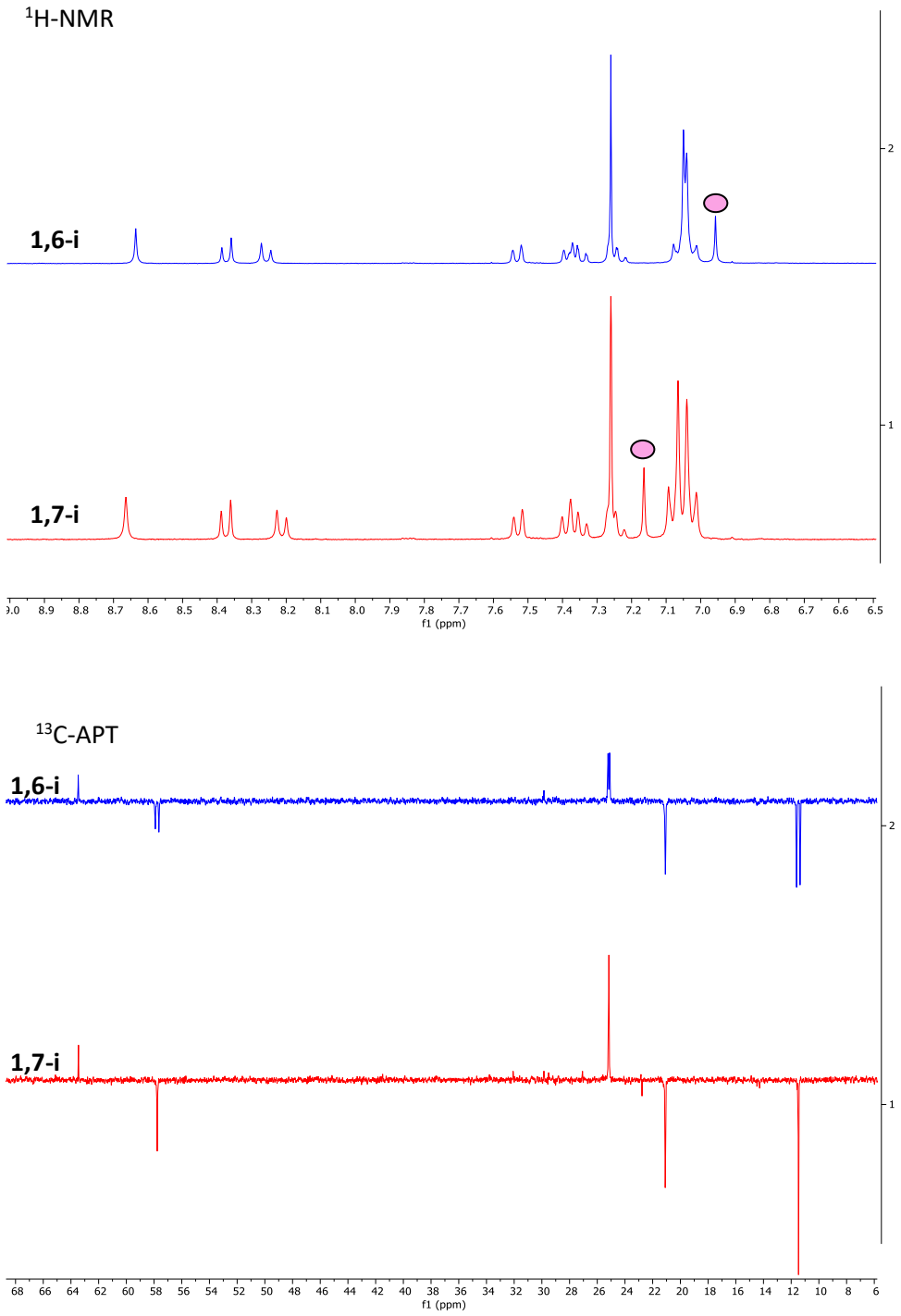

Figure 26. *^{1}H NMR (top) and ^{13}C APT (bottom) spectra of **1,6-i** (blue) and **1,7-i** (red) in $CDCl_3$ at 25 °C. ^{13}C APT: CH_3 and CH negative.*

Structural attribution can be deduced from the ^{13}C NMR spectra, and more precisely from the number of aliphatic carbon that are symmetry dependent. Albeit the signature along the spectra is nearly identical for the two compounds, the signals located at 57, 25 and 11 ppm split in two peaks in the case of **1,6-i**, due to its lower symmetry (Figure 26, ^{13}C APT, blue spetrum).

Besides, single crystals of both isomers were successfully grown by the solvent evaporation method. While slow evaporation from dichloromethane was used for **1,7-i**, it is noteworthy that stable and suitable single crystals of its *1,6* couterpart were only obtained from toluene. Beyond confirming the structure of each isomer (Figure 27), X-ray diffraction analyses also revealed, in both cases, regardless of the grafting position, relatively twisted PDI backbones with similar dihedral angles (of *ca* 19°) between the two subplanes and high torsion angles (> 44°) between the PDI core and the bulky IDT arms, hindering their aggregation and resulting in a good solubility of each isomer in common organic solvents.

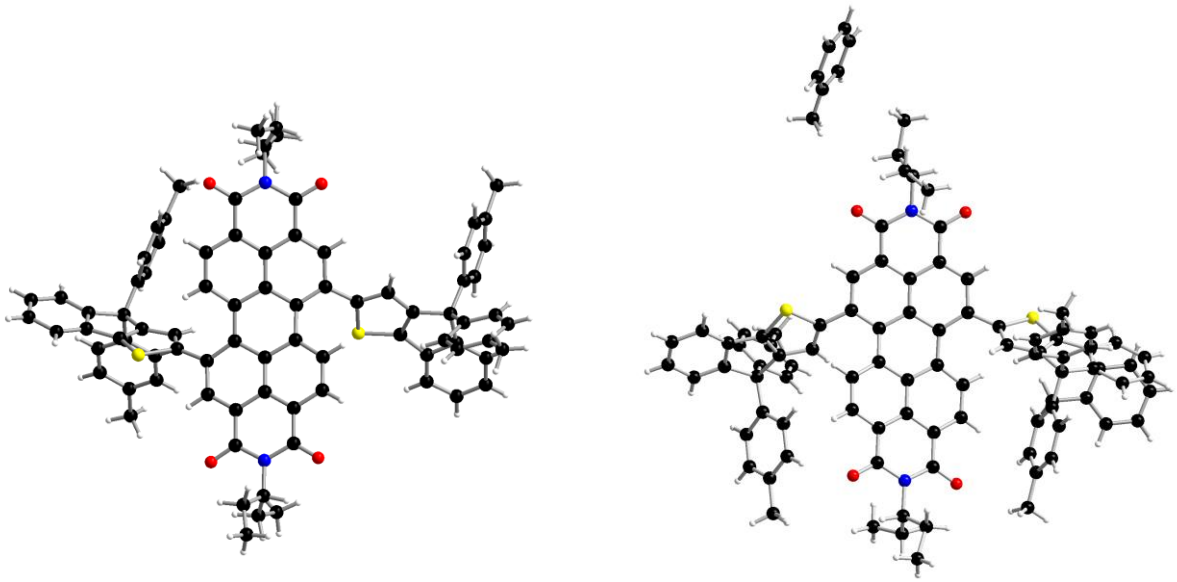

*Figure 27. Molecular structures of **1,7-i** (left) and **1,6-i** (right) obtained by X-ray diffraction.*

1.3 Optical and electrochemical analysis

The two isomers were analyzed by UV-visible spectroscopy revealing a strong absorption in the visible region in both solution and as thin films (Figure 28). As expected, similar patterns were recorded showing three main bands with maxima at *ca* 320 nm, 460 nm and in the 550-650 nm region assigned to π-π* transitions localized on each building blocks, *ie*, on the IDT and on the PDI units, and to a charge transfer (CT) transition from the electron rich substituents (IDT) to the electron deficient central core (PDI), respectively. Nonetheless, comparison of the spectra clearly highlights the impact of the grafting positions on the electronic properties since all absorption bands of **1,7-i** are significantly red shifted with respect to those of **1,6-i**, particularly in the low energy region (CT band). In parallel, the absorption spectra in the solid-state present a bathochromic shift compared to the spectra in

solution, resulting in an optical bandgap of 1.56 eV and 1.66 eV for **1,7-i** and **1,6-i**, respectively, as measured from the absorption band edge at low energy.

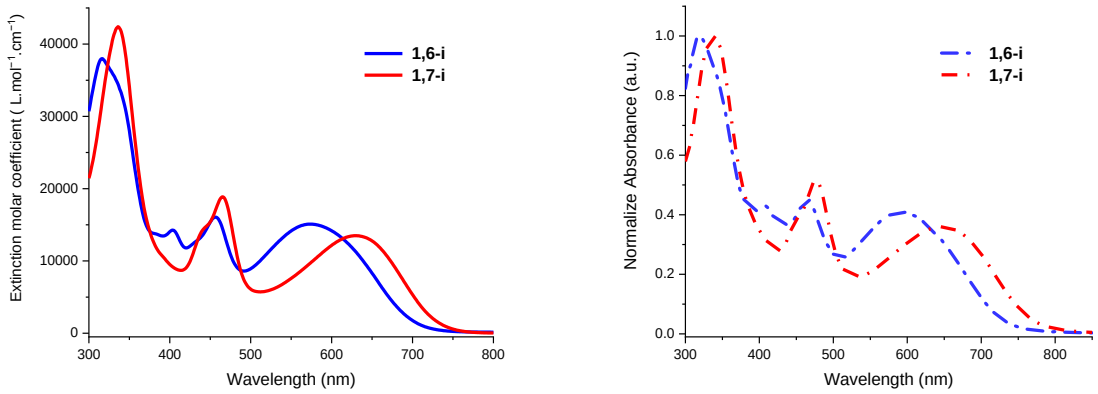

*Figure 28. UV-Vis absorption spectra of **1,6-i** (blue line) and **1,7-i** (red line) in CH_2Cl_2 (left) and as thin film on glass (right).*

*Table 2. Optical data of **1,6-i** and **1,7-i** recorded in dichloromethane (10^{-6} M) and on glass sheets.*

Compound	λ_{max}^{ABS} (nm) in DCM	ε (M^{-1} cm^{-1})	λ_{max}^{ABS} (nm) in film	E_g^{opt} (eV)
1,6-i	573	16000	591	1.66
	456	17000	465	
	316	41000	318	
1,7-i	630	14000	650	1.56
	465	17000	478	
	336	41000	338	

The electrochemical properties of both isomers were characterized by cyclic voltammetry (CV), performed in dichloromethane using NBu_4PF_6 as supporting electrolyte (0.1 M). Both isomers show one reversible reduction wave associated to the formation of a stable radical anion, at the same reduction peak potential (E_{pc} = - 1.05 V *vs* Fc/Fc^+) (Figure 29). In the positive potentials region, a quasi-reversible oxidation wave leading to the generation of a radical cation species, was observed at different oxidation peak potentials (E_{pa}) of 0.83 V and 0.89 V for **1,7-i** and **1,6-i** respectively, thus revealing a deeper highest occupied molecular orbital (HOMO) level for **1,6-i** (Table 3).

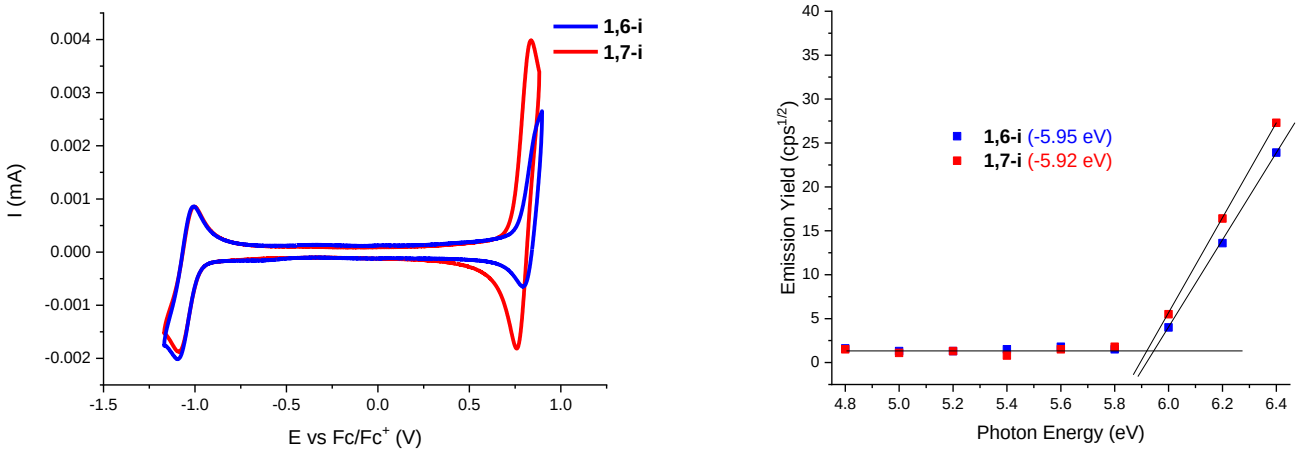

*Figure 29. Cyclic voltammograms of **1,7-i** (red) and **1,6-i** (blue) at a concentration of 0.5 mM in 0.10 M Bu_4NPF_6/CH_2Cl_2, 100 mV s^{-1}, Pt working electrode (left). Photoelectron Spectroscopy in Air (PESA) and measured work function of **1,6-i** and **1,7-i** on spun-cast thin films (right).*

Table 3. Electrochemical data recorded at a concentration of 0.5 mM in 0.10 M Bu_4NPF_6/CH_2Cl_2, 100 mV.s^{-1}, Pt working electrode, Reference: (Fc/Fc^+).

Compound	E_{pa} ($V_{Fc/Fc+}$)	E_{pc} ($V_{Fc/Fc+}$)	E_{HOMO}[eV]	E_{LUMO}[eV]	ΔE^{elec} [eV]
1,6-i	0.89	-1.05	-5.64	-3.75	1.89
1,7-i	0.83	-1.05	-5.60	-3.75	1.85

E_{HOMO} (eV) = - ($E_{ox(onset)}$ (V *vs* Fc/Fc^+) + 4.80)
E_{LUMO} (eV) = - ($E_{red(onset)}$ (V *vs* Fc/Fc^+) + 4.80)

The electrochemical gap determined by the difference of the onset of oxidation and reduction was estimated to 1.89 eV and 1.85 eV for **1,6-i** and **1,7-i** respectively. Besides, the energy levels were studied as well in solid-state (thin film spun-cast) by photoelectron spectroscopy in air (PESA, see Experimental Section, General procedures, for more details). The experiments showed lower ionization potential for **1,6-i** (-5.95 eV *vs* -5.92 for **1,7-i**, in agreement with the CV (Figure 29).

The better conjugation in the *1,7*-substituted derivative and the deeper HOMO level of the *1,6*-regioisomer experimentally observed were afterward investigated from a computational chemistry point of view. Optimized geometries, orbital density distributions and energies of the frontier molecular levels were thus simulated by density functional theory (DFT) method using B3LYP model with a 6-311G(d) basis set (Figure 30).

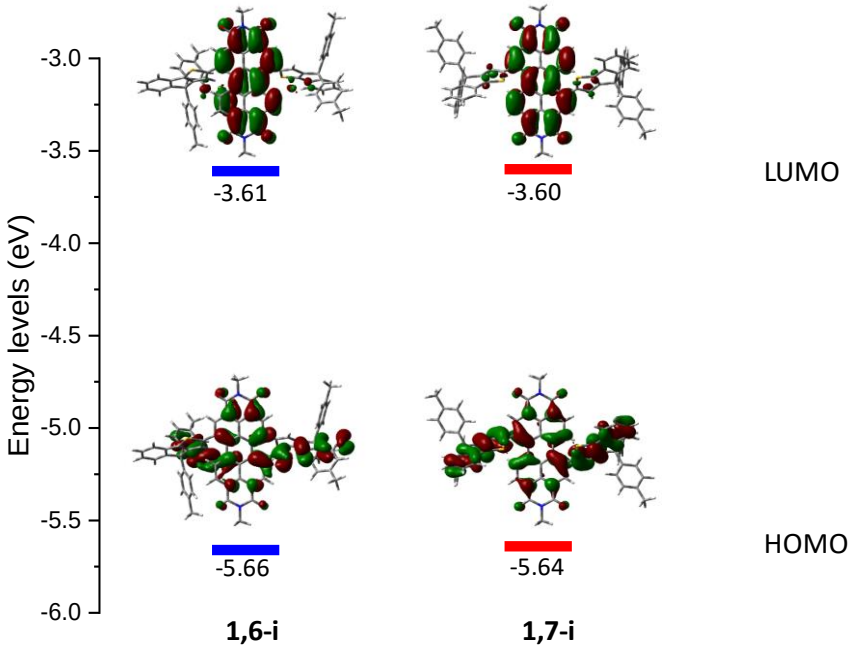

*Figure 30. HOMO and LUMO electron density and energy levels calculated by the DFT for **1,6-i** and **1,7-i**.*

While the electron density in the LUMO levels is centered on the PDI units, it turns out that in the case of the HOMO, it is partially delocalized along the different building blocks. Interestingly, and contrary to **1,6-i**, the HOMO distribution in **1,7-i** appears to be nearly symmetrical and well balanced between the two constituting naphthyl moieties of the PDI core. The charge transfer (CT) character of the lowest energy absorption bands, assigned to HOMO → LUMO transitions, was confirmed by time-dependent DFT (TD-DFT) calculations.[180] Theory also emphasized, through a population analysis, the higher contribution of the IDT arms to the HOMO of **1,7-i** (77% *vs* 71% for **1,6-i**). Hence, with almost similar LUMO levels, the stronger CT character of **1,7-i** contributes in increasing its HOMO level and therefore reducing its band gap.

1.4 Photovoltaic Characterization

Air-processed BHJ solar cells were fabricated to further investigate the impact of the grafting position of PDI derivatives and more specifically, the influence on their photovoltaic properties. Inverted devices of architecture (ITO/ZnO/**PTB7-Th** : **1,6-i** or **1,7-i**/MoO_x/Ag) were thus fabricated in the group of Gregory Welch (University of Calgary). For the sake of

comparison, each regioisomer was first blended with the same donor polymer, namely the **PTB7-Th**, in a 1:1 w/w ratio at 10 mg/mL total concentration in chlorobenzene (see Experimental Section). The resulting devices were tested and the typical current density-voltage (*J-V*) curves recorded under an AM 1.5 simulated solar illumination in air, are depicted in Figure 31 together with their respective EQE spectra.

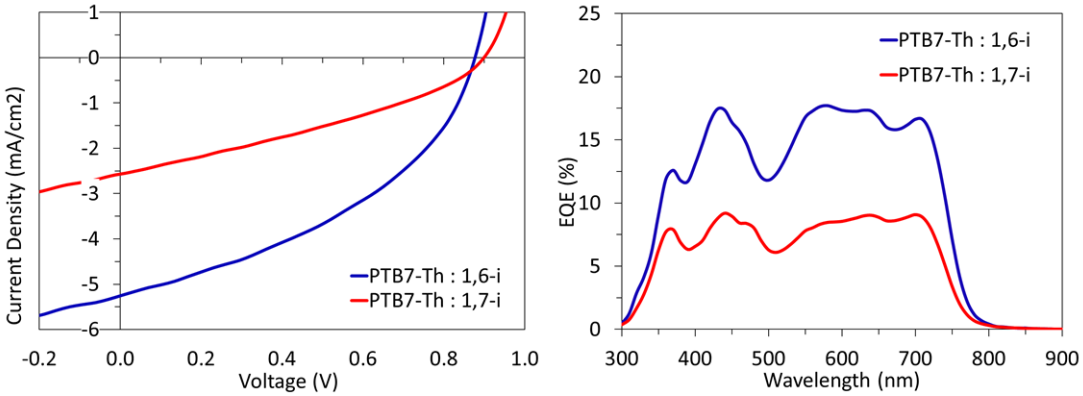

*Figure 31. J –V curves (left) and EQE spectra (right) of **1,7-i** (red) and **1,6-i** (blue) based OSCs.*

Devices prepared with **1,6-i** led to better power conversion efficiencies than those of **1,7-i**, mainly due to the higher short circuit current density (J_{sc}) and fill factor (*FF*) parameters (Table 4).

*Table 4. Organic solar cell device parameters for 1:1 PTB7-Th : **1,7-i** and PTB7-Th : **1,6-i** active layers, obtained from 10 mg/mL solutions in chlorobenzene. Average values in brackets (6 devices).*

Acceptor	V_{oc} (V)		J_{sc} (mA/cm^2)		*FF %*		PCE %	
1,6-i	0.87	(0.86)	5.3	(4.7)	41	(41)	1.9	(1.6)
1,7-i	0.89	(0.89)	2.6	(2.4)	34	(33)	0.8	(0.7)

While comparable open circuit voltage (V_{oc}) of 0.86 V for **1,6-i** and 0.89 V for **1,7-i** were measured, in agreement with their similar LUMO levels, **1,6-i** based devices exhibited a *FF* of 41% and a J_{sc} of 4.7 mA cm^{-2} *vs* 33% and 2.4 mA cm^{-2} for **1,7-i**, resulting in PCEs of 1.6% *vs* 0.7% respectively. This two-fold reduction of J_{sc} can also be observed in the external quantum efficiency spectra since the maximum photon-to-electron conversion of **1,7-i** based organic solar cell (OSC) barely exceeded 9% while a two-fold improvement (18%) was reached for **1,6-i** based devices. The nanoscale topography of the active layers was subsequently investigated

by atomic force microscopy (AFM). As shown in Figure 32, both **1,6-i** and **1,7-i** based blends appear similar in roughness, with comparable RMS values of 1.0 and 1.1 nm, respectively.

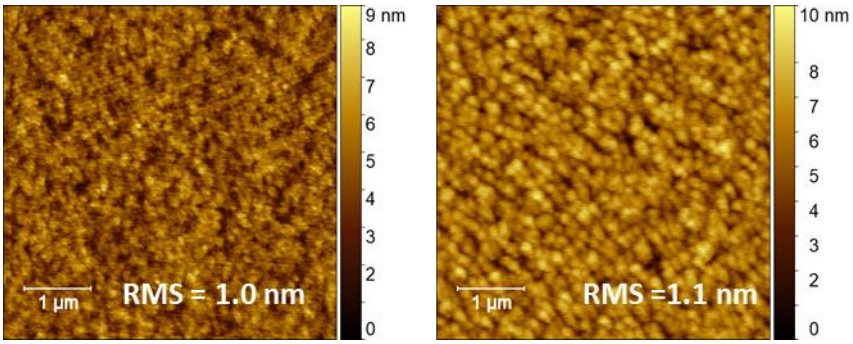

*Figure 32. AFM images of **1,6-i** (left) and **1,7-i** (right) based photoactive layers.*

The slightly more granular nature of the PTB7-Th : **1,7-i** films might contribute to the lower density of carriers generated (and collected) in the devices, although the effect of these small variations is difficult to corroborate. Consequently, the electron mobility (μ_e) of each regioisomer was evaluated in neat films through the use of the space charge limited current (SCLC) method (Figure 33).

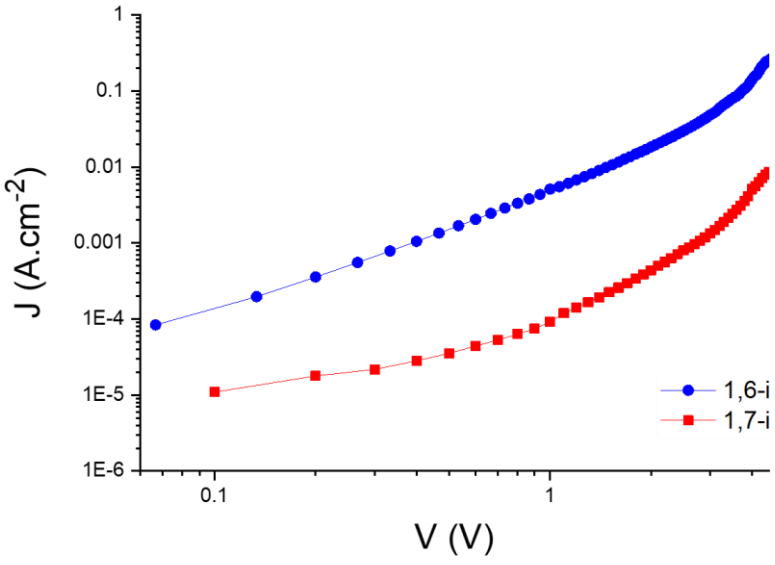

*Figure 33. Electron mobility μ_e of **1,6-i** (blue) and **1,7-i** (red) based devices.*

Electron-only devices (ITO/ZnO/**1,6-i** or **1,7-i**/Al) were thus fabricated revealing a difference of mobility between the two PDI derivatives of *ca* an order of magnitude. While a μ_e of *ca* 7.1 $\times 10^{-6}$ cm^2 V^{-1} s^{-1} was measured for **1,7-i**, the *1,6*-isomer was indeed characterized by an

electron mobility of *ca* 8.5 $\times 10^{-5}$ $cm^2 V^{-1} s^{-1}$, which in consistency with the difference of J_{sc} and *FF*. Consequently, adding an increasing quantity of the *1,7*-isomer to pure **1,6-i** based devices would normally have an impact on their photovoltaic performances, and conversely. Hence, devices made from mixtures of isomers with **1,6-i** : **1,7-i** ratios of 9:1, 7:3, 5:5, 3:7 and 1:9 were finally prepared, characterized and compared to their pure counterparts. As depicted in Figure 34, increasing the quantity of **1,7-i** results in a significant decrease of both the J_{SC} and *FF* (Table 5), thus demonstrating that the latter has, in this case, a detrimental effect on the overall performances.

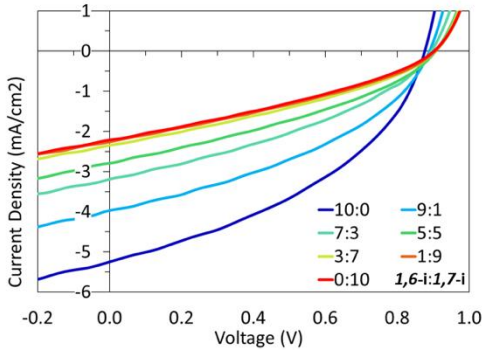

1,6-i : 1,7-i	V_{oc} (V)	J_{sc} (mA/cm²)	FF %	PCE %
10:0	0.86	4.7	41	1.6
9:1	0.89	4.1	39	1.4
7:3	0.89	3.2	37	1.0
5:5	0.89	2.7	35	0.8
3:7	0.90	2.4	33	0.7
1:9	0.89	2.3	33	0.7
0:10	0.89	2.4	33	0.7

*Figure 34 and Table 5. J –V curves of devices (left) and organic solar cell device parameters (right) prepared with different ratios of **1,6-i** and **1,7-i.***

1.5 Conclusions

Generated during the dibromination of the PDIs as a minor product and usually considered as an impurity, the *1,6*-dibromo PDI has not attracted much attention, particularly in the field of organic photovoltaics. In addition to the seminal paper reported by Ge *et al*.,[177] we have demonstrated that using the more conjugated *1,7*-isomer to prepare new non fullerene acceptors is not an absolute rule of efficiency.[180] In our case, the less conjugated *1,6*-derivative indeed led to a two-fold improvement of the power conversion efficiency in comparative devices, which could be slightly enhanced by optimizing the active layer preparation and deposition (PCE up to 1.9%). Moreover, adding an increasing quantity of the *1,7*-isomers to **1,6-i** based devices resulted in a significant decrease of their photovoltaic performances, confirming that the commonly used *1,7*-isomer can be herein considered as a contaminant.

Consequently, this study highlights the impact of both the grafting position of the PDI and the nature of the end-capping moieties on photovoltaic and charge transport properties

and will hopefully contribute in reconsidering conventional design principles and above all, the use of *1,6*-difunctionalized isomer in some organic electronics.

2 Indacenodithiophene based Non-Fullerene acceptors

2.1 Introduction

In recent years, indaceno[1,2-*b*:5,6-*b*']dithiophene (IDT) derivatives broke the ''what fullerene materials do best'', *i.e.*, the 10% PCE borderline and increased the record to more than 13% for solution processed OSCs in a short amount of time. These achievements have thus generated a craze within the community resulting in the development, optimization and evaluation of various IDT based NFAs.

Largely studied in organic electronics,[178] IDT was firstly introduced in OPVs as the electron-rich block in alternated D-A low band gap polymers,[181,182] showing effective conjugation and excellent charge mobility. The IDT moiety was then adopted as the core in A-D-A small-molecules,[183–185] thus functionalized with strong electron-withdrawing terminal groups (*i.e.* dicyanovinylindanone, DCI), generating a solid quadrupole moment in the molecule. Eventually, out-of-plane side chains were also introduced to avoid high crystallinity and improve the processability (Figure 35).

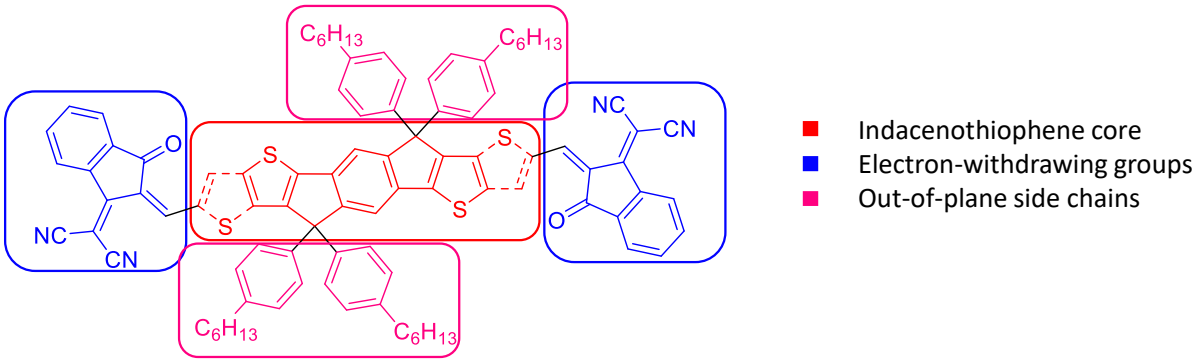

Figure 35. Chemical structure of ITIC, an example of IDT based NFA.

Among IDT derivatives, indacenodithieno[3,2-*b*]-thiophene (IDTT) based materials swiftly stood out. The latter structure is characterized by two thieno[3,2-*b*]-thiophene replacing the two outward thiophenes of the IDT donor block, notably improving the charge carrier properties and performance. First published by Zhan *et al.*,[125] the **ITIC**, an IDTT based NFA reached a PCE of 6.8% when blended with the **PTB7-Th**. Shortly afterwards, Hou and co-

workers[186] improved this result till 11.2% by preparing and combining **ITIC** with a home-made wide-band gap polymer, namely **PBDB-T**.

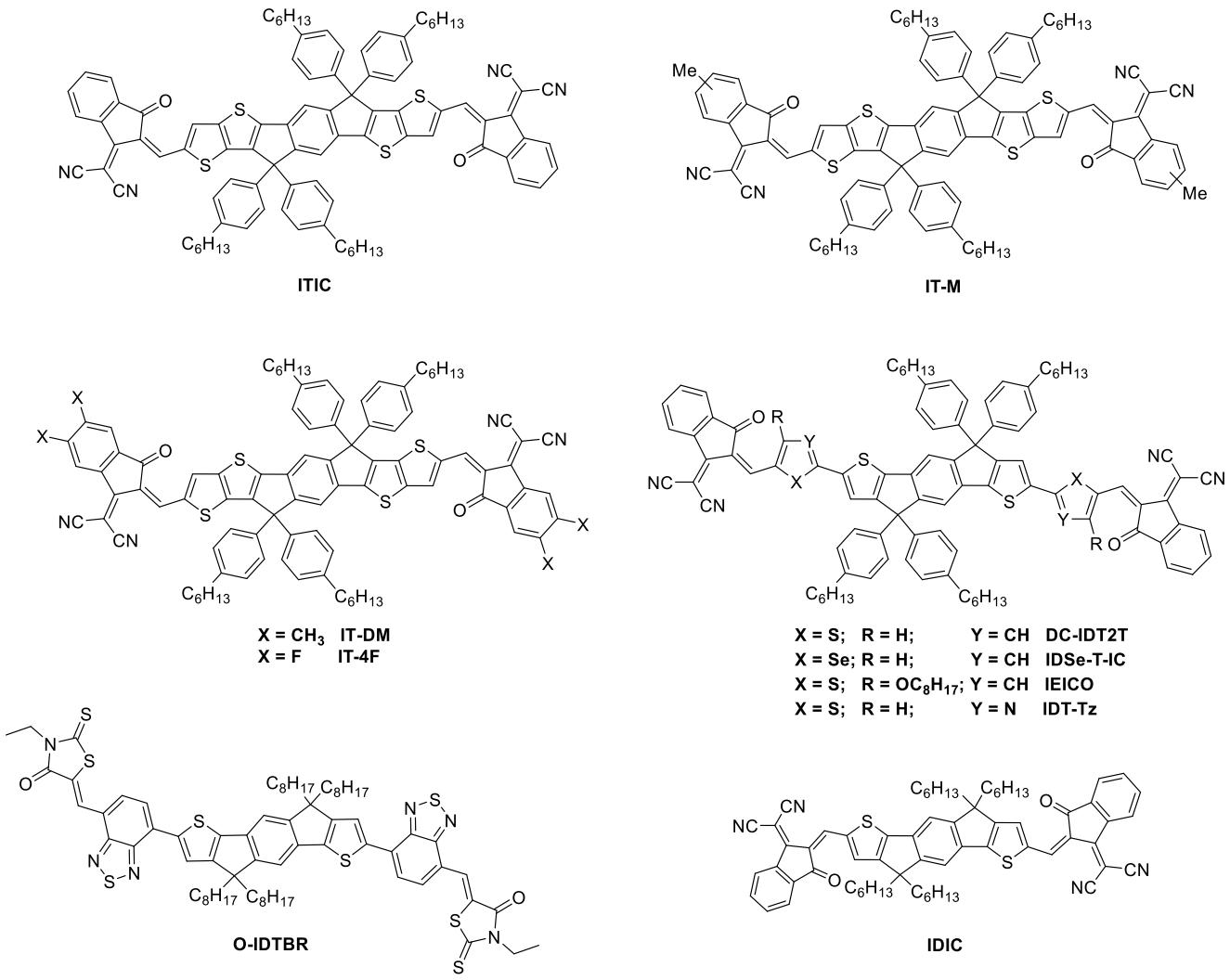

Figure 36. Examples of IDT and IDTT based NFAs.

Functionalization of the DCI phenyl ring was also found to significantly affect the power conversion efficiencies (Figure 36). To raise the LUMO energy level and therefore, improving the V_{OC} without any additional modification in the morphology (resulting in a PCE of 12.1%), methyl groups were introduced in the peripheral positions of the accepting moiety (**IT-M**).[187] Introduction of a second methyl groups per accepting unit (**IT-DM**), turns out to be still beneficial for the V_{OC}, while inducing a slight drop in $J_{SC,}$ thus impacting the PCE (11.3%). In a similar way, the electron-withdrawing end groups were modified with two fluorine atoms affording the **IT-4F**.[188] By improving both the intermolecular interactions, through F···H and F···S non-covalent bridges, and the absorption range (red shifted absorption), the resulting

IT-4F was able to reach a PCE of 13.1% once combined with a modified **PBDB-T-SF** donor polymer and even more recently 17.1% by doping the active layer.[189] Finally, it is noteworthy that these families of NFAs are particularly suitable for the preparation of ternary blend solar cells, leading to impressive PCE up to *ca* 17%.[190–193]

Although remarkable results have been obtained with the IDT derivatives, all of them have been carried out in solution-process polymer solar cells. With high molecular weight and not really discussed stabilities, no examples of *vacuum*-processing IDT based devices are currently reported in the literature. Indeed, our colleagues from Heliatek GmbH have observed that small indaceno based materials, such as **IDIC** or **O-IDTBR** (*vide supra*),[51,194] still degrade during thermal evaporation under *vacuum*, since residues higher than 60% were found in the sublimation chamber/crucibles.

Hence, investigation of IDT derivatives with good evaporability and their behaviour in OSCs were carried out in collaboration with Heliatek, the leader enterprise in *vacuum*-processed solar cells. To that end, our first strategy was to simplify IDT molecules to its half structure (Figure 37), reducing the molecular weight, enhancing evaporability and last but not less important, economizing the synthetic process and cost.

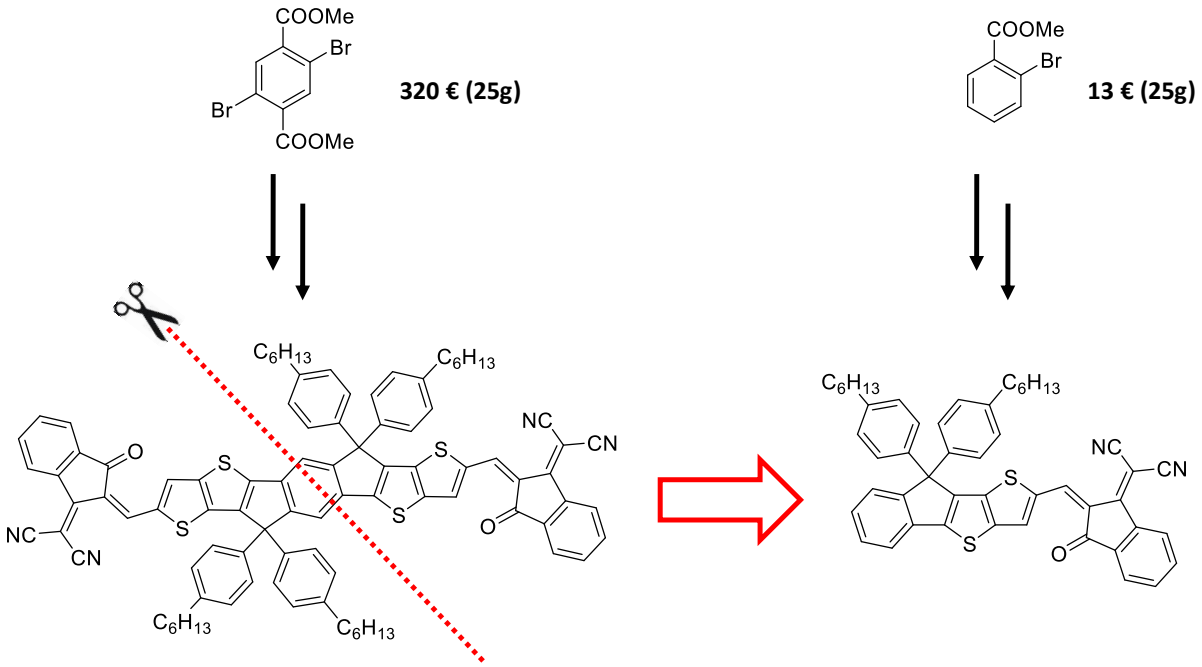

*Figure 37. h-IDT strategy over **ITIC**.*

2.2 Half IDT based NFAs

2.2.1 Synthesis

Common with the above discussed PDI based NFA **(head 1.2)**, compound **4** was first synthesized in gram-scale following the same procedure. In comparison with the reported analogues, the bulky side chains were here replaced by simple methyl groups to minimize the number of atoms and thus favouring the compatibility with the sublimation process (Scheme 4).

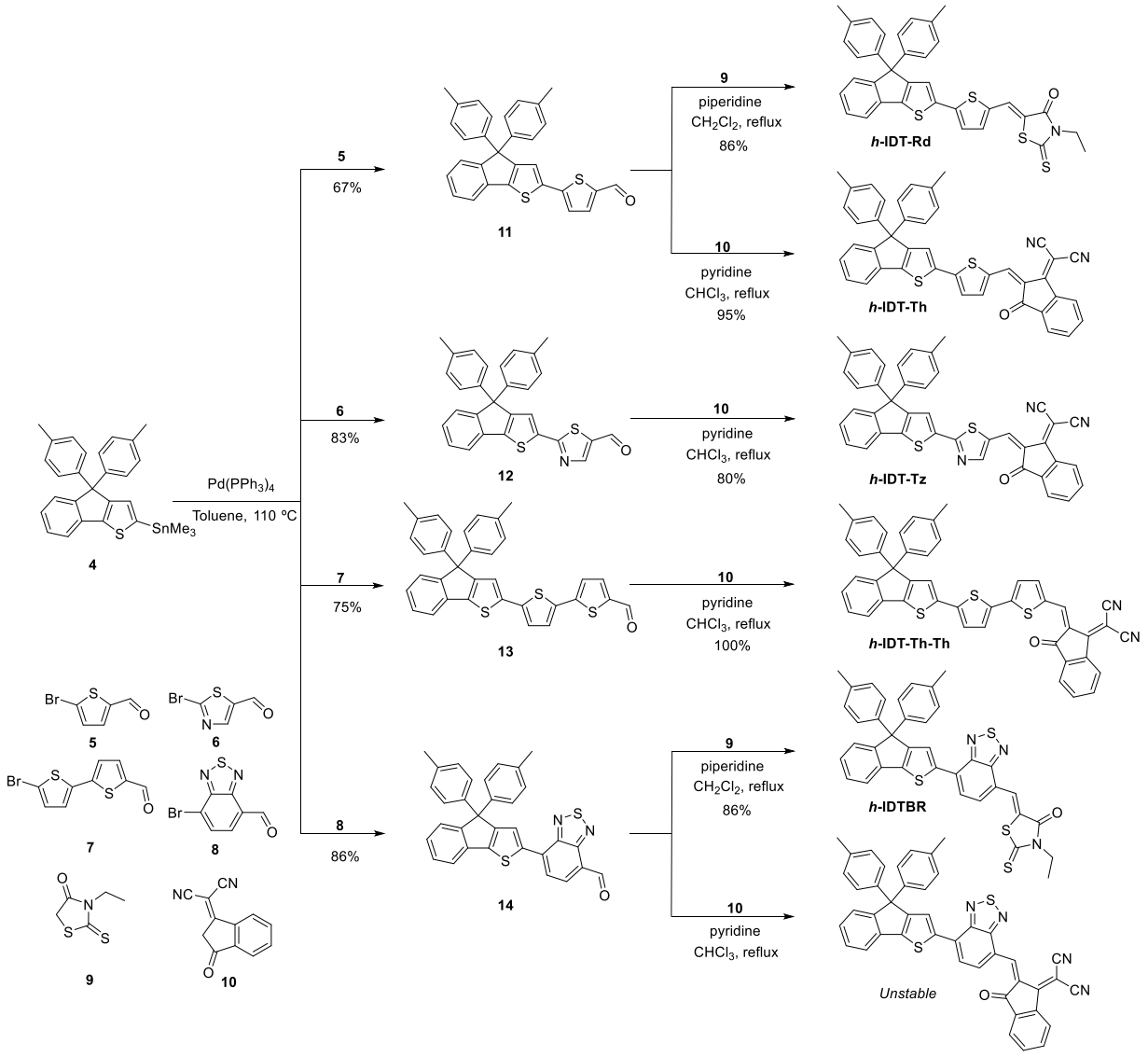

Scheme 4. Synthetic route to h-IDT derivatives.

With a large amount of the stannic **4** in hand, different π-spacers were subsequently introduced by Stille cross-coupling reaction, namely a thiophene, a thiazole, a 2,2'-bithiophene and benzothiadiazole units. Moreover, to limit the number of synthetic steps,

commercially available bromo-carbaldehydes derivatives were used. Hence, the final compounds, ***h*-IDT-Th**, ***h*-IDT-Tz**, ***h*-IDT-Th-Th**, were directly obtained in excellent yields by a Knoevenagel condensation with dicyanovinylindanone **10**. Unfortunately, product obtained from the reaction of **10** and **14**, was highly unstable. Therefore, similarly to their quadrupole counterpart **O-IDTBR**, ethyl-rhodanine (**9**) was condensed over **14** to afford ***h*-IDTBR**. In this context, ***h*-IDT-Rd** was synthesized to cover a wider wavelength range.

Even if the alkyl chains were reduced to methyl groups, all molecules show good solubility in common organic solvents, thus, they were easily characterized by ^{1}H, ^{13}C NMR and FTIR spectroscopy and mass spectrometry. In parallel of the latter family of materials, the corresponding *half*-molecule of **ITIC** was prepared keeping the side chains in the out-of-plane aromatic ring. The synthetic pathway was modified from the literature (**ITIC**), starting from the more efficient Stille (*vs* Negishi) coupling between methyl 2-bromobenzoate and thienothiophene formerly stannylated (Scheme 5).

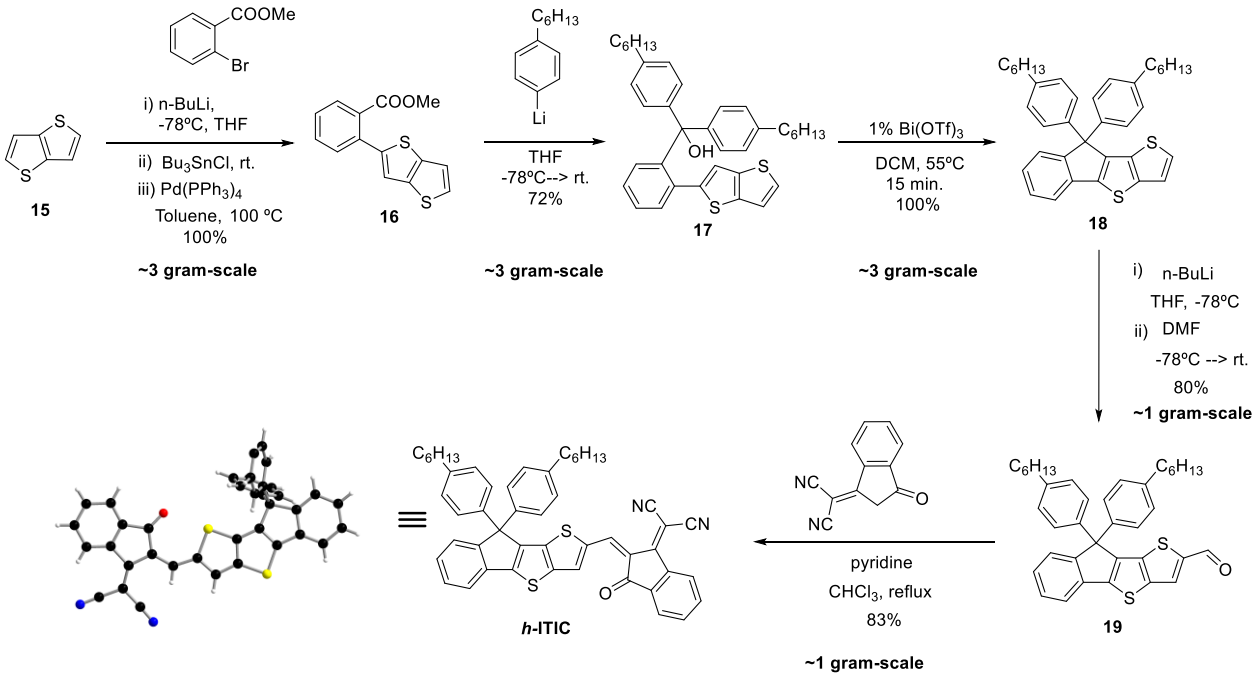

*Scheme 5. Synthetic route to **h-ITIC** and its molecular structure obtained from X-ray diffraction.*

Then, compound **16** was treated with (4-hexylphenyl)lithium to afford the benzyl alcohol **17**. To avoid the classic and tedious conditions for cyclization, which consists of refluxing the reagents in a mixture of acetic and sulfuric acids, the activation of the tertiary alcohol by a Lewis acid was carried out.[195] As a result, **18** was prepared in quantitative yield

after catalytic addition of $Bi(OTf)_3$ in mild conditions. Finally, successive formylation and Knoevenagel reactions provided the target ***h*-ITIC** in gram scale.

2.2.2 Optical and electrochemical analysis

Absorption and emission profiles of all molecules were first studied in diluted dichloromethane solutions. Similar spectral signatures were observed for the *h*-NFA materials, thus characterized by a broad intense band, which position is directly affected by the nature of the end-capped acceptor and the π-spacer (Figure 38 and Table 6).

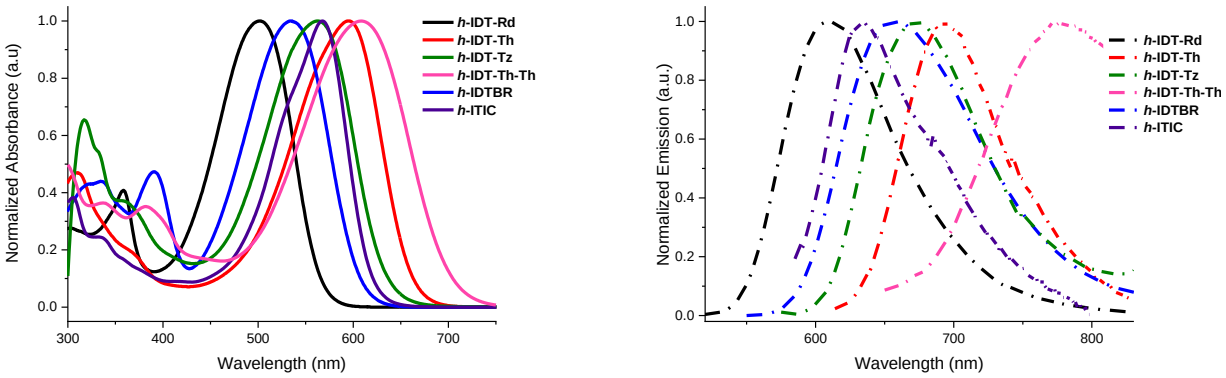

Figure 38. UV-Vis absorption (left) and emission (right) spectra of h-IDT based NFAs in CH_2Cl_2.

Table 6. Optical data of h-IDT based NFA recorded in dichloromethane (10^{-6} M) and on quartz sheets.

Compound	λ_{max}^{ABS} (nm) in DCM	ε (M^{-1} cm^{-1})	λ_{max}^{EM} (nm) in DCM	λ_{max}^{ABS} (nm) in film	$E_g^{(opt)}$ (eV)
***h*-IDT-Rd**	502	39000	610	503	2.22
	358	16000			
***h*-IDT-Th**	595	47000	694	596	1.91
	309	22000			
***h*-IDT-Tz**	563	34000	662	580	2.02
	317	22000			
***h*-IDT-Th-Th**	609	65000	779	624	1.80
	300	17000			
***h*-IDTBR**	535	33000	657	540	2.07
	390	16000			
***h*-ITIC**	568	52000	634	598	1.85
	305	20000			

Compared to the other compounds, the two rhodanine derivatives ***h*-IDT-Rd** and ***h*-IDTBR** present an absorption band with a maximum at higher energy while the absorption spectrum of ***h*-IDTBR** is bathochromically-shifted due to the acceptor character of the

benzothiadiazole (λ_{max} = 535 nm *vs* λ_{max} = 502 nm for ***h*-IDT-Rd**). Functionalization with DCI moieties (***h*-IDT-Tz**, ***h*-IDT-Th** and ***h*-IDT-Th-Th**) leads to absorption bands with maxima higher than 550 nm with a more red-shifted absorption reached for the more π-extended bithiophene derivative (***h*-IDT-Th-Th**). On the other hand, the main absorption band of ***h*-IDT-Tz** appears to be 32 nm hypsochromically shifted with respect to ***h*-IDT-Th** attributed to the less donor properties of the thiazole ring.[196] Finally, ***h*-ITIC** displays an absorption maximum (λ_{max} = 568 nm) close to that of ***h*-IDT-Tz** (λ_{max} = 563 nm) but with a smaller full width at half maximum (FWHM) and an improved molar extinction coefficient.

From an emission point of view, all compounds follow the same tendency as in absorption and exhibit a Stokes shift of c*a* 100 nm (2397 cm^{-1}). It is noteworthy that the band of ***h*-IDT-Th-Th** presents a higher Stokes shift of 170 nm (3583 cm^{-1}), as a direct consequence of the extended conjugation with a 2,2'-bithiophene prone to rotational disorder. In contrast, a lower Stokes value of 66 nm (1832 cm^{-1}) was observed for ***h*-ITIC** that can be attributed to the intrinsic rigidity of the backbone.

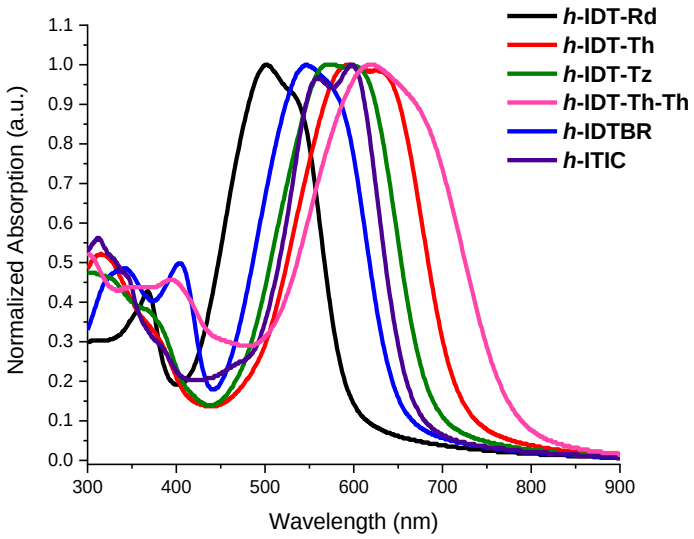

Figure 39. UV-Vis absorption spectra of h-IDT based NFAs evaporated on quartz films.

Evaporated films on quartz substrates were prepared to evaluate the behaviour in solid state (Figure 39). Compared to solution, the absorption band of the thin-films is highly widened by the appearance of a new red-shifted shoulder or a new band in the case of *h*-ITIC, which can be ascribed to the presence of a J-type aggregation. The optical band gap of the

compounds has been estimated from the absorption band edge at low energy giving values between 2.22 and 1.80 eV (Table 6).

Thereafter, electrochemical properties of the series were investigated by cyclic voltammetry. All the compounds show comparable voltammograms with one reversible oxidation peak and one irreversible process in the negative region, with exception of the benzothiadiazol π-spacer derivative ***h*-IDTBR** that is characterized by two reversible oxidation waves (Figure 40).

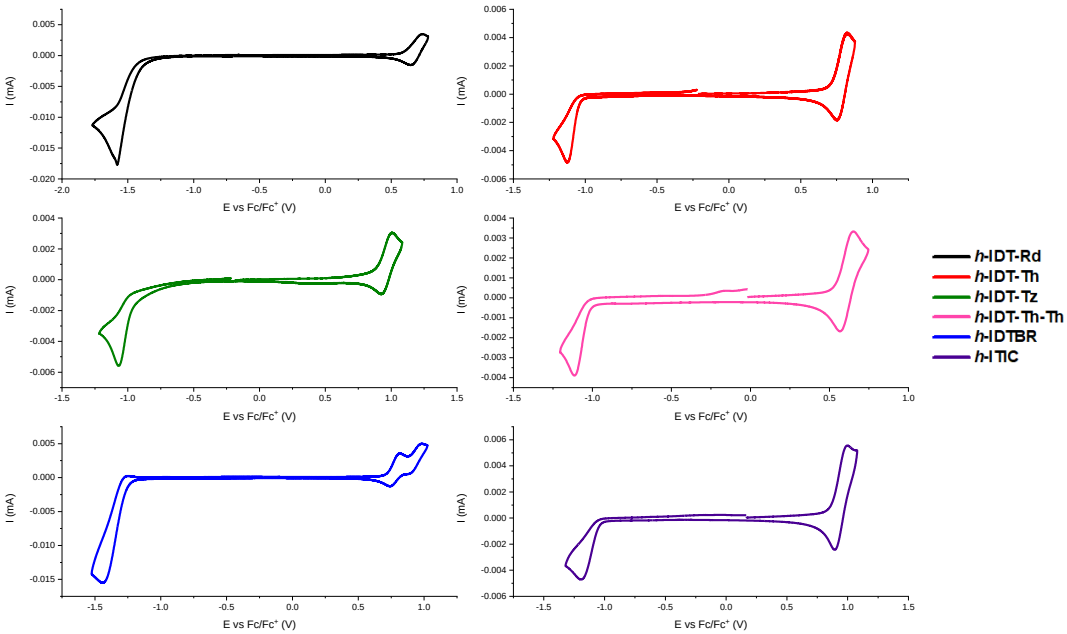

Figure 40. Cyclic voltammograms of h-IDT based NFAs at a concentration of 0.5 mM in 0.10 M Bu_4NPF_6/CH_2Cl_2, 100 mV s^{-1}, Pt working electrode.

Table 7. Electrochemical data recorded at a concentration of 0.5 mM in 0.10 M Bu_4NPF_6/CH_2Cl_2, 100 mV.s^{-1}, Pt working electrode. Reference: Fc/Fc^+.

Compound	E_{pa} ($V_{Fc/Fc+}$)	E_{pc} ($V_{Fc/Fc+}$)	E_{HOMO} (eV)	E_{LUMO} (eV)	ΔE^{elec} (eV)
***h*-IDT-Rd**	0.74	-1.57	-5.49	-3.40	2.09
***h*-IDT-Th**	0.83	-1.13	-5.58	-3.76	1.82
***h*-IDT-Tz**	1.01	-1.07	-5.77	-3.88	1.87
***h*-IDT-Th-Th**	0.65	-1.11	-5.41	-3.79	1.62
***h*-IDTBR**	0.81	-1.44	-5.58	-3.58	2.00
***h*-ITIC**	0.99	-1.20	-5.70	-3.81	1.89

E_{HOMO} (eV) = - ($E_{ox(onset)}$ (V *vs* Fc/Fc^+) + 4.80)

E_{LUMO} (eV) = - ($E_{red(onset)}$ (V *vs* Fc/Fc^+) + 4.80)

The values of the oxidation and reduction potentials are gathered in Table 7, as well as the estimated energy levels of the corresponding frontier orbitals. Hence, with almost similar HOMOs, higher LUMO levels were estimated for ***h*-IDT-Rd** and ***h*-IDTBR** (-3.40 eV and -3.58 eV, respectively), in constancy with their weaker accepting terminal group. On the contrary, DCI was found to stabilize the LUMOs resulting in values bellow -3.75 eV for the other four molecules, namely ***h*-IDT-Th**, ***h*-IDT-Tz**, ***h*-IDT-Th-Th** and ***h*-ITIC**. Intriguingly, ***h*-IDT-Tz** and ***h*-ITIC** exhibited an extra reduction/stabilization of both HOMO and LUMO levels, in comparison to their analogue ***h*-IDT-Th**, attributed to the rigidification of the backbone structure, thus enhancing the conjugation and therefore improving the acceptor character of the NFA. Hence, results are in agreement with the tendency observed for the optical band gap.

To gain further insight into the electronic properties, DFT optimization at the range-separated hybrid (RSH) functional level of theory ωB97X-D was performed over the six molecules (Figure 41).

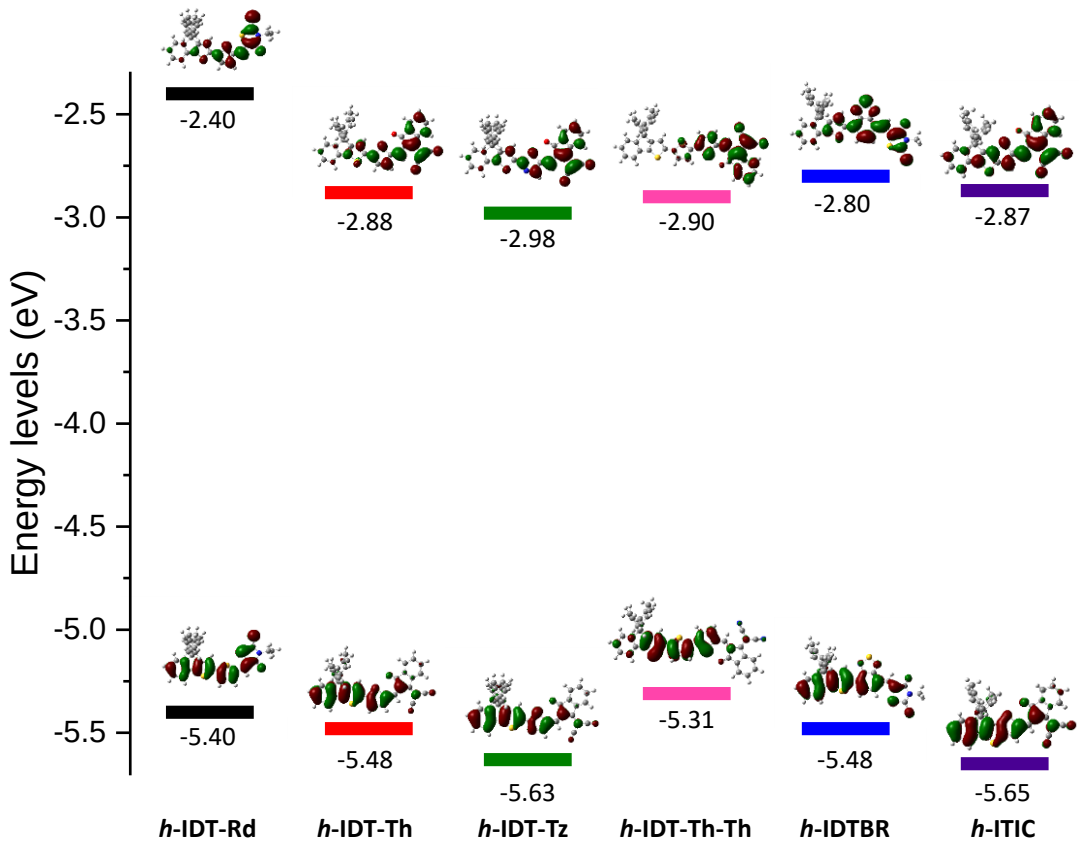

Figure 41. HOMO and LUMO electron density and energy levels calculated by the DFT for h-IDT based NFA.

As expected, HOMO levels are located along the indacenothiophene moiety and the π-spacer, while the LUMOs are delocalized on both the acceptor blocks and the π-spacer. This phenomenon confirms the CT character of the HOMO -> LUMO transition, characteristic of D-π-A molecules. Besides, the same trend followed by CV can be extracted from the theoretical values: i) ***h*-IDT-Tz** and ***h*-ITIC** stabilize the energy levels and show deeper HOMO levels than the rest of the series, ii) a *ca* 0.10 eV lower LUMO was generated for ***h*-IDT-Tz** with respect to ***h*-ITIC** and ***h*-IDT-Th**, iii) addition of an extra thiophene induces higher delocalization of the frontier molecular orbitals in ***h*-IDT-Th-Th**, leading to an enhancement of the CT character and therefore reduction of the HOMO-LUMO gap (*ca* 0.20 eV *vs* ***h*-IDT-Th**) and iv) due to its weaker accepting character, rhodanine containing NFAs (***h*-IDT-Rd** and ***h*-IDTBR**) are characterized by both higher LUMO levels and HOMO-LUMO gap.

2.2.3 *Vacuum*-processing and photovoltaic characterization

In collaboration with Heliatek GmbH, all compounds were evaluated as NFA in PHJ *vacuum*-processed solar cells. However, before going to that end, the materials were subjected to a conventional protocol to assess the viability of large-scale manufacture. Hence, the sublimation temperature (T_{sub}) and stability during the evaporation were studied. While high T_{sub} favors the degradation of organic materials, low T_{sub} hinders the co-evaporation in the fabrication process. On the other hand, high degradation observed after sublimation results in a non-negligible amount of material needed for the deposition and thus preventing the application of such material in the non-academic field.

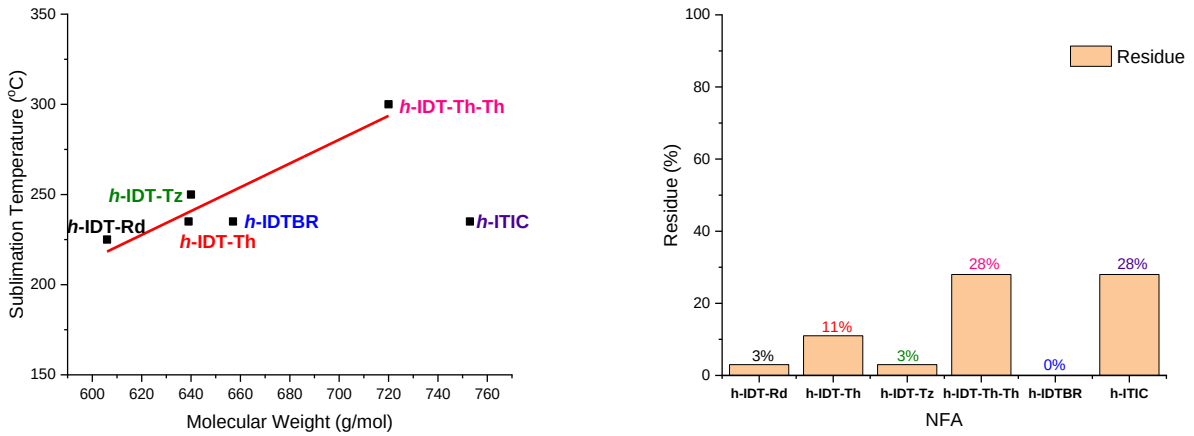

Figure 42. T_{sub}/M_w (left) and stability (right) representation for the h-IDT based NFAs.

As depicted in Figure 42, the *h*-IDT based NFAs display optimal T_{sub} in the range of 200-250 °C, excluding ***h*-IDT-Th-Th**, which ideal T_{sub} appears in the border of 300 °C, thus increasing the risk of degradation. Comparing the values obtained for ***h*-IDT-Th-Th** and ***h*-ITIC** (300 °C *vs* 235 °C), reveal that T_{sub} seems independent of the molecular weight (M_w), since ***h*-ITIC** is the heaviest of the family. Nevertheless, it is likely to find a relation between T_{sub}/M_w for molecules with the same core and aromatic substitution (methyl) that can facilitate the design of new analogues without high T_{sub} and risk of decomposition. Stability studies show that neither rhodanine nor dicyanovinylindanone moieties present a huge problem upon *vacuum* evaporation, due to the low residue observed for ***h*-IDT-Rd**, ***h*-IDT-Th**, ***h*-IDT-Tz** and ***h*-IDTBR** (3%, 11%, 3% and 0% respectively). Conversely, 28% of residue was obtained for ***h*-IDT-Th-Th** and ***h*-ITIC** meaning that: i) temperatures close to 300 °C start to be detrimental for this family

of materials and ii) long alkyl chain substitution in the out-of-plane phenyl rings increase the instability during the *vacuum*-process.

At this point, *vacuum*-processed PHJ solar cells were fabricated with the inverted architecture ITO/***h*-NFA/BF-DPB**/NHT169:NDP9/NDP9/Al, being NHT169 a HTL and NPD9 a commercial *p*-dopant. Using the HTL **BF-DPB** as donor, high efficient structure are clearly not expected, since this colourless material does not participate to the absorption process, however it is used to assess the carrier generation originating from the absorption by the NFA, thus, the energy level adequacy and charge transport of the NFA can be evaluated. Photovoltaic parameters are gathered in Table 8 and best *J-V* characteristics are plotted in Figure 43.

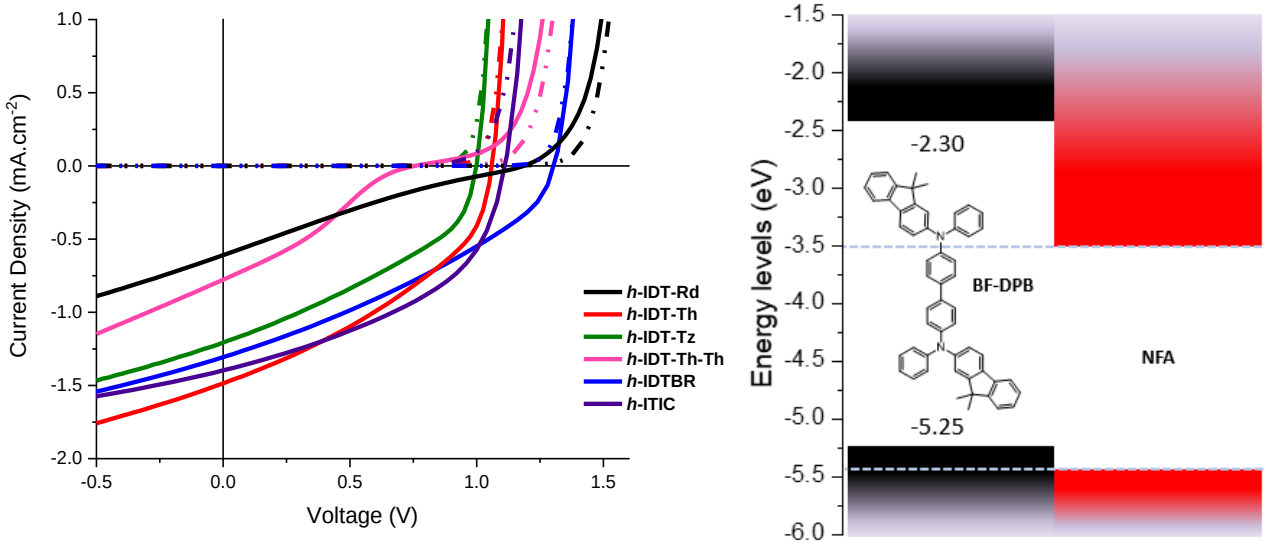

*Figure 43. J –V curves of h-IDT-NFA based OSCs under illumination (solid line) and dark (dashed line). Chemical structure of **BF-DPB** and energy level landscape.*

Table 8. Organic solar cell device parameters for ITO/NFA (10nm)/Donor (10nm)/NHT169:NDP9 (45nm)/NDP9 (1nm)/Al (100nm).

Acceptor	V_{oc} (V)	J_{sc} (mA/cm²)	*FF* %	PCE %
C_{60}	0.95	1.4	75	1.0
DCV3T	1.05	3.5	63	2.3
***h*-IDT-Rd**	1.12	0.5	21	0.1
***h*-IDT-Th**	1.08	1.1	38	0.5
***h*-IDT-Tz**	1.02	1.1	38	0.5
***h*-IDT-Th-Th**	0.62	0.6	26	0.2
***h*-IDTBR**	1.39	1.3	32	0.6

***h*-ITIC**	1.12	1.4	45	0.7

It turned out that poor performance were achieved with ***h*-IDT-Rd** (0.1% of PCE) and ***h*-IDT-Th-Th** (0.2% of PCE) based OSCs. In the case of ***h*-IDT-Rd** these low performance can be related to its high LUMO level, which seems to be detrimental for optimal driving forces while for ***h*-IDT-Th-Th**, its too strong donor character leads to the lowest V_{oc} value (0.62 V) measured for all the series. Nonetheless, the *J-V* curves of ***h*-IDT-Th**, ***h*-IDT-Tz**, ***h*-IDTBR** and ***h*-ITIC** present relative decent shapes denoting charge separation between **BF-DPB** and the new NFAs and thereby highlighting their photovoltaic potential. Albeit similar values to C_{60} were obtained, J_{sc} and *FF* are far from the Heliatek reference NFA, namely **DCV3T** (see Chapter 1), suggesting recombination and charge transport issues.

To summarize, although compatible with the *vacuum*-process, the synthesized acceptors suffer from low performances, maybe due to their low dimensionality and D-A type structures, which impede network formation and clear charge mobility and transport. Indeed, the group of Andrienko has demonstrated through recent theoretical insights, that quadrupole moments of active materials and their implication in the molecular conjugation, directly affects the interfacial dissociation and charge transport.[197] Thereby, large quadrupole moments improve the electrostatic driving forces, favouring the exciton splitting and therefore enhancing the PCE of the solar cells.

As an attempt to reach higher efficiencies, a new family of IDT derivatives based on a more conventional A-D-A structure was targeted, thus characterized with quadrupole moments but still with low molecular weights. Conscious that long alkyl chains increase the possibility of degradation, the preparation of **IDIC** analogues was carried out by reducing the out-of-plane chain length (Figure 44).

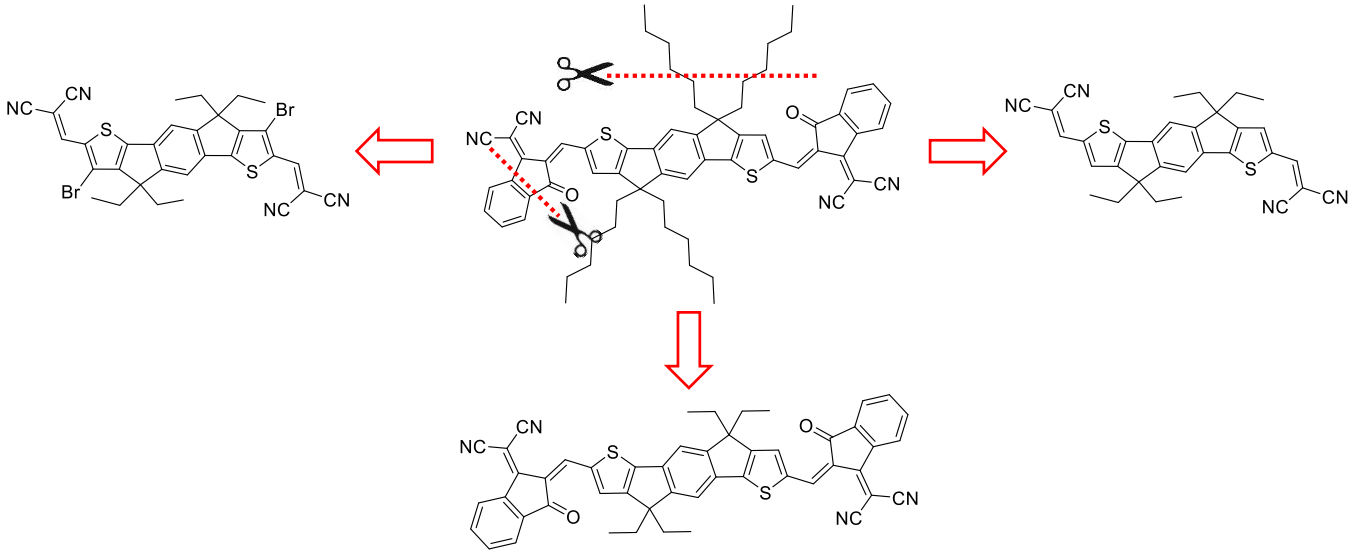

*Figure 44. Miniaturization strategy of **IDIC**.*

Furthermore, the dicyanovinyl moiety was implemented instead of DCI, to minimize the π-π interaction and to buffer the sublimation process.

2.3 IDIC based NFAs

2.3.1 Synthesis

Preparation of the IDT derivative **24** was achieved from a modified reported procedure (Scheme 6).[198,199]

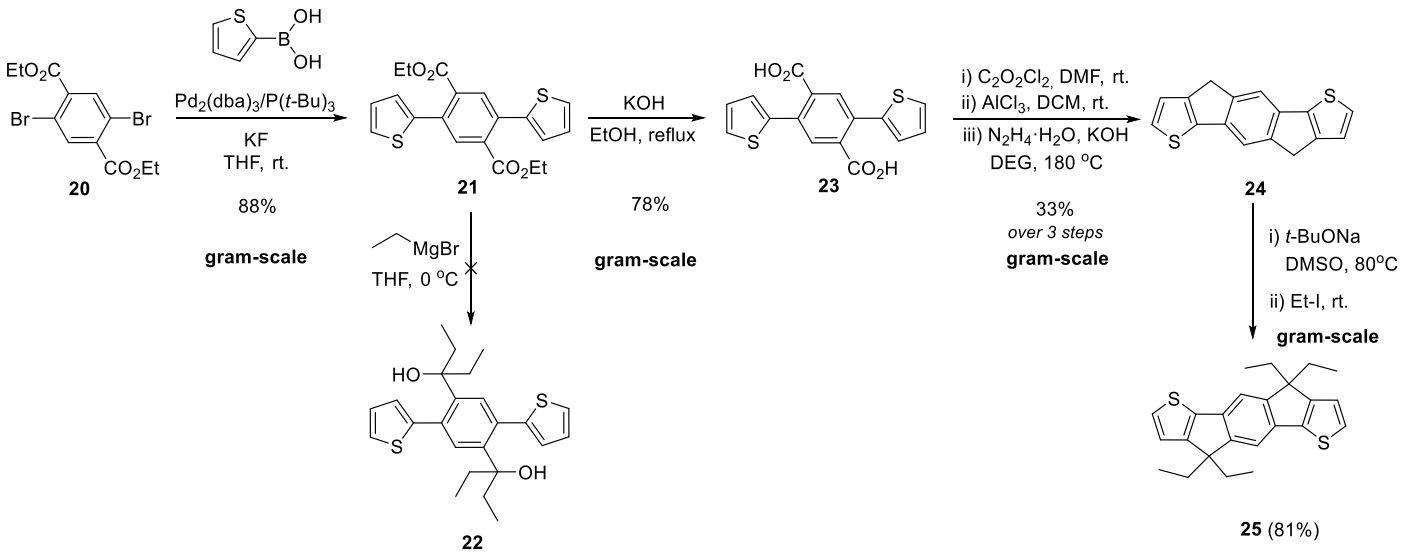

*Scheme 6. Synthetic route to intermediate **20**.*

The synthesis started with the double Suzuki reaction between the commercially available 2-thiophene boronic acid and the dibromo ester **20**, as a greener alternative to the conventional reported Stille or Negishi couplings. After optimization, mild Suzuki conditions using tri-*tert*butylphosphine as ligand,[200] afforded compound **21** in 88% yield in gram-scale. Though several attempts to synthesize tertiary alcohol **22** were engaged, the molecule was not isolated, probably due to the prompted unimolecular elimination (E1) of the resulted tertiary alcohol. Compound **21** was thus transformed in its corresponding terephthalic acid (**23**) under basic saponification, before being treated with oxalyl chloride and subsequently engaged in a Friedel Crafts electrophilic aromatic substitution to afford an insoluble diketo intermediate, which was in turn reduced into **24**, in a modest 33% yield over 3 steps, through a Huang-Minlon modification of the Wolff-Kishner reaction. Eventually, taking advantage of the acidity of the proton of the dihydroindacenodithiophene (**24**), the latter was simply deprotonated in presence of *t*-BuONa and alkylated with ethyl iodide affording **25** in good yields (81%).

Starting from the intermediate **25**, final compounds were easily prepared in two steps, consisting of a formylation followed by a Knoevenagel condensation. In this manner, two different NFAs containing DCI and DCV as terminal accepting groups were synthesized, namely **Et-IDIC** and **Et-IDIV**. Afterwards, and to modify the energy levels keeping the structural and morphology properties, the introduction of two bromine atoms at the thiophene β-positions was investigated.

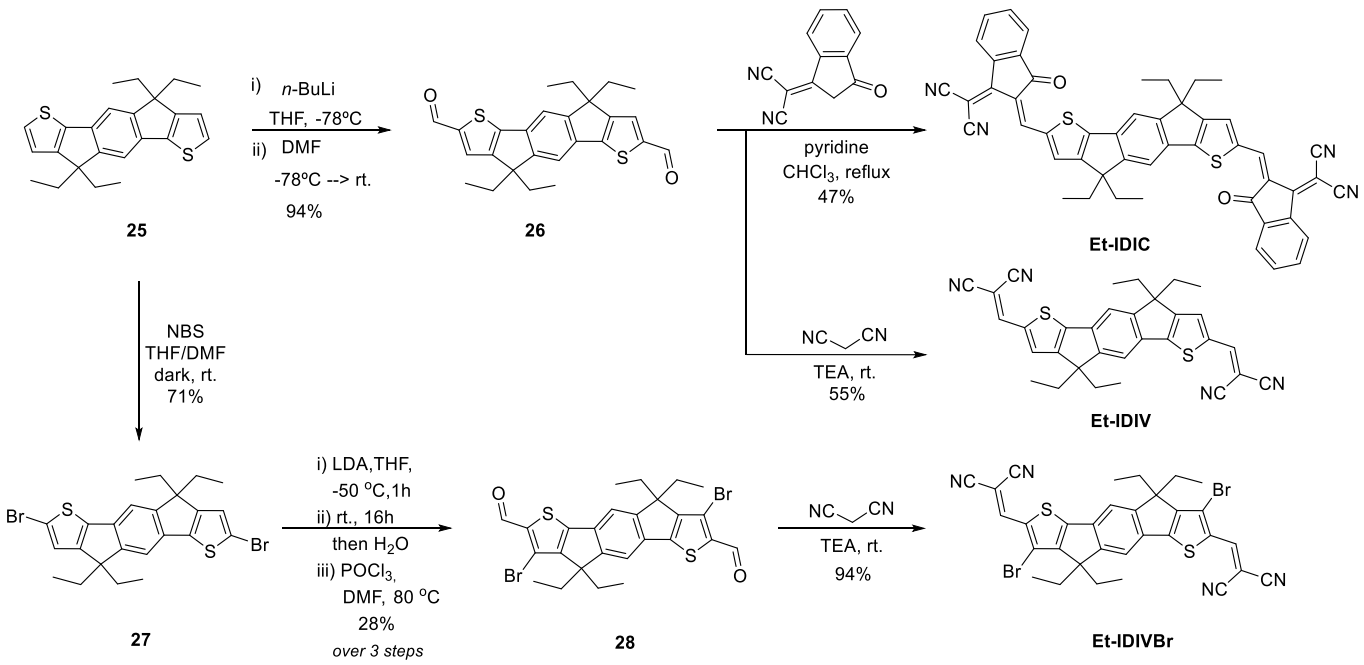

Scheme 7. Synthetic route to IDIC based NFAs.

To that end, bromination of **25** was carried out with *N*-bromosuccinimide (NBS) to afford **27** in good 71% yield. Thereafter, the halogen-dance was achieved after the addition of LDA, followed by Vilsmeier-Haack formylation to afford **28** in a modest 28% yield, over 3 steps. Similarly to **Et-IDIV**, **Et-IDIVBr** was prepared in excellent yields by Knoevenagel reaction with malononitrile (Scheme 7).

As expected, upon reducing the alkyl chains, the compounds suffer from an important diminution of solubility, particularly the DCI containing molecule (**Et-IDIC**) where the benzene rings of the DCI scaffold probably induce an enhancement of the π–π stacking. Hence, the sets of ^{1}H NMR signals of **Et-IDIV** and **Et-IDIVBr** were compared to check the efficiency of conjugation along the molecule (Figure 45). Though the aromatic protons located in the IDT phenyl ring show similar shifts (7.54 ppm **Et-IDIVBr** *vs* 7.51 ppm **Et-IDIV**), the vinylic proton of **Et-IDIVBr** moved to 8.06 ppm, resulting from a *ca* 0.25 ppm deshielding compared to the analogous proton in **Et-IDIV**, which can be translated (or interpreted as) by a higher delocalization.

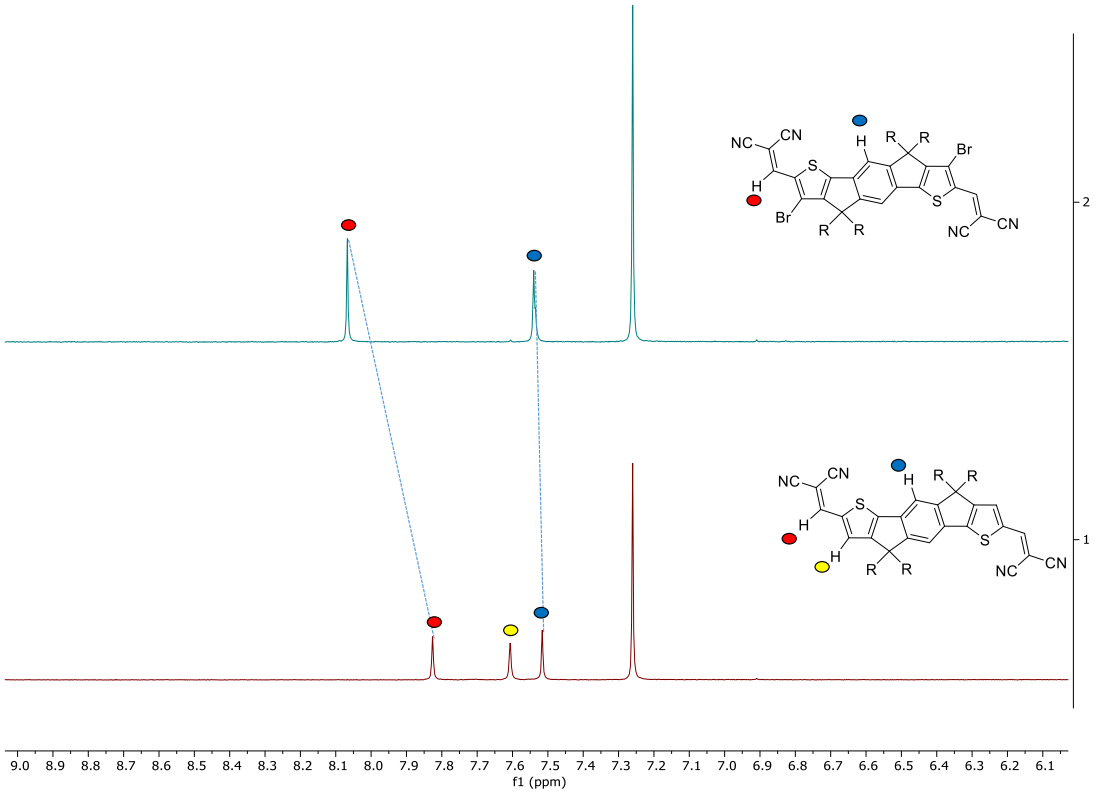

Figure 45. *^{1}H NMR spectra of **Et-IDIVBr** (blue) and **Et-IDIV** (red) in $CDCl_3$ at 25 °C.*

2.3.2 Electronic properties

The UV-vis spectra of the three compounds in dichloromethane exhibit one structured band with high extinction coefficients attributed to an HOMO -> LUMO (Figure 46.a).

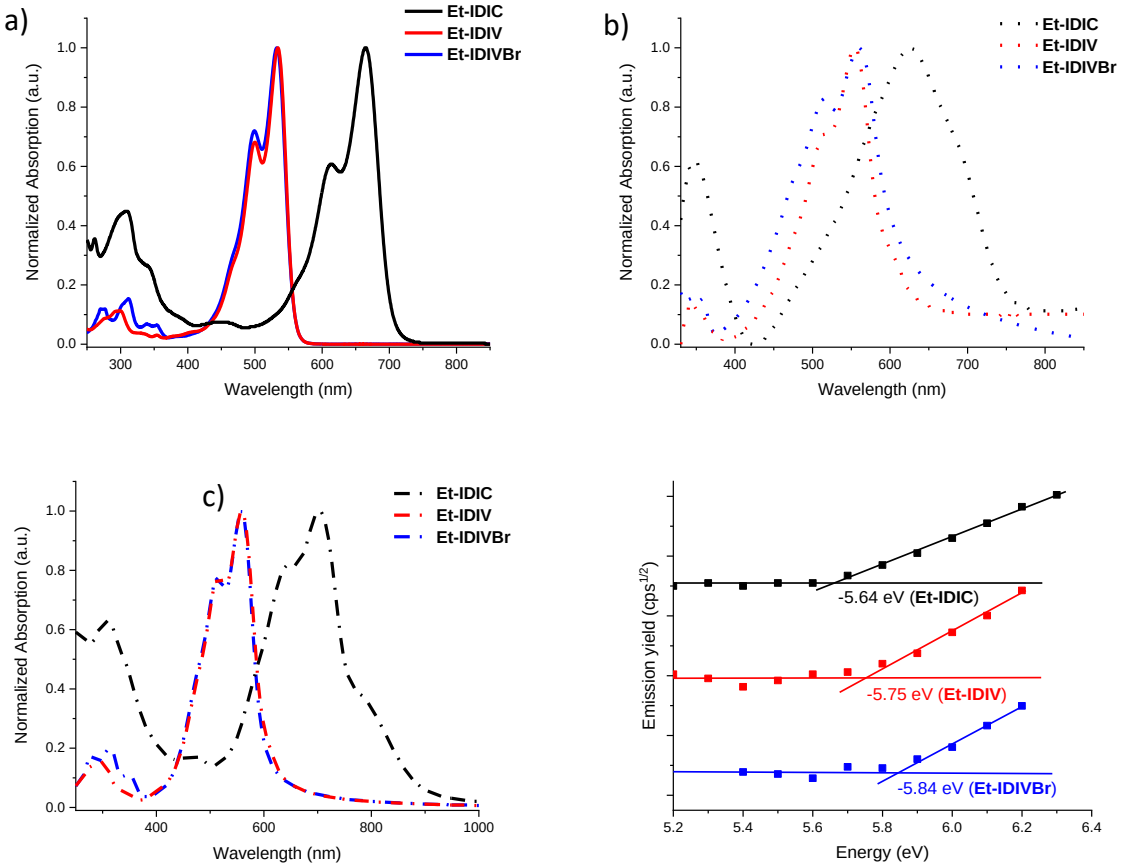

*Figure 46. UV-Vis absorption spectra of **Et-IDIC**, **Et-IDIV** and **Et-IDIVBr**: a) in DCM, b) as thin-film spun-cast on glass, c) as thin-film evaporated on quartz and d) Photoelectron Spectroscopy in Air (PESA).*

Comparison of the normalized spectra revealed nearly identical spectra for **Et-IDIV** and the brominated analogue (**Et-IDIVBr**), with the maximum of the main band at 534 nm. Interestingly, the addition of bromine atoms improved notably the absorption extinction coefficient of the material, presumably due to an increase of the quadrupole momentum. Moreover, the CT-band of **Et-IDIC** is subjected to a significant bathochromic shift (λ_{max} = 665 nm) with respect to the DCV end-capped compounds, absorbing in the 550-750 nm region *vs* 450-600 nm for **Et-IDIV** and **Et-IDIVBr**. The red-shifted spectra could be attributed to the stronger accepting character of the DCI group.

As usually observed for π-conjugated systems, the spectra in thin films present a broadening of the absorption band, both in spun-cast and evaporated films (Figure 46.b and c). **Et-IDIV** and **Et-IDIVBr** reveal also a red shift of the absorption maxima (*ca* 20 nm) suggesting intermolecular interactions in the solid state due to the packing in the film. Surprisingly, **Et-IDIC** exhibits a hypsochromic shift (*ca* 40 nm) when spun-cast on glass, probably due to the poor solution-processability resulting from the low solubility of the material. In stark contrast,

evaporated film shows a red shift of *ca* 40 nm ascribable to a J-type organization, with a red-shifted shoulder characterized by an extended absorption in the NIR region (*ca* 900 nm). Optical data are gathered in Table 9.

*Table 9. Electronic properties of **Et-IDIC**, **Et-IDIV** and **Et-IDIVBr** recorded in dichloromethane (10^{-5} M) and as thin-films.*

Compound	λ_{maxSOL}(nm)	ε(M^{-1} cm^{-1})	$\lambda_{maxSPIN}$(nm)	$\lambda_{maxEVAP}$(nm)	E_{HOMO}[eV][a]	E_{LUMO}[eV][b]	E_g^{opt}(eV)
Et-IDIC	665	66500	625	705	-5.64	-4.00	1.64
Et-IDIV	534	48000	555	558	-5.75	-3.70	2.05
Et-IDIVBr	534	90000	560	558	-5.85	-3.85	2.00

E_{HOMO} obtained from PESA ionization potential.

$E_{LUMO} = E_{HOMO} + E_g^{opt}$

Due to the modest solubility of the compounds in common solvents, their analysis by cyclic voltammetry was hindered, and consequently, energy levels were evaluated on thin films by PESA (Figure 46.d and Table 9).

Hence, with an optical band gap of 1.64 eV, **Et-IDIC** has the lower ionization potential giving rise to a HOMO level at -5.64 eV and the deepest LUMO level at -4.00 eV, as expected owing to the strong DCI electron-withdrawing groups. By comparing the two IDIV derivatives, it is possible to observe that the addition of bromine atoms in the IDT core stabilize the HOMO level from -5.75 eV, for **Et-IDIV**, to -5.85 eV (**Et-IDIVBr**). These measurements confirm that the addition of bromine atoms can easily tune the energetics without affecting the optical and morphological properties of the material.

In parallel, the impact of the molecular engineering on the frontier energy levels was also investigated by DFT calculations. Ethyl chains were substituted by methyl groups to reduce computational time (Figure 47).

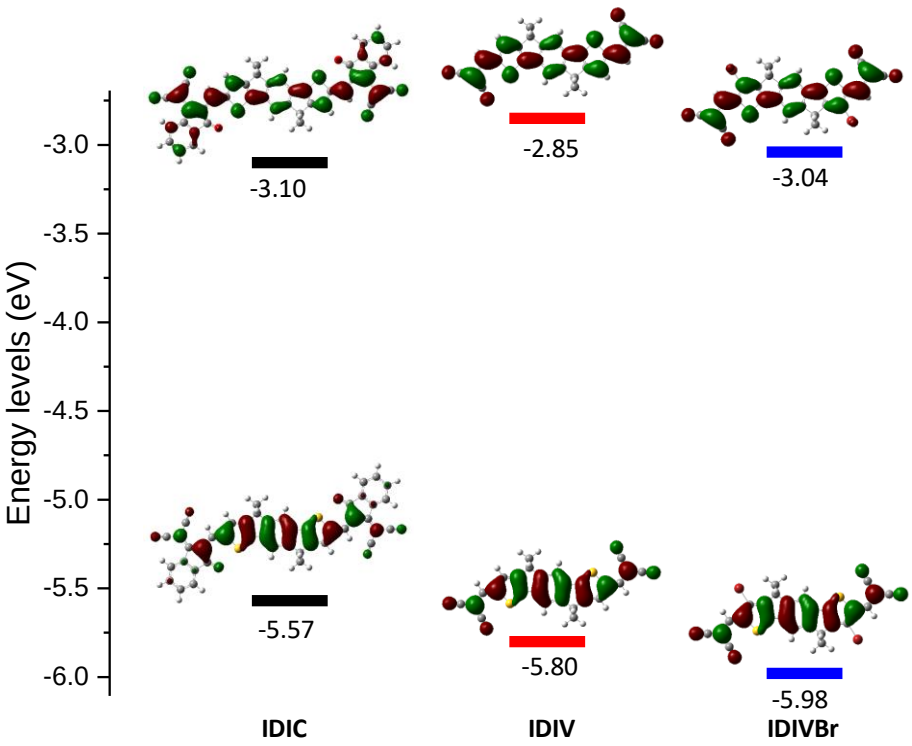

Figure 47. HOMO and LUMO electron density and energy levels calculated by the DFT for IDIC-based NFAs.

As depicted above, frontier MO levels are distributed all over the backbone with a major density found on the electron-rich blocks (IDT core) for the HOMO and on the acceptor moieties for the LUMOs. **IDIC** showed the lowest band gap in agreement with the experimental trend. Moreover, comparison of IDIV and IDIVBr revealed that while similar HOMO-LUMO gaps were measured, frontier orbitals of the latter brominated NFA (**IDIVBr**) are significantly stabilized by *ca* 0.2 eV, confirming the stronger acceptor character of the latter, simply induced by the bromination of the backbone.

2.3.3 *Vacuum*-processing and photovoltaic characterization

Engaged in sublimation test, the T_{sub} of the NFAs increases with the M_w as shown in Figure 48.

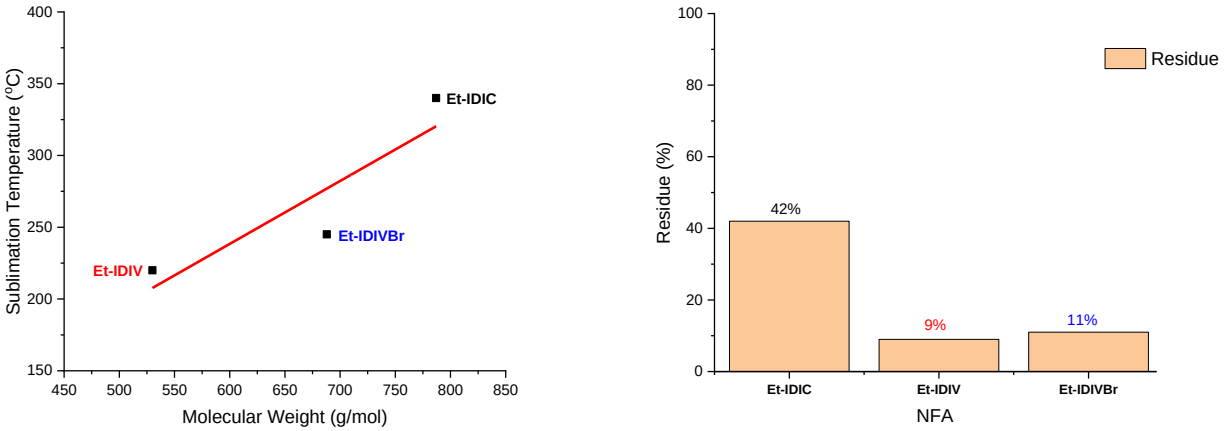

Figure 48. T_{sub}/M_w (left) and stability (right) representation for the IDIC-based NFAs.

Under high *vacuum* (10^{-6} mbar), the lighter material (**Et-IDIV**) starts to evaporate (deposition of 0.2 Å/s) at *ca* 220 °C while its brominated analogue needs 25 extra degrees Celsius (*ca* 245 °C), with an acceptable amount of residues after total evaporation for both compounds (9% and 11% respectively). Regarding **Et-IDIC,** the heavier compound of the series has a risky T_{sub} of 330 °C leading to the degradation of large part of the material in the crucible, (*i.e.* 42% of residue), resulting in the non-evaluation of its photovoltaic properties by Heliatek.

Consequently, **Et-IDIV** and **Et-IDIVBr** were embedded in all-*vacuum*-processed PHJ solar cells and combined with two HTL as donor materials, **BF-DPB** and **NHT169** (Figure 49 and Table 10).

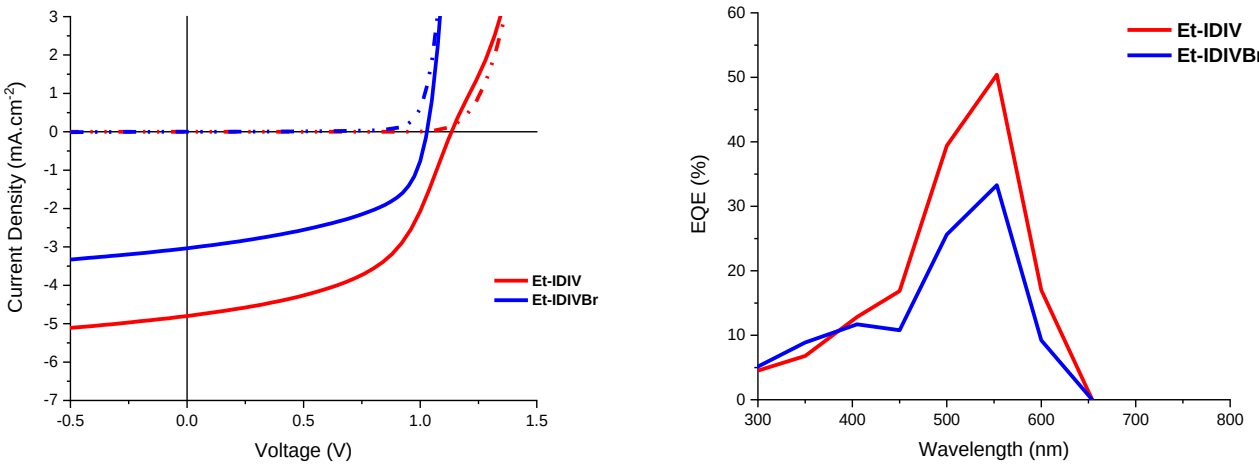

*Figure 49. J-V and EQE curves obtained for ITO/NFA (10nm)/BF-DPB (10nm)/NHT169:NDP9 (45nm)/NDP9 (1nm)/Al (100nm) devices under illumination (solid line) and dark (dashed line). The J-V curves using **NHT169** are confidential, since this material is intellectual property of Heliatek.*

Table 10. Organic solar cell device parameters for ITO/NFA (10nm)/Donor (10 nm)/NHT169:NDP9 (45nm)/NDP9 (1nm)/ Al (100nm).

Acceptor	Donor	V_{oc} (V)	J_{sc} (mA/cm^2)	*FF* %	PCE %
DCV3T	**BF-DPB**	1.05	3.5	63	2.3
	NHT169	1.26	2.9	65	2.4
Et-IDIV	**BF-DPB**	1.05	5.2	50	2.7
	NHT169	1.29	4.7	56	3.4
Et-IDIVBr	**BF-DPB**	1.01	2.8	51	1.4
	NHT169	1.24	2.7	54	1.8

Comparison of the *J-V* curves first revealed very high V_{OC} with a minimal value of 1.01 V for **Et-IDIVBr** combined with **BF-DPB** and a maximum of 1.29 V reached for **Et-IDIV** once associated with **NHT169**, in consistency with the high-lying LUMO level of both acceptors. In addition, the slight difference in the V_{OC} of *ca* 50 mV in favour of the **Et-IDIV** is correlated to its slightly destabilized LUMO level. On the other hand, a *ca* 2 mA.cm^{-2} J_{SC} difference was recorded between the two acceptors, thus affecting the corresponding power conversion efficiencies. Finally, it is noteworthy that these results are particularly promising since they already outperform (for **Et-IDIV**) the reference NFA used by Heliatek (**DCV3T**).

To summarize, a series of new low-molecular weight NFAs, stemming from the highly efficient indacenodithiophene derivatives, were synthesized and used in all-*vacuum* processed solar cells. The compatible energetics, suitable absorption in the UV-visible and even NIR region and the good evaporability of the IDIV based compounds confirmed the potency and compatibility of these materials with the *vacuum* technology. Besides, this work has evidenced the importance of molecular engineering to: i) tune the sublimation process by controlling the molecular weight and ii) tailored the electronic properties and the intermolecular interactions, paving the way to optimized structures.

Finally, comparison with the reference material **DCV3T** highlights the potential of this series since improved PV performances were reached in standard testing conditions. The preliminary results in PHJ devices afforded an impressive 3.4% PCE with a non-absorbing hole-transporting material used as donor (**NHT169**), suggesting that there is still room for progress.

References

(151) Herbst, W.; Hunger, K. *Industrial Organic Pigments*, 2nd ed.; Wiley-VCH Verlag GmbH: weinheim, 1997.

(152) Kardos, M. German Patent. DE 276357, 1913.

(153) Burnstock, A., de Keijzer, M., Krueger, J., Learner, T., de Tagle, A., Heydenreich, G., van den Berg, K. J. *Issues in Contemporary Oil Paint*; Springer US, 2014.

(154) Huang, C.; Barlow, S.; Marder, S. R. Perylene-3,4,9,10-Tetracarboxylic Acid Diimides: Synthesis, Physical Properties, and Use in Organic Electronics. *J. Org. Chem.* **2011**, *76* (8), 2386–2407.

(155) Jones, B. A.; Facchetti, A.; Wasielewski, M. R.; Marks, T. J. Effects of Arylene Diimide Thin Film Growth Conditions on N-Channel OFET Performance. *Adv. Funct. Mater.* **2008**, *18* (8), 1329–1339.

(156) Jung, B. J.; Tremblay, N. J.; Yeh, M. L.; Katz, H. E. Molecular Design and Synthetic Approaches to Electron-Transporting Organic Transistor Semiconductors. *Chem. Mater.* **2011**, *23* (3), 568–582.

(157) Navarro-Fuster, V.; Calzado, E. M.; Boj, P. G.; Quintana, J. A.; Villalvilla, J. M.; Díaz-García, M. A.; Trabadelo, V.; Juarros, A.; Retolaza, A.; Merino, S. Highly Photostable Organic Distributed Feedback Laser Emitting at 573 Nm. *Appl. Phys. Lett.* **2010**, *97* (17), 2008–2011.

(158) Trabadelo, V.; Juarros, A.; Retolaza, A.; Merino, S.; Ramírez, M. G.; Navarro-Fuster, V.; Villalvilla, J. M.; Boj, P. G.; Quintana, J. A.; Díaz-García, M. A. Highly Photostable Solid-State Organic Distributed Feedback Laser Fabricated via Thermal Nanoimprint Lithography. *Microelectron. Eng.* **2010**, *87* (5–8), 1428–1430.

(159) Gvishi, R.; Reisfeld, R.; Burshtein, Z. Spectroscopy and Laser Action of the “Red Perylimide Dye” in Various Solvents. *Chem. Phys. Lett.* **1993**, *213* (3–4), 338–344.

(160) Liang, N.; Jiang, W.; Hou, J.; Wang, Z. New Developments in Non-Fullerene Small Molecule Acceptors for Polymer Solar Cells. *Mater. Chem. Front.* **2017**, *1* (7), 1291–1303.

(161) Hartnett, P. E.; Ramakrishna Matte, H. S. S.; Eastham, N. D.; Jackson, N. E.; Wu, Y.; Chen, L. X.; Ratner, M. A.; Chang, R. P. H.; Hersam, M. C.; Wasielewski, M. R.; et al. Ring-Fusion as a Perylenediimide Dimer Design Concept for High-Performance Non-Fullerene Organic Photovoltaic Acceptors. *Chem. Sci.* **2016**, *7* (6), 3543–3555.

(162) Wu, C. H.; Chueh, C. C.; Xi, Y. Y.; Zhong, H. L.; Gao, G. P.; Wang, Z. H.; Pozzo, L. D.; Wen, T. C.; Jen, A. K. Y. Influence of Molecular Geometry of Perylene Diimide Dimers and Polymers on Bulk Heterojunction Morphology Toward High-Performance Nonfullerene Polymer Solar Cells. *Adv. Funct. Mater.* **2015**, *25* (33), 5326–5332.

(163) Sun, D.; Meng, D.; Cai, Y.; Fan, B.; Li, Y.; Jiang, W.; Huo, L.; Sun, Y.; Wang, Z. Non-Fullerene-Acceptor-Based Bulk-Heterojunction Organic Solar Cells with Efficiency over 7%. *J. Am. Chem. Soc.* **2015**, *137* (34), 11156–11162.

(164) Meng, D.; Sun, D.; Zhong, C.; Liu, T.; Fan, B.; Huo, L.; Li, Y.; Jiang, W.; Choi, H.; Kim, T.; et al. High-Performance Solution-Processed Non-Fullerene Organic Solar Cells Based on Selenophene-Containing Perylene Bisimide Acceptor. *J. Am. Chem. Soc.* **2016**, *138* (1), 375–380.

(165) Zhong, Y.; Trinh, M. T.; Chen, R.; Wang, W.; Khlyabich, P. P.; Kumar, B.; Xu, Q.; Nam, C. Y.; Sfeir, M. Y.; Black, C.; et al. Efficient Organic Solar Cells with Helical Perylene Diimide Electron Acceptors. *J. Am. Chem. Soc.* **2014**, *136* (43), 15215–15221.

(166) Zhong, Y.; Trinh, M. T.; Chen, R.; Purdum, G. E.; Khlyabich, P. P.; Sezen, M.; Oh, S.; Zhu, H.; Fowler, B.; Zhang, B.; et al. Molecular Helices as Electron Acceptors in High-Performance Bulk Heterojunction Solar Cells. *Nat. Commun.* **2015**, *6*, 1–8.

(167) Zhang, J.; Li, Y.; Huang, J.; Hu, H.; Zhang, G.; Ma, T.; Chow, P. C. Y.; Ade, H.; Pan, D.; Yan, H. Ring-Fusion of Perylene Diimide Acceptor Enabling Efficient Nonfullerene Organic Solar Cells with a Small Voltage Loss. *J. Am. Chem. Soc.* **2017**, *139* (45), 16092–16095.

(168) Teraoka, T.; Hiroto, S.; Shinokubo, H. Iridium-Catalyzed Direct Tetraborylation of Perylene Bisimides. *Org. Lett.* **2011**, *13* (10), 2532–2535.

(169) Nakazono, S.; Easwaramoorthi, S.; Kim, D.; Shinokubo, H.; Osuka, A. Synthesis of Arylated Perylene Bisimides through C - H Bond Cleavage under Ruthenium Catalysis. *Org. Lett.* **2009**, *11* (23), 5426–5429.

(170) Battagliarin, G.; Li, C.; Enkelmann, V.; Müllen, K. 2,5,8,11-Tetraboronic Ester Perylenediimides: A next Generation Building Block for Dye-Stuff Synthesis. *Org. Lett.* **2011**, *13* (12), 3012–3015.

(171) Li, X.; Wang, H.; Schneider, J. A.; Wei, Z.; Lai, W. Y.; Huang, W.; Wudl, F.; Zheng, Y. Catalyst-Free One-Step Synthesis of Ortho-Tetraaryl Perylene Diimides for Efficient OPV Non-Fullerene Acceptors. *J. Mater. Chem. C* **2017**, *5* (11), 2781–2785.

(172) Seybold, G.; Wagenblast, G. New Perylene and Violanthrone Dyestuffs for Fluorescent Collectors. *Dye. Pigment.* **1989**, *11* (4), 303–317.

(173) Nazari, M.; Cieplechowicz, E.; Welsh, T. A.; Welch, G. C. A Direct Comparison of Monomeric vs. Dimeric and Non-Annulated vs. N-Annulated Perylene Diimide Electron Acceptors for Organic Photovoltaics. *New J. Chem.* **2019**, *43* (13), 5187–5195.
(174) Handa, N. V.; Shirtcliff, L. D.; Lavine, B. K.; Powell, D. R.; Berlin, D. K. 1,6-and 1,7-Regioisomers of Perylene Tetracarboxylic Dianhydride and Diimide: The Effects of Neutral Bay Substituents on the Electrochemical and Structural Properties. *Phosphorus, Sulfur Silicon Relat. Elem.* **2014**, *189* (6), 738–752.
(175) Kozma, E.; Mróz, W.; Andicsová Eckstein, A.; Lukeš, V.; Galeotti, F.; Šišková, A.; Danko, M.; Catellani, M. A Joint Experimental and Theoretical Study on the Electro-Optical Properties of 1,6- and 1,7-Fluorenyl Disubstituted Perylene Diimide Isomers. *New J. Chem.* **2018**, *42* (2), 1061–1066.
(176) Würthner, F.; Stepanenko, V.; Chen, Z.; Saha-Möller, C. R.; Kocher, N.; Stalke, D. Preparation and Characterization of Regioisomerically Pure 1,7-Disubstituted Perylene Bisimide Dyes. *J. Org. Chem.* **2004**, *69* (23), 7933–7939.
(177) Liu, Y.; Wang, Y.; Ai, L.; Liu, Z.; Ouyang, X.; Ge, Z. Perylenebisimide Regioisomers: Effect of Substituent Position on Their Spectroscopic, Electrochemical, and Photovoltaic Properties. *Dye. Pigment.* **2015**, *121*, 363–371.
(178) Pouchain, L.; Alévêque, O.; Nicolas, Y.; Oger, A.; Régent, C. H. Le; Allain, M.; Blanchard, P.; Roncali, J. Quaterthiophenes with Terminal Indeno[1,2-b]Thiophene Units as p-Type Organic Semiconductors. *J. Org. Chem.* **2009**, *74* (3), 1054–1064.
(179) Rajasingh, P.; Cohen, R.; Shirman, E.; Shimon, L. J. W.; Rybtchinski, B. Selective Bromination of Perylene Diimides under Mild Conditions. *J. Org. Chem.* **2007**, *72* (16), 5973–5979.
(180) Simón Marqués, P.; Tintori, F.; Andrés Castán, J. M.; Josse, P.; Dalinot, C.; Allain, M.; Welch, G.; Blanchard, P.; Cabanetos, C. Indeno[1,2-b]Thiophene End-Capped Perylene Diimide: Should the 1,6-Regioisomers Be Systematically Considered as a Byproduct? *Sci. Rep.* **2020**, *10* (1), 3262.
(181) Zhang, M.; Guo, X.; Wang, X.; Wang, H.; Li, Y. Synthesis and Photovoltaic Properties of D-A Copolymers Based on Alkyl-Substituted Indacenodithiophene Donor Unit. *Chem. Mater.* **2011**, *23* (18), 4264–4270.
(182) Xu, Y.-X.; Chueh, C.-C.; Yip, H.-L.; Ding, F.-Z.; Li, Y.-X.; Li, C.-Z.; Li, X.; Chen, W.-C.; Jen, A. K. Y. Improved Charge Transport and Absorption Coefficient in Indacenodithieno[3,2-b]Thiophene-Based Ladder-Type Polymer Leading to Highly Efficient Polymer Solar Cells. *Adv. Mater.* **2012**, *24* (47), 6356–6361.
(183) Wu, Y.; Bai, H.; Wang, Z.; Cheng, P.; Zhu, S.; Wang, Y.; Ma, W.; Zhan, X. A Planar Electron Acceptor for Efficient Polymer Solar Cells. *Energy Environ. Sci.* **2015**, *8* (11), 3215–3221.
(184) Yu, S.; Chen, Y.; Yang, L.; Ye, P.; Wu, J.; Yu, J.; Zhang, S.; Gao, Y.; Huang, H. Significant Enhancement of Photovoltaic Performance through Introducing S···N Conformational Locks. *J. Mater. Chem. A* **2017**, *5* (41), 21674–21678.
(185) Wadsworth, A.; Moser, M.; Marks, A.; Little, M. S.; Gasparini, N.; Brabec, C. J.; Baran, D.; McCulloch, I. Critical Review of the Molecular Design Progress in Non-Fullerene Electron Acceptors towards Commercially Viable Organic Solar Cells. *Chem. Soc. Rev.* **2019**, *48* (6), 1596–1625.
(186) Bin, H.; Zhang, Z. G.; Gao, L.; Chen, S.; Zhong, L.; Xue, L.; Yang, C.; Li, Y. Non-Fullerene Polymer Solar Cells Based on Alkylthio and Fluorine Substituted 2D-Conjugated Polymers Reach 9.5% Efficiency. *J. Am. Chem. Soc.* **2016**, *138* (13), 4657–4664.
(187) Li, S.; Ye, L.; Zhao, W.; Zhang, S.; Mukherjee, S.; Ade, H.; Hou, J. Energy-Level Modulation of Small-Molecule Electron Acceptors to Achieve over 12% Efficiency in Polymer Solar Cells. *Adv. Mater.* **2016**, *28* (42), 9423–9429.
(188) Zhao, W.; Li, S.; Yao, H.; Zhang, S.; Zhang, Y.; Yang, B.; Hou, J. Molecular Optimization Enables over 13% Efficiency in Organic Solar Cells. *J. Am. Chem. Soc.* **2017**, *139* (21), 7148–7151.
(189) Lin, Y.; Firdaus, Y.; Nugraha, M. I.; Liu, F.; Karuthedath, S.; Emwas, A. H.; Zhang, W.; Seitkhan, A.; Neophytou, M.; Faber, H.; et al. 17.1% Efficient Single-Junction Organic Solar Cells Enabled by n-Type Doping of the Bulk-Heterojunction. *Adv. Sci.* **2020**, *7* (7), 1–9.
(190) Nian, L.; Kan, Y.; Wang, H.; Gao, K.; Xu, B.; Rong, Q.; Wang, R.; Wang, J.; Liu, F.; Chen, J.; et al. Ternary Non-Fullerene Polymer Solar Cells with 13.51% Efficiency and a Record-High Fill Factor of 78.13%. *Energy Environ. Sci.* **2018**, *11* (12), 3392–3399.
(191) Li, Y.; Lin, J.-D.; Liu, X.; Qu, Y.; Wu, F.-P.; Liu, F.; Jiang, Z.-Q.; Forrest, S. R. Near-Infrared Ternary Tandem Solar Cells. *Adv. Mater.* **2018**, *30* (45), 1804416.
(192) Che, X.; Li, Y.; Qu, Y.; Forrest, S. R. High Fabrication Yield Organic Tandem Photovoltaics Combining Vacuum- and Solution-Processed Subcells with 15% Efficiency. *Nat. Energy* **2018**, 8–13.
(193) Wang, Y.; Ke, X.; Xiao, Z.; Ding, L.; Xia, R.; Yip, H. Organic and Solution-Processed Tandem Solar Cells with 17.3% Efficiency. **2018**, *1098* (September), 1094–1098.
(194) Lin, Y.; He, Q.; Zhao, F.; Huo, L.; Mai, J.; Lu, X.; Su, C. J.; Li, T.; Wang, J.; Zhu, J.; et al. A Facile Planar Fused-

Ring Electron Acceptor for As-Cast Polymer Solar Cells with 8.71% Efficiency. *J. Am. Chem. Soc.* **2016**, *138* (9), 2973–2976.

(195) Chen, L.; Yin, X.-P.; Wang, C.-H.; Zhou, J. Catalytic Functionalization of Tertiary Alcohols to Fully Substituted Carbon Centres. *Org. Biomol. Chem.* **2014**, *12* (32), 6033.

(196) Josse, P.; Chávez, P.; Dindault, C.; Dalinot, C.; McAfee, S. M.; Dabos-Seignon, S.; Tondelier, D.; Welch, G.; Blanchard, P.; Leclerc, N.; et al. Thiophene vs Thiazole: Effect of the π-Connector on the Properties of Phthalimide End-Capped Diketopyrrolopyrrole Based Molecular Acceptors for Organic Photovoltaics. *Dye. Pigment.* **2017**, *137*, 576–583.

(197) Alamoudi, M. A.; Khan, J. I.; Firdaus, Y.; Wang, K.; Andrienko, D.; Beaujuge, P. M.; Laquai, F. Impact of Nonfullerene Acceptor Core Structure on the Photophysics and Efficiency of Polymer Solar Cells. *ACS Energy Lett.* **2018**, *3* (4), 802–811.

(198) Li, Y.; Tatum, W. K.; Onorato, J. W.; Barajas, S. D.; Yang, Y. Y.; Luscombe, C. K. An Indacenodithiophene-Based Semiconducting Polymer with High Ductility for Stretchable Organic Electronics. *Polym. Chem.* **2017**, *8* (34), 5185–5193.

(199) Zhang, W.; Smith, J.; Watkins, S. E.; Gysel, R.; McGehee, M.; Salleo, A.; Kirkpatrick, J.; Ashraf, S.; Anthopoulos, T.; Heeney, M.; et al. Indacenodithiophene Semiconducting Polymers for High-Performance, Air-Stable Transistors. *J. Am. Chem. Soc.* **2010**, *132* (33), 11437–11439.

(200) Littke, A. F.; Dai, C.; Fu, G. C. Versatile Catalysts for the Suzuki Cross-Coupling of Arylboronic Acids with Aryl and Vinyl Halides and Triflates under Mild Conditions. *J. Am. Chem. Soc.* **2000**, *122* (17), 4020–4028.

Chapter 3
New Functionalization of the Benzothioxanthene Block

1 Introduction

As previously discussed, rylene based materials are an important family in the field of organic electronics and more especially in OPVs, where, for instance, PDI derivatives play an essential role as low-cost and efficient NFAs. However, the latter are also know to suffer from detrimental high crystallinity, if not properly functionalized, which hampers the ideal morphology of the active layer and therefore the photovoltaic performances. In addition, these crystallites, resulting from strong intermolecular interactions, notably increase the sublimation temperature during the *vacuum*-processing, leading to extreme conditions where organic materials usually decompose. On the other hand, the heavier twisted derivatives, as the ones depicted in Chapter 2 (Figure 25), show too high molecular weights ending-up with the same limitations. Thereby, promising **PDI** derivatives cannot be easily *vacuum*-processed to form thin-films to reach high efficient solar cells.

In this context, the *N*-(alkyl)benzothioxanthene-3,4-dicarboximide (**BTXI**, Scheme 8) has attracted lately our attention, owing to its photophysical properties and synthetic versatility.[201–203] Disregarded by the organic electronics community, its first synthesis was reported by Peters *et al.* in 1974 as a potential vat dye for textile industry.[204] Since then, only a bunch of publications has been found in the literature. Mainly used for its fluorescent properties in bio-imaging and photodynamic therapy applications, it is noteworthy that the BTXI was only functionalized at its imide constituting nitrogen atom to improve the solubility and/or introduce an anchoring group (**S1**, **A4** and **B4**).[201,205]

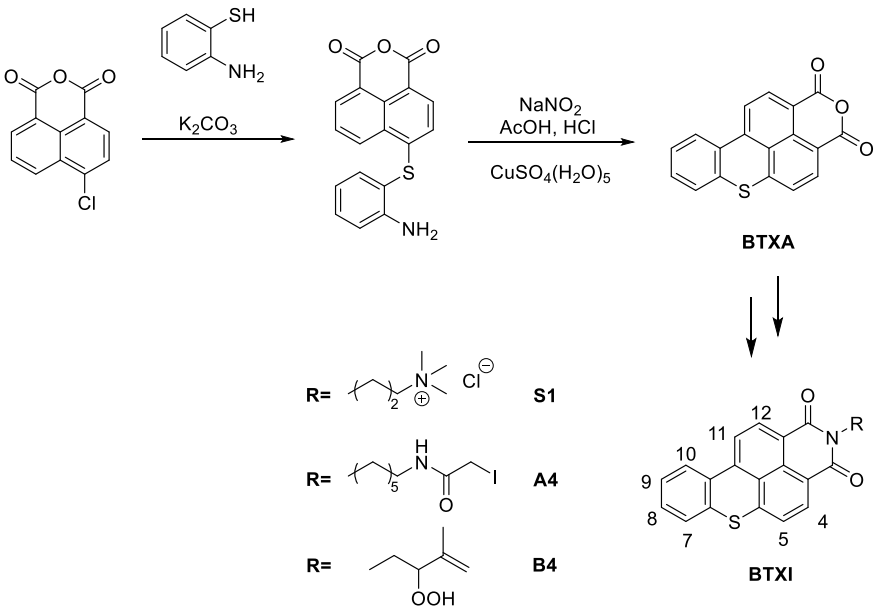

Scheme 8. Preparation of reported N-subsituted BTXI derivatives.

Hence, our group has recently focused its attention on the functionalization of the rylene core to prepare π-conjugated BTXI based derivatives (Scheme 9). As a first step, we reported the successful and selective monohalogenation of **BTXI** at the 5-position.[206] This new functionalized dye opened new doors towards palladium-catalyzed couplings, resulting in novel structures and their demonstration as active materials for OPV applications.[206,207] Thereafter, and in parallel to multihalogenation studies, attempts of nitration of the dye were successfully carried out.[208,209]

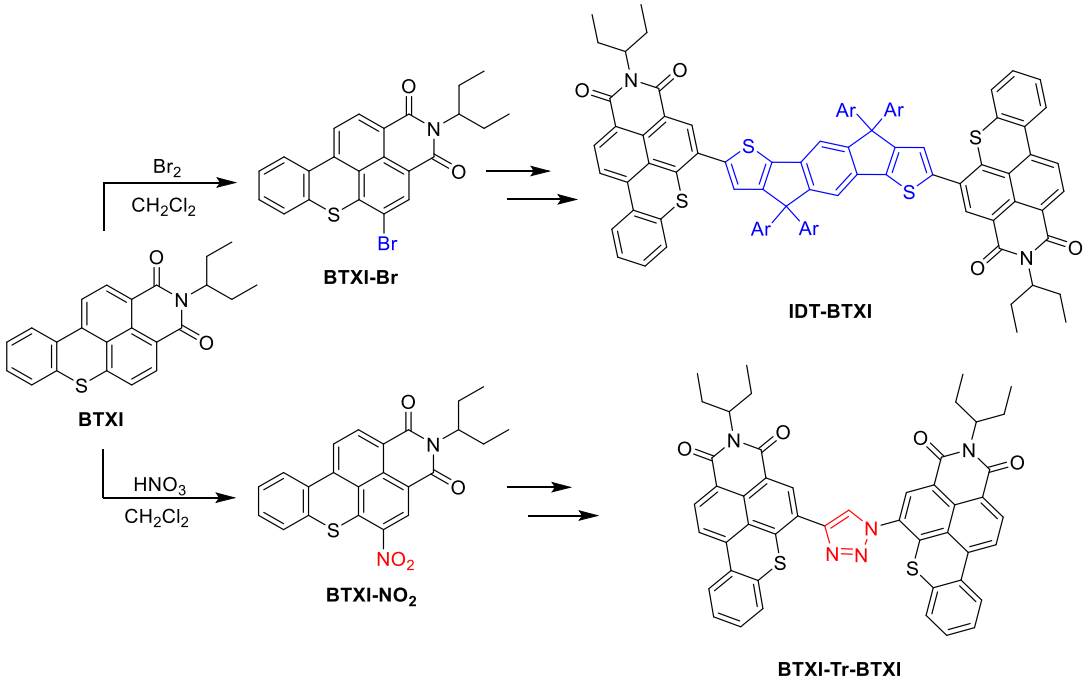

Scheme 9. Synthetic pathway to BTXI-based organic semiconductors.

In addition to a better structure-property understanding, these multiple approaches highlighted unexplored photophysical and electrochemical properties. For instance, the **BTXI** turns out to be a promising dual redox active molecule with a fully reversible and stable one-electron processes in both anodic and cathodic regions and defining an impressive electrochemical gap of *ca* 3 V. Moreover, investigation of the photoluminescence properties revealed an emission quantum yield of Φ_f = 0.99 for the bare dye and singlet-oxygen generation quantum yield close to Φ_Δ = 1.00 for its sulfone derivative, interesting feature for biophotonics and theranostics applications.[210]

Consequently, and based on preliminary evaporation tests, the use of the BTXI to afford *vacuum*-processable NFAs has been investigated. Hence, to tune the energetic levels and frustrate/hinder the donor character of this ambipolar block, the decoration with electron-withdrawing nitrile groups was explored.

2 Synthesis of BTXI-CN

In addition to modulating the optoelectronical properties, the nitrile group offers a large variety of transformation (for instance into acids, aldehydes, amines, amides or even nitrilium ions)[211–213] or can undergo copper-catalyzed azide-alkyne 1,3-dipolar cycloaddition (CuAAC), transition metal complexation, Pinner reaction or simple nucleophilic attacks.[214–217]

Hence, cyanation attempts of the 5-bromo *N*-(ethyl)benzothioxanthene-3,4-dicarboximide (**BTXI-Br**) were carried out (Scheme 10) and selected results are gathered in Table 11.

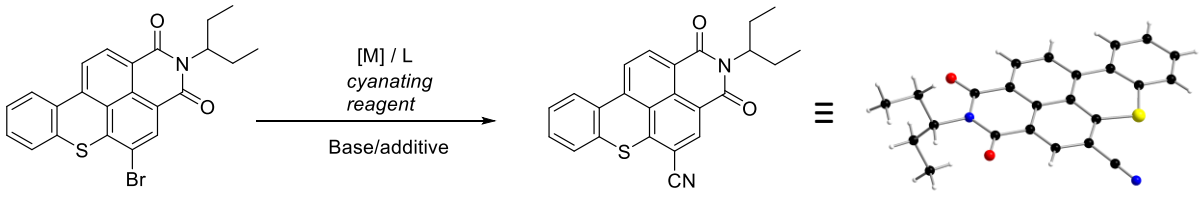

BTXI-Br **BTXI-CN**

Scheme 10. Cyanation of the brominated BTXI block.

Though being a key functional group, only Rosendmund-von Braun or palladium mediated reactions, using stoichiometric amounts of highly toxic and insoluble metal cyanide salts (NaCN, CuCN, $Zn(CN)_2$) have been employed so far for the synthesis of nitrile-functionalized

rylenes.[218–222] Application of this classic strategy (Table 11, entry 1) resulted herein in no conversion and the full recovery of the starting material.

Consequently, Beller's group conditions[223] were subsequently tested. Based on the use of potassium hexacyanoferrate(II) ($K_4[Fe(CN)_6]$), a non-toxic and inexpensive food additive,[224] with a palladium(II) acetate/bis(diphenylphosphino)ferrocene ($Pd(AcO)_2$/dppf) catalyst system. It is noteworthy that a total conversion was monitored by thin layer chromatography (Entry 2). However, only minor amount of target compound was recovered after the purification.

*Table 11. Variation of reaction conditions for the cyanation of **BTXI-Br**.*

Entry	RCN (eq.)	Solvent	Cat. (mol%)	Ligand (%)	temp./time	Yield
1	CuCN (9)	DMF	-	-	150 °C, 7 h	0%
2[a]	$K_4[Fe(CN)_6]$ (0.25)	DMAC	$Pd(OAc)_2$ (5)	dppf (10)	140 °C, 24 h	15%
3[a]	$K_4[Fe(CN)_6]$ (0.25)	DMAC	$Pd(OAc)_2$ (5)	dppf (10)	100 °C, 24 h	traces
4	$K_4[Fe(CN)_6]$ (0.25)	DMAC	$Pd(OAc)_2$ (5)	dppf (10)	140 °C, 2 h	68%
5	$K_4[Fe(CN)_6]$ (0.25)	DMF	$Pd(OAc)_2$ (5)	dppf (10)	140 °C, 2 h	43%
6	$K_4[Fe(CN)_6]$ (0.25)	DMAC	$Pd(OAc)_2$ (5)	PCy_3 (10)	140 °C, 2 h	27%
7	$K_4[Fe(CN)_6]$ (0.25)	DMAC	$Pd(OAc)_2$ (5)	SPhos (10)	140 °C, 2 h	0%
8	$K_4[Fe(CN)_6]$ (0.25)	DMAC	$Pd(OAc)_2$ (5)	Xantphos (10)	140 °C, 2 h	70%
9	$K_4[Fe(CN)_6]$ (0.25)	DMAC	$Pd(OAc)_2$ (5)	-	140 °C, 2 h	34%
10	$K_4[Fe(CN)_6]$ (0.25)	DMAC	$Pd(dppf)Cl_2$ (5)	-	140 °C, 2 h	traces
11	$K_4[Fe(CN)_6]$ (0.25)	DMAC	Silia*Cat*® (5)	Xantphos (10)	140 °C, 2 h	traces
12	**$K_4[Fe(CN)_6]$ (1.00)**	**DMAC**	**$Pd(OAc)_2$ (10)**	**Xantphos (20)**	**140 °C, 0.5 h**	**95%**

[a]Reaction without microwave radiation.

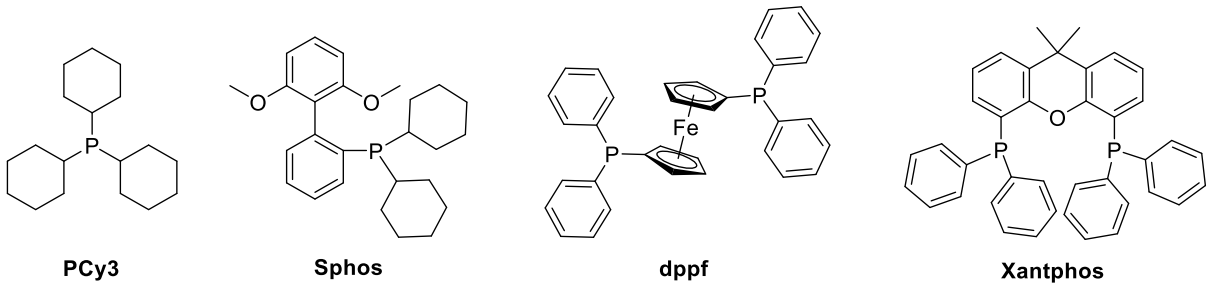

Figure 50. Chemical structure of phosphine ligands considered in this study.

This phenomenon was correlated to the moderate **BTXI-CN** stability in these reaction conditions. On the other hand, decreasing the reaction temperature to 100 °C was not found to be efficient since only traces of the final compound were recovered (Entry 3). Considering that the cyanide transfer from the ionic center is (partially) disabled in this range of temperatures, it was thus decided to shorten the reaction times. Surprisingly, reducing the

timing from 24 h to 2 h, and taking advance of a microwave reactor, results in a significant improvement of the synthetic yield, *i.e.*, from 15% to 68% (Entry 4). In parallel, dimethylacetamide (DMAC) was replaced by the dimethylformamide (DMF) known for its high solubilizing power (entry 5). However, lower synthetic yields were actually achieved, even under anhydrous conditions, probably due to the limited thermal stability of the DMF.

Regarding the catalytic system, the use of monodentate phosphine ligands was found to be detrimental for the reactivity, resulting in a poor synthetic yield for the electron-rich tricyclohexylphosphine and even no evidence of target product for the biaryl phosphine analogue SPhos (Entries 6 and 7). Conversely, chelating phosphine ligands such as the Xantphos (Figure 50) gave the best results with a promising 70% yield due to a facilitated purification and reduction of dehalogenation side-reactions (Entry 8).

Thereafter, Weissman *et al.* ligand free conditions (Entry 9),[225] were also tested to assess the potential of this greener alternative. Although some conversion was emphasized after 2 hours of reaction, the resulting modest yield of *ca* 34% could be correlated to the lower reactivity of electron-rich BTXI starting materials. Changing the palladium source to $Pd(dppf)Cl_2$ was also considered affording the target compound as trace levels, thus highlighting the importance of the Pd/Ligand ratio and nature (Entry 10). Inconclusive results were indeed obtained, even in presence of Xantphos, with the Silia*Cat*®, a heterogeneous palladium catalyst supported on silica which purification only requires a filtration (Entry 11).

Consequently and among all tested conditions using a palladium catalyst, the couple palladium(II) acetate/Xantphos turned out to be the most effective combination to reach decent synthetic yields. To reduce the reaction time, the number of $K_4[Fe(CN)_6]$ equivalents was increasing to one and the catalytic system was doubled, resulting in a full conversion in only 30 minutes and the best isolated quantity of **BTXI-CN** with an overall yield of *ca* 95% (Entry 12). Moreover, conscious of the growing importance of sustainable synthesis and purifications, especially in large manufacture, highly pure **BTXI-CN** was isolated in an excellent 86% yield by substituting the solvent consuming silica-gel chromatography by a fast filtration on a small silica-plug, followed by a precipitation of the crude product using a DCM/MeOH mixture of solvents (see Experimental Section, Synthesis, for details).

Finally, in order to extend the scope of the cyanation reaction, the optimal conditions were also applied to electron-rich and electron-poor substituted monobrominated BTXI derivatives (Scheme 11).

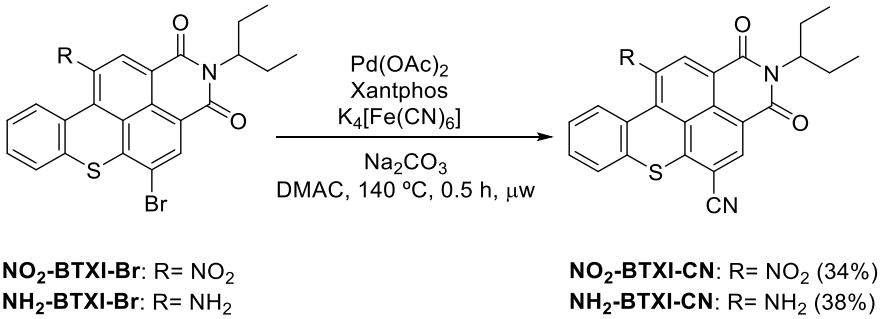

NO_2-BTXI-Br: R= NO_2
NH_2-BTXI-Br: R= NH_2

NO_2-BTXI-CN: R= NO_2 (34%)
NH_2-BTXI-CN: R= NH_2 (38%)

*Scheme 11. Synthesis of **NO_2-BTXI-CN** and **NH_2-BTXI-CN**.*

Hence, amine containing **NH_2-BTXI-CN** and nitro derivative **NO_2-BTXI-CN** were successfully prepared from their respective brominated cores thus evidencing the potency of this strategy for the preparation of newly functionalized materials. Modest yields could be ascribed to the possible formation of a carbazole, in the presence of the palladium source and/or the aryl phosphine[226,227] or to a palladium-catalysed aryne annulation, for the nitro or amino derivative respectively.[228–230]

3 Dicyanation of the benzothioxanthene

Once the monocyanation of the BTXI core was demonstrated, attempts of di-functionalization was considered. To that end, a benzothioxanthene (**Br-BTXI-Br**) functionalized with a bromine atom in positions 5 and 11, was subjected to a cyanation reaction with opitmized conditions, *i.e.*, two equivalent of $K_4[Fe(CN)_6]$ in presence of 10 mol % palladium(II) acetate and 20 mol % of Xantphos (Scheme 12).

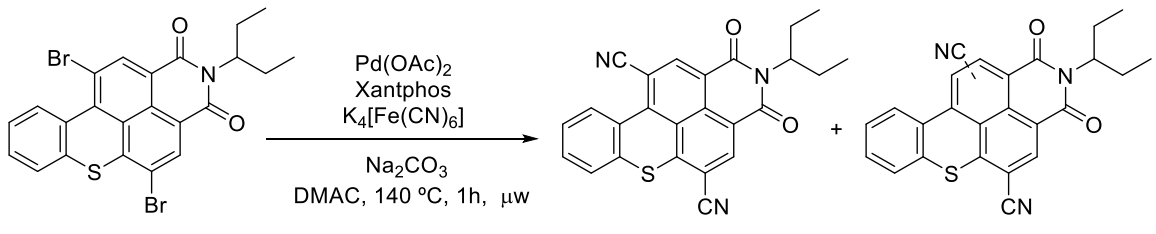

45%
23%

Br-BTXI-Br

11-NC-BTXI-CN (45%)

X-NC-BTXI-CN (23%)

Scheme 12. Synthetic route to NC-BTXI-CN

After one hour of reaction, TLCs revealed the full consumption of the starting material and its conversion into two new products. Purified by column chromatography on silica gel, the first and major fraction (45% yield) turned out to be the expected 5,11-dicarbonitrile product (**11-NC-BTXI-CN**, Scheme 12). More surprisingly, the second spot, isolated in a significant yield of *ca* 23%, turned out to be, according to both the ^{1}H MNR and mass spectrometry, a regioisomer of **11-CN-BTXI-CN**. While the ^{1}H NMR spectra of **Br-BTXI-Br** and **11-CN-BTXI-CN** show two singlets between 9.0 ppm and 8.5 ppm ascribed to the di-functionalization of the naphthyl block (Figure 51), one of the two singlets of the new regioisomer splits in two doublets, suggesting that one of the cyano group is localized at the distant phenyl ring (Figure 51, blue spectrum). Moreover, the unknown compound displays in the range of 8.0-7.5 ppm an ABA' system characteristic of the disappearance of one of the phenyl protons. Investigated by NOESY NMR experiment, the functionalization of the second cyano group appeared to take place at the 10-position, owing to the absence of cross relaxation between nearby bay protons (Figure 52).

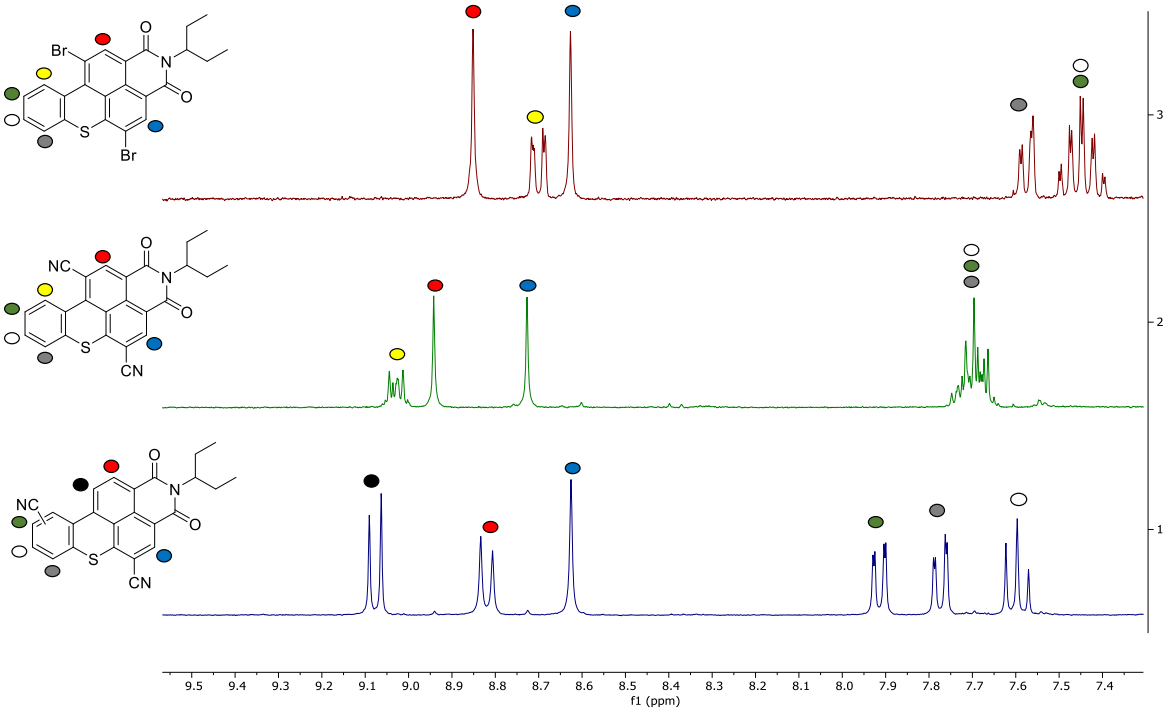

*Figure 51. Comparison of the ^{1}H NMR ($CDCl_3$, 300 MHz) spectra of **Br-BTXI-Br** and the two region isomers of **NC-BTXI-CN**.*

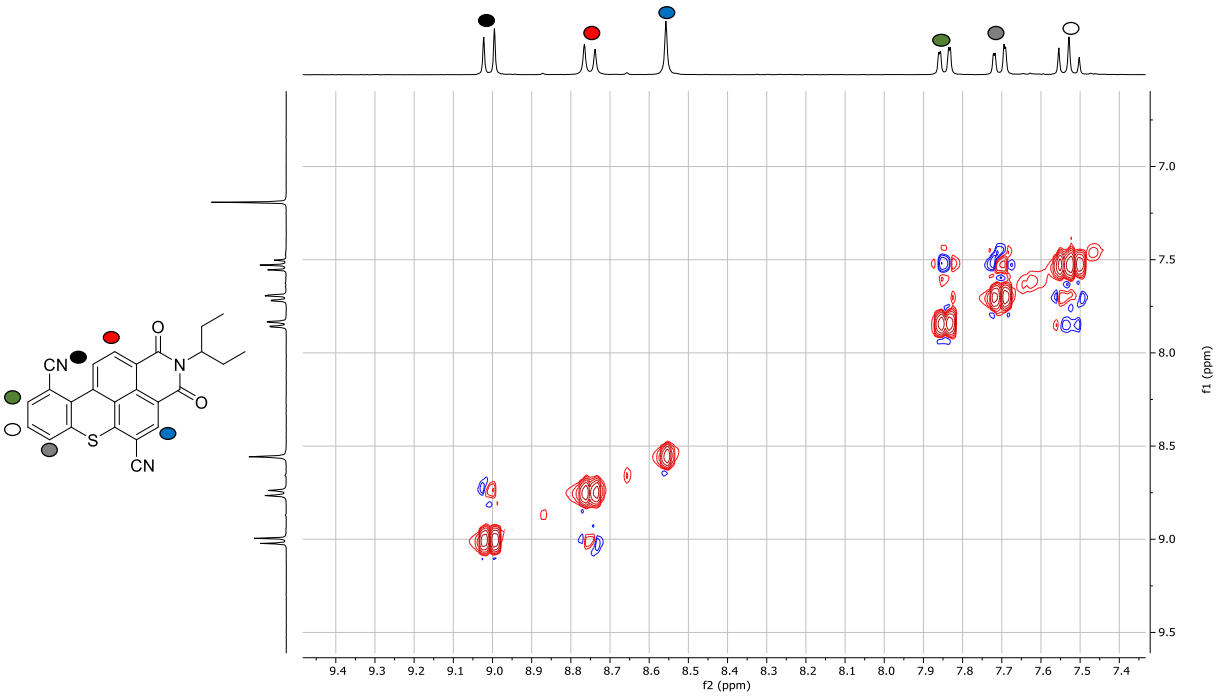

*Figure 52. NOESY NMR spectra ($CDCl_3$, 300 MHz) of **10-CN-BTXI-CN**.*

Thereafter confirmed by X-ray diffraction on single crystals, the structure of both region isomers are thus depicted in Figure 53.

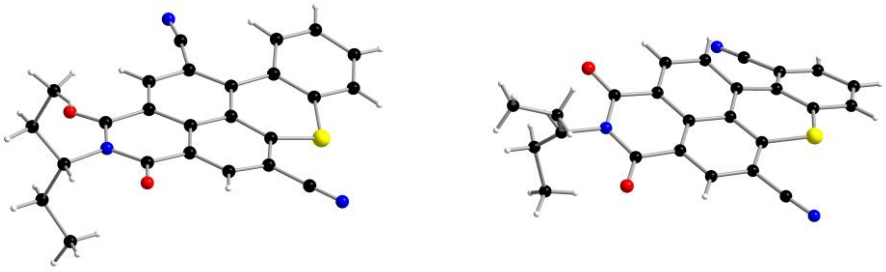

Figure 53. X-ray structures of both NC-BTXI-CN 5,11 (left) and 5,10 (right) regioisomers.

To understand this unexpected functionalization, the 5-position of the dibromo BTXI was protected with an alkyl chain via a Suzuki-Miyaura cross coupling reaction. Once engaged in the cyanation reaction, both regioisomers were isolated in similar yield than those of the dicyano derivatives, *i.e.* 45% and 29% for the **11-NC-BTXI-*i*Bu** and **10-NC-BTXI-*i*Bu** respectively (Scheme 13). Presumably, a C-H activation process occurs resulting from a five-membered palladacycle generated after the oxidative addition on the brominated specie at the 11-position (see Experimental Section, Figure 63).

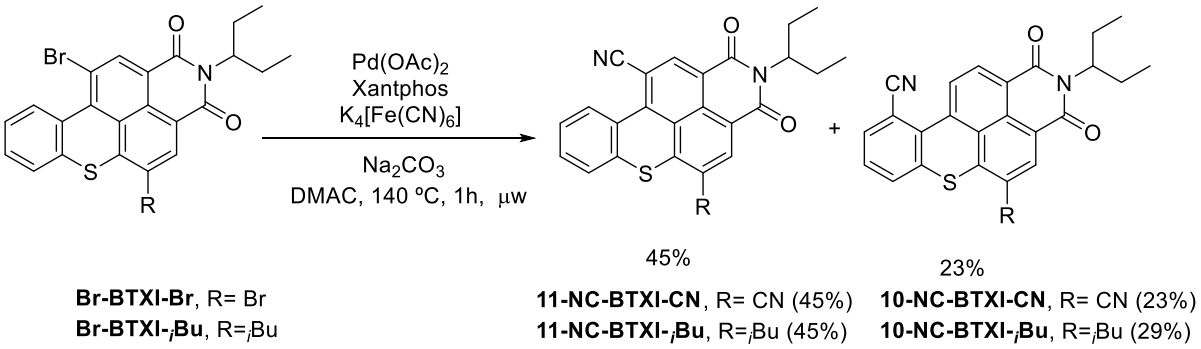

*Scheme 13. Cyanation reaction over **Br-BTXI-Br** and **Br-BTXI-$_i$Bu**.*

Hence, to shed light over the possible mechanism, the reaction was first carried out in presence of deuterated water (D_2O). Interestingly, ^{1}H NMR (Figure 54) and mass spectrometry experiments confirmed the deuterium-proton exchange in the final compounds as depicted in Scheme 14.

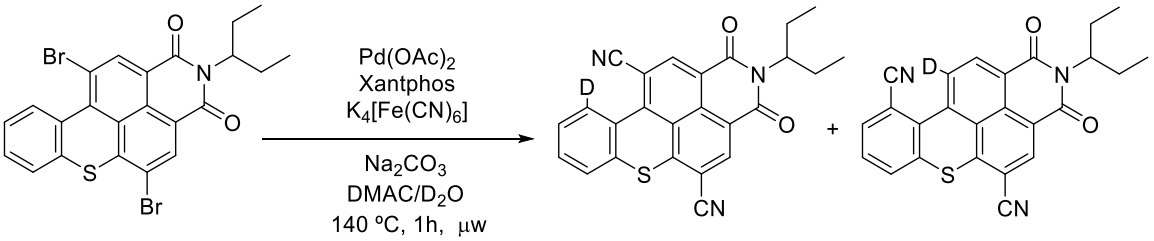

*Scheme 14. Cyanation reaction over **Br-BTXI-Br** in presence of D_2O.*

Indeed, integration of the doublet at 9.08 ppm assigned to the proton in position 11, revealed a conversion of *ca* 90% in the monodeuterated compound for the isolated **10-NC-BTXI-CN**, thus confirming the catalytic cycle hypothesis where the five-membered palladacylce is generated after the elimination of HBr. ^{1}H NMR of **11-NC-BTXI-CN** also proved the presence of a deuterated species (73%) resulting from the reversibility of the isomerization, thus highlighting that most of the catalytic turnovers pass through the palladacycle complex (see Experimental Section, Isotope labelling, for more details).

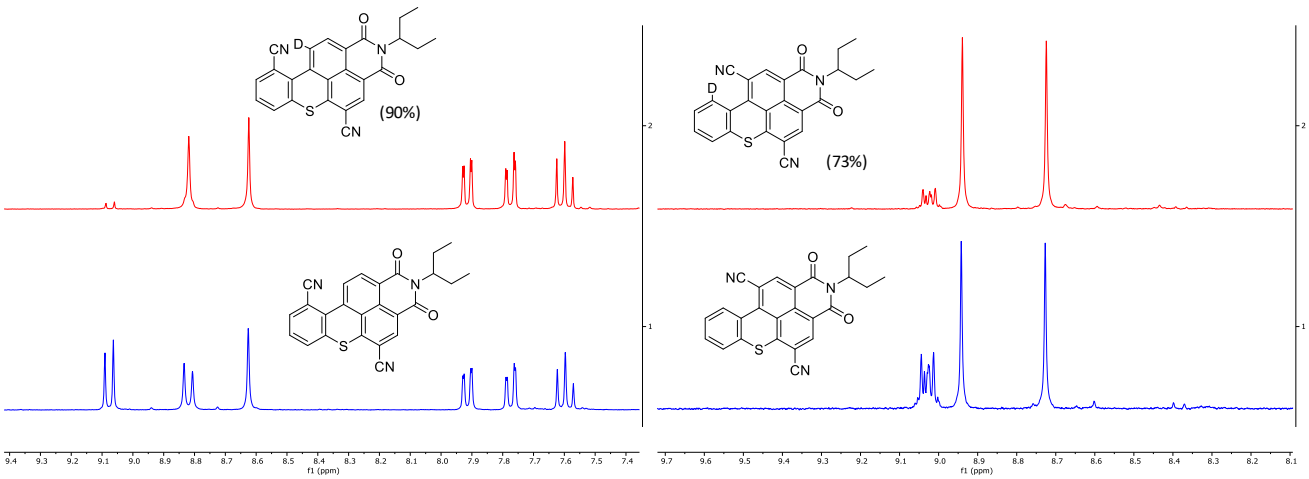

*Figure 54. Aromatic zoom of ^{1}H NMR ($CDCl_3$, 300 MHz) spectra of deuterated (red) and non-deuterated (blue) of **11-NC-BTXI-CN** (right) and **10-NC-BTXI-CN** (left).*

Consequently, two possible catalytic cycles can be hypothesized from the latter observations (Scheme 15).

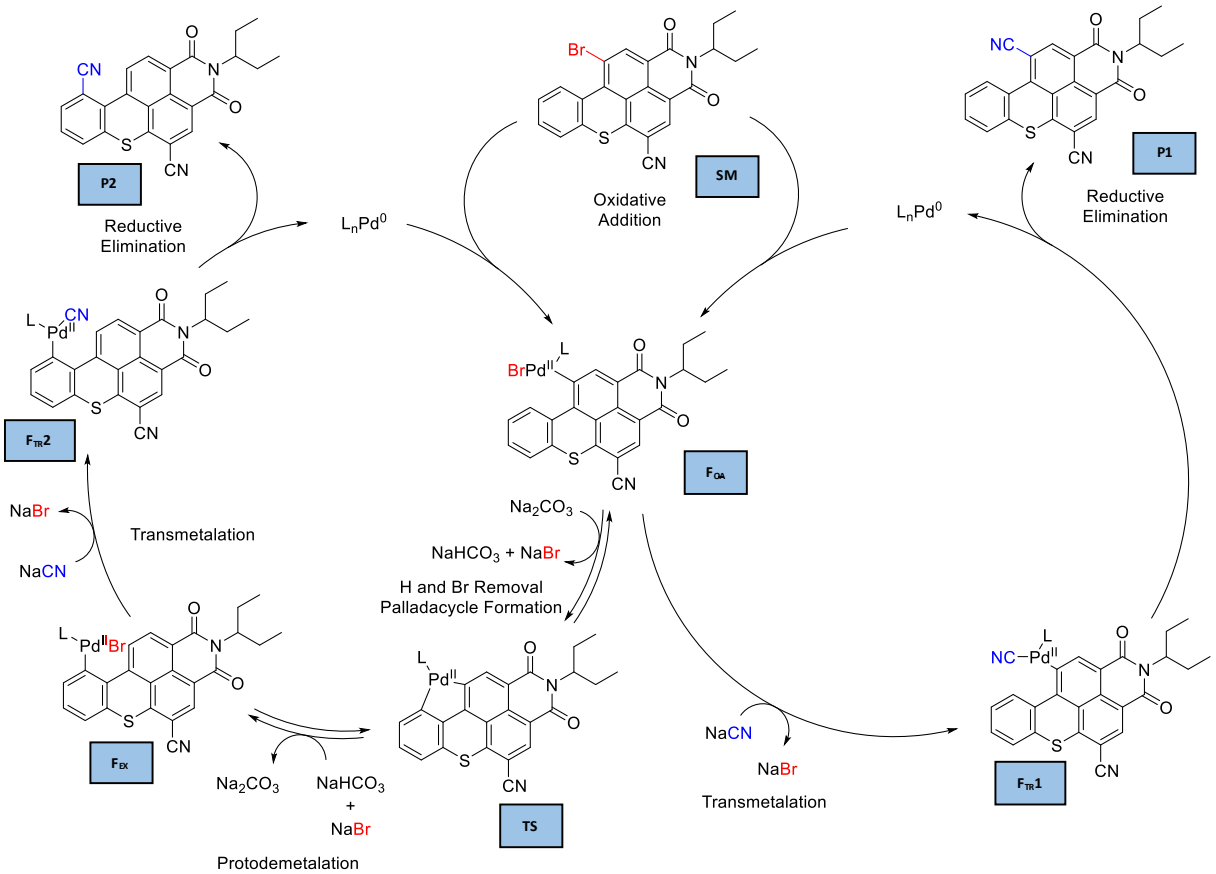

*Scheme 15. Mechanisms of the cyanation reaction of **Br-BTXI-CN** leading to **11-NC-BTXI-CN** or **10-NC-BTXI-CN** using Xantphos as ligand.*

Following the oxidative addition, $\mathbf{F_{OA}}$ can undergo the NaCN transmetalation and thus be involved in the classical mechanism to afford $\mathbf{F_{TR}1}$ and therefore the "expected" 5,11-

regioisomer (**11-NC-BTXI-CN**, **P1**). In parallel, $\mathbf{F_{OA}}$ can also be engaged in a C-H activation process thus generating the five-member palladacycle **TS** that subsequently afford $\mathbf{F_{EX}}$, to achieve the unexpected isomerization step. Alike $\mathbf{F_{OA}}$, $\mathbf{F_{EX}}$ can be transformed in $\mathbf{F_{TR}2}$ via transmetalation, yielding **10-NC-BTXI-CN** (**P2**) after the reductive elimination process. To support this hypothesized catalytic path, DFT calculation were performed to build the energetic diagram of all catalytic involved species (Figure 55 and Scheme 17 in Experimental section, Computational Calculation Methodology).[231]

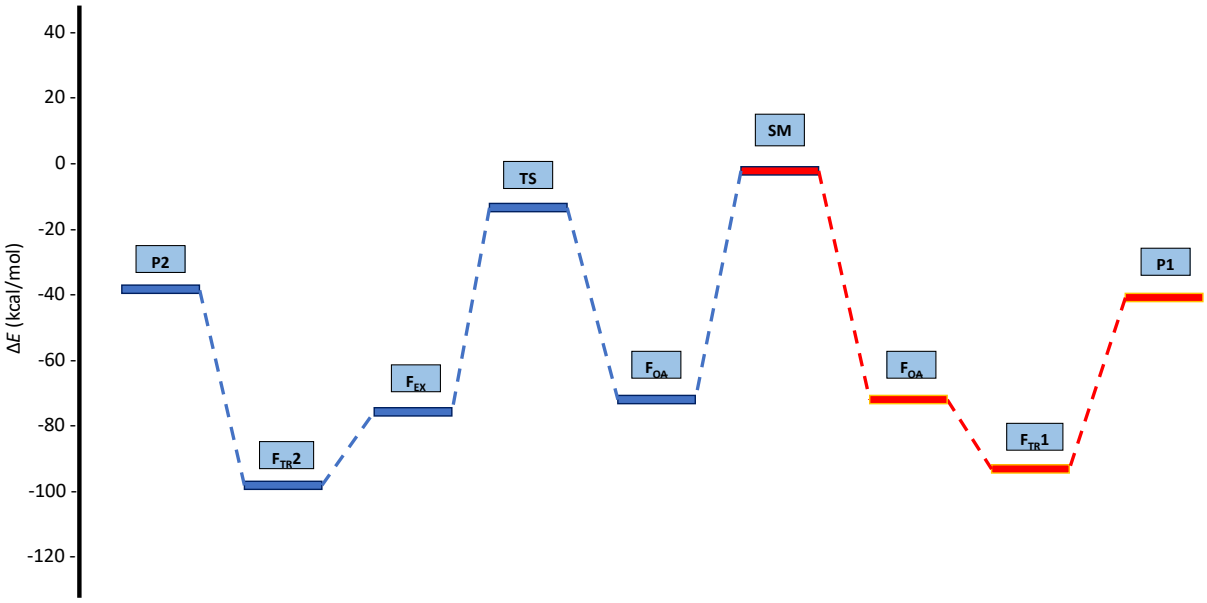

*Figure 55. Free energy profile of cyanation reaction of **Br-BTXI-CN** (red) leading to **11-NC-BTXI-CN** (orange) or **10-NC-BTXI-CN** (blue) using Xantphos as ligand. Transition states are not calculated for simplicity.*

Interestingly, even though the formation of the palladacycle complex (**TS**) requires a significant activation energy (*ca* 59 kcal/mol), the resulting $\mathbf{F_{ex}}$ turns out to be slightly more stable than $\mathbf{F_{OA}}$ of *ca* 1 kcal/mol. Thus, **TS** appears to be a non-rate-determining transition state, since the isotope labelling experiments show that most of the turnovers produce deuterated species. Consequently, with almost similar free energy for both isomers namely **P1** and **P2**, the unbalanced experimental ratio seems to be presumably dictated by the energy demanding transition state of the reductive elimination (between $\mathbf{F_{TR}}$ and **P**).

4 Characterization

4.1 Single crystals X-ray diffraction

The single crystals of **BTXI-CN**, **11-NC-BTXI-CN** and **10-NC-BTXI-CN** were obtained from vapour solvent diffusion of pentane in a solution of the named compounds in

dichloromethane. Determined by X-Ray diffraction, monoclinic *P* $2_1/c$, *P* $2_1/n$ and *C 2/c* spaces groups were assigned respectively with one independent molecule. In all cases, the structure elucidated by NMR spectroscopy was corroborated by the observed coordinates, confirming the nature of the dicyano derivatives with substitutions in 5,11- and 5,10-positions (Figure 56).

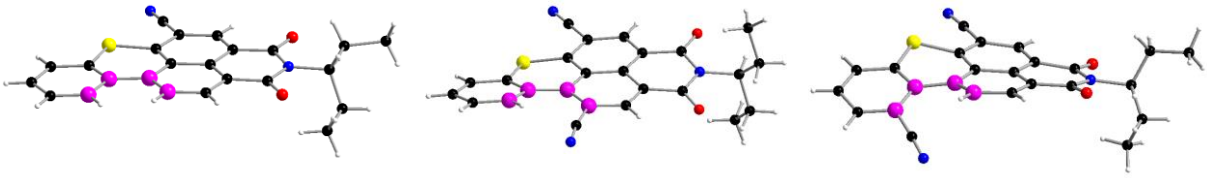

*Figure 56. Molecular structure of **BTXI-CN, 11-NC-BTXI-CN** and **10-NC-BTXI-CN** obtained from X-Ray diffraction of single crystals and each bay region represented by the carbon atoms in violet.*

Interestingly, the planarity of the aromatic backbone was compared to assess the influence of the different substitutions and more importantly, the effect of the functionalization in the bay-position. The distortion of the core was measured by calculating the dihedral angle θ between the four carbon atoms conforming the bay-region (violet atoms, Figure 56). As expected, **BTXI-CN** appears as totally planar with negligible modifications in the rylene scaffold (θ ≈ 1º), while the two regioisomers show a twisted block induced by the bulky effect of the nitrile group. Moreover, while **11-NC-BTXI-CN** displays a modest distortion (θ ≈ 12°), the dihedral angle increases to 20° in the bay functionalized counterpart, namely **10-NC-BTXI-CN**.

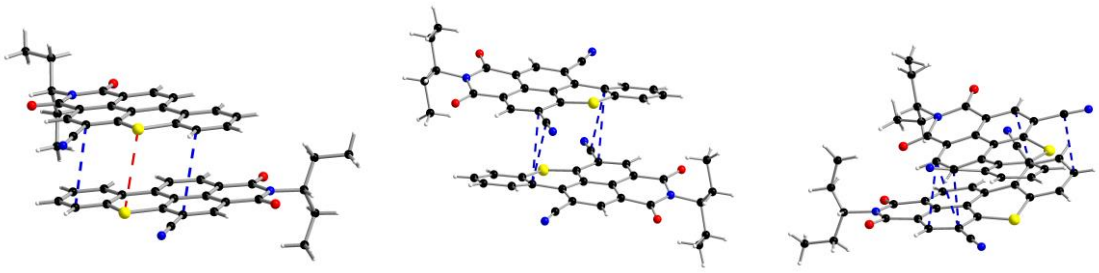

*Figure 57. Vertical intermolecular interaction of **BTXI-CN, 11-NC-BTXI-CN** and **10-NC-BTXI-CN**.*

The careful examination of the neighbouring molecules highlighted, in all cases, strong intermolecular interactions. On the one hand, the monocyanated derivatives present a matched π-π stacking between parallel aromatic cores with a minimum distance of 3.69 Å. Regarding the dicyano BTXI derivatives, twisting the rylene results in lowering the intermolecular π-π distances (3.33 Å **11-NC-BTXI-CN** and 3.26 Å **10-NC-BTXI-CN**) due to higher

interactions between the nitrile moieties and the aromatic rings but in return, the degree of distortion reduces the overlapped surfaces.

On the other hand, hydrogen bonding could also be detected with the peripheral/lateral neighboring molecules in the lamellar packing (Figure 58).

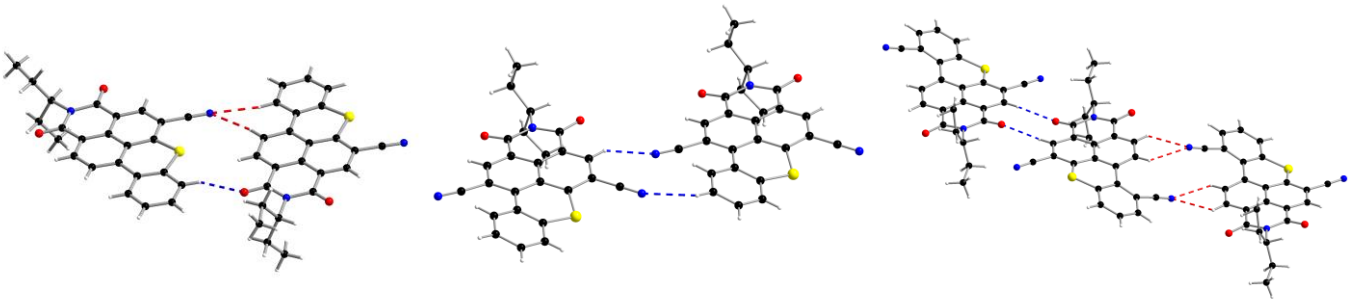

*Figure 58. Lateral intermolecular interactions in the crystal structure of **BTXI-CN**, **11-NC-BTXI-CN** and **10-NC-BTXI-CN**.*

The nitrile group of one molecule is involved in an intermolecular hydrogen bond N···H-C with a neighboring molecule while the imide group of the later generates another hydrogen bond O···H-C with the former molecule (Table 12).

*Table 12. Distances of intermolecular interactions of **BTXI-CN**, **11-NC-BTXI-CN** and **10-NC-BTXI-CN**.*

Compound	π-π (Å)	O···H (Å)	N···H (Å)
BTXI-CN	3.69	2.36	2.52/2.57
11-NC-BTXI-CN	3.33	-	2.45/2.70
10-NC-BTXI-CN	3.26	2.46	2.67

Contrary to the aforementioned π-π stacking, these non-covalent bonds decrease with the growth of the torsion angle, which could be a reason of the improved solubility of both dicyano derivative compared to **BTXI-CN**.

4.2 Optical and electrochemical analysis

The electrochemical and optical properties of **BTXI-CN**, **11-NC-BTXI-CN** and **10-NC-BTXI-CN** were studied by cyclic voltammetry and absorption and emission spectroscopy and compared with the reference benzothioxanthene block, namely **BTXI**. The CV of each compound, recorded in the same conditions described formerly, are depicted in Figure 59. Contrary to the **BTXI**, the nitrile-substituted compounds, **BTXI-CN**, **11-NC-BTXI-CN** and **10-NC-BTXI-CN** exhibit an irreversible oxidation peak at higher voltage, *i.e.* E_{pa} = 1.40 V, 1.20 V and

1.41 V, respectively, *vs* 0.90 V for **BTXI**. The CVs in negative potentials show a one-electron reversible wave for all the compounds, again with a positive shift for the cyano derivatives (E_{pc} = -1.46 V, -1.59 V and -1.34 V, respectively) with respect to the unsubstituted rylene (E_{pc} = -1.81 V). As expected, the introduction of electron-withdrawing cyano group(s) tends to stabilize the resulting radical anion whereas the radical cation becomes less stable.

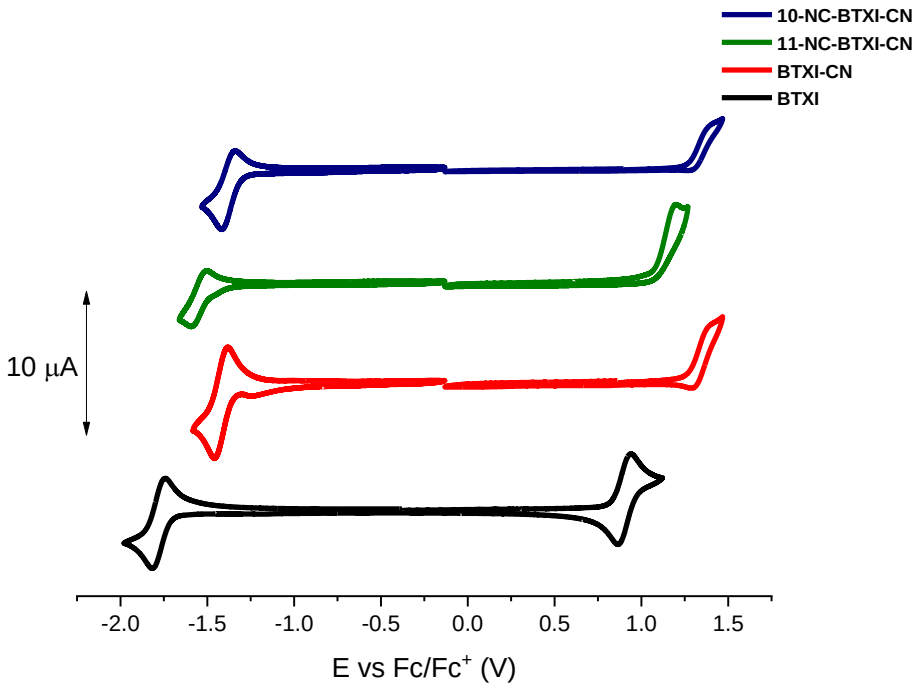

Figure 59. Cyclic voltammograms of BTXI derivatives at a concentration of 0.5 mM in 0.10 M Bu_4NPF_6/CH_2Cl_2, 100 mV s^{-1}, Pt working electrode.

The HOMO and LUMO energy levels were estimated from the onset of the first oxidation and reduction waves giving electrochemical gaps of *ca* 2.65 eV for all species. The HOMO and LUMO levels are stabilized after cyanation of the core with respect to the E_{HOMO} = -5.70 eV and E_{LUMO} = -3.03 eV values obtained for the **BTXI** (Table 13). Interestingly, **BTXI-CN** and **10-NC-BTXI-CN**, which shows no-substitution at position 11, display similar E_{HOMO} of *ca* -6.05 eV and E_{LUMO} of *ca* -3.40 eV, meaning that the functionalization at the 10-postion does not tune/change/affect robustly the energy landscape. On the other hand, the introduction of the second cyano group at the 11 position in **11-NC-BTXI-CN** raises the HOMO and LUMO levels up to -5.87 eV and -3.25 eV, respectively.

Table 13. Electrochemical data recorded from the CVs.

Compound	E_{pa} ($V_{Fc/Fc+}$)	E_{pc} ($V_{Fc/Fc+}$)	E_{HOMO}[eV]	E_{LUMO}[eV]	ΔE^{elec} [eV]
BTXI	0.94	-1.81	-5.70	-3.03	2.67
BTXI-CN	1.40	-1.46	-6.05	-3.38	2.67
11-NC-BTXI-CN	1.20	-1.59	-5.87	-3.25	2.62
10-NC-BTXI-CN	1.41	-1.34	-6.03	-3.42	2.61

E_{HOMO} (eV) = - ($E_{ox(onset)}$ (V *vs* Fc/Fc^+) + 4.80)

E_{LUMO} (eV) = - ($E_{red(onset)}$ (V *vs* Fc/Fc^+) + 4.80)

All compounds present similar absorption and emission signatures, however at different wavelengths (Figure 60). The absorption spectra are dominated by a broad structured band between 410 and 525 nm with two main peaks at lower energy separated by *ca*. 20 nm with similar intensities (Table 14) and a distinguishable shoulder at higher energy (*ca* 430 nm). Surprisingly, the presence of one cyano group in **BTXI-CN** leads to a 5-8 nm hypsochromic shift compared to **BTXI**. When the second cyano group is introduced at the 10 position, a further hypsochromic shift is observed for **10-NC-BTXI-CN**. By contrast, the **11-NC-BTXI-CN** isomer shows a 15 nm bathochromically shifted spectrum compared to **10-NC-BTXI-CN**. It is worth noting that the molar absorption coefficient decreases with the number of cyano groups.

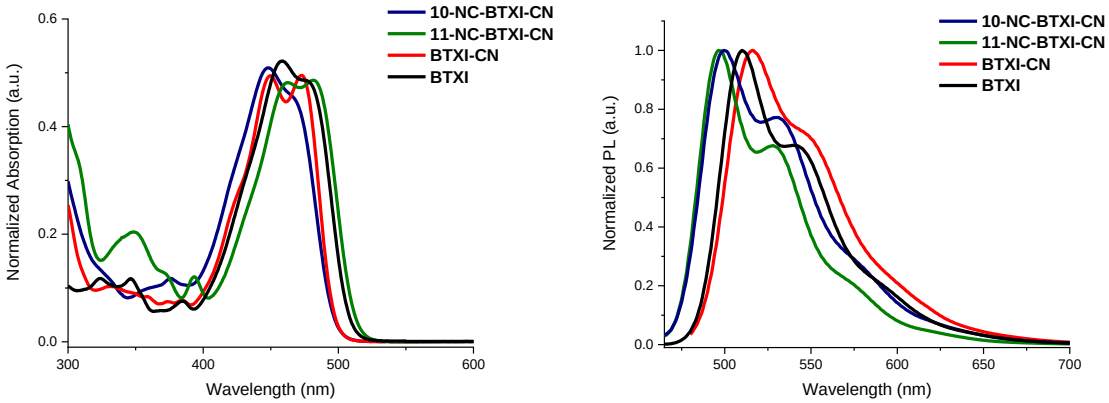

*Figure 60. Absorption (left) and emission (right) spectra of **BTXI**, **BTXI-CN**, **11-NC-BTXI-CN** and **10-NC-BTXI-CN** in CH_2Cl_2.*

Emission is characterized by a structured band and a moderate Stokes shift, suggesting a transition of nature π-π* of the emissive state. The planar compounds **BTXI** and **BTXI-CN** exhibit an emission band with the maxima at *ca* 545 nm, while the more distorted **11-NC-BTXI-**

CN and **10-NC-BTIX-CN** show a blue-shifted maxima at *ca* 530 nm. As a consequence, **11-NC-BTXI-CN** present the smaller Stokes shift of the series leveling the energy gap of both regioisomers.

*Table 14. Optical data of **BTXI**, **BTXI-CN**, **11-NC-BTXI-CN** and **10-NC-BTXI-CN** recorded in CH_2Cl_2 solutions.*

Compound	λ_{max}^{ABS} (nm)	ε (M^{-1} cm^{-1})	λ_{max}^{EM} (nm)	SS (cm^{-1})[a]	HOMO-LUMO (eV)[b]
BTXI	477	20000	541	2480	2.51
	458	22000	510		
BTXI-CN	472	12000	546	2871	2.52
	450	12000	516		
11-NC-BTXI-CN	481	7000	528	1851	2.53
	463	7000	496		
10-NC-BTXI-CN	467	8500	530	2545	2.56
	448	9500	500		

[a] Stokes shift.
[b] Determined by the intercept of absorption and emission spectra.

5 Functionalization of BTXI-CN

Owing to an optimized synthetic procedure generating comfortable amount of the cyanated rylene-imide, the latter can further be functionalized to fully exploit the potential of the nitrile group (Scheme 16). Hence, **BTXI-CN** was firstly engaged in a bromination reaction, based on our recently published conditions,[208] thus, affording the halogenated **Br-BTXI-CN** in excellent 95% yield. It is noteworthy that this new compound opens new doors to unprecedented π-conjugated derivatives prepared either by palladium catalysed reactions[232–234] or copper mediated Ullmann couplings.[235,236]

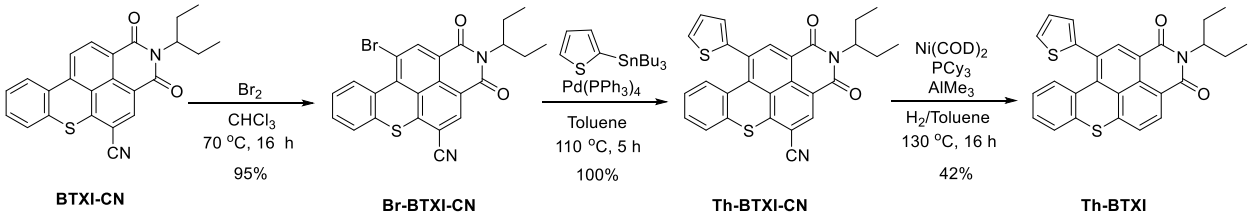

*Scheme 16. Functionalization path of **BTXI-CN**.*

As a result, **Th-BTXI-CN** was prepared in quantitative yield by Stille coupling reaction, avoiding the abovementioned isomerization (observed also in Suzuki or Buchwald coupling) and demonstrating the excellent reactivity of the brominated derivative. Beyond impacting the energetics, the cyano group can be also used as an orthogonal protecting group. Hence,

based on the nickel-catalysed hydrogenolysis reaction reported by Patra *et al.*,[237] the cyano group was thereafter removed to afford the first mono-functionalized BTXI derivative in position 11, namely the **Th-BTXI**.

Properties of the latter were naturally compared to those of its regioisomer **BTXI-Th** prepared from the **BTXI-Br** via a Stille cross-coupling reaction with a stannylthiophene (Figure 61).

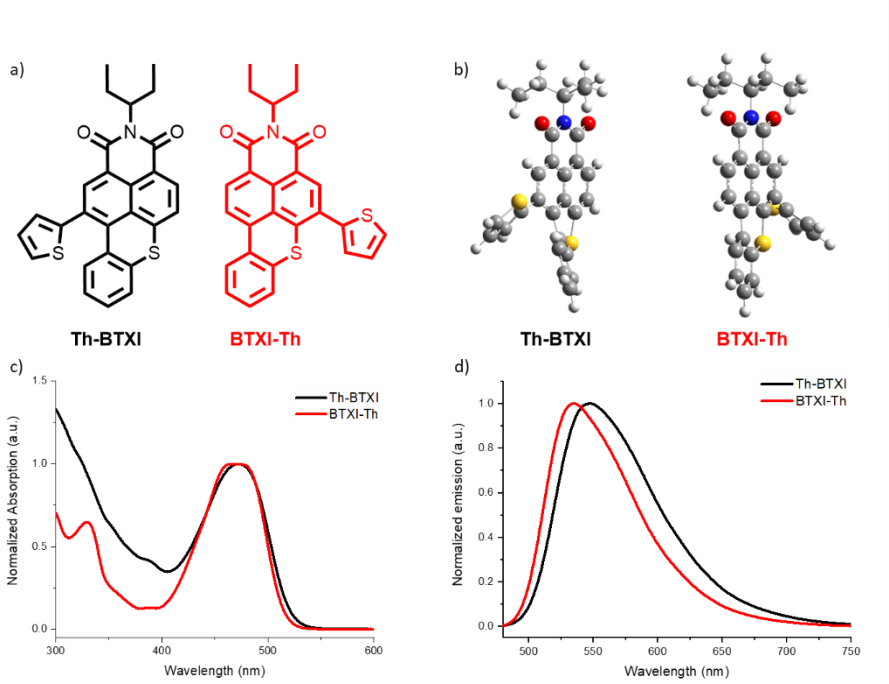

*Figure 61. Properties of **Th-BTXI** (black) and **BTXI-Th** (red): a) chemical structures, b) geometry optimization calculated at the ωB97xD/6-31G(d,p) level of theory, c) normalized absorption and d) normalized emission in CH_2Cl_2.*

Ground-state geometric structures were optimized at the density functional theory (DFT) level and revealed important differences between the two molecules. While the BTXI core adopts a twisted conformation with a dihedral angle *ca* 30° in **Th-BTXI**, the rylene block of the 5-substituted analogue turns out to be quasi-planar while the torsion angle with the thienyl unit is increased (49° for **Th-BTXI** vs 69° for **BTXI-Th**) and therefore, reducing the conjugation.

The impact of the geometry on the optoelectronic properties can be experimentally observed by UV-visible and fluorescence spectroscopy. While both derivatives show similar absorption patterns with a main transition centered at *ca* 470 nm, the characteristic band of **BTXI-Th** turns out to be slightly broaden, in agreement with the higher π-π interaction favoured by the planar isomer (Figure 61.c).[238,239] Nonetheless, the difference is way more

notable from the photoluminescence spectra since the stronger torsion in the polyaromatic core (**Th-BTXI**) led to a higher Stokes shift and consequently to a lower energy gap (E_{gap}) (Table 15). This feature was corroborated by the theoretical calculations where **Th-BTXI** shows a major contribution of the thiophene ring to both LUMO and HOMO levels in comparison with its isomer counterpart (Figure 64, Experimental Section).

*Table 15. Optical data of **Th-BTXI** and **BTXI-Th** recorded in dichloromethane solutions.*

Compound	λ_{max}^{ABS} (nm)	ε (M^{-1} cm^{-1})	λ_{max}^{EM} (nm)	E_{gap} (eV)
Th-BTXI	473	14000	548	2.42
BTXI-Th	464	17000	534	2.45

6 Conclusion and perspectives

In conclusion of this chapter, the cyanation of the **BTXI** block was explored through the use of $K_4[Fe(CN)_6]$, a non-toxic cyanide source, in lieu of the hazardous metal cyanide salts previously reported for rylene derivatives. After a methodological optimization, the scalability of the reaction at gram scale was demonstrated for further functionalization and also for potential large-scale manufacture. Intriguingly, exploration of the dicyanation reaction from the dibromo **BTXI** revealed the formation, in the reaction mixture, of the 5,11-dinitrile derivative and the unexpected 5,10-regioisomer. Isolated in decent yields (*ca* 30%), the latter seems to result from a pallado catalysed C-H activation of position 10, which mechanism was further experimentally and theoretically investigated. Thereafter, bromination and cross-coupling chemistry was performed over the **BTXI-CN** block as an early proof of concept to demonstrate its high versatility and compatibility with conventional cross-coupling reactions. Moreover, Ni-based decyanation was also carried out affording the first example of 11-mono functionalized benzothioxanthene derivative. Finally, the 11-thienyl and 5-thienyl regioisomers of BTXI were compared to study the relevance of the grafting position, both experimental and theoretical analysis highlighted the influence of the substitution on the geometry, optical and electrochemical properties. Hence, in this study different functionalized BTXI molecules were engaged in the cyanation conditions opening doors for new advanced materials with different electronic characteristics, therefore, possible applications in organic electronics can be envisioned.

Preliminary studies have been performed to evaluate the processability of the new materials, prior to investigating their photovoltaic performances (collaboration with Heliatek). Evaporation test under high *vacuum* (10^{-6} mbar) have been performed for **BTXI-CN** and **11-NC-BTXI-CN**, which could be synthesized in good quantity. Both compounds first present a desirably low sublimation temperature for deposition on transparent substrates, indeed, **BTXI-CN** shows a residue of 0% after thermal sublimation while evaporating at *ca* 175 °C (deposition rate of 0.2 Å/s). On the other hand, **11-NC-BTXI-CN** displays a lower evaporation temperature (*ca* 155 °C) with an acceptable 12% of residue (Figure 62). Eventually, the BTXI nature of the evaporated-thin-films UV-vis spectra (Figure 62), confirms the stability of the cyanated compounds after sublimation and the potential of BTXI derivatives towards an evaporable rylene family for *vacuum*-processing devices in the field of organic electronics.

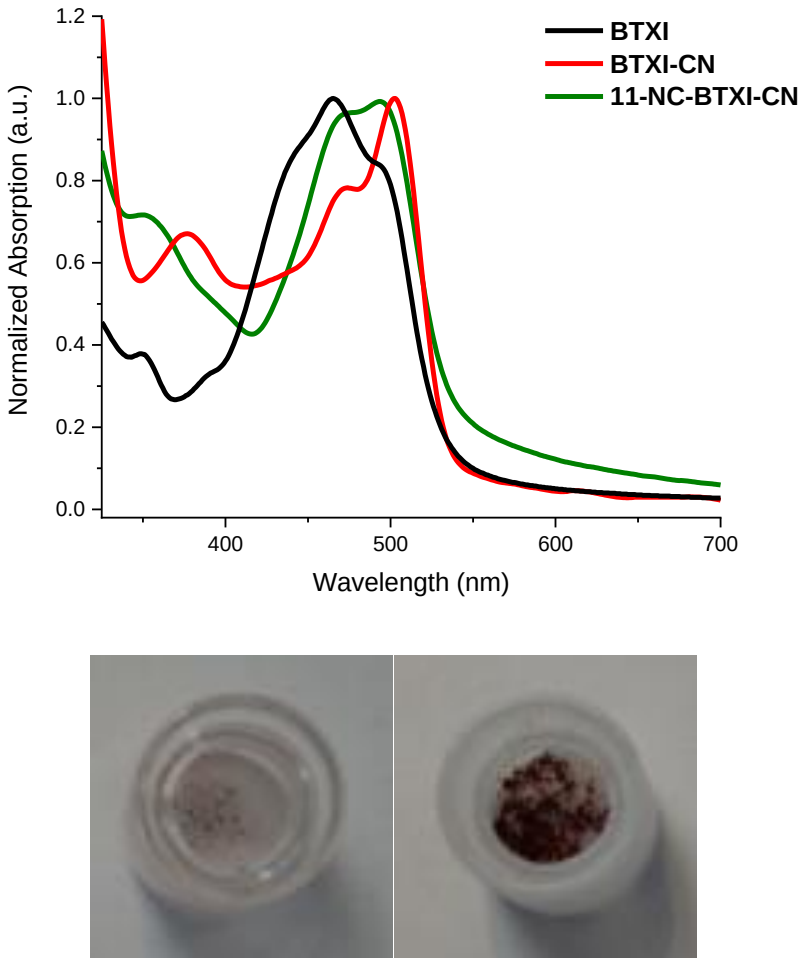

*Figure 62. Normalized UV-visible of **BTXI-CN** and **11-NC-BTXI-CN** evaporated thin films (30 nm) on quartz. Crucible images after total evaporation of the compounds **BTXI-CN** (left) and **11-NC-BTXI-CN** (right).*

References

(201) Mao, P.; Qian, X.; Zhang, H.; Yao, W. Benzothioxanthene Dyes as Fluorescent Label for DNA Hybridization: Synthesis and Application. *Dye. Pigment.* **2004**, *60* (1), 9–16.

(202) Zhang, W.; Chen, M.; Ling Wu, Y.; Tanaka, Y.; Juan Ji, Y.; Lin Zhang, S.; He Wei, C.; Xu, Y. Formation and Stabilization of the Telomeric Antiparallel G-Quadruplex and Inhibition of Telomerase by Novel Benzothioxanthene Derivatives with Anti-Tumor Activity. *Sci. Rep.* **2015**, *5*, 13693.

(203) Kollár, J.; Chmela, Š.; Hrdlovič, P. Spectral Properties of Bichromophoric Probes Based on Pyrene and Benzothioxanthene in Solution and in Polymer Matrices. *J. Photochem. Photobiol. A Chem.* **2013**, *270*, 28–36.

(204) Grayshan, P. H.; Kadhim, A. M.; Perters, A. T. Heterocyclic Derivalives of Naphthalene-1,8-dicar Boxylie Anhydride. Part III. Benzo[k,l] Thioxanthene-3,4-dicarboximides. *Journal of Heterocyclic Chemistry*. 1974, pp 33–38.

(205) Qian, X.; Mao, P.; Yao, W.; Guo, X. Synthesis and Properties of Benzothioxanthene Dicarboximide Hydroperoxide: An Efficient “time-Resolved” DNA Photocleaver with Long-Wavelength. *Tetrahedron Lett.* **2002**, *43* (16), 2995–2998.

(206) Josse, P.; Li, S.; Dayneko, S.; Joly, D.; Labrunie, A.; Dabos-Seignon, S.; Allain, M.; Siegler, B.; Demadrille, R.; Welch, G. C.; et al. Bromination of the Benzothioxanthene Bloc: Toward New π-Conjugated Systems for Organic Electronic Applications. *J. Mater. Chem. C* **2018**, *6* (4), 761–766.

(207) Payne, A. J.; Rice, N. A.; Mcafee, S. M.; Li, S.; Josse, P.; Cabanetos, C.; Risko, C.; Lessard, B. H.; Welch, G. C. Donor or Acceptor? How Selection of the Rylene Imide End Cap Impacts the Polarity of π-Conjugated Molecules for Organic Electronics. *ACS Appl. Energy Mater.* **2018**, *1* (9), 4906–4916.

(208) Dalinot, C.; Simón Marqués, P.; Andrés Castán, J. M.; Josse, P.; Allain, M.; Abad Galán, L.; Monnereau, C.; Maury, O.; Blanchard, P.; Cabanetos, C. Regioselective Monohalogenation and Homo/Hetero Dihalogenation of Benzothioxanthene Monoimide. *European J. Org. Chem.* **2020**, *2020* (14), 2140–2145.

(209) Andrés Castán, J. M.; Abad Galán, L.; Li, S.; Dalinot, C.; Simón Marqués, P.; Allain, M.; Risko, C.; Monnereau, C.; Maury, O.; Blanchard, P.; et al. Nitration of Benzothioxanthene: Towards a New Class of Dyes with Versatile Photophysical Properties. *New J. Chem.* **2020**, *44* (3), 900–905.

(210) Galán, L. A.; Andrés Castán, J. M.; Dalinot, C.; Marqués, P. S.; Blanchard, P.; Maury, O.; Cabanetos, C.; Le Bahers, T.; Monnereau, C. Theoretical and Experimental Investigation on the Intersystem Crossing Kinetics in Benzothioxanthene Imide Luminophores, and Their Dependence on Substituent Effects. *Phys. Chem. Chem. Phys.* **2020**, *22* (22), 12373–12381.

(211) Rossi, S. A.; Shimkin, K. W.; Xu, Q.; Mori-Quiroz, L. M.; Watson, D. A. Selective Formation of Secondary Amides via the Copper-Catalyzed Cross-Coupling of Alkylboronic Acids with Primary Amides. *Org. Lett.* **2013**, *15* (9), 2314–2317.

(212) Jayachitra, G.; Yasmeen, N.; Srinivasa Rao, K.; Ralte, S. L.; Srinivasan, R.; Singh, A. K. Borontrifluoride Etherate Promoted One-Pot Conversion of Nitriles to Esters. *Synth. Commun.* **2003**, *33* (19), 3461–3466.

(213) Barrault, J.; Pouilloux, Y. Synthesis of Fatty Amines. Selectivity Control in Presence of Multifunctional Catalysts. *Catal. Today* **1997**, *37* (2), 137–153.

(214) Pfaff, D.; Nemecek, G.; Podlech, J. A Lewis Acid-Promoted Pinner Reaction. *Beilstein J. Org. Chem.* **2013**, *9*, 1572–1577.

(215) Kesornpun, C.; Aree, T.; Mahidol, C.; Ruchirawat, S.; Kittakoop, P. Water-Assisted Nitrile Oxide Cycloadditions: Synthesis of Isoxazoles and Stereoselective Syntheses of Isoxazolines and 1,2,4-Oxadiazoles. *Angew. Chemie - Int. Ed.* **2016**, *55* (12), 3997–4001.

(216) Nakao, Y.; Yada, A.; Ebata, S.; Hiyama, T. A Dramatic Effect of Lewis-Acid Catalysts on Nickel-Catalyzed Carbocyanation of Alkynes. *J. Am. Chem. Soc.* **2007**, *129* (9), 2428–2429.

(217) Wang, Y.; Song, L. J.; Zhang, X.; Sun, J. Metal-Free [2+2+2] Cycloaddition of Ynamides and Nitriles: Mild and Regioselective Synthesis of Fully Substituted Pyridines. *Angew. Chemie - Int. Ed.* **2016**, *55* (33), 9704–9708.

(218) Chang, J.; Ye, Q.; Huang, K.-W.; Zhang, J.; Chen, Z.-K.; Wu, J.; Chi, C. Stepwise Cyanation of Naphthalene Diimide for N-Channel Field-Effect Transistors. *Org. Lett.* **2012**, *14* (12), 2964–2967.

(219) Jones, B. A.; Ahrens, M. J.; Yoon, M. H.; Facchetti, A.; Marks, T. J.; Wasielewski, M. R. High-Mobility Air-Stable n-Type Semiconductors with Processing Versatility: Dicyanoperylene-3,4:9,10-Bis(Dicarboximides). *Angew. Chemie - Int. Ed.* **2004**, *43* (46), 6363–6366.

(220) Ahrens, M. J.; Fuller, M. J.; Wasielewski, M. R. Cyanated Perylene-3,4-Dicarboximides and Perylene-3,4:9,10-Bis(Dicarboximide): Facile Chromophoric Oxidants for Organic Photonics and Electronics. *Chem.*

Mater. **2003**, *15* (14), 2684–2686.

(221) Kumar, Y.; Kumar, S.; Mandal, K.; Mukhopadhyay, P. Isolation of Tetracyano-Naphthalenediimide and Its Stable Planar Radical Anion. *Angew. Chemie - Int. Ed.* **2018**, *57* (50), 16318–16322.

(222) Tsuji, Y.; Taniguchi, M.; Yasuda, T.; Kawamura, T.; Obora, Y. Palladium-Catalyzed Cyanation of Propargylic Carbonates with Trimethylsilyl Cyanide. *Org. Lett.* **2000**, *2* (17), 2635–2637.

(223) Schareina, T.; Zapf, A.; Beller, M. Potassium Hexacyanoferrate(II)—a New Cyanating Agent for the Palladium-Catalyzed Cyanation of Aryl Halides. *Chem. Commun.* **2004**, *4* (12), 1388–1389.

(224) Wen, Q.; Jin, J.; Zhang, L.; Luo, Y.; Lu, P.; Wang, Y. Copper-Mediated Cyanation Reactions. *Tetrahedron Lett.* **2014**, *55* (7), 1271–1280.

(225) Weissman, S. A.; Zewge, D.; Chen, C. Ligand-Free Palladium-Catalyzed Cyanation of Aryl Halides. *J. Org. Chem.* **2005**, *70* (4), 1508–1510.

(226) Bouchard, J.; Wakim, S.; Leclerc, M. Synthesis of Diindolocarbazoles by Cadogan Reaction: Route to Ladder Oligo(p-Aniline)S. *J. Org. Chem.* **2004**, *69* (17), 5705–5711.

(227) Creencia, E. C.; Kosaka, M.; Muramatsu, T.; Kobayashi, M.; Iizuka, T.; Horaguchi, T. Microwave-Assisted Cadogan Reaction for the Synthesis of 2-Aryl-2 H -Indazoles, 2-Aryl-1 H -Benzimidazoles, 2-Carbonylindoles, Carbazole, and Phenazine. *J. Heterocycl. Chem.* **2009**, *46* (6), 1309–1317.

(228) Lu, C.; Markina, N. A.; Larock, R. C. Synthesis of N-Acylcarbazoles through Palladium-Catalyzed Aryne Annulation of 2-Haloacetanilides. *J. Org. Chem.* **2012**, *77* (24), 11153–11160.

(229) Tsang, W. C. P.; Zheng, N.; Buchwald, S. L. Combined C-H Functionalization/C-N Bond Formation Route to Carbazoles. *J. Am. Chem. Soc.* **2005**, *127* (42), 14560–14561.

(230) Tsang, W. C. P.; Munday, R. H.; Brasche, G.; Zheng, N.; Buchwald, S. L. Palladium-Catalyzed Method for the Synthesis of Carbazoles via Tandem C-H Functionalization and C-N Bond Formation. *J. Org. Chem.* **2008**, *73* (19), 7603–7610.

(231) Anand, M.; Nørskov, J. K. Scaling Relations in Homogeneous Catalysis: Analyzing the Buchwald–Hartwig Amination Reaction. *ACS Catal.* **2020**, *10* (1), 336–345.

(232) Huang, C.; Barlow, S.; Marder, S. R. Perylene-3,4,9,10-Tetracarboxylic Acid Diimides: Synthesis, Physical Properties, and Use in Organic Electronics. *J. Org. Chem.* **2011**, *76* (8), 2386–2407.

(233) Hendsbee, A. D.; Sun, J.-P.; Law, W. K.; Yan, H.; Hill, I. G.; Spasyuk, D. M.; Welch, G. C. Synthesis, Self-Assembly, and Solar Cell Performance of N-Annulated Perylene Diimide Non-Fullerene Acceptors. *Chem. Mater.* **2016**, *28* (19), 7098–7109.

(234) Yue, W.; Lv, A.; Gao, J.; Jiang, W.; Hao, L.; Li, C.; Li, Y.; Polander, L. E.; Barlow, S.; Hu, W.; et al. Hybrid Rylene Arrays via Combination of Stille Coupling and C-H Transformation as High-Performance Electron Transport Materials. *J. Am. Chem. Soc.* **2012**, *134* (13), 5770–5773.

(235) Shi, Y.; Qian, H.; Li, Y.; Yue, W.; Wang, Z. Copper-Mediated Domino Process for the Synthesis of Tetraiodinated Di(Perylene Bisimide). *Org. Lett.* **2008**, *10* (12), 2337–2340.

(236) Jiang, W.; Xiao, C.; Hao, L.; Wang, Z.; Ceymann, H.; Lambert, C.; Di Motta, S.; Negri, F. Localization/Delocalization of Charges in Bay-Linked Perylene Bisimides. *Chem. - A Eur. J.* **2012**, *18* (22), 6764–6775.

(237) Patra, T.; Agasti, S.; Modak, A.; Maiti, D. Nickel-Catalyzed Hydrogenolysis of Unactivated Carbon-Cyano Bonds. *Chem. Commun.* **2013**, *49* (75), 8362–8364.

(238) Shao, C.; Grüne, M.; Stolte, M.; Würthner, F. Perylene Bisimide Dimer Aggregates: Fundamental Insights into Self-Assembly by NMR and UV/Vis Spectroscopy. *Chem. - A Eur. J.* **2012**, *18* (43), 13665–13677.

(239) Schlosser, F.; Moos, M.; Lambert, C.; Würthner, F. Redox-Switchable Intramolecular π-π-Stacking of Perylene Bisimide Dyes in a Cyclophane. *Adv. Mater.* **2013**, *25* (3), 410–414.

(240) Holliday, S.; Ashraf, R. S.; Nielsen, C. B.; Kirkus, M.; Röhr, J. A.; Tan, C. H.; Collado-Fregoso, E.; Knall, A. C.; Durrant, J. R.; Nelson, J.; et al. A Rhodanine Flanked Nonfullerene Acceptor for Solution-Processed Organic Photovoltaics. *J. Am. Chem. Soc.* **2015**, *137* (2), 898–904.

Conclusion

Conclusion

Along these three years, efforts have been devoted to the preparation, characterization and use of a large number of pi-deficient organic semiconductors for organic photovoltaic applications. Following the philosophy of the SCL group, a special emphasis was placed on the simplification and optimization of the synthetic routes, thus ensuring a potential compatibility with large-scale manufacturing processes.

Hence, after a brief introductory chapter on OPVs, exploration of two families of non-fullerene acceptors (NFAs) has been investigated namely the perylene diimide (PDI) and the indenothiophene (IDT) based molecular systems. First, two 1,6- and 1,7-difunctionalized PDI regioisomers, resulting from the bis-bromination of the PDI, were isolated and compared to rationalize the impact of the isomerism on the device performances. In our case, the 1,6-derivative turned out to be more efficient while the 1,7-regioisomer is commonly used, concluding that an absolute rule cannot be claimed and highlighting the importance of considering and characterizing all possible regioisomers.

Thereafter, the second part of this chapter was conducted in collaboration with the German company Heliatek GmbH, since vacuum processable NFAs were targeted. Based on a simple strategy consisting in cutting the commercially available, but not compatible with such technology, ITIC in half, a series of indenothiophene-based push-pull semiconductors were successfully prepared and embedded in devices. Unfortunately, power conversion efficiencies recorded with these systems were not promising enough to commit more efforts in their optimization. Consequently, the synthetic strategy was quickly adapted to the preparation of symmetrical low molecular weight NFAs characterized by large quadrupole moments. Interestingly, efficiencies were significantly improved, exceeding the standard results of the company opening doors to further device and material optimizations.

Last but not least, a more exploratory chapter was carried out on an unnoticed dye, namely the N-(alkyl)benzothioxanthene-3,4-dicarboximide. To tune the energetics of this ambipolar material and limiting its molecular weight, the aromatic core was selectively decorated with nitrile groups. An alternative strategy to the common toxic reaction was optimized through the use of an inexpensive food additive, namely the potassium hexacyanoferrate(II) ($K_4[Fe(CN)_6]$). Optimized conditions were then successfully applied to the dibrominated starting material resulting in the separation of two regioisomers. Theoretical and experimental investigations converge toward a possible formation of a five-membered palladacycle favoured by the bay-region of the rylene. Eventually, the thermal and photo

physical characterization of these new molecules confirmed the stabilization of their energy levels and potential compatibility with *vacuum*-processing technologies.

Experimental Section

1 General methods

All reagents and chemicals from commercial sources were used without further purification unless specified. 7-Bromo-2,1,3-benzothiadiazole-4-carboxaldehyde (**8**) was prepared according to literature.[240] Tetrakis(triphenylphosphine) palladium (0) ($Pd(PPh_3)_4$) was prepared from $PdCl_2$ following the previously reported procedure.[241] $Pd_2(dba)_3$ was repurified from commercial available sources as described by Ananikov *et al*.[242] *N*-bromosuccinimide (NBS) was recrystallized from water before use. $K_4[Fe(CN)_6]$, *t*-BuONa and KF inorganic salts were powdered and dried overnight in *vacuum* at 100 °C. Both **1,6-PDI** and **1,7-PDI** isomers were prepared according to a publication by Rybtchinski *et al*.[179] Solvents were dried and purified using standard techniques. Microwave assisted reactions were performed in the cavity of a Biotage Initiator+ system in sealed reactors. Flash chromatography was performed with analytical-grade solvents using ALDRICH silica gel (technical grade, pore size 60 Å, 230-400 mesh particle size). Flexible plates ALUGRAM Xtra SIL G UV254 from MACHEREY-NAGEL were used for TLC. Compounds were detected by UV irradiation (BIOBLOCK SCIENTIFIC). NMR spectra were recorded with a BRUKER AVANCE III 300 (^1H, 300 MHz and ^{13}C, 75MHz) or a BRUKER AVANCE DRX500 (^1H, 500 MHz; ^{13}C, 125 MHz). ^{13}C APT show CH_2 and quaternary as positive signals while CH and CH_3 as negative signals. Chemical shifts are given in ppm relative to TMS and coupling constants J in Hz. IR spectra were recorded on a BRUKER spectrometer VERTEX 70 and UV-vis spectra with a PERKIN ELMER 950 spectrometer. Matrix Assisted Laser Desorption/Ionization was performed on MALDI-TOF MS BIFLEX III BRUKER DALTONICS spectrometer. High resolution mass spectrometry (HRMS) was performed with a JEOL JMS-700 B/E or a JEOL Spiral-TOF JMS3000. AFM measurements were performed by using a TT-2 AFM (AFM Workshop, USA) in the tapping mode and WSxM software with a 0.01-0.025 Ohm/cm Sb (n) doped Si probe with a reflective back side aluminium coating. Recycling-preparative HPLC purification was performed on a LC-9160NEXT system from the Japan Analytical Industry Co., Ltd. (JAI) equipped with coupled UV-vis 4Ch NEXT and RI-700 II detectors at room temperature through a set of two JAIGEL-2H and 2.5H columns at an elution rate of 10 mL min^{-1}.

Cyclic voltammetry was performed using a BIOLOGIC SP-150 potentiostat with positive feedback compensation in 0.10 M Bu_4NPF_6/CH_2Cl_2 (HPLC grade). Experiments were carried out in a one-compartment cell equipped with a platinum working electrode (2 mm of diameter)

and a platinum wire counter electrode. A silver wire immersed in a 0.01 M solution of $AgNO_3$ in CH_3CN was used as pseudo-reference electrode and checked against the ferrocene/ferrocenium couple (Fc/Fc^+) before and after each experiment. The potentials were then expressed *vs* Fc/Fc^+.

Photoelectron spectroscopy in air (PESA) measurements were recorded using a Riken Keiki PESA spectrometer (Model AC-2); samples were spun-cast over ITO substrates and irradiated with a laser beam with power settings of *ca* 20 nW; the electron detector allows to measure the ionization potential operating in atmospheric air. X-ray single-crystal diffraction data were collected on an AGILENT SUPERNOVA diffractometer equipped with Atlas CCD detector and micro-focus Cu-K_α radiation. The structures were solved by direct methods and refined on F^2 by full matrix least-squares techniques using SHELX programs (G. M. SHELDRICK 2013-2016). All non-H atoms were refined anisotropically and multiscan empirical absorption was corrected using CRYSALISPRO program (CRYSALISPRO, AGILENT TECHNOLOGIES, 2015-2019). The H atoms were included in the calculation without refinement

2 Synthetic procedures

Methyl 2-(thiophen-2-yl)benzoate (2): Degassed toluene (30 mL) was added to a mixture of

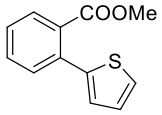

methyl-2-bromobenzoate **1** (5 g, 22.79 mmol) and tributyl(thiophen-2-yl)stannane (10.2 g, 27.34 mmol). $Pd(PPh_3)_4$ (526 mg, 0.46 mmol) was further added before refluxing the reaction mixture for 24 h. The latter was then cooled to room temperature and the solvent removed under *vacuum*. Purification of the crude was performed by column chromatography on silica gel (eluent: petroleum ether/dichloromethane, 1:3) affording 4.97 g of a colourless oil (quantitative). **^{1}H-NMR** (300 MHz, $CDCl_3$): δ 7.73 (dt, J = 7.6 Hz, 1.1 Hz, 1H), 7.51 – 7.47 (m, 2H), 7.40 (ddd, J = 8.8 Hz, 7.8 Hz, 4.2 Hz, 1H), 7.35 (dd, J = 4.9 Hz, 1.4 Hz, 1H), 7.09-7.02 (m, 2H), 3.78 (s, 3H).

4,4-di-*p*-tolyl-4*H*-indeno[1,2-*b*]thiophene (3): To a solution of 4-bromotoluene (9.4 g, 54.98

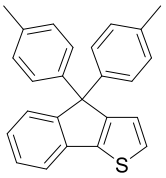

mmol) in distilled THF (40 mL) cooled to -78 °C was added dropwise *n*-BuLi (2.5 M in hexane, 22 mL, 54.98 mmol). After 1 h, a diluted solution of **2** (4.8 g, 22 mmol) in dry THF (40 mL) was slowly added at -78 °C. The mixture was then stirred for 16 h at room temperature before being poured in water (125 mL). The aqueous layer was extracted with dichloromethane (200 mL x 2), the organic phase was dried over

$MgSO_4$ and the solvent removed under reduced pressure. The resulting crude was thereafter suspended in a mixture of glacial acetic acid (125 mL) and H_2SO_4 (2 mL). After 3 h of reflux, the reaction was cooled to room temperature and the precipitated filtrated and washed with water, ethanol and petroleum ether. Once dried, 4.8 g of a white powder were recovered (62%). **^{1}H-NMR** (300 MHz, $CDCl_3$): δ 7.45 (d, J = 7.5 Hz, 1H), 7.35 (d, J = 7.6 Hz, 1H), 7.32-7.26 (m, 2H), 7.16 (dt, J = 7.5 Hz, 1.1 Hz, 1H), 7.10 (d, J = 8.1 Hz, 4H), 7.05 – 6.99 (m, 1H), 2.29 (s, 6H).

(4,4-di-*p*-tolyl-4*H*-indeno[1,2-*b*]thiophen-2-yl)trimethylstannane (4): 3 (2 g, 5.67 mmol) was

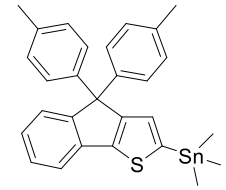

dissolved in distilled THF (20 mL) under argon, then *n*-BuLi (2.5 M in hexane, 2.2 mL, 7.94 mmol) was added dropwise at -78 °C and the reaction was stirred for 1 h 30 min. Trimethyl tin chloride (1 M in hexane, 8.5 mL, 8.51 mmol) was then added before warming the reaction mixture to room temperature. The overnight stirred solution was quenched with water and extracted with EtOAc. The organic layer was successively washed with a saturated aqueous solution of KF and water, dried over $MgSO_4$ and the solvent evaporated under *vacuum*. The resulting crude was used without further purification. **^{1}H-NMR** (300 MHz, $CDCl_3$): δ 7.43 (d, J = 7.4 Hz, 1H), 7.32 (d, J = 7.6 Hz, 1H), 7.26 (td, J = 7.6 Hz, J = 1.1 Hz, 1H), 7.17 – 7.07 (m, 5H), 7.08 – 6.99 (m, 5H), 2.29 (s, 6H), 0.36 (s, 9H). **^{13}C-NMR** (75 MHz, $CDCl_3$): δ 157.6, 153.9, 147.1, 142.2, 141.9, 137.3, 136.2, 130.4, 130.0, 127.9, 127.8, 127.3, 126.4, 125.4, 119.5, 62.3, 21.0. **MS** (MALDI-dit+) m/z: 516.0 [M+].

1,7-i

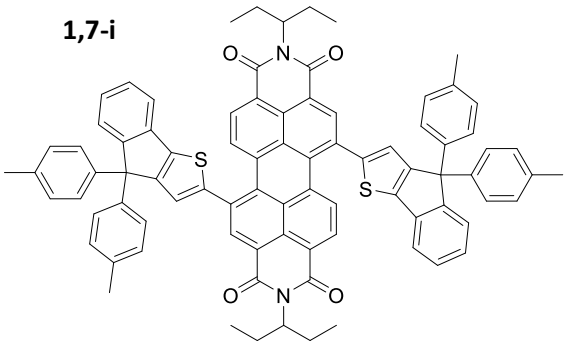

1,6-i

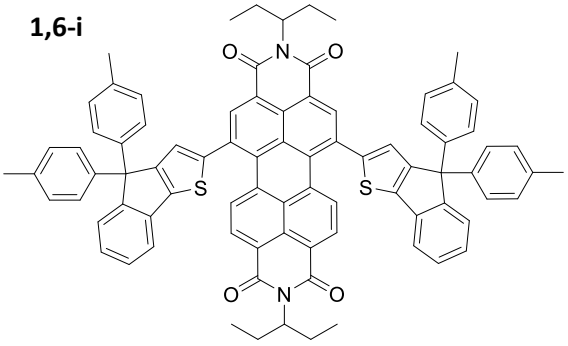

Synthesis of 1,6-i and 1,7-i: To a blend of halogenated perylene diimide (**1,7-** and **1,6-PDI**) (150 mg, 0.25 mmol) were added **4** (317 mg, 0.62 mmol), $Pd(PPh_3)_4$ (25 mg, 0.02 mmol) and 10 mL of dry toluene. The reaction mixture was then stirred and refluxed for 24 h under inert conditions. Once concentrated under *vacuum*, the crude was purified by column chromatography (eluent: dichloromethane/petroleum ether) affording **1,6-i** and **1,7-i** in 21% and 79% yield respectively.

1,6-i: **^{1}H-NMR** (300 MHz, $CDCl_3$): *δ* 8.64 (s, 2H), 8.38 (d, *J* = 8.1 Hz, 2H), 8.26 (d, *J* = 8.2 Hz, 2H), 7.53 (d, *J* = 7.6 Hz, 2H), 7.42 – 7.32 (m, 4H), 7.24 (td, *J* = 7.6, 1.2 Hz, 2H), 7.10 – 7.00 (m, 16H), 6.96 (s, 2H), 5.16-4.97 (m, 2H), 2.42 – 1.78 (m, 20H), 0.94 (t, *J* = 7.6 Hz, 12H). **^{13}C-NMR** (75 MHz, $CDCl_3$): *δ* 157.5, 153.5, 146.5, 143.5, 141.3, 136.9, 136.8, 134.9, 134.0, 129.6, 129.4, 129.2, 129.0, 128.9, 128.0, 127.9, 127.8, 126.6, 126.4, 123.1, 122.4, 120.0, 63.5, 57.9, 57.7, 25.2, 25.1 , 21.1, 11.6, 11.4. **IR** (neat): *v* = 3090-3015 cm^{-1} (C_{sp2}-H, Ar), 2965-2862 cm^{-1} (C_{sp3}-H), 1699 cm^{-1} (C=O), 1653 cm^{-1} (C=O), 1580-1458 cm^{-1} (C=C, Ar), 1336 cm^{-1} (C_{sp3}-N), 1321 cm^{-1} (C_{sp3}-N). **UV-Vis** (CH_2Cl_2): λ_{max} (ε) = 573 nm (16000 $L.mol^{-1}.cm^{-1}$), 456 nm (17000 $L.mol^{-1}.cm^{-1}$), 316 nm (41000 $L.mol^{-1}.cm^{-1}$). **MS** (MALDI-dctb+) m/z: 1230.6 [M+]. **HRMS** (FAB+): calculated for $C_{84}H_{66}N_2O_4S_2$ 1230.4458, found 1230.4446.

1,7-i: ^{1}H-NMR (300 MHz, $CDCl_3$): *δ* 8.67 (s, 2H), 8.38 (d, *J* = 8.2 Hz, 2H), 8.22 (d, *J* = 8.2 Hz, 2H), 7.53 (d, *J* = 7.3 Hz, 2H), 7.42 – 7.32 (m, 4H), 7.25 (td, *J* = 7.5, 1.1 Hz, 2H), 7.17 (s, 2H), 7.08 (d, *J* = 8.5 Hz, 8H), 7.03 (d, *J* = 8.2 Hz, 8H), 5.11 – 5.00 (m, 2H), 2.35 – 2.18 (m, 16H), 2.00 – 1.84 (m, 4H), 0.91 (t, *J* = 7.5 Hz, 12H). **^{13}C-NMR** (75 MHz, $CDCl_3$): *δ* 157.7, 153.5, 146.3, 143.8, 141.3, 136.8, 136.8, 135.0, 133.8, 129.8, 129.5, 129.2, 128.4, 127.9, 127.8, 126.7, 126.5,123.8, 120.1, 63.5, 57.8, 25.2, 21.1, 11.5. **IR** (neat): *v* = 3056-3018 cm^{-1} (C_{sp2}-H, Ar), 2962-2876 cm^{-1} (C_{sp3}-H), 1696 cm^{-1} (C=O), 1654 cm^{-1} (C=O), 1594-1506 cm^{-1} (C=C, Ar), 1324 cm^{-1} (C_{sp3}-N). **UV-Vis** (CH_2Cl_2): λ_{max} (ε) = 630 nm (14000 $L.mol^{-1}.cm^{-1}$), 465 nm (17000 $L.mol^{-1}.cm^{-1}$), 336 nm (41000 $L.mol^{-1}.cm^{-1}$). **MS** (MALDI-dctb+) m/z: 1230.6 [M+]. **HRMS** (FAB+): calculated for $C_{84}H_{66}N_2O_4S_2$ 1230.4458, found 1230.4434.

General procedure for Stille coupling

A mixture of **4** (1.2 eq.) and the corresponding bromo-carbaldehyde (1.0 eq.) in toluene (10 mL) was bubbled with argon for 30 min, thereafter $Pd(PPh_3)_4$ (0.025 eq.) was added and the reaction was stirred refluxing for 24 h. After removing the solvent, the crude was purified by column chromatography (eluent: dichloromethane) to afford the final compound.

5-(4,4-di-*p*-tolyl-4*H*-indeno[1,2-*b*]thiophen-2-yl)thiophene-2-carbaldehyde (11): Following

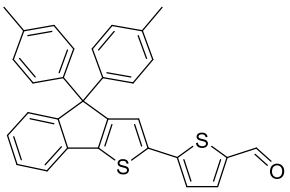

the general procedure, 687 mg of the final compound were achieved obtained as a yellow solid (67%). **^{1}H-NMR** (300 MHz, $CDCl_3$): *δ* 9.80 (s, 1H), 7.60 (d, *J* = 4.0 Hz, 1H), 7.45 (d, *J* = 7.4 Hz, 1H), 7.35 (d, *J* = 7.5 Hz, 1H), 7.29 (td, *J* = 7.6 Hz, 1.3 Hz, 1H), 7.23 – 7.17 (m, 3H), 7.11 (d, *J* = 8.4 Hz, 4H), 7.04 (d, *J* = 8.4

Hz, 4H), 2.28 (s, 1H). **^{13}C-NMR** (75 MHz, $CDCl_3$): δ 182.4, 156.7, 153.6, 147.9, 142.9, 141.3, 141.2, 138.8, 137.4, 136.7, 136.4, 129.2, 127.8, 126.7, 126.3, 123.7, 121.9, 119.9, 63.3, 21.1. **IR** (neat): ν =3082-3018 cm^{-1} (C_{sp2}-H, Ar), 2916-2730 cm^{-1} (C_{sp3}-H), 1652 cm^{-1} (C=O), 1503-1433 cm^{-1} (C=C, Ar). **MS** (MALDI-dctb+) m/z: 462.0 [M+]. **HRMS** (FAB+): calculated for $C_{30}H_{22}OS_2$ 462.1107, found 462.1111.

2-(4,4-di-*p*-tolyl-4*H*-indeno[1,2-*b*]thiophen-2-yl)thiazole-5-carbaldehyde (12): Following the general procedure, 320 mg of the final compound were obtained as a yellow solid (82%). **^{1}H-NMR** (300 MHz, $CDCl_3$): δ 9.98 (s, 1H), 8.30 (s, 1H), 7.59 – 7.53 (m, 2H), 7.41 – 7.27 (m, 3H), 7.13 (d, J = 8.3 Hz, 4H), 7.05 (d, J = 8.3 Hz, 4H), 2.31 (s, 6H). **^{13}C-NMR** (75 MHz, $CDCl_3$): δ 181.7, 169.3, 156.9, 154.2, 152.4, 147.0, 141.1, 138.7, 137.92, 137.0, 136.08, 129.4, 128.0, 127.8, 127.6, 126.6, 125.1, 120.7, 63.4, 21.1. **IR** (neat): ν = 3061-3005 cm^{-1} (C_{sp2}-H, Ar), 2919-2823 cm^{-1} (C_{sp3}-H), 1661 cm^{-1} (C=O), 1530-1462 cm^{-1} (C=C, Ar), 1328 cm^{-1} (C_{sp2}-N). **MS** (MALDI-) m/z: 464.1 [MH+]. **HRMS** (FAB+): calculated for $C_{29}H_{21}NOS_2$ 463.1059, found 463.1061.

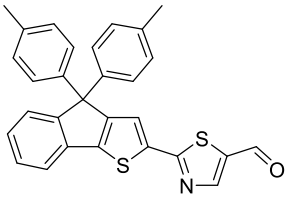

5'-(4,4-di-*p*-tolyl-4*H*-indeno[1,2-*b*]thiophen-2-yl)-[2,2'-bithiophene]-5-carbaldehyde (13): Following the general procedure, 150 mg of the final compound were obtained as an orange solid (75%). **^{1}H-NMR** (300 MHz, $CDCl_3$): δ 9.85 (s, 1H), 7.66 (d, J = 4.0 Hz, 1H), 7.44 (d, J = 7.5 Hz, 1H), 7.35 (d, J = 7.5 Hz, 1H), 7.30 (td, J = 7.5, 1.2 Hz, 1H), 7.23 – 7.16 (m, 2H), 7.13 (d, J = 8.2 Hz, 4H), 7.06 (d, J = 8.2 Hz, 4H), 2.30 (s, 6H). **^{13}C-NMR** (75 MHz, $CDCl_3$): δ 182.5, 156.7, 153.5, 146.9, 141.7, 141.5, 141.1, 140.0, 139.4, 137.5, 136.9, 136.7, 134.3, 129.3, 127.9, 127.8, 127.0, 126.3, 124.3, 124.1, 120.4, 119.6, 63.4, 21.1. **IR** (neat): ν = 3094-3022 cm^{-1} (C_{sp2}-H, Ar), 2975-2864 cm^{-1} (C_{sp3}-H), 1657 cm^{-1} (C=O), 1507-1438 cm^{-1} (C=C, Ar). **MS** (MALDI-) m/z: 544.0 [M+]. **HRMS** (FAB+): calculated for $C_{34}H_{24}OS_3$ 544.098, 544.0989 found.

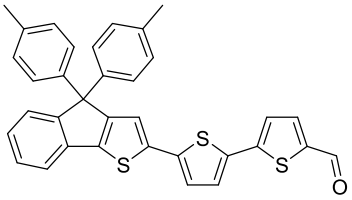

7-(4,4-di-*p*-tolyl-4*H*-indeno[1,2-*b*]thiophen-2-yl)benzo[*c*][1,2,5]thiadiazole-4-carbaldehyde (14): Following the general procedure, 329 mg of the final compound were obtained as an orange solid (86%). **^{1}H-NMR** (300 MHz, $CDCl_3$): δ 10.69 (s, 1H), 8.27 (s, 1H), 8.19 (d, J = 7.6 Hz, 1H), 7.98 (d, J = 7.5 Hz, 1H), 7.57 (d, J = 7.0 Hz, 1H), 7.39 (d, J = 7.5 Hz, 1H), 7.35 (td, J = 7.5, 1.2 Hz, 1H), 7.26 (td, J = 7.5, 1.2 Hz, 1H), 7.18 (d, J = 8.3 Hz, 4H), 7.06 (d, J = 8.0 Hz, 4H), 1.54

(s, 6H). **^{13}C-NMR** (75 MHz, $CDCl_3$): δ 188.5, 157.0, 154.0, 153.8, 152.1, 146.0, 141.5, 141.4, 136.7, 136.5, 133.7, 132.8, 129.2, 127.8, 127.1, 126.4, 126.0, 125.2, 123.1, 120.3, 63.3, 21.0. **IR** (neat): ν = 3026 cm^{-1} (C_{sp2}-H, Ar), 2921 cm^{-1} (C_{sp3}-H), 1677 cm^{-1} (C=O), 1532-1477 cm^{-1} (C=C, Ar). **MS** (MALDI-) m/z: 514.0 [M+]. **HRMS** (EI+): calculated for $C_{32}H_{22}N_2OS_2$ 514.1168, found 514.1174.

General procedure for dicyanovinylindanone Knoevenagel condensation

To a suspension of aldehyde (1 eq.) and 2-(3-oxo-2,3-dihydro-1H-inden-1-ylidene)malononitrile (5 eq.) in chloroform (25-50 mL), 0.3 mL of pyridine were added before refluxing the reaction overnight. Thereafter, the solvent was evaporated in *vacuum* and the crude purified by column chromatography (eluent: dichloromethane). The resulting solid was triturated in petroleum ether, filtrated, washed with petroleum ether and distilled pentane.

(Z)-2-(2-((5-(4,4-di-*p*-tolyl-4*H*-indeno[1,2-*b*]thiophen-2-yl)thiophen-2-yl)methylene)-3-oxo-2,3-dihydro-1*H*-inden-1-ylidene)malononitrile (*h*-IDTI-Th): Following the general procedure,

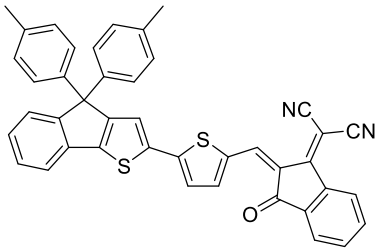

130 mg of the final compound were obtained as an green solid (86%). **^{1}H-NMR** (300 MHz, $CDCl_3$): δ 8.84 (s, 1H), 8.72 – 8.65 (m, 1H), 7.96 – 7.88 (m, 1H), 7.80 – 7.70 (m, 3H), 7.49 (d, J = 7.3 Hz, 1H), 7.47 (s, 1H), 7.40 (d, J = 7.3 Hz, 1H), 7.37 – 7.29 (m, 2H), 7.25 (d, J = 1.3 Hz, 1H), 7.12 (d, J = 8.2 Hz, 4H), 7.07 (d, J = 8.2 Hz, 4H), 2.31 (s, 6H). **^{13}C-NMR** (75 MHz, $CDCl_3$): δ 188.5, 160.2, 157.4, 154.5, 153.9, 146.5, 144.9, 141.1, 139.9, 137.6, 136.8, 136.2, 135.6, 135.2, 134.5, 129.3, 127.9, 127.8, 127.2, 126.4, 125.3, 124.4, 123.7, 123.2, 121.7, 120.2, 114.6, 114.5, 69.3, 63.3, 21.1. **IR** (neat): ν = 3070-3014 cm^{-1} (C_{sp2}-H, Ar), 2953-2849 cm^{-1} (C_{sp3}-H), 2213 (C≡N), 1697 cm^{-1} (C=O), 1587-1508 cm^{-1} (C=C, Ar). **UV-Vis** (CH_2Cl_2): λ_{max} (ε) = 595 nm (47000 L.mol^{-1}.cm^{-1}), 309 nm (22000 L.mol^{-1}.cm^{-1}). **MS** (MALDI-dctb+) m/z: 638.0 [M+]. **HRMS** (EI): calculated for $C_{42}H_{26}N_2OS_2$ 638.1481, found 638.1476.

(Z)-2-(2-((2-(4,4-di-*p*-tolyl-4*H*-indeno[1,2-*b*]thiophen-2-yl)thiazol-5-yl)methylene)-3-oxo-2,3-dihydro-1*H*-inden-1-ylidene)malononitrile (*h*-IDTI-Tz):

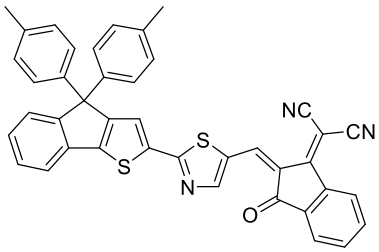

Following the general procedure, 280 mg of the final compound were obtained as an green solid (80%). **^{1}H-NMR** (300 MHz, $CDCl_3$): δ 8.88 (s, 1H), 8.73 (d, J = 6.9 Hz, 1H), 8.34

(s, 1H), 7.97 – 7.92 (m, 1H), 7.86 – 7.75 (m, 2H), 7.74 (s, 1H), 7.57 (d, *J* = 6.9 Hz, 1H), 7.42 (d, *J* = 7.5 Hz, 1H), 7.36 (td, *J* = 7.5, 1.3 Hz, 2H), 7.30 (dd, *J* = 7.4, 1.3 Hz, 1H), 7.13 (d, *J* = 8.5 Hz, 4H), 7.07 (d, *J* = 8.2 Hz, 4H), 2.31 (s, 6H). **^{13}C-NMR** (75 MHz, $CDCl_3$): 173.09, 160.38, 159.57, 157.35, 154.22, 140.92, 140.08, 139.01, 136.84, 136.74, 136.11, 135.96, 135.69, 135.09, 134.83, 131.33, 129.26, 127.96, 127.79, 127.68, 126.45, 126.06, 125.65, 125.53, 124.75, 124.07, 123.32, 122.58, 120.74, 114.13, 112.12, 63.24, 21.02. **IR** (neat): *v* = 3066-3017 cm^{-1} (C_{sp2}-H, Ar), 2948-2864 cm^{-1} (C_{sp3}-H), 2223 (C≡N), 1705 cm^{-1} (C=O), 1589-1517 cm^{-1} (C=C, Ar). **UV-Vis** (CH_2Cl_2): λ_{max} (ε) = 563 nm (34000 $L.mol^{-1}.cm^{-1}$), 317 nm (22000 $L.mol^{-1}.cm^{-1}$). **MS** (MALDI-dit+) m/z: 640.1 [M+H]. **HRMS** (EI): calculated for $C_{41}H_{25}N_3OS_2$ 639.1434, found 639.1433.

(Z)-2-(2-((5'-(4,4-di-*p*-tolyl-4*H*-indeno[1,2-*b*]thiophen-2-yl)-[2,2'-bithiophen]-5-yl)methylene)-3-oxo-2,3-dihydro-1*H*-inden-1-ylidene)malononitrile (*h*-IDTI-Th-Th):

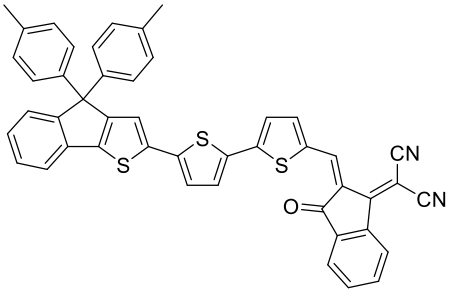

Following the general procedure, 178 mg of the final compound were obtained as a blue solid (100%). **^{1}H-NMR** (300 MHz, $CDCl_3$): *δ* 8.83 (s, 1H), 8.68 (d, *J* = 6.7 Hz, 1H), 7.92 (d, *J* = 8.2 Hz, 1H), 7.79 – 7.70 (m, 3H), 7.49 – 7.40 (m, 2H), 7.38 – 7.28 (m, 2H), 7.24 – 7.03 (m, 12H). **^{13}C-NMR** (75 MHz, $CDCl_3$): not recorded due to solubility issues. **IR** (neat): *v* = 3095-3016 cm^{-1} (C_{sp2}-H), 2921 cm^{-1} (C_{sp3}-H), 2215 cm^{-1} (C≡N), 1695 cm^{-1} (C=O), 1584-1433 (C_{sp2}=C_{sp2}). **UV-Vis** (CH_2Cl_2): λ_{max} (ε) = 595 nm (47000 $L.mol^{-1}.cm^{-1}$). **MS** (MALDI-dit+) m/z: 720.0 [M+]. **HRMS** (EI): calculated for $C_{46}H_{28}N_2OS_3$ 720.1358, found 720.1359.

General procedure for rhodanine Knoevenagel condensation

To a suspension of aldehyde (1 eq.) and 3-ethylrhodanine (5 eq.) in *t*-BuOH (25 mL), two drops of piperidine were added before refluxing the reaction overnight. Once the starting material was totally consumed, the solvent was removed under reduced pressure.

(Z)-5-((5-(4,4-di-*p*-tolyl-4*H*-indeno[1,2-*b*]thiophen-2-yl)thiophen-2-yl)methylene)-3-ethyl-2-thioxothiazolidin-4-one (*h*-IDTI-Rh): Following the general procedure, the crude was triturated in MeOH and filtrated. Then, the resulting solid was solubilized in chloroform and injected in a recycling preparative HPLC. Finally, 70 mg of the pure red compounds were isolated after recrystallization in dichloromethane (65%). **^{1}H-NMR** (300

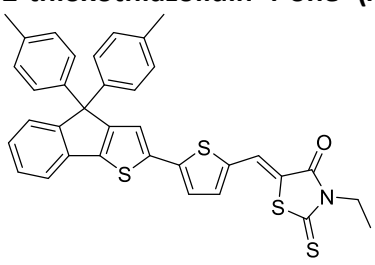

MHz, $CDCl_3$): δ 7.81 (s, 1H), 7.46 (d, *J* = 7.1 Hz, 1H), 7.36 (d, *J* = 7.5 Hz, 1H), 7.34-7.29 (m, 2H), 7.25 – 7.18 (m, 3H),7.13 (d, *J* = 8.2 Hz, 4H), 7.07 (d, *J* = 8.2 Hz, 4H), 4.19 (q, *J* = 7.1 Hz, 2H), 2.31 (s, 6H), 1.29 (t, *J* = 7.1 Hz, 3H). **^{13}C-NMR** (75 MHz, $CDCl_3$): δ 192.0, 167.4, 157.0, 153.7, 149.5, 146.4, 143.7, 142.5, 141.3, 138.0, 136.8, 136.6, 136.3, 135.4, 129.3, 129.3, 127.9, 126.7, 126.4, 125.1, 124.6, 121.3, 120.5, 119.9, 65.9, 63.4, 21.1, 12.4. **IR** (neat): *v* = 3093-3017 cm^{-1} (C_{sp2}-H, Ar), 2985-2847 cm^{-1} (C_{sp3}-H), 1695 cm^{-1} (C=O), 1576 cm^{-1} (C=C, Ar), 1225 cm^{-1} (C=S). **UV-Vis** (CH_2Cl_2): λ_{max} (ε) = 502 nm (39000 $L.mol^{-1}.cm^{-1}$), 358 nm (16000 $L.mol^{-1}.cm^{-1}$). **MS** (MALDI-dctb+) m/z: 605.0 [M+]. **HRMS** (EI+): calculated for $C_{35}H_{27}NOS_4$ 605.0970, found 605.0972.

(Z)-5-((7-(4,4-di-p-tolyl-4*H*-indeno[1,2-*b*]thiophen-2-yl)benzo[*c*][1,2,5]thiadiazol-4-yl)methylene)-3-ethyl-2-thioxothiazolidin-4-one (*h*-IDTBR): Following the general procedure,

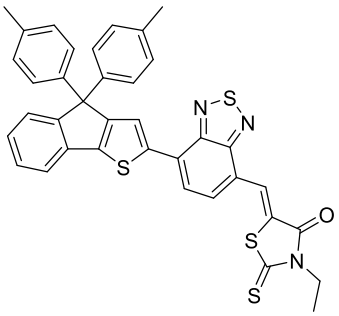

the crude was purified by column chromatography (eluent: petroleum ether/dichloromethane 3:7). The violet product was triturated in petroleum ether, filtrated and washed with MeOH and distilled pentane, affording 109 mg of a dark powder (86%). **^{1}H-NMR** (300 MHz, $CDCl_3$): δ 8.46 (s, 1H), 8.18 (s, 1H), 7.87 (d, *J* = 7.7 Hz, 1H), 7.62 (d, *J* = 7.8 Hz, 1H), 7.55 (d, *J* = 7.5 Hz, 1H), 7.40 (d, *J* = 7.5 Hz, 1H), 7.34 (td, *J* = 7.5, 1.2 Hz, 1H), 7.22 (td, *J* = 7.5, 1.2 Hz, 1H), 7.19 (d, *J* = 8.3 Hz, 4H), 7.08 (d, *J* = 8.0 Hz, 4H), 4.23 (q, *J* = 7.1 Hz, 2H), 2.31 (s, 6H), 1.32 (t, *J* = 7.1 Hz, 3H). **^{13}C-NMR** (75 MHz, $CDCl_3$): δ 193.1, 167.6, 157.0, 154.5, 154.0, 151.7, 145.2, 141.9, 141.6, 136.8, 137.7, 131.3, 130.2, 129.3, 127.9, 127.9, 127.2, 127.0, 126.5, 125.2, 124.9, 124.7, 124.2, 120.3, 63.4, 40.1, 21.1, 12.5. **IR** (neat): *v* = 3058-3021 cm^{-1} (C_{sp2}-H, Ar), 2921-2852 cm^{-1} (C_{sp3}-H), 1705 cm^{-1} (C=O), 1587-1434 cm^{-1} (C=C, Ar), 1234 cm^{-1} (C=S). **UV-Vis** (CH_2Cl_2): λ_{max} (ε) = 535 nm (33000 $L.mol^{-1}.cm^{-1}$), 390 nm (16000 $L.mol^{-1}.cm^{-1}$). **MS** (MALDI-dctb+) m/z: 657.1 [M+]. **HRMS** (EI+): calculated for $C_{37}H_{27}N_3OS_4$ 657.1031, found 657.1040.

Methyl 2-(thieno[3,2-*b*]thiophen-2-yl)benzoate (16): Anhydrous toluene (20 mL) was added

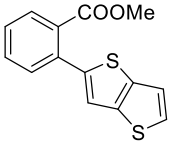

to a mixture of methyl-2-bromobenzoate **1** (2.2 g, 10.03 mmol) and tributyl(thieno[3,2-b]thiophen-2-yl)stannane (6.6 g, 15.35 mmol). $Pd(PPh_3)_4$ (236 mg, 0.20 mmol) was further added before refluxing the reaction mixture for 16 h. The latter was then cooled to room temperature and the solvent removed under *vacuum*. Purification of the crude was performed by column chromatography on silica gel (eluent: petroleum ether/dichloromethane, 3:2) affording 2.8 g of a yellow oil (quantitative).

^{1}H-NMR (300 MHz, $CDCl_3$): δ 7.75 (dt, *J* = 7.6, 0.8 Hz, 1H), 7.55 – 7.48 (m, 2H), 7.43 (ddd, *J* = 7.6, 5.8, 3.1 Hz, 1H), 7.37 (t, *J* = 5.2 Hz, 1H), 7.22 (d, *J* = 0.7 Hz, 1H), 3.75 (s, 3H). **^{13}C-NMR** (75 MHz, $CDCl_3$): δ 169.1, 144.0, 139.7, 139.4, 134.4, 131.8, 131.4, 131.2, 129.7, 128.2, 126.9, 119.6, 118.6, 52.5. **MS** (EI+) m/z: 274.0 [M+]. **HRMS** (EI+): calculated for $C_{14}H_{10}O_2S_2$ 274.0117, found 274.0121.

Bis(4-hexylphenyl)(2-(thieno[3,2-*b*]thiophen-2-yl)phenyl)methanol (17): To a solution of 1-bromo-4-hexylbenzene (4.3 g, 17.64 mmol) in distilled THF (10 mL) cooled to 78 °C, was added dropwise *n*-BuLi (2.5 M in hexane, 7.06 mL, 17.64 mmol). After 1 h, a diluted solution of **16** (2.2 g, 8.02 mmol) in dry THF (10 mL) was slowly added at -78 °C. The mixture was then stirred for 16 h at room temperature before being poured in water (75 mL). The aqueous layer was extracted with EtOAc (100 mL x 2), the organic phase was dry over $MgSO_4$ and the solvent removed under reduced pressure. The reaction mixture was purified by column chromatography (eluent: petroleum ether/dichloromethane 7:3), achieving 3.25 g of a colourless solid that was used without further purification (72%). **^{1}H-NMR** (300 MHz, $CDCl_3$): δ 7.39 – 7.19 (m, 4H), 7.16 (dd, *J* = 5.3, 0.7 Hz, 1H), 7.10 (s, 8H), 6.84 (dd, *J* = 7.9, 1.5 Hz, 1H), 6.22 (s, 1H), 3.44 (d, *J* = 0.7 Hz, 1H), 2.69 – 2.56 (m, 4H), 1.70 – 1.58 (m, 4H), 1.39 – 1.28 (m, *J* = 5.3, 4.4 Hz, 12H), 0.91 – 0.86 (m, 6H).

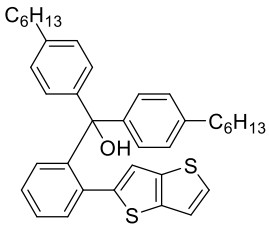

9,9-bis(4-hexylphenyl)-9*H*-indeno[1,2-*b*]thieno[2,3-*d*]thiophene (18): 17 (3.25 g, 5.73 mmol) was dissolved in dichloromethane (18 mL) under inert atmosphere and degassed for 30 min by Ar bubbling. Then, $Bi(OTf)_3$ (38 mg, 0.06 mmol) was added and the solution was stirred at 55 °C, following the reaction by ^{1}H-NMR. After 15 minutes, the solvent was removed in *vacuum* and the crude purified by column chromatography (eluent: petroleum ether/dichloromethane 9:1), giving 3.15 g of a colourless oil (100%).**^{1}H-NMR** (300 MHz, $CDCl_3$): δ 7.45 (t, *J* = 7.5 Hz, 2H), 7.30 (m, 3H), 7.19 (dt, *J* = 6.6 Hz, 1.0 Hz, 1H), 7.13 (d, *J* = 8.2 Hz, 4H), 7.04 (d, *J* = 8.2 Hz, 4H), 2.58 – 2.49 (m, 4H), 1.60 – 1.51 (m, 4H), 1.34 – 1.24 (m, 12H), 0.88-0.84 (m, 6H). **^{13}C-NMR** (75 MHz, $CDCl_3$): δ 153.4, 146.2, 143.1, 142.1, 141.8, 140.5, 138.1, 133.9, 128.5, 128.0, 127.7, 126.7, 126.1, 126.0, 120.5, 119.3, 63.3, 35.7, 31.8, 31.4, 29.3, 22.7, 14.2. **MS** (EI+) m/z: 548.0 [M+]. **HRMS** (EI+): calculated for $C_{37}H_{40}S_2$ 548.2566, found 548.2565.

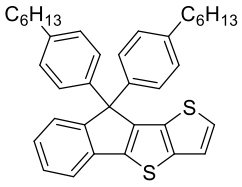

9,9-bis(4-hexylphenyl)-9*H*-indeno[1,2-*b*]thieno[2,3-*d*]thiophene-2-carbaldehyde (19): **18**

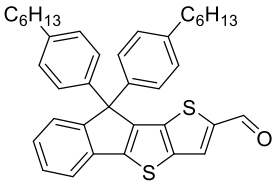

(600 mg, 1.09 mmol) was dissolved in distilled THF (10 mL) under argon, then *n*-BuLi (2.5 M in hexane, 0.52 mL, 1.31 mmol) was added dropwise at -78 °C and the reaction was stirred for 1.5 h, giving a dark blue solution. Anhydrous *N,N*-dimethylformamide (0.17 mL, 2.19 mmol) was then added before warming the reaction mixture to room temperature. The overnight-stirred yellow solution was quenched with water and extracted with dichloromethane, the organic phase dried over $MgSO_4$ and the solvent evaporated under *vacuum*. The resulting crude was purified by column chromatography (eluent: petroleum ether/dichloromethane 1:1), affording 500 mg of the yellow aldehyde (80%).**^{1}H-NMR** (300 MHz, $CDCl_3$): *δ* 9.89 (s, 1H), 7.94 (s, 1H), 7.54 (dd, *J* = 7.5, 1.3 Hz, 1H), 7.49 (dd, *J* = 7.5, 1.3 Hz, 1H), 7.36 (td, *J* = 7.5, 1.3 Hz, 1H), 7.29 (td, *J* = 7.5, 1.3 Hz, 1H), 7.10 (d, *J* = 8.5 Hz, 4H), 7.05 (d, *J* = 8.5 Hz, 4H), 2.57 – 2.49 (m, 4H), 1.60 – 1.51 (m, 4H), 1.33 – 1.23 (m, 12H), 0.89 – 0.84 (m, 6H). **^{13}C-NMR** (75 MHz, $CDCl_3$): *δ* 183.1, 154.3, 149.9, 146.1, 144.3, 142.2, 141.7, 140.5, 139.6, 137.0, 130.1, 128.7, 128.0, 127.9, 127.6, 126.4, 120.4, 63.4, 35.7, 31.8, 31.4, 29.2, 22.7, 14.2. **IR** (neat): *v* = 3039-3018 cm^{-1} (C_{sp2}-H), 2951-2850 cm^{-1} (C_{sp3}-H), 1658 cm^{-1} (C=O), 1493 (C_{sp2}=C_{sp2}). **MS** (EI+) m/z: 576.3 [M+]. **HRMS** (EI+): calculated for $C_{38}H_{40}OS_2$ 576.2515, found 576.2516.

(Z)-2-(2-((9,9-bis(4-hexylphenyl)-9*H*-indeno[1,2-*b*]thieno[2,3-*d*]thiophen-2-yl)methylene)-3-oxo-2,3-dihydro-1*H*-inden-1-ylidene)malononitrile (*h*-ITIC): Following the general procedure for dicyanovinylindanone Knoevenagel, 486 mg of the final compound were obtained as a green solid (83%). **^{1}H-NMR** (300 MHz, $CDCl_3$): *δ* 8.76 (s, 1H), 8.53 (dd, *J* = 6.7, 1.8 Hz, 1H), 7.91 (dd, *J* = 6.5, 2.3 Hz, 1H), 7.76 (s, 1H), 7.74 – 7.65 (m, 2H), 7.57 – 7.48 (m, 2H), 7.43 – 7.31 (m, 2H), 7.18 (d, *J* = 8.4 Hz, 4H), 7.12 (d, *J* = 8.4 Hz, 4H), 2.55 (t, *J* = 7.7 Hz, 4H), 1.60-1.54 (m, 4H), 1.32-1.24 (m, 12H), 0.90 – 0.76 (m, 6H). **^{13}C-NMR** (75 MHz, $CDCl_3$): 188.2, 160.2, 155.0, 153.7, 147.6, 146.6, 143.3, 142.4, 140.0, 139.5, 139.2, 138.7, 137.5, 136.9, 135.2, 134.6, 128.9, 128.5, 128.2, 128.0, 126.6, 125.3, 123.8, 122.3, 120.9, 114.8, 114.6. **IR** (neat): *v* = 3067 cm^{-1} (C_{sp2}-H, Ar), 2958-2855 cm^{-1} (C_{sp3}-H), 2220 cm^{-1} (C≡N), 1701 cm^{-1} (C=O), 1546-1391 cm^{-1} (C=C, Ar). **UV-Vis** (CH_2Cl_2): λ_{max} (ε) = 568 nm (52000 $L.mol^{-1}.cm^{-1}$), 305

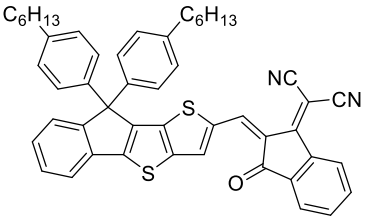

nm (20000 $L.mol^{-1}.cm^{-1}$). **MS** (MALDI-dit+) m/z: 752.3 [M+]. **HRMS** (EI+): calculated for $C_{50}H_{44}N_2OS_2$ 752.2890, found 752.2891.

4,9-dihydro-*s*-indaceno[1,2-*b*:5,6-*b'*]dithiophene (24): This compound was synthesized as previously reported.[198,199]

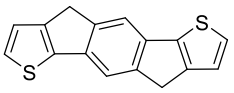

4,4,9,9-tetraethyl-4,9-dihydro-*s*-indaceno[1,2-*b*:5,6-*b'*]dithiophene (25): To a suspension of **24** (250 mg, 0.94 mmol) in anhydrous dimethylsulfoxide (10 mL), *t*-BuONa (541 mg, 5.63 mmol) was added under a positive argon pressure. The deep-blue suspension was heated to 80 °C for 1.5 h and then warmed to 25 °C before adding ethyl iodide (0.45 mL, 5.63 mmol) dropwise. Thereafter, the reaction was heated to 70 °C overnight, cooled to room temperature and then poured into water (100 mL). The crude was extracted with hexanes (3 x 50 mL), the organic layer dried over MgSO4 and the solvent evaporated under *vacuum*. The resulting crude was purified by column chromatography (eluent: petroleum ether) affording 273 mg of a pale withe solid (77%). **^{1}H-NMR** (300 MHz, $CDCl_3$): δ 7.29 – 7.26 (m, 4H), 6.96 (d, J = 4.8 Hz, 2H), 2.11 – 1.88 (m, 8H), 0.48 (t, J = 7.4 Hz, 12H). **^{13}C-NMR** (75 MHz, $CDCl_3$): 154.4, 152.6, 142.2, 136.2, 126.4, 121.7, 113.3, 54.9, 31.7, 9.0. **MS** (MALDI-dit+) m/z: 378.1 [M+H]. **HRMS** (EI+): calculated for $C_{24}H_{26}S_2$ 378.1470, found 378.1482.

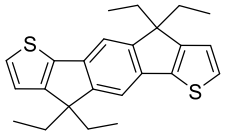

4,4,9,9-tetraethyl-4,9-dihydro-*s*-indaceno[1,2-*b*:5,6-*b'*]dithiophene-2,7-dicarbaldehyde (26): 25 (200 mg, 0.53 mmol) was dissolved in distilled THF (10 mL) under argon, then *n*-BuLi (1.6 M in hexane, 0.73 mL, 1.76 mmol) was added dropwise at -78 °C and the reaction was warmed to room temperature for 1 h 30 min. *N,N*-dimethylformamide (0.16 mL, 2.10 mmol) was then added at -78 °C before warming the reaction mixture to room temperature. The overnight-stirred solution was quenched with water and extracted twice with chloroform (50 mL), the organic phase dried over $MgSO_4$ and the solvent evaporated under *vacuum*. The crude was recrystallized from petroleum ether/dichloromethane (1:1), affording eventually 215 mg of the orange aldehyde after filtration (94%).**^{1}H-NMR** (300 MHz, $CDCl_3$): δ 9.92 (s, 2H), 7.65 (s, 2H), 7.47 (s, 2H), 2.08 (m, 8H), 0.51 (t, J = 7.3 Hz, 12H). **^{13}C-NMR** (75 MHz, $CDCl_3$): not recorded due to solubility issues. **MS** (EI+) m/z: 434.1 [M+]. **HRMS** (EI+): calculated for $C_{26}H_{26}O_2S_2$ 434.1369, found 434.1375.

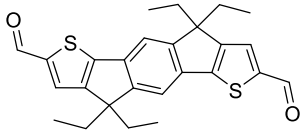

2,2'-((2Z,2'Z)-((4,4,9,9-tetraethyl-4,9-dihydro-*s*-indaceno[1,2-*b*:5,6-*b*']dithiophene-2,7-diyl)bis(methaneylylidene))bis(3-oxo-2,3-dihydro-1*H*-indene-2,1-diylidene))dimalononitrile (Et-IDIC): To a suspension of **26** (70 mg, 0.16 mmol) and 2-(3-oxo-2,3-dihydro-1H-inden-1-ylidene)malononitrile (188 mg, 0.97 mmol) in chloroform (25 mL), 0.3 mL of pyridine were added before refluxing the reaction overnight. Thereafter, the solvent was evaporated in *vacuum* and the crude triturated in MeOH and filtrated. The solid cake was washed with abundant quantity of chloroform affording the desired product as a highly-insoluble blue solid. Eventually 60 mg of the latter were obtained after evaporating the solvent (47%). **MS** (MALDI-dctb-) m/z: 786.3 [M+]. **HRMS** (MALDI-dctb-): calculated for $C_{50}H_{34}N_2O_2S_2$ 786.2117, found 786.2126.

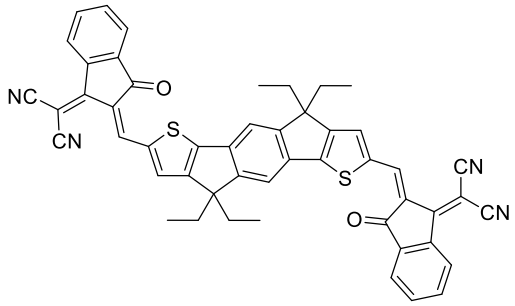

2,2'-((4,4,9,9-tetraethyl-4,9-dihydro-*s*-indaceno[1,2-*b*:5,6-*b*']dithiophene-2,7-diyl)bis(methaneylylidene))dimalononitrile (Et-IDIV): Over a solution of **26** (112 mg, 0.26 mmol) and malononitrile (43 mg, 0.64 mmol) in chloroform (30 mL), three drops of trimethylamine were added. The reaction was monitored by TLC until the total transformation to the final product, then the solvent was removed under *vacuum*. The crude was purified by column chromatography (eluent: dichloromethane), yielding 75 mg of a red powder (55%). **^{1}H-NMR** (300 MHz, $CDCl_3$): δ 7.83 (s, 2H), 7.61 (s, 2H), 7.52 (s, 2H), 2.05 (m, 8H), 0.51 (t, J = 7.3 Hz, 12H). **^{13}C-NMR** (75 MHz, $CDCl_3$): not recorded due to solubility issues. **MS** (MALDI-dctb+) m/z: 530.0 [M+]. **HRMS** (FAB+): calculated for $C_{32}H_{26}N_4S_2$ 530.1593, found 530.1584.

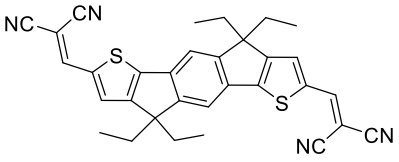

2,7-dibromo-4,4,9,9-tetraethyl-4,9-dihydro-*s*-indaceno[1,2-*b*:5,6-*b*']dithiophene (27): **25** (800 mg, 2.11 mmol) was solubilized in a THF/DMF mixture (2:1, 100 mL) and *N*-bromosuccinimide (827 mg, 4.65 mmol) was added to the solution. After stirring 3 h at room temperature, the crude was poured into water and the precipitate was filtrated and washed with water. Finally, 803 mg of the solid final compound was obtained (71%).**^{1}H-NMR** (300 MHz, $CDCl_3$): δ 7.19 (s, 2H), 6.98 (s, 2H), 1.95 (m, 8H), 0.47 (t, J = 7.3 Hz, 12H). **^{13}C-NMR** (75 MHz, $CDCl_3$): δ 153.4, 151.5, 142.4, 136.1, 124.9, 113.2, 112.7, 77.6, 77.2, 76.7, 55.9, 31.6, 8.9. **MS** (MALDI-dctb+) m/z: 534.0 [M+]. **HRMS** (MALDI-dctb+): calculated for $C_{24}H_{24}S_2Br_2$ 533.9680, found 533.9693.

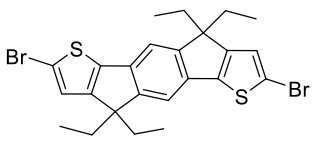

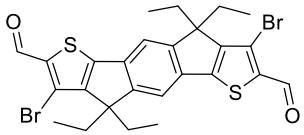

3,8-dibromo-4,4,9,9-tetraethyl-4,9-dihydro-*s*-indaceno[1,2-*b*:5,6-*b*']dithiophene-2,7-dicarbaldehyde (28): To a solution of **27** (1 g, 1.86 mmol) in distilled THF (50 mL), lithium diisopropylamide (2 M in THF, 3.73 mL, 7.46 mmol) was dropwise added at -50 °C and the reaction was stirred for 1 h. Thereafter, the flask was warmed at room temperature and stirred overnight before quenching the reaction with water. The crude was extracted with dichloromethane and the organic layer dried over $MgSO_4$ and the solvent removed under reduced pressure. The mixture of compounds was separated by column chromatography (eluent: petroleum ether/dichloromethane 9:1) and the halogen-dance product was dissolved in anhydrous *N,N*-dimethylformamide (5 mL) under inert atmosphere. The solution was heated for 16 h at 85 °C after addition of phosphoryl chloride (0.10 mL, 1.12 mmol). The reaction was quenched with a saturated aqueous solution of ammonium chloride, stirred for 30 minutes and extracted with dichloromethane. The organic layer was dried over $MgSO_4$, the solvent removed under *vacuum* and the crude purified by column chromatography (eluent: dichloromethane). 199 mg of an orange product were isolated over 3 steps (28%). **^{1}H-NMR** (300 MHz, $CDCl_3$): δ 10.06 (s, 2H), 7.49 (s, 2H), 2.49 (m, 4H), 2.13 (m, 4H), 0.41 (t, J = 7.4 Hz, 12H). **^{13}C-NMR** (75 MHz, $CDCl_3$): δ not recorded due to solubility issues. **MS** (MALDI-dctb+) m/z: 590.0 [M+]. **HRMS** (MALDI-dctb+): calculated for $C_{26}H_{24}O_2S_2Br_2$ 589.9579, found 589.9576.

2,2'-((3,8-dibromo-4,4,9,9-tetraethyl-4,9-dihydro-s-indaceno[1,2-b:5,6-b']dithiophene-2,7-diyl)bis(methaneylylidene))dimalononitrile (Et-IDIVBr): To a solution of **28** (125 mg, 0.20 mmol) and malononitrile (33 mg, 0.60 mmol) in chloroform (30 mL), three drops of trimethylamine were added. The reaction was monitored by TLC until the total transformation to the final product, then the solvent was removed under *vacuum*. The crude was purified by column chromatography (eluent: dichloromethane), yielding 131 mg of a red powder (94%). **^{1}H-NMR** (300 MHz, $CDCl_3$): δ 8.07 (s, 2H), 7.54 (s, 2H), 2.45 (m, 4H), 2.11 (m, 4H), 0.51 (t, J = 7.3 Hz, 12H). **^{13}C-NMR** (75 MHz, $CDCl_3$): not recorded due to solubility issues. **MS** (MALDI-dctb-) m/z: 686.0 [M+]. **HRMS** (MALDI-dctb-): calculated for $C_{32}H_{24}N_4S_2Br_2$ 685.9804, found 685.9817.

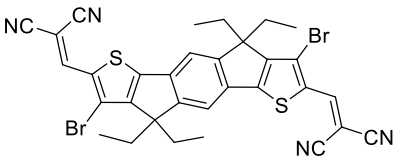

General procedure for $K_4[Fe(CN)_6]$ cyanation

To a microwave vial containing 5-bromo-2-(pentan-3- yl)-1*H*-thioxantheno[2,1,9-*def*]isoquinoline-1,3(2*H*)-dione (**BTXI-Br**) (50 mg, 110.54 µmol), $K_4[Fe(CN)_6]$ (10 mg, 27.63 µmol), sodium carbonate (12 mg, 110.53 µmol), palladium source (5.53 µmol) and the phosphine ligand (11.05 µmol) under argon atmosphere, *N,N*-dimethylacetamide (3 mL) was added. The mixture was irradiated in the microwave cavity with the pre-selected temperature (100 °C to 140 °C), monitoring the reaction by thin-layer chromatography (TLC). The reaction mixture was cooled to room temperature and the solvent removed in *vacuum*. *Purification protocol A:* The crude was purified by column chromatography silica gel using dichloromethane as eluent to obtain a yellow solid. *Purification protocol B:* The crude was slurried in dichloromethane and passed through a silica plug and the solution evaporated under reduced pressure. The solid was triturated in a methanol/dichloromethane mixture (4:1), filtrated and washed with hot methanol and distilled pentane to achieve a yellow solid. **BTXI-CN: ^{1}H-NMR** (300 MHz, $CDCl_3$): δ 8.75 (d, J = 8.2 Hz, 1H), 8.60 (s, 1H), 8.39 (d, J = 8.4 Hz, 1H), 8.34 – 8.28 (m, 1H), 7.60 – 7.50 (m, 3H), 5.03 (tt, J = 9.4, 5.7 Hz, 1H), 2.31 – 2.12 (m, 2H), 1.98-1.84 (m, 2H), 0.89 (t, J = 7.5 Hz, 8H). **^{13}C NMR** (125 MHz, $CDCl_3$): δ 146.5, 136.9, 134.5, 133.5, 133.5, 131.3, 130.8, 130.2, 128.9, 127.6, 127.2, 126.5, 125.5, 120.9, 115.9, 103.6, 58.1, 25.1, 11.4. **HRMS** (EI+): calculated for $C_{24}H_{18}N_2O_2S$ 398.1083, found 398.1088.

Scaled up synthesis of BTXI-CN to gram-scale

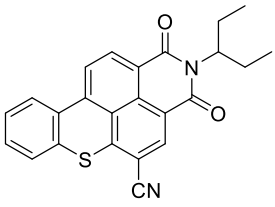

Two microwave flask were charged respectively with 5-bromo-2-(pentan-3- yl)-1*H*-thioxantheno[2,1,9-*def*]isoquinoline-1,3(2*H*)-dione (**BTXI-Br**) (500 mg, 1.11 mmol), $K_4[Fe(CN)_6]$ (407 mg, 1.11 mmol), sodium carbonate (175 mg, 1.11 µmol), palladium(II) acetate (50 mg, 0.22 mmol) and Xantphos (255 mg, 0.44 mmol). Under argon atmosphere, *N,N*-dimethylacetamide (20 mL x 2) was added and the two containers were subsequently irradiated in the microwave cavity at 140 °C. After 1 h of reaction, the obtained solutions were cooled to room temperature and put together. The solvent was removed in *vacuum* and the product purified following *purification protocol A* (79% yield) and *B* (70% yield).

Synthesis of NO_2-BTXI-CN: 5-bromo-11-nitro-2-(pentan-3-yl)-1*H*-thioxantheno[2,1,9-*def*]isoquinoline-1,3(2*H*)-dione (**NO_2-BTXI-Br**) (50 mg, 100.53 µmol), $K_4[Fe(CN)_6]$ (37 mg, 100.53 µmol), sodium carbonate (11 mg, 100.53 µmol), palladium(II) acetate (2 mg, 10.05 µmol) and Xantphos (12 mg, 20.11 µmol) were placed under inert atmosphere in a microwave vial.

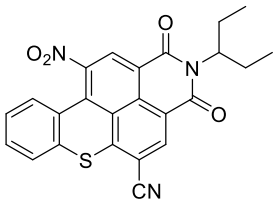

The mixture was irradiated at 140 °C for 0.5 hour, then cooled to room temperature and the solvent evaporated in vacuo. The crude was purified by column chromatography using dichloromethane as eluent. Finally, 15 mg of a reddish solid were afforded (34% yield). **^{1}H-NMR** (300 MHz, $CDCl_3$): *δ* 8.91 (s, 1H), 8.65 (s, 1H), 7.70 – 7.61 (m, 2H), 7.55 (t, *J* = 7.5 Hz, 1H), 7.44 (dd, *J* = 11.3, 4.2 Hz, 1H), 5.00 – 4.86 (m, 1H), 2.22 – 2.05 (m, 2H), 1.91 – 1.77 (m, 2H), 0.81 (t, *J* = 7.5 Hz, 6H). **^{13}C NMR** (75 MHz, $CDCl_3$): *δ* ^{13}C NMR (76 MHz, $CDCl_3$) δ 146.7, 146.5, 134.6, 131.9, 131.7, 131.5, 131.2, 129.9, 129.7, 129.4, 127.6, 127.4, 124.4, 122.4, 119.3, 115.3, 105.5, 58.5, 24.9, 11.3. **HRMS** (MALDI+): calculated for $C_{24}H_{17}N_3O_4S$ 443.0934; found 443.0946.

Synthesis of NH_2-BTXI-Br: THF (2 mL) was added to a solid mixture of 5-bromo-11-nitro-2-(pentan-3-yl)-1*H*-thioxantheno[2,1,9-*def*]isoquinoline-1,3(2*H*)-dione (**NO_2-BTXI-Br**) (80.0 mg, 0.16 mmol) and powdered iron (62.9 mg, 1.13 mmol). HCl (0.67 mL, 37 *wt*%) was added and the mixture was heated at 65 °C for 1 hour. Water was added to quench the reaction and the resulting solid was filtered and washed thoroughly with water. The product was purified by column chromatography on silica gel using dichloromethane as eluent yielding 52 mg of **NH_2-BTXI-Br** as a red powder (69% yield). **^{1}H-NMR** (300 MHz, $CDCl_3$): *δ* 8.57 – 8.51 (m, 1H), 8.37 (s, 1H), 8.11 (s, 1H), 7.50 – 7.44 (m, 1H), 7.36 – 7.28 (m, 2H), 5.05 – 4.94 (m, 1H), 4.56 (s, 2H), 2.30 – 2.12 (m, 2H), 1.95 – 1.80 (m, 2H), 0.87 (t, *J* = 7.5 Hz, 6H). **^{13}C NMR** (75 MHz, $CDCl_3$): *δ* 142.8, 137.7, 132.7, 131.5, 131.2, 129.4, 128.9, 127.7, 127.2, 127.1, 124.5, 122.4, 119.6, 119.2, 115.8, 57.7, 25.1, 11.4. **HRMS** (FAB+): calculated for $C_{23}H_{19}BrN_2O_2S$: 466.0345, found: 466.0358.

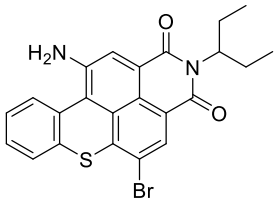

Synthesis of NH_2-BTXI-CN: 11-amino-5-bromo-2-(pentan-3-yl)-1*H*-thioxantheno[2,1,9-def]isoquinoline-1,3(2*H*)-dione (**NH_2-BTXI-Br**) (30 mg, 64.19 µmol), $K_4[Fe(CN)_6]$ (24 mg, 64.19 µmol), sodium carbonate (10 mg, 64.19 µmol), palladium(II) acetate (1 mg, 6.42 µmol) and Xantphos (7.43 mg, 12.84 µmol) were placed under inert atmosphere in a microwave vial.

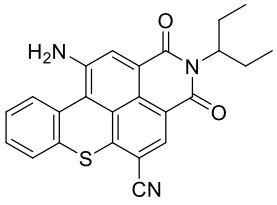

The mixture was irradiated at 140 °C for 0.5 hour, then cooled to room temperature and the solvent evaporated in vacuo. The crude was purified by column chromatography using dichloromethane as eluent. Finally, 10 mg of an orange solid were afforded (38% yield). **^{1}H-NMR** (300 MHz, $CDCl_3$): δ 8.61 – 8.51 (m, 1H), 8.33 (s, 1H), 8.21 (s, 1H), 7.54 - 7.48 (m, 1H), 7.43 – 7.34 (m, 2H), 5.05 – 4.92 (m, 1H), 4.69 (s, 2H), 2.30 – 2.12 (m, 2H), 1.98 – 1.80 (m, 2H), 0.87 (t, *J* = 7.5 Hz, 6H). **^{13}C NMR** (75 MHz, $CDCl_3$): δ 143.8, 143.3, 131.1, 130.0, 129.9, 129.4, 129.2, 127.9, 127.1, 123.9, 119.2, 116.4, 104.6, 57.9, 25.0, 11.4. **HRMS** (MALDI+): calculated for $C_{24}H_{19}N_3O_2S$ 413.1192; found 413.1185.

11-NC-BTXI-CN **10-NC-BTXI-CN**

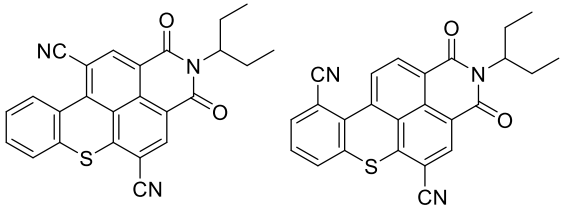

Synthesis of NC-BTXI-CN: Anhydrous *N,N*-dimethylacetamide (3 mL) was added to a mixture of 5,11-dibromo-2-(pentan-3-yl)-1*H*-thioxantheno[2,1,9-*def*]isoquinoline-1,3(2*H*)-dione (**Br-BTXI-Br**) (50 mg, 94.12 µmol), $K_4[Fe(CN)_6]$ (69 mg, 180.23 µmol), sodium carbonate (15 mg, 141.17 µmol), palladium(II) acetate (50 mg, 18.82 µmol) and Xantphos (22 mg, 37.65 µmol). The reaction mixture was then stirred and heated for 1 h in the microwave cavity at 140 °C. The reaction mixture was cooled to room temperature and the solvent removed in *vacuum*. The crude was purified by silica gel column chromatography using dichloromethane as eluent to obtain 18 mg of **11-NC-BTXI-CN** (45% yield) in the first fraction and 9 mg of **10-NC-BTXI-CN** (23% yield) in the second fraction, both of them as a yellow solids.

11-NC-BTXI-CN: ^{1}H-NMR (300 MHz, $CDCl_3$): δ 9.06-9.00 (m, 1H), 8.94 (s, 1H), 8.73 (s, 1H), 7.76 – 7.64 (m, 3H), 5.06-5.00 (m, 1H), 2.31 – 2.10 (m, 2H), 2.02 – 1.83 (m, 2H), 0.88 (t, *J* = 7.5 Hz, 6H). **^{13}C NMR** (75 MHz, $CDCl_3$): δ 146.1, 140.7, 139.0, 134.9, 132.2, 131.8, 131.6, 129.8, 129.1, 127.2, 126.5, 125.8, 122.3, 119.1, 115.2, 106.0, 105.3, 58.3, 24.7, 11.2. **HRMS** (FAB-): calculated for $C_{25}H_{17}N_3O_2S$ 423.1036, found 423.1041.

10-NC-BTXI-CN: ^{1}H-NMR (300 MHz, $CDCl_3$): δ 9.07 – 9.00 (m, 1H), 8.94 (s, 1H), 8.73 (s, 1H), 7.76 – 7.64 (m, 3H), 5.06-4.94 (m, 1H), 2.29 – 2.11 (m, 2H), 2.01 – 1.84 (m, 2H), 0.88 (t, *J* = 7.5 Hz, 6H). **^{13}C NMR** (75 MHz, $CDCl_3$): δ 143.75, 136.98, 133.72, 133.49, 131.19, 130.48, 130.00, 129.83, 127.01, 125.81, 118.97, 115.53, 111.73, 104.33, 58.22, 24.93, 11.39. **HRMS** (FAB-): calculated for $C_{25}H_{17}N_3O_2S$ 423.1036, found 423.1048.

11-NC-BTXI-*i*Bu **10-NC-BTXI-*i*Bu**

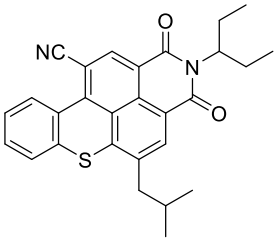

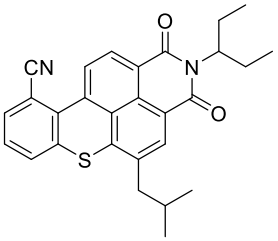

Synthesis of NC-BTXI-*i*Bu: 11-bromo-5-isobutyl-2-(pentan-3-yl)-1*H*-thioxantheno[2,1,9-*def*]isoquinoline-1,3(2*H*)-dione (50 mg, 98.33 µmol), $K_4[Fe(CN)_6]$ (36 mg, 98.33 µmol), sodium carbonate (11 mg, 98.33 µmol), palladium(II) acetate (2 mg, 9.83 µmol) and Xantphos (11 mg, 19.67 µmol) were dissolved in *N,N*-dimethylacetamide (3 mL) under argon, then the reaction was stirred for 30 min in the microwave cavity at 140 °C. The reaction mixture was cooled to room temperature and the crude was purified by column chromatography silica gel using dichloromethane as eluent affording 20 mg of **11-NC-BTXI-*i*Bu** (45% yield) and 13 mg of **10-NC-BTXI-*i*Bu** (29% yield).

11-NC-BTXI-*i*Bu: ^{1}H-NMR (300 MHz, $CDCl_3$): δ 8.88 – 8.80 (m, 1H), 8.77 (s, 1H), 8.43 (s, 1H), 7.66 – 7.58 (m, 1H), 7.58 – 7.49 (m, 2H), 5.03 (tt, *J* = 9.6, 5.9 Hz, 1H), 2.83 (d, *J* = 7.2 Hz, 2H), 2.33- 2.11 (m, 3H), 1.99 – 1.83 (m, 2H), 1.04 (d, *J* = 6.6 Hz, 6H), 0.89 (t, *J* = 7.5 Hz, 6H). **^{13}C NMR** (75 MHz, $CDCl_3$): δ 135.9, 135.6, 135.1, 133.7, 133.3, 133.0, 131.1, 131.0, 130.9, 129.0, 128.9, 128.5, 128.1, 124.8, 123.6, 119.4, 118.5, 111.3, 57.7, 43.3, 27.9, 25.1, 22.8, 11.45. **HRMS** (FAB-): calculated for $C_{28}H_{26}N_2O_2S$ 454.1710; found 454.1720.

10-NC-BTXI-*i*Bu: ^{1}H-NMR (300 MHz, $CDCl_3$): δ 8.83 (d, *J* = 8.1 Hz, 1H), 8.63 (d, *J* = 8.1 Hz, 1H), 8.34 (s, 1H), 7.78 (dd, *J* = 7.5, 1.4 Hz, 1H), 7.66 (dd, *J* = 8.0, 1.4 Hz, 1H), 7.45 (t, *J* = 7.8 Hz, 1H), 5.05 (tt, *J* = 9.6, 5.9 Hz, 1H), 2.75 (d, *J* = 7.3 Hz, 2H), 2.32 – 2.10 (m, 3H), 2.00 – 1.83 (m, 2H), 1.03 (d, *J* = 6.6 Hz, 6H), 0.90 (t, *J* = 7.5 Hz, 6H). **^{13}C NMR** (75 MHz, $CDCl_3$): δ 135.88, 135.62, 135.11, 133.74, 133.28, 133.06, 131.09, 131.04, 130.93, 128.97, 128.85, 128.54, 128.08, 124.77, 123.65, 119.45, 118.52, 111.29, 57.66, 43.29, 27.90, 25.07, 22.77, 11.45. **HRMS** (FAB+): calculated for $C_{28}H_{26}N_2O_2S$ 454.1710; found 454.1722.

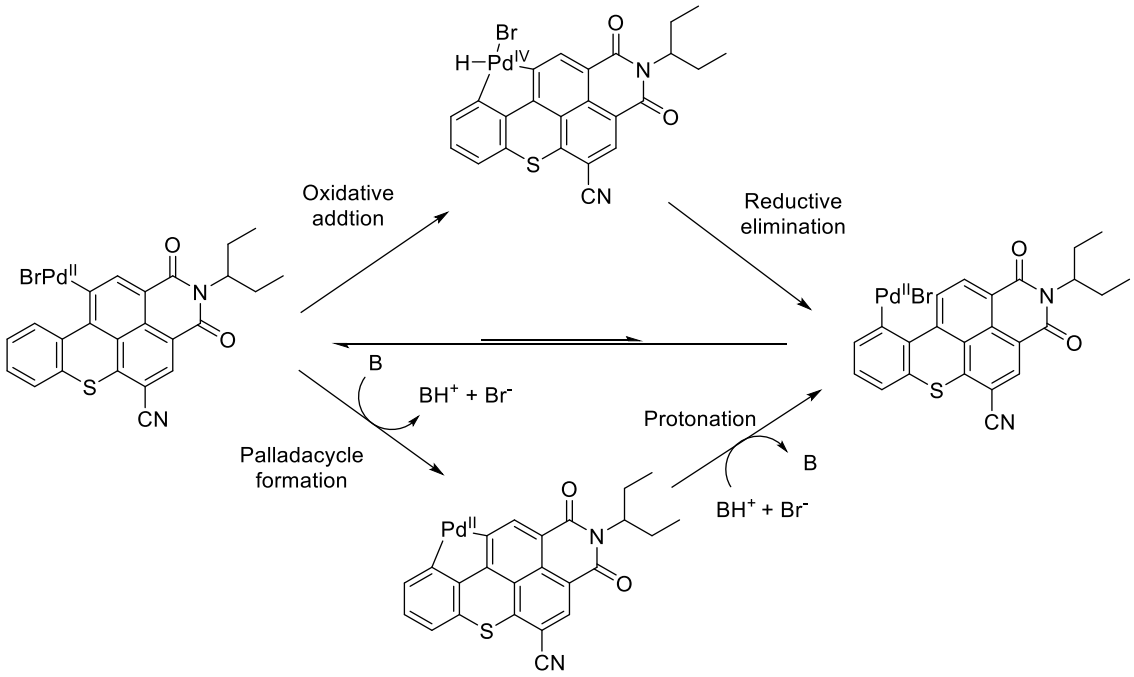

Figure 63. Possible mechanisms proposed for the isomerization reaction.

Synthesis of Br-BTXI-CN: Bromine (129 µL, 401 mg, 2.5 mmol) was added over a solution of

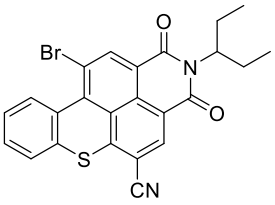

BTXI-CN (50 mg, 0.13 mmol) in dichloromethane (5 mL). The reaction mixture was refluxed for 16 h before being washed with saturated $Na_2S_2O_3$, water and brine. After drying over $MgSO_4$, the solvent was removed by rotary evaporation and the crude was subjected to silica gel column chromatography using toluene as eluent. 57 mg of the final product was obtained as an orange solid (95% yield). **^{1}H-NMR** (300 MHz, $CDCl_3$): δ 8.93 (s, 1H), 8.76 (dd, J = 7.8, 1.8 Hz, 1H), 8.57 (s, 1H), 7.60 (dd, J = 7.6, 1.8 Hz, 1H), 7.60 (dd, J = 7.6, 1.8 Hz, 1H), 7.56 – 7.43 (m, 2H), 5.05 – 4.93 (m, 1H), 2.20 (m, 2H), 1.97 – 1.82 (m, 2H), 0.87 (t, J = 7.4 Hz, 1H). **^{13}C NMR** (75 MHz, $CDCl_3$): δ 162.9, 162.6, 144.8, 140.8, 137.0, 132.9, 131.3, 131.1, 130.8, 129.2, 129.0, 128.0, 127.4, 127.2, 122.2, 119.2, 118.6, 115.8, 105.0, 58.2, 24.9, 11.4. **HRMS** (FAB-): calculated for $C_{24}H_{17}BrN_2O_2S$ 476.0189; found 476.0981.

Synthesis of Th-BTXI-CN: To a mixture of **Br-BTXI-CN** (50 mg, 104.74 µmol) and

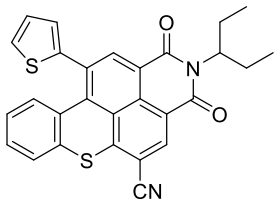

tributyl(thiophen-2-yl)stannane (78 mg, 209,48 µmol) was added degassed toluene (3 mL). $Pd(PPh_3)_4$ (6 mg, 5.24 µmol) was then added before refluxing the mixture for 16 h. The reaction was cooled to room temperature and the solvent removed under *vacuum*. Purification of the crude was performed by column chromatography on silica gel using dichloromethane as

eluent, achieving the 50 mg of an orange solid (100% yield). **^{1}H-NMR** (300 MHz, $CDCl_3$): δ 8.81 (s, 1H), 8.59 (s, 1H), 7.66 (dd, *J* = 8.4, 0.9 Hz, 1H), 7.55 (dd, *J* = 8.0, 1.1 Hz, 1H), 7.41 (dd, *J* = 5.1, 1.2 Hz, 1H), 7.34 (td, *J* = 7.7, 1.2 Hz, 1H), 7.21 (dd, *J* = 3.6, 1.2 Hz, 1H), 7.11 – 7.03 (m, 2H), 5.08 – 4.96 (m, 1H), 2.33 – 2.12 (m, 2H), 2.00 – 1.79 (m, 2H), 0.88 (t, *J* = 7.5 Hz, 6H). **^{13}C NMR** (75 MHz, $CDCl_3$): δ 163.7, 163.6, 146.2, 143.8, 138.8, 136.3, 132.9, 132.1, 131.5, 131.3, 129.9, 129.6, 128.7, 128.6, 128.4, 127.9, 127.8, 127.3, 127.2, 121.6, 119.2, 116.1, 104.7, 58.0, 25.0, 11.4. **HRMS** (MALDI+): calculated for $C_{28}H_{20}N_2O_2S_2$ 480.0961; found.480.0968.

Synthesis of Th-BTXI: An oven-dried screw-cap reaction tube was charged with **Th-BTXI-CN**

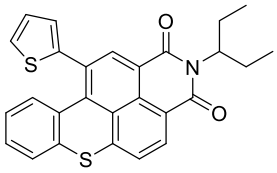

(30 mg, 62.42 µmol), $Ni(COD)_2$ (5 mg, 18.73 µmol) and PCy_3 (16 mg, 56.18 µmol) inside a glovebox under inert atmosphere. The tube was sealed and taken out from the glovebox before repeating three vacuum-hydrogen cycles. Then, H_2 purged toluene (3 mL) and $AlMe_3$ (94 µL, 187.27 µmol, 2M in toulene) were added and the reaction was heated at 130 ^{o}C for 16 h. Thereafter, the mixture was cooled to room temperature and the crude filtrated through celite using ethyl acetate as eluent. The filtrate was concentrated and purified by column chromatography using dichloromethane as eluent. Finally, 12 mg of the expected product were obtained as an orange solid (42% yield) whereas 5 mg of the starting material **Th-BTXI-CN** (18% yield) were recovered. **^{1}H-NMR** (300 MHz, $CDCl_3$): δ 8.63 (s, 1H), 8.33 (d, *J* = 7.9 Hz, 1H), 7.59 – 7.48 (m, 2H), 7.38 – 7.26 (m, 2H), 7.18 – 7.09 (m, 2H), 7.00 (dd, *J* = 5.1, 3.5 Hz, 1H), 6.92 (ddd, *J* = 8.5, 7.2, 1.5 Hz, 1H), 5.06 – 4.92 (m, 2H), 2.28 – 2.11 (m, 2H), 1.88 – 1.78 (m, 2H), 0.82 (t, *J* = 7.5 Hz, 6H). **^{13}C NMR** (75 MHz, $CDCl_3$): δ 144.5, 139.9, 137.0, 136.1, 133.3, 132.0, 129.9, 129.4, 129.1, 129.0, 128.0, 127.4, 127.3, 127.0, 126.9, 126.7, 126.3, 121.6, 57.5, 25.0, 11.3. **HRMS** (MALDI+): calculated for $C_{27}H_{21}NO_2S_2$ 455.1008; found 455.1015.

Synthesis of BTXI-Th: 5-bromo-2-(pentan-3- yl)-1H-thioxantheno[2,1,9-*def*]isoquinoline-

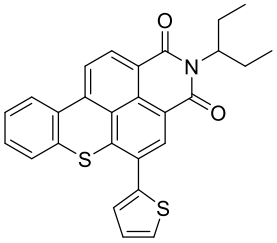

1,3(2*H*)-dione (**BTXI-Br**) (100 mg, 0.22 mmol), tributyl(thiophen-2-yl)stannane (140 µL, 165 mg, 0.44 mmol) and $Pd(PPh_3)_4$ (13 mg, 11.05 µmol) were dissolved in dry and deoxygenated toluene (7mL). The reaction mixture was then stirred and refluxed for 5 h under inert conditions. Once concentrated under *vacuum*, the crude was purified by column chromatography using dichloromethane as eluent affording 89 mg of an orange powder (88% yield). **^{1}H-NMR** (300 MHz, $CDCl_3$): δ 8.61 (d, *J* = 8.2 Hz, 1H), 8.48 (s, 1H), 8.24 (d, *J* = 8.3 Hz, 1H),

8.22 – 8.17 (m, 1H), 7.53 (dd, *J* = 5.1, 1.2 Hz, 1H), 7.43 – 7.30 (m, 4H), 7.22 (dd, *J* = 5.1, 3.5 Hz, 1H), 5.06 (tt, *J* = 9.6, 5.8 Hz, 1H), 2.39 – 2.14 (m, 2H), 2.01 – 1.82 (m, 2H), 0.90 (t, *J* = 7.5 Hz, 6H). **^{13}C NMR** (75 MHz, $CDCl_3$): *δ* 164.8, 140.1, 139.0, 136.8, 133.6, 132.4, 131.8, 129.9, 129.8, 128.2, 127.7, 127.6, 127.5, 127.2, 126.7, 126.6, 126.1, 125.9, 121.6, 119.5, 117.8, 57.4, 25.0, 11.4. **HRMS** (MALDI+): calculated for $C_{27}H_{21}NO_2S_2$ 455.1008; found 455.1009.

Isotopic labeling experiments

Dicyanation reaction was carried out following the same procedure described above in presence of 100 µL of D_2O. Both regioisomers were isolated in similar yields and analyses by ^{1}H NMR and MS spectrometry to assess the presence of deuterated species. In this context, proton HMR of **10-NC-BTXI-CN** (Figure 54) shows the almost disappearance of the doblet ascribed to the H in position 11 and a singlet assigned to the H in position 12 instead of the common AB coupled system. Integration of the peaks reveals an enriched sample in the deuterated compound of *ca* 90% (10% of the non-deuterated molecule). As for **11-NC-BTXI-CN**, the integrations surprisingly displays a 73% of the deuterated compound (27% of non-deuterated). The results can be translate in: i) first, the palladacycle is obtained after HBr elimination, recovering the H from the reaction medium for the isomerization; ii) most of the catalytic turnover go through the palladacycle formation and can undergo via isomerization or recovering of the 11-coordinated complex.

3 Devices fabrication and testing

3.1 PDI based NFAs

PTB7-Th : **1,6-i** or **1,7-i** solutions were prepared in air, from 10 mg/mL solutions of the single components, which were stirred for approximatively 2 hours before mixing in the required proportions. The final solutions were stirred for at least 1 hour before deposition on substrates. ZnO precursor solutions were prepared following the sol-gel method proposed by Sun *et al.*[40]: 1.0 g of zinc acetate dihydrate, 0.280 mL of ethanolamine and 10.0 mL of 2-methoxy ethanol were mixed in air and stirred overnight at room temperature before use. All studied films were prepared as follow: ITO-coated glass substrates were first cleaned by surfactant/water scrubbing, followed by sequentially ultra-sonicating in de-ionized water, acetone and isopropanol (10+ minutes each) before use. ITO substrates were then dried with pressurized air and UV-Ozone treated for 30 minutes. A ZnO precursor solution was spin-

coated onto the ITO substrate at a speed of 4200 rpm for 55 s and then thermally annealed at 200 °C in air for 20 min. The organic layer was then spin-coated at room temperature, in air at 1000 rpm for 50 s. Solar cells were fabricated following the initial procedure for cleaning, ZnO deposition and organic layer deposition reported above. The fabricated films were then moved to an N_2 atmosphere glovebox and left overnight before evaporating the top electrodes consisting of 10 nm of MoO_x (electron transport interlayer) followed by 100 nm of Ag (anode), which were thermally deposited under high vacuum (10^{-5} mbar). Current density-voltage (*J-V*) characteristics were measured using a Keithley 2420 Source Measure Unit. Solar cell performance used an Air Mass 1.5 Global (AM 1.5G) Solar Simulator (Newport, Model 92251A-1000) with an irradiation intensity of 100 mW cm^{-2}, which was measured by a calibrated silicon solar cell and a readout meter (Newport, Model 91150V).

3.2 IDT based NFAs

Thin films and heterojunction solar cell devices were prepared by thermal vapour deposition onto room temperature substrates in an ultra-high vacuum chamber with a base pressure of 10^{-7} mbar. Thin films for absorption and emission measurements were prepared on quartz substrates; solar cells on tin-doped indium oxide (ITO) coated glass (Thin Film Devices, USA, sheet resistance of 30 Ω sq^{-1}). Layer thicknesses were determined during evaporation by using quartz crystal monitors calibrated for the respective material. The thin films prepared for absorption and emission measurements were approximately 30 nm thick. Solar cells were prepared layer by layer with-out breaking the *vacuum* as follows: ITO; 10 nm ***h*-NFA**; 10 nm **BF-DPB** or **NHT169**; 45 nm **NHT169** doped with **NDP9** (purchased from Novaled AG Germany, 10 wt%); 1 nm **NDP9**; 100 nm Al.

J–V and *EQE* measurements were carried out in a solvent-free N_2 filled glovebox (O_2 and H_20 levels < 1ppm). *J–V* characteristics were measured using a source-measure unit (Keithley SMU 2400) and an AM 1.5G sun simulator (KHS Technical Lighting SC1200). The intensity was monitored with a silicon photodiode (Hamamatsu S1337), which was calibrated at Fraunhofer ISE. The mismatch between the spectrum of the sun simulator and the solar AM 1.5G spectrum was taken into account for the calculation of current density. Aperture masks (2.76 mm^2) were used to obtain well-defined active solar cell areas.

4 Computational Calculation Methodology

The gas-phase ground-state equilibrium geometry of representative molecules was obtained by performing DFT optimization at energy functional B3LYP or the range-separated hybrid (RSH) functional level of theory ωB97X-D[243] and using the 6-31G(d,p) or 6-311G(d) split-valence Pople's basis set for all the atomic species. For the sake of simplicity and to speed up the calculations. The same levels of theory were used for all the structural optimizations in *vacuum*, check thereafter the influence of optimally tuning (OT) the ω value (a key parameter in the class of RSH functionals) on the resulting optimized structures. For tuning the ω value, we resorted to a polarizable continuum model (PCM)[244] to take into account the electrostatic effects of the polarizable environment using a dielectric constant. The ω parameter was finely adjusted with PCM according to the "gap tuning" procedure[245,246] in order to accurately estimate (~ 50 meV of error) the energy of the frontier molecular orbitals. Ground-state population analysis was performed at the OT-RSH+PCM level of theory. Ultimately, as for the optical properties, OT-RSH+PCM TD-DFT calculations were carried out. All DFT and TD-DFT simulations were performed using the GAUSSIAN16 package suite.[247]

The proposed catalytic cycles for the obtantion of **11-NC-BTXI-CN** and **10-NC-BTXI-CN** were theoretically studied comprising geometry optimization and internal energy variation, performing DFT in the B3LYP energy functional and the 3-21G basis set for all the atomic species with the inclusion of Grimme's D2 dispersion correction.

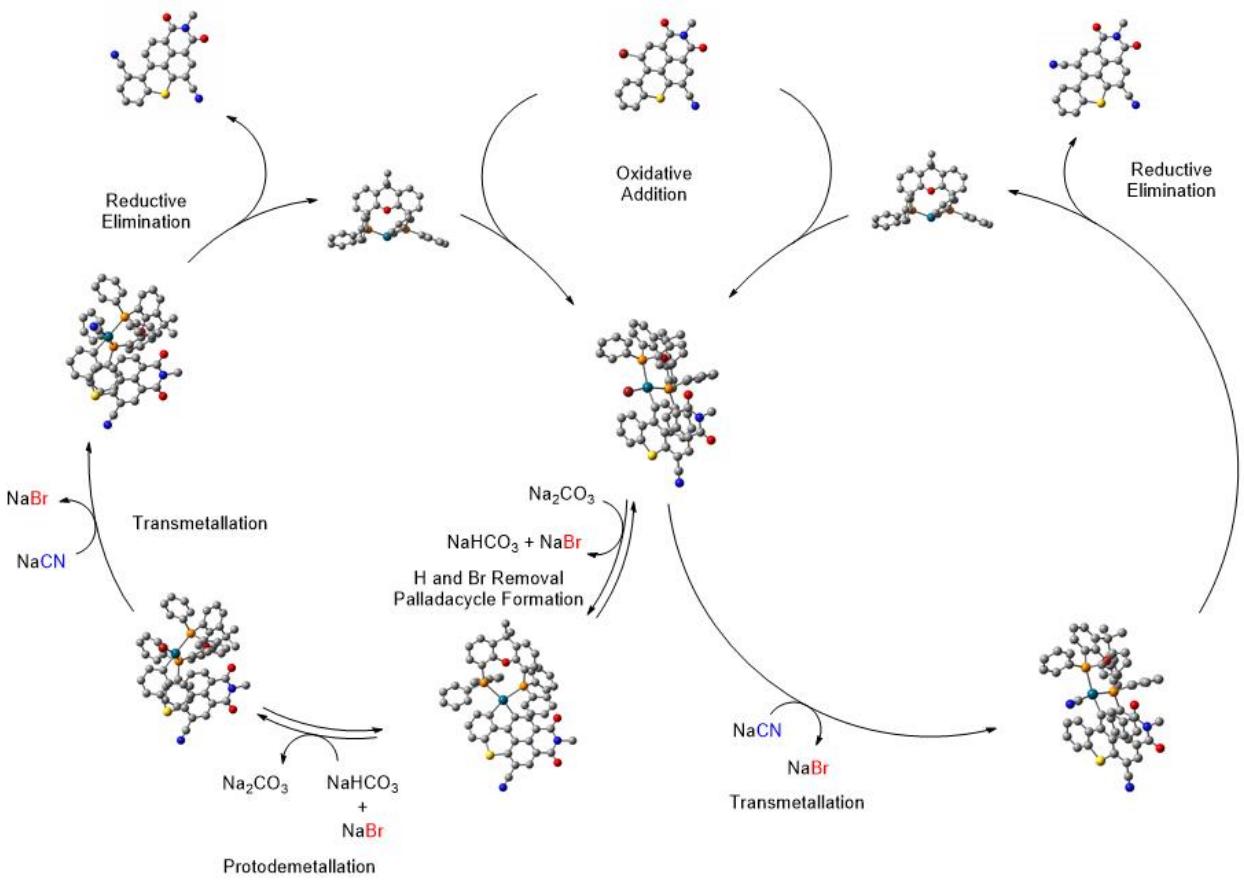

*Scheme 17. Mechanisms of cyanation reaction between **Br-BTXI-CN** to obtain **11-NC-BTXI-CN** or **10-NC-BTXI-CN** using Xantphos as ligand.*

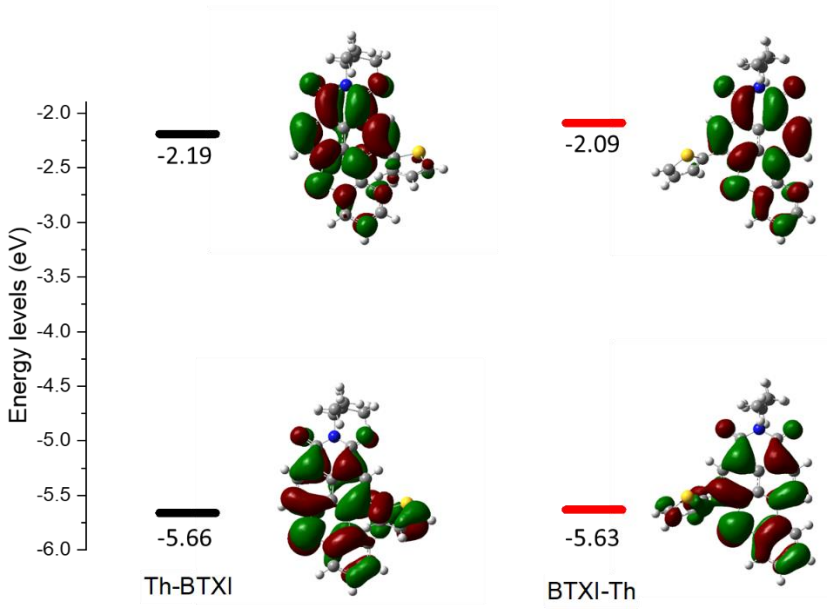

*Figure 64. Frontier molecular orbital depicted for compounds **Th-BTXI** and **BTXI-Th**. Theoretical calculations corroborate experimental observations, narrowing the E_{gap} upon substitution in 11-position. Besides, higher contribution of the thiophene moiety is visualized for **Th-BTXI**.*

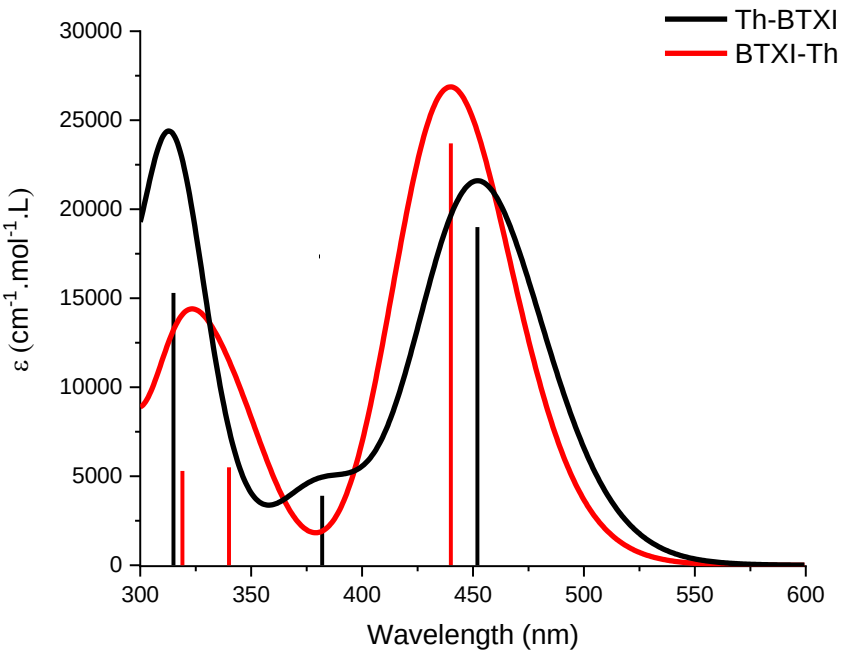

Figure 65. TD-DFT simulated spectra. Solid straight-lines the main excited states which contributes to the absorption band.

5 SCLC measurements

A solution of neat isomers, namely **1,6-i** or **1,7-i** (20 mg/mL) in chloroform was spun-cast at 1000 rpm on the above described ZnO coated substrates to provide organic layers of *ca* 140 nm and 180 nm respectively. Calcium (7 nm) and aluminium (100 nm) were thermally evaporated under a *vacuum* of 1.5 x 10^{-5} Torr, through a shadow mask defining active areas of 12.60 mm², 3.10 mm² and 0.78 mm² per substrate. Electron mobilities μ_e were evaluated using the Mott-Gurney law, *i.e.*, JSCLC = $(9/8)\varepsilon_0\varepsilon_r\mu_e(V^2/d^3)$ where ε_r is the static dielectric constant of the medium (ε_r = 3) and d, the thickness of the active layer.

References

(241) Friesen, R. W.; Allouche, E. M. D. Tetrakis(Triphenylphosphine)Palladium(0). In *Encyclopedia of Reagents for Organic Synthesis*; John Wiley & Sons, Ltd: Chichester, UK, 2017; pp 1–7.

(242) Zalesskiy, S. S.; Ananikov, V. P. Pd 2 (Dba) 3 as a Precursor of Soluble Metal Complexes and Nanoparticles: Determination of Palladium Active Species for Catalysis and Synthesis. *Organometallics* **2012**, *31* (6), 2302–2309.

(243) Chai, J.-D.; Head-Gordon, M. Long-Range Corrected Hybrid Density Functionals with Damped Atom–Atom Dispersion Corrections. *Phys. Chem. Chem. Phys.* **2008**, *10* (44), 6615–6620.

(244) Tomasi, J.; Mennucci, B.; Cammi, R. Quantum Mechanical Continuum Solvation Models. *Chem. Rev.* **2005**, *105* (8), 2999–3094.

(245) Stein, T.; Kronik, L.; Baer, R. Reliable Prediction of Charge Transfer Excitations in Molecular Complexesusing Time-Dependent Density Functional Theory. *J. Am. Chem. Soc.* **2009**, *131* (8), 2818–2820.

(246) Stein, T.; Kronik, L.; Baer, R. Prediction of Charge-Transfer Excitations in Coumarin-Based Dyes Using a Range-Separated Functional Tuned from First Principles. *J. Chem. Phys.* **2009**, *131* (24), 244119.

(247) M. J. Frisch, G. W. Trucks, H. B. Schlegel, G. E. Scuseria, M. A. Robb, J. R. Cheeseman, G. Scalmani, V. Barone, G. A. Petersson, H. Nakatsuji, X. Li, M. Caricato, A. V. Marenich, J. Bloino, B. G. Janesko, R. Gomperts, B. Mennucci, H. P. H. Gaussian 16. 2016.

List of publications

- Impact of the replacement of a triphenylamine by a diphenylmethylamine unit on the electrochemical behavior of pentaerythritol-based push-pull tetramers. Claudia Malacrida, Amir Hossein, Sergio Gámez-Valenzuela, Illia Lenk, Pablo Simón Marqués, Antoine Labrunie, Jeremie Grolleau, Juan T. López Navarrete, M. Carmen Ruiz Delgado, Clement Cabanetos, Philippe Blanchard, Sabine Ludwigs. *ChemElectroChem.* **2019**, 6, 4215-4228.

- Cyclopentadithiophene and Fluorene Spiro-Core based Hole Transporting Materials for Perovskite Solar Cells. Rana Nakar, F. Javier Ramos, Clément Dalinot, Pablo Simón Marqués, Clément Cabanetos, Philippe Leriche, Lionel Sanguinet, Marwan Kobeissi, Philippe Blanchard, Jérôme Faure-Vincent, François Tran-Van, Nicolas Berton, Jean Rousset, Bruno Schmaltz. *J. Phys. Chem. C* **2019**, 123, 22767−22774.

- Indeno[1,2-b]thiophene End-capped Perylene Diimide: Should the 1,6-Regioisomers be systematically considered as a contaminant?. Pablo Simón Marqués, Francesco Tintori, José María Andrés Castán, Pierre Josse, Clément Dalinot, Magali Allain, Gregory Welch, Philippe Blanchard, Clément Cabanetos. *Sci Rep* **2020**, 10, 3262.

- Nitration of the benzothioxanthene: a new step towards functionalization of the core. José M. Andrés Castán, Laura Abad Galán, Shi Li, Clément Dalinot, Pablo Simón Marqués, Benjamin Siegler, Chad Risko, Cyrille Monnereau, Olivier Maury, Philippe Blanchard, Clément Cabanetos. *New J. Chem.* **2020**, 44, 900-905. (2019 NJC HOT article)

- Regioselective mono and homo/hetero dihalogenation of the benzothioxanthene monoimide. Clément Dalinot, Pablo Simón Marqués, José M. Andrés Castán, Pierre Josse, Laura Abad Galán, Magali Allain, Cyrille Monnereau, Olivier Maury, Philippe Blanchard, Clément Cabanetos. *Eur. J. Org. Chem.* **2020**, 2140–2145.

- Theoretical and experimental investigation on the intersystem crossing kinetics in benzothioxanthene imide luminophores, and their dependence on substituents effects. Laura Abad Galán, José M. Andrés Castán, Clément Dalinot, Pablo Simón Marqués, Philippe Blanchard, Olivier Maury, Clément Cabanetos, Tangui Le Bahers, Cyrille Monnereau. *Phys. Chem. Chem. Phys.* **2020**, 22, 12373-12381. (Front Cover)

- Do Lewis Acids Dope Organic Semiconductors? Pablo Simón Marqués, Giacomo Londi, Brett Yurash, Thuc-Quyen Nguyen, David Beljonne. Manuscript submitted.

- Effect of 4-biphenyl groups on the charge transport and photovoltaic properties of arylamine based push-pull systems. Pablo Simón Marqués, José María Andrés Castán, Pierre Josse, Martin Blais, Amir Hossein Habibi, Ivan Ramirez, Karsten Walzer, Jean Roncali, Philippe Blanchard, Clément Cabanetos. *New J. Chem.* **2020**, 44, 11441-11447. (Front cover & 2020 HOT article)

- Triphenylamine/Tetracyanobutadiene-based π-Conjugated Push-Pull Molecules End-capped with Arene Platforms: Synthesis, Photophysics, and Photovoltaic Response. Pablo Simón Marqués, José María Andrés Castán, Benedito A. L. Raul, Giacomo Londi, Ivan Ramirez, Maxim S. Pshenichnikov, David Beljonne, Karsten Walzer, Martin Blais, Magali Allain, Clément Cabanetos, Philippe Blanchard. Manuscript accepted in *Chem. Eur. J.* **https://doi.org/10.1002/chem.202002810** (HOT article)

- Synthesis, characterization and use of benzothioxanthene imide based dimers. José María Andrés Castán, Clément Dalinot, Sergey Dayneko, Laura Abad Galan, Pablo Simón Marqués, Olivier Alévêque, Magali Allain, Olivier Maury, Ludovic Favereau, Philippe Blanchard, Gregory Welch, Clément Cabanetos. Manuscript accepted in *Chem. Comm.* **2020**, 56, 10131-10134.

- Charge Photogeneration in Non-Fullerene Organic Solar Cells: Influence of Excess Energy and Electrostatic Interactions. Maria Saladina, Pablo Simón Marqués, Anastasia Markina, Safakath Karuthedath, Christopher Wöpke, Clemens Göhler, Yue Chen, Magali Allain, Philippe Blanchard, Clément Cabanetos, Denis Andrienko, Frédéric Laquai, Julien Gorenflot, Carsten Deibel. Manuscrit accepted in *Adv. Funct. Mat.*

UNIVERSITE MATIERE BRETAGNE MOLECULES LOIRE ET MATERIAUX

université angers

Titre : Nouveaux systèmes pi-conjugués déficients en électrons pour une application potentielle en photovoltaïque organique.

Mots clés : Synthèse Organique, Électronique Organique, Accepteurs non-fullerène, Couches minces déposées sous vide

Résumé : Le développement récent d'accepteurs moléculaires non-fullerène (NFAs) est à l'origine d'un nouvel essor du photovoltaïque organique (OPV). Grâce à eux, des cellules solaires organiques à simple jonction peuvent désormais atteindre des rendements de photoconversion de 18%. Cependant, ces résultats exceptionnels sont obtenus avec des molécules de structure complexe et par des procédés de dépôt en solution à la tournette, ce qui complique la fabrication de modules photovoltaïques commerciaux.

Après un premier chapitre introduisant l'OPV, un secondprésente les différentes séries de NFA préparées au cours de cette thèse.

Deux nouveaux régioisomères du pérylène-diimide (PDI) ont été synthétisés et caractérisés. Ensuite, l'impact de la position de substitution sur les propiétés optoélectroniques et les performances photovoltaïques a été étudié. De plus, en collaboration avec Heliatek, des NFAs derivés du motif indénothiophène (IDT) ont été conçus pour la réalisation de dispositifs photovoltaïques préparés par dépôts sous vide.

Finalement, le dernier chapitre décrit de nouveaux derivés du benzothioxanthène (BTXI), fonctionnalisés par des groupes électro-attracteurs. Ces composés électro-déficients de la famille des rylènes ouvrent des perspectives en électronique organqiue.

Title : New electron-deficient pi-conjugated systems for potential application in organic photovoltaics.

Keywords : Organic Synthesis, Organic Electronics, Non-Fullerene Acceptors, Vacuum-processed thin-films

Abstract: Major contributors to the revival of the organic photovoltaic (OPV) field, non-fullerene acceptors (NFAs) have attracted considerable research interest and efforts in recent years. As a result, power conversion efficiencies now exceed 18% in single junction solar cells. However, these outstanding results have been obtained with complex and expensive structures and processed by spin-coating, thus making the up-scaling a true challenge for large surface areas.

Hence, in the first chapter a brief overview of the organic photovoltaics and its recent progress is addressed. Thereafter, the second chapter presents the different series of NFA prepared during this thesis.

Two perylene-diimide (PDI) disubstituted regioisomers were newly synthesized and characterized. Then, the impact of the grafting nature and position on the optoelectronic properties and the photovoltaic performances were studied. Thereafter, in collaboration with Heliatek, our efforts were focused in preparing *vacuum*-processable non-fullerene acceptors, derived from the indenothiophene (IDT) scaffold.

Eventually, the last chapter aims at preparing new benzothioxanthene (BTXI) derivatives, enhancing its electron-withdrawing behaviour towards a promising family of rylenes for sublimable organic electronics.